Department of Energy

Award Number: DE-FC26-08NT01584

High Extraction Phosphors for Solid State Lighting

Final Report

Reporting Period: July 2008 - September 2011

Prepared for:
Dr. Brian Dotson
Program Manager
Buildings Industrial Technologies Division
U.S. Department of Energy
National Energy Technology Laboratory
3610 Collins Ferry Road
P.O. Box 880
Morgantown, WV 26507-0880
(304)285-4545

Prepared by:
Dr. Chris Summers, Dr. Hisham Menkara and Dr. Brent Wagner

Phosphor Tech Corporation
3645 Kennesaw North Industrial Pkwy, Ga 30144
chris@phosphortech.com
(404) 664-5008 (phone) - (770) 828-0672 (Fax)
www.phosphortech.com

August 2012

TABLE OF CONTENTS

LIST OF FIGURES

LIST OF TABLES

1. Introduction and Background

This 3-year project involved the development of high efficiency bulk luminescent materials, as well as novel nano-sized phosphors for solid-state white LED lamps. Solid-state LEDs are expected to revolutionize lighting and provide the US industry with competitive technologies that will significantly reduce global energy use and environmental pollution.

Solid state lighting is rapidly gaining momentum as a highly energy efficient replacement technology for incandescent and eventually fluorescent lighting. However, current high brightness solid state devices suffer from reduced luminous efficiencies due to scattering, re-absorption, and thermal quenching losses inherent in conventional phosphors and LEDs. The bulk and nanostructured luminescent materials that were investigated in this project have broad and size-tunable absorption bands, size and impurity tuned emission bands, size-driven elimination of scattering effects, and a distinct separation between absorption and emission bands. Furthermore, these materials have high and tunable refractive indices (n~2.2-2.8) that enable them to match that of the GaN-based LED for maximum light extraction. In addition, some compositions even display the unique ability to maintain, or even improve, luminescent efficiency at higher temperatures similar to those experienced in today's high brightness LEDs. These innovations were accomplished through the use of novel synthesis techniques suitable for high volume production for LED lamp applications. The program goal was a full-color set of high quantum yield phosphors with high chemical stability.

These technologies are applicable to most LED light sources where a fluorescent color conversion layer is used. Examples are applications such as lighting in portable electronics, indoor/outdoor lighting, and traffic signaling which can always benefit from increased efficiency and color flexibility. Also, increased efficiency will open new markets where traditional light sources currently dominate and will increase the existing market penetration of LED lamps. Finally, increased lighting efficiency and use of LEDs will lead to significantly reduced energy requirements, lower levels of pollution, reduced toxic waste (e.g., Hg from fluorescent lamps) and a reduced dependence on foreign oil suppliers.

2. Program Highlights

We present below a bullet point summary of the highlights of this program. Full details are given in the following section: Program Achievements

- **Optimized ZnSeS:Cu,Ag bulk phosphor to achieve efficiency of 91% using erbium (Er) as a sensitizer**
- **Detailed analysis of temperature quenching effects was performed on a large quantity of ZnSeS:Cu,Ag,X and Strontium- and Calcium-thiogallate phosphors**
- **Optimized phosphor blends for high efficiency and color performance: Demonstrated 2-component phosphor system with good white chromaticity, color temperature, and high color rendering**
- **Breakthrough achieved in understanding of "anti-quenching" behavior**
  - **physical bandgap model developed**
- **Optimization of ZnSe:Mn nanophosphors achieved ~85% QE**

- **"Large" (>20nm) nanocrystals were synthesized and exhibited bulk-like behavior and blue light absorption**
- **Limitations of core-shell nanocrystal systems explained and alternative delta-doped structures developed**
- **Developed one-pot manufacturing protocols for ZnSe:Mn nanophosphors**
- **ZnSeS screens and ZnSeS particle phosphors encapsulated with Al_2O_3 and TiO_2 using ALD significantly enhanced stability (>8X better) and increased luminescence efficiency due to improved surface passivation and optical coupling**
- **A large-volume fluidized bed ALD system was designed and can be adapted to any future commercial ALD or vapor deposition system. A small-scale fluidized ALD system was implemented.**
- **Optical simulations developed to evaluate and optimize various phosphor mixtures and device configurations**

  - Used to define scattering properties of nanophosphors
- **Promoted and assisted in the implementation of realistic phosphor material models into commercial modeling programs**
- **In 2009, recognized by U.S. Department of Energy award for "significant achievements in solid-state lighting"**
- **Based on above developments, PhosphorTech offers a broad range of conventional particle phosphors and nanophosphors**

Presentations

1. **Invited**: B. K. Wagner, Z. Kang, H. Menkara and C. J. Summers, "Quantum Dots, their Properties, Synthesis and Applications," 14th International Diffuse Reflectance Conference, Wilson College, Chambersburg, PA., Aug. 4, 2008
2. R. A. Gilstrap Jr., H. M. Menkara, B. K. Wagner, and C. J. Summers, "Doped Quantum Dots for Solid-State Lighting," Proceedings of the 2008 Conference on Electroluminescence and the Science and Technology of Phosphors and Emissive Materials. Rome, Italy, 7-11th September, 2008
3. H. Menkara, T. R. Morris II, R. A. Gilstrap Jr, B. K. Wagner, and C. J. Summers, "Sulfoselenide Phosphors And Nanophosphors For Solid-State Lighting", Proceedings of the 33rd International Conference & Exposition on Advanced Ceramics & Composites, Daytona, January 2009.
4. Christopher J. Summers, Hisham M. Menkara, Richard A. Gilstrap Jr., Mazen Minkara, and Thomas Morris, "Nanocrystalline Phosphors for Lighting and Detection," Pacific Rim International Materials Conference: PRICM 7, Nanomaterials: Symposium D, Cairns, Australia, 2-6th August (2010)
5. C. J. Summers, T. R. Morris, M. Minkara, A. Thamban, R. Gilstrap, B. Wagner, and H. Menkara, "Broadband Nanocrystalline Phosphors for UV to White LED Applications", 2rd NanoToday Conference, 9-12 December 2011, Hawaii

Publications

1. Christopher J. Summers, Hisham M. Menkara, Richard A. Gilstrap Jr., Mazen Minkara, and Thomas Morris, "Nanocrystalline Phosphors for Lighting and Detection," Proceedings of Pacific Rim International Materials Conference: PRICM 7, Nanomaterials: Symposium D, Cairns, Australia, 2-6th August (2010)

2. **Invited**: H. Menkara, R. A. Gilstrap Jr., T. Morris, M. Minkara, B. K. Wagner, and C. J. Summers, "Development of nanophosphors for light emitting diodes," Special Edition on Solid State Lighting; Optics Express, 19, A972 (2011)

Task 1: Optimization of Phosphor Quantum & Extraction Efficiencies

In this task, a variety of synthesis and annealing procedures were developed for significantly enhancing the luminosity and color performance on sulfur-selenide based phosphors. The initial studies concentrated on the synthesis and doping of ZnSeS based materials and understanding their physical properties, most significantly their anti-quenching behavior and saturation properties. The investigations continued by developing the Sr- and Ca-based thiogallates to improve the color spectrum. In addition to sintering powder phosphors several investigations were made to develop "slab-like" phosphor materials for lower scattering and higher brightness. Procedures were developed for incorporating these materials into commercial LED devices structures and their properties studied. Some of these results as they pertain to material properties are presented in this task and other more device related results are presented in Task 5.

At the very beginning of this task, in order to address the goal of obtaining QE exceeding 90%, all processing procedures were critically reviewed and dedicated facilities set up. Sources for higher purity materials (mainly ZnS, ZnSe, Cu and Ag) were identified and orders placed for 4 nines and 6 nines materials. High purity grinding balls and crucibles suitable for existing planetary mills were also identified. A planetary mill was mechanically modified to allow for inert atmosphere (Argon or Nitrogen) milling at high speeds and dedicated for material processing related to this task. This will limit oxygen and other potential contaminants or oxidizers from interacting and reacting with the precursors during the extended milling process required to prepare homogenous and uniformly-doped precursors.

Furthermore, due to the wide range of material and process parameters, as well as the sensitivity of this material system to processing conditions, a design of experiment tool, Design-Expert®, by Stat-Ease, Inc was used for experimental design and data analysis. The data was analyzed using a response surface method (RSM) and cube plots. RSM is a statistical technique designed to determine ideal process settings and achieve optimal performance. A cube plot displays the average response values at all combinations of process parameters settings. An investigation of over 200 samples of yellow- to orange-emitting sulfoselenide $ZnSe_xS_{(1-x)}$:Cu,Al,Cl samples was conducted using a wide range of Se/S ratios, Cu, Al, and Cl concentrations. The four factors used in the analysis were (A) "Se Mol%" (x=0.15-0.55 mol%), (B) "$AlCl_3$ Doping" (0-900 ppm), (C) "$CuCl_2$ Doping" (40-200 ppm), and (D) "$ZnCl_2$ Doping (0-600 ppm). In addition, over a dozen annealing experiments were conducted on yellow to red sulfoselenide samples $ZnSe_xS_{(1-x)}$:Cu,Ag (x = 0.4 - 1.0) using H_2S vapor annealing for a range of temperatures and annealing times. The annealing time was used to control the amount of sulfur gas reacting with the phosphor powders. For the annealing experiments, the three design factors were (A) "Annealing Time" (1-3 hrs), (B) "Annealing Temperature" (700-900^oC), and (C) "x" value (0.4-1.0) representing the Se/S stoichiometric ratio in $ZnSe_xS_{(1-x)}$. The peak intensity (under blue excitation) of each phosphor was used as the response parameter in the analysis

because it can be accurately measured to within <1%. Measurement of quantum efficiency (QE) is far less accurate (>5%) due to the complexity of the measurement and assumptions required. Therefore, QE measurements were performed following the optimizations on the best samples.

Figure 1 illustrates the dependence of peak intensity on annealing time and temperature for $ZnSe_{0.5}S_{0.5}$:Cu,Ag (x = 0.5), where the predicted optimal conditions correspond to an annealing time of 1.5 hours and annealing temperature around 900 ^{o}C.

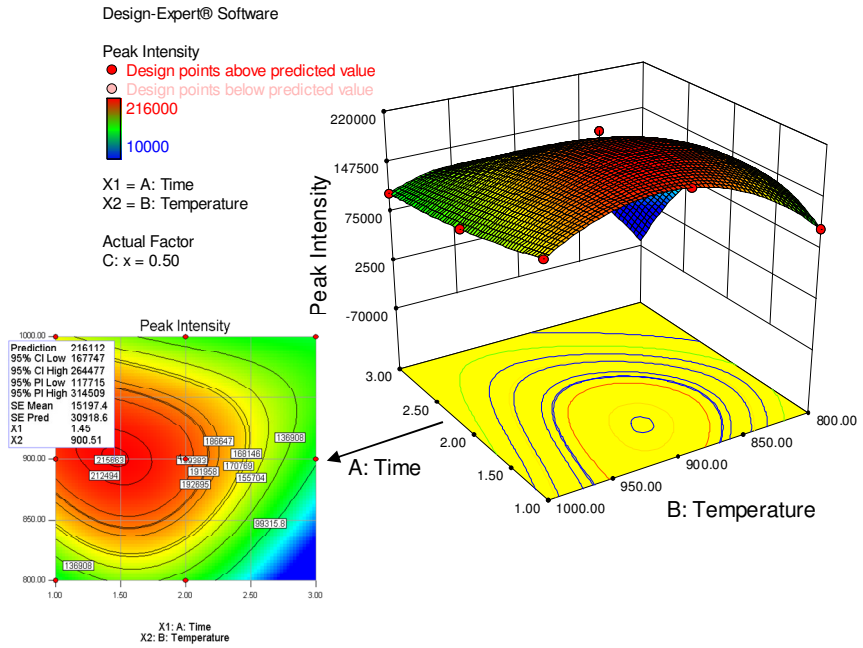

Figure 1. Response surface and contour plots for ZnSeS (x=0.5) showing dependence of peak intensity on annealing time (A) and temperature (B), as well as predicted optimal annealing parameters.

Figure 2 displays a cube plot for $ZnCl_2$=150 ppm showing the best and worst combination of Se, $CuCl_2$, and $AlCl_3$ factors for achieving the optimal peak intensity response of the phosphor under blue LED (455 nm) excitation.

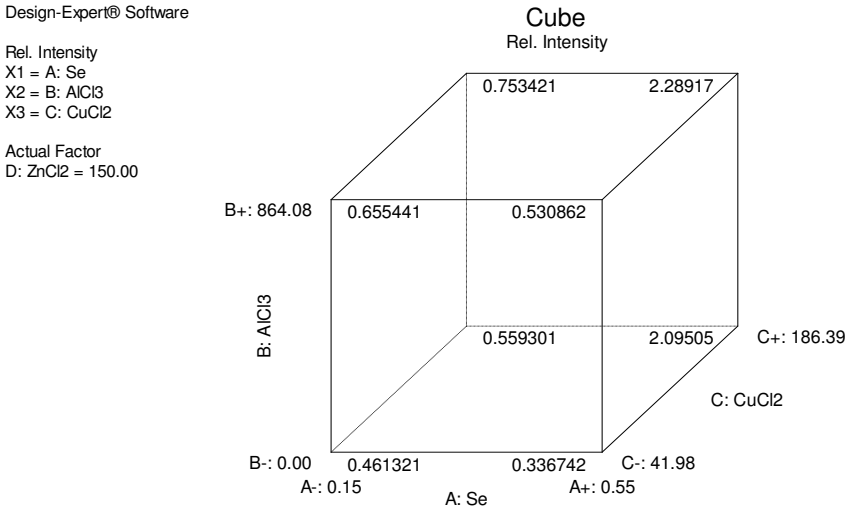

Figure 2. Cube plot showing the best and worst combination of Se, $CuCl_2$, and $AlCl_3$ factors for achieving the optimal peak intensity response of ZnSeS:Cu,Al,Cl ($ZnCl_2$ =150 ppm).

As expected, the above plot shows that the effect of Cu concentration on emission intensity (under blue excitation) becomes more significant for higher Se content, due to better blue light absorption by ZnSe. Furthermore, even though higher Cu concentration alone results in increased intensity for a fixed Al co-doping concentration, the effect on emission intensity is more prominent when both Cu (acceptor) and Al (donor) are increased simultaneously. However,

increasing both Cu and Al results in an undesirable shift to longer wavelengths, as shown in Figure 3. This is caused by the fact that Al constitutes a shallow donor level in the ZnSeS bandgap and, therefore, effectively reduces the energy of emitted photons, resulting in longer wavelengths. Therefore, an optimal doping must be maintained in order to keep the emission of the phosphor in the yellow-orange part of the spectrum for white light applications using blue LEDs.

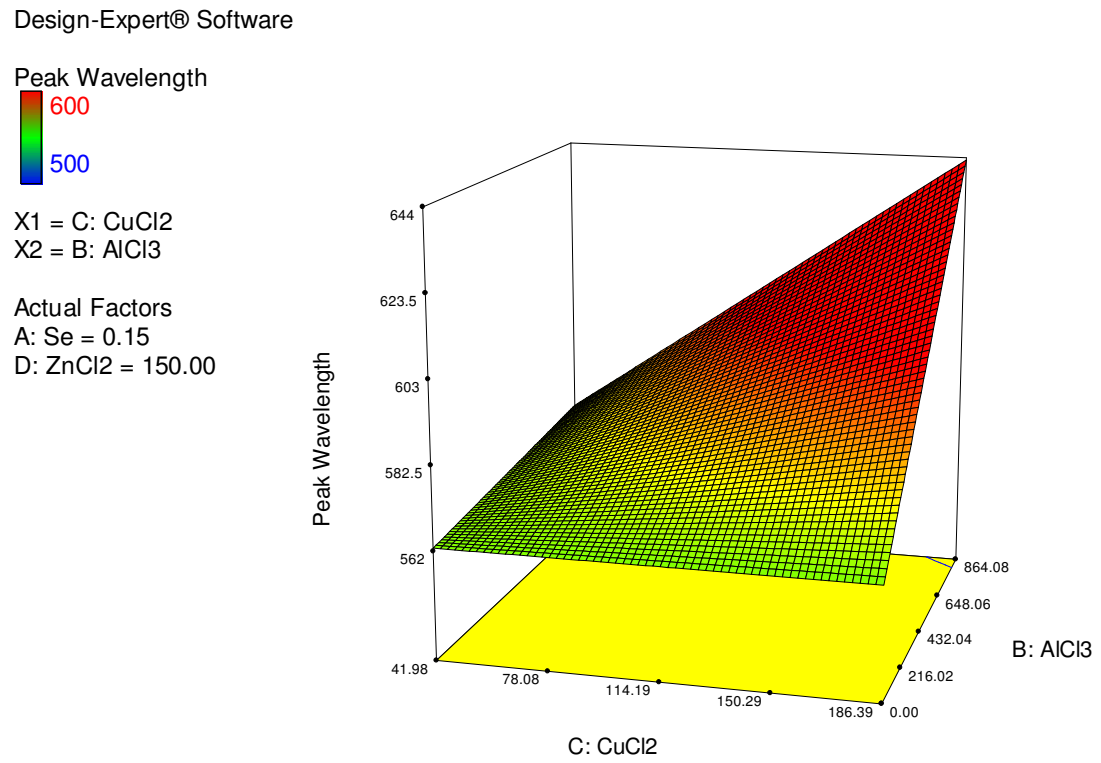

Figure 3. Response surface plot showing the effect of changing $CuCl_2$ and $AlCl_3$ on peak wavelength for a fixed Se (0.15 mol%) and $ZnCl_2$ (150 ppm).

All of the synthesized samples were characterized and compared to the most efficient commercial YAG:Ce phosphors, produced by Nichia. Unlike YAG:Ce, which has a peak between 555-570 nm and a full-width at half max (FWHM) ~118nm, the ZnSeS yellow-to-red-emitting materials peak between 575-650 nm with a FWHM of 88nm, as shown in Figure 4. The peak intensity can be green-shifted down to ~535nm by further increasing the S/Se ratio, and therefore the ZnSeS bandgap (from 2.67eV for ZnSe to 3.66eV for ZnS). However, a trade-off between blue light (465 nm => 2.67 eV) absorption and phosphor emission color is required, as for maximum blue light absorption a 100% ZnSe composition is required, which as shown in Figure 4 is not suitable (on its own) for white light generation. The figure shows the blue LED peak at ~455nm used to excite these phosphors.

Finally, to confirm the viability of this procedure, elemental analysis of selected ZnSeS samples was conducted using ICP-MS (Inductively coupled plasma mass spectrometry), which is a highly sensitive technique capable of the determination of a range of elements at very small concentrations with detection limits around 2.5 ppm. ICP-MS is based on combining inductively-coupled plasma to produce ions (ionization) with a mass spectrometer for separating and detecting the ions. The various phosphor samples were first digested using hydrofluoric acid (HF) solution followed by a nitric acid (HNO_3) solution. Any remaining solids were then re-digested using hydrochloric acid (HCl) and then microwaved in sealed Teflon containers for 20

minutes at 400 Watts followed by 20 additional minutes at 300 Watts. The process was repeated until all solids were dissolved and the solution turned clear. The results of the ICP-MS testing are shown in Table 1 (top) and are very consistent with the actual concentrations of the various elements used during synthesis of these samples (bottom). This confirms the stoichiometry of the various samples, as well as the levels and ratios of the Cu and Ag doping concentrations, as predicted by the synthesis conditions.

Table 1. ICP-MS analysis results on various ZnSeS:Cu/Ag phosphor samples (top). Actual percentages of various elements used in the synthesis of the analyzed samples (bottom)

Sample#	Zn (ppm)	S (ppm)	Se (ppm)	Ag (ppm)	Cu (ppm)
CZ88	50.78485%	10.48326%	38.68069%	0.00024%	0.02561%
CZ74	50.98932%	10.84969%	38.11058%	0.00024%	0.02521%
CZ1	58.35244%	23.43434%	18.15409%	0.00024%	0.02957%
CZ12	58.16449%	23.10859%	18.65456%	0.01892%	0.02673%

Sample #	Zn (ppm)	S (ppm)	Se (ppm)	Ag (ppm)	Cu(ppm)
CZ88	52%	10%	38%	0.0000%	0.0257%
CZ74	52%	10%	38%	0.0000%	0.0257%
CZ1	60%	22%	18%	0.0000%	0.0296%
CZ12	60%	22%	18%	0.0228%	0.0296%

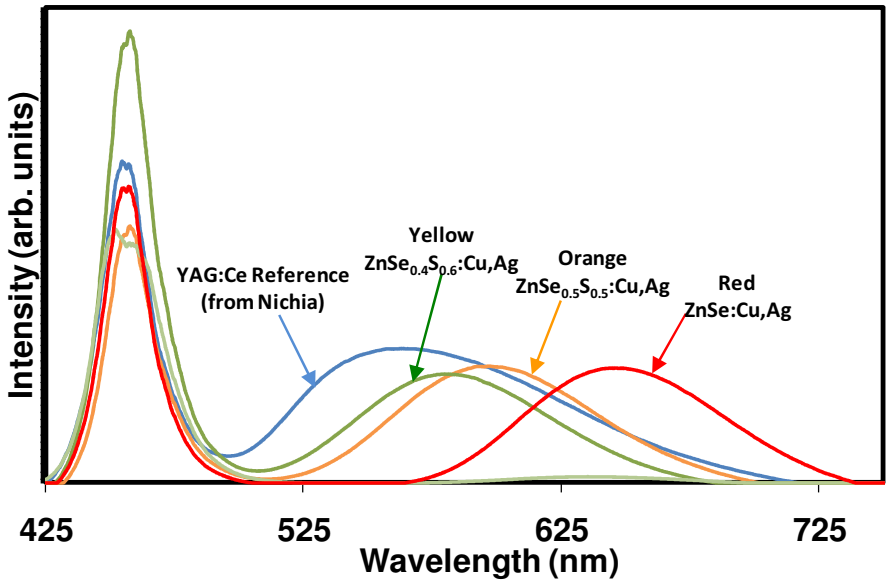

Figure 4. Spectral comparison of YAG:Ce phosphor with various ZnSeS pumped by a blue LED at 455nm.

In addition to conventional annealing, several additional high temperature phosphor treatments were conducted in vacuum using vapors produced from solid sources of ZnS and ZnSe materials. This involved sealing of yellow-orange emitting ZnSeS:Cu,Ag (ZSS) phosphor powders inside quartz tubes along with undoped ZnSe and/or ZnS crystals used for chemical vacuum deposition (CVD) of thin-films. The samples were fired at 800 ^{o}C for 2 hours and slowly cooled to room temperature before removing the materials and separating the phosphor powders from the un-evaporated crystals using a fine mesh. The luminescent performance of the treated phosphor powders were compared to Nichia's YAG:Ce (reference) and to the original (untreated) ZnSeS:Cu,Ag materials using a blue LED operating at 455 nm. The luminescence results from these experiments are shown in Figure 5 where the effect of ZnS/ZnSe-treatment on the peaks and shapes of the emission spectra is clearly visible.

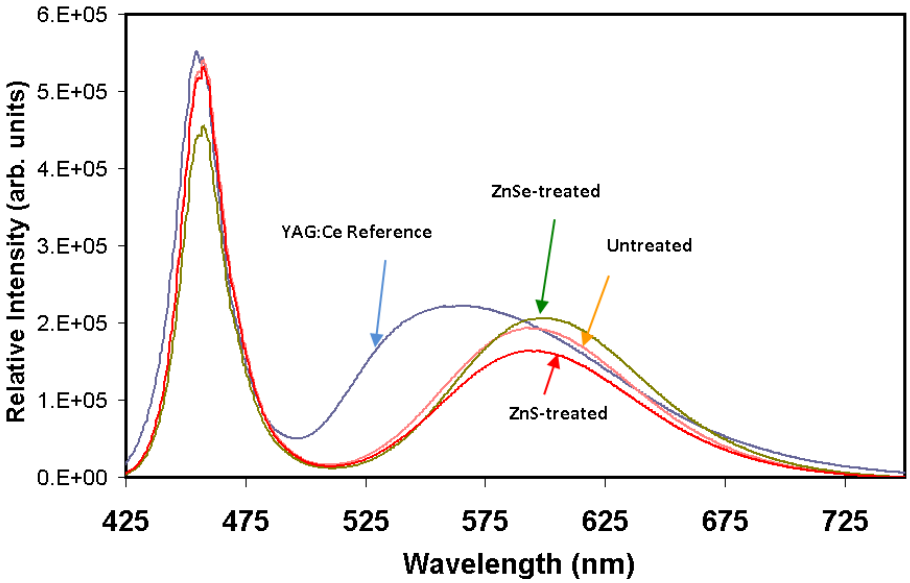

Figure 5. Spectral comparison between untreated and ZnS/ZnSe-treated ZnS:Cu(Ag) phosphor under 370nm UV excitation.

The above experiments demonstrated that heat treatment of ZnSeS phosphors with ZnSe vapor can increase the emission intensity under blue LED excitation, while treatment with ZnS vapors has the opposite effect. This is clearly due to enhancement in blue absorption efficiency by the smaller bandgap (2.7 eV) ZnSe layer as the larger bandgap of ZnS (3.66 eV) is too large to absorb blue light.

As a result of **the various optimization experiments, we have been able to determine the ideal host composition, activator/co-activator doping concentrations, and process conditions that yielded the best quantum efficiency (QE)** of any $ZnSe_xS_{(1-x)}$:Cu,Ag sample made to date. **This resulted in an increase of QE from ~75% at the beginning of the program to ~91%** for the sample shown in Figure 6.

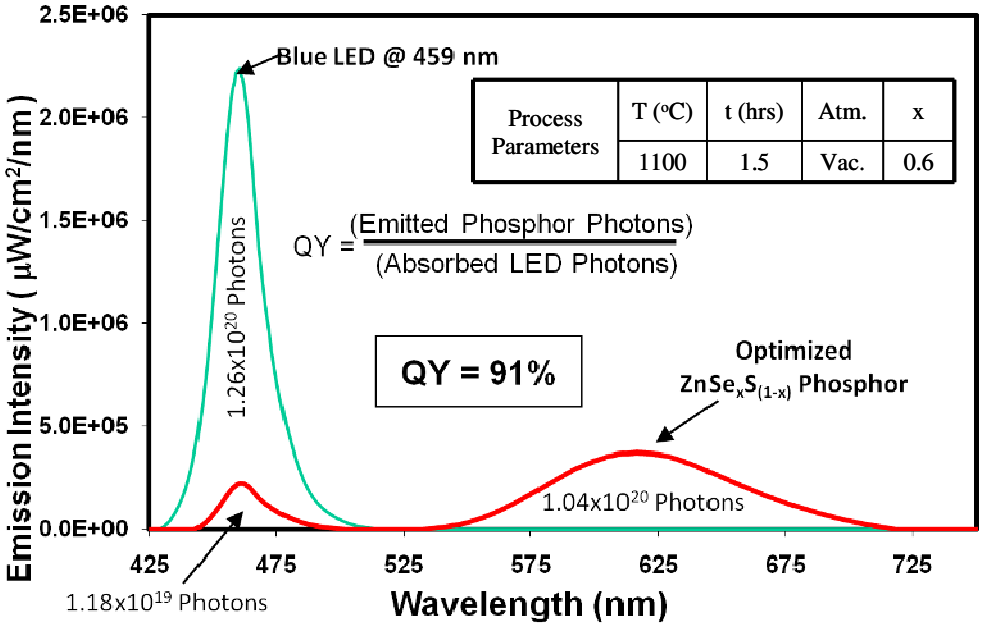

Figure 6. Spectral data collected in an integrating sphere showing QE calculation of the best $ZnSe_xS_{(1-x)}$:Cu,Ag sample and corresponding material and process parameters.

Anti-quenching Behavior

As mentioned previously on the highlights, one of the most attractive properties of the ZnSeS based system is that it displays an "anti-quenching" behavior. As shown in Figure 7, the PL intensity normalized to room-temperatures, was found to increase with increasing temperature up to a maximum increase of ~5% between 150 and 170 C. This is very close to the operating temperature of an LED. Additionally, for many other phosphors, including YAG:Ce their brightness is shown to decrease, potentially giving the ZnSeS material system a 15% advantage over other phosphors. However, note that the "anti-quenching" behavior only occurs for certain Ag/Cu ratios. So far, the best result was observed at 52% Ag and that either too high or too low Ag concentration results in worse performance. The sample with 100% Ag has poorer thermal performance than that with 100% Cu, implying that Cu-Ag interactions are key for improved intensity maintenance at high temperature.

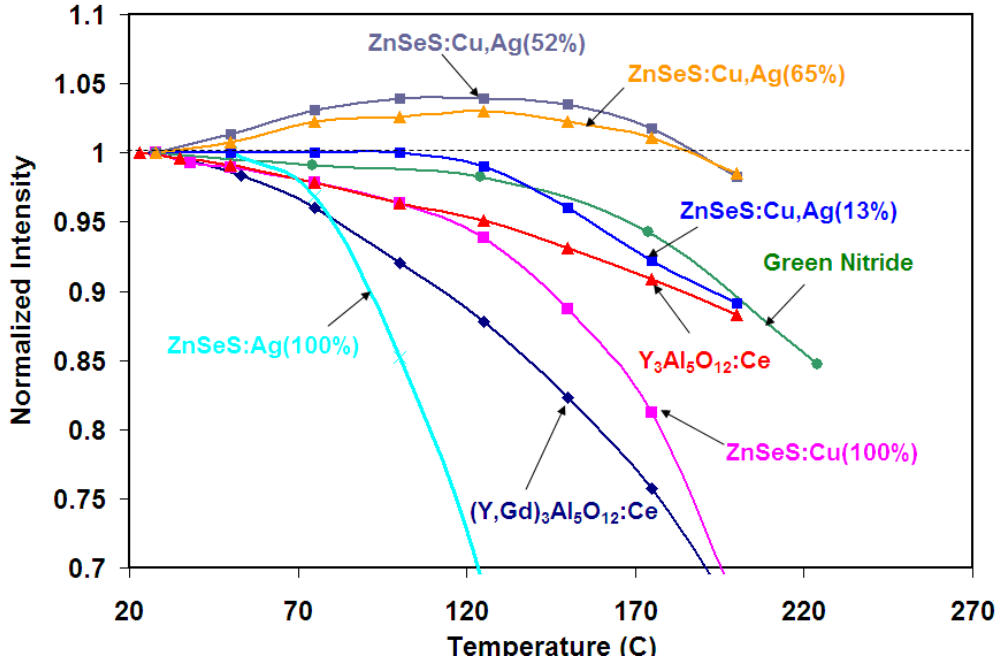

Figure 7. Thermal behavior of ZnSeS:Cu,Ag phosphors compared to conventional materials.

To explain this unique "anti-quenching" phenomenon and to investigate the role that Ag plays in the "anti-quenching" observed in co-doped phosphor materials, over a dozen Cu- and/or Ag-doped sulfoselenide ZnSeS samples were synthesized with a wide range of Ag/Cu molar ratios from 0% to 100% Ag. Then extensive photoluminescence (PL) and PL excitation (PLE) spectroscopy characterizations were made under blue light excitation, and used to develop a physical model to explain these effects from an energy band gap perspective. As expected, some of the Ag/Cu doped samples exhibited an initial increase of emission intensity with temperature under blue LED (455 nm) excitation, followed by the typical thermal quenching observed in other conventional phosphors, as shown in Figure 7. **From the PL/PLE studies, a major breakthrough was achieved in our understanding of the "anti-quenching" phenomena observed in Cu/Ag-doped ZnSeS phosphors**. Using bandgap energy physics, along with the PL/PLE data, we have accurately identified the exact bandgap locations of the various donor and acceptor levels in Cu- and Ag-doped ZnSeS materials, as shown in Figure 8. This, in turn, helped explain the unique thermal behavior of these phosphors at temperatures below those where thermal ionization (into the conduction band) takes over. Once thermal ionization dominates, the

ZnSeS:Cu,Ag phosphors behave similar to other conventional materials. As in conventional phosphors, thermal quenching occurs due to the photo-ionization of carriers from excited energy levels near the conduction band (Al and Cl in this case). These ionized carriers are then converted into phonon (heat) and lost inside the lattice instead of creating additional photons. However, in the case of donor-acceptor (D-A) activators in ZnSeS, a competing thermally-induced phenomenon occurs in energy levels close to the valence band (e.g, Ag in this case). These shallow acceptors appear to contribute to electron-hole pair generation from thermal energy at high temperatures. As a result, the transfer of energy between Cu and Ag helps to enhance the conversion efficiency of high energy blue photons to lower energy yellow-orange photons, thereby increasing the quantum yield of the phosphor at higher temperatures.

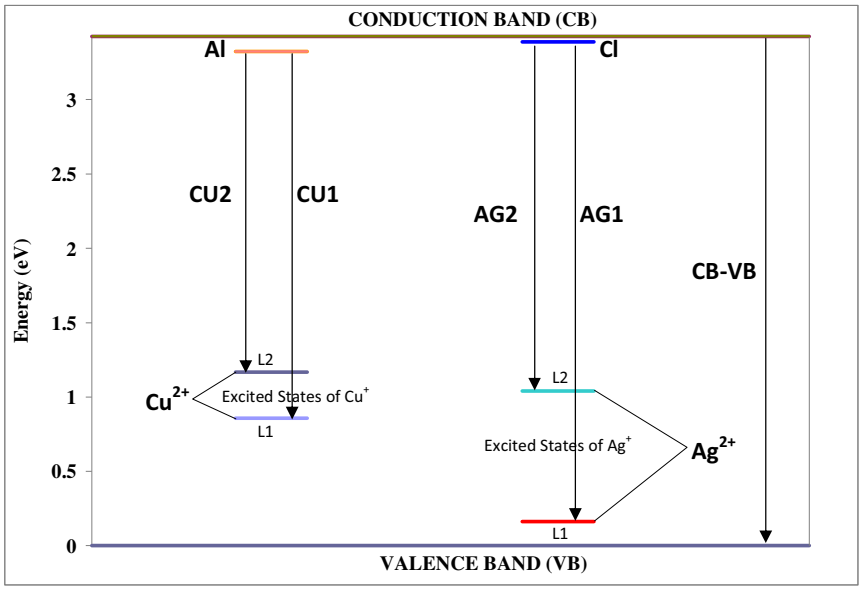

Figure 8. Energy bandgap and exact donor/acceptor positions of Cu/Ag-doped $ZnSe_{0.25}S_{0.75}$ constructed using room temperature PL and PLE data.

Figure 9 displays the room temperature PL data of a Cu/Ag-doped $ZnSe_{0.25}S_{0.75}$ yellow-orange emitting phosphor, excited by an above-bandgap source at 320 nm. The data shows two major emission bands: a weak one extending from around 350-420nm and a strong one extending from 420-670nm. Since these two bands are clearly made up of several overlapping emissions from various centers, a Gaussian curve fit analysis was performed, as shown below. The best fit revealed the presence of two higher-energy sub-bands and three lower-energy ones. The CB-VB sub-band at ~362 nm corresponds to host emission from the conduction band (CB) to the valence band (VB), while the AG1 sub-band corresponds to the shallow excited acceptor state (L1) of Ag^{2+}, shown in Figure 8. For the lower-energy (longer wavelength) sub-band, CU1 and CU2 correspond to the two excited states of Cu^{2+}, while AG2 corresponds to the higher excited state (L2) of Ag^{2+}.

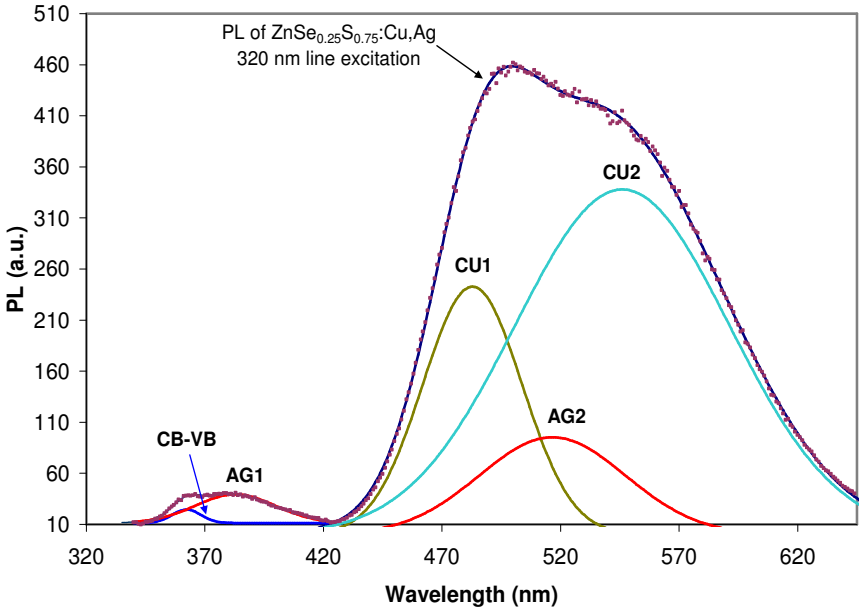

Figure 9. PL data from Cu/Ag-doped $ZnSe_{0.25}S_{0.75}$ under 320nm excitation. Line graphs show Gaussian fits used to identify various emission centers within the bandgap. Based on this data, energies of various luminescent centers were determined, as shown in the bandgap energy diagram in Figure 8.

Figure 10 shows high resolution PLE data for Cu/Ag-doped $ZnSe_{0.25}S_{0.75}$ phosphor at room temperature (RT) and 130°C. This data was acquired by monitoring the 552nm CU2 PL peak while the excitation wavelength is scanned from 355nm to around 475nm. Two major bands were identified on the PLE spectra. The first, at 362 nm, corresponds to the fundamental absorption edge of the $ZnSe_{0.25}S_{0.75}$ host crystal. The second, at 377 nm in the longer wavelength region, is characteristic of the shallow Ag^{2+} (L1) acceptor to conduction band transition. In addition, two weaker donor excitation bands were identified. One at 366nm corresponding to the VB to Cl transition, while the second one at 371nm corresponding to the VB to Al transition. All four bands are illustrated on the band diagram schematic shown in the inset of Figure 10.

Based on the PL and PLE data, we postulate that the "anti-quenching" behavior observed in Cu/Ag-doped ZnSeS phosphor system is a result of thermal stimulation (TS) into the near-VB excited Ag^{2+} level (L1), which is situated at around 0.16 eV from the valence band. At 130°C, the available thermal energy (kT) is about 0.035 eV, placing the shallow Ag^{2+} energy band well within its range. On the other hand, thermal quenching (TQ) is also at play due to the thermal ionization from the shallow donor levels (Al & Cl) into the conduction band. Therefore, at any given temperature, both TS and TQ mechanisms are occurring simultaneously. Once a threshold temperature is reached, TQ begins to dominate and the Cu/Ag-doped ZnSeS phosphor begins to behave like a conventional phosphor system at higher temperatures.

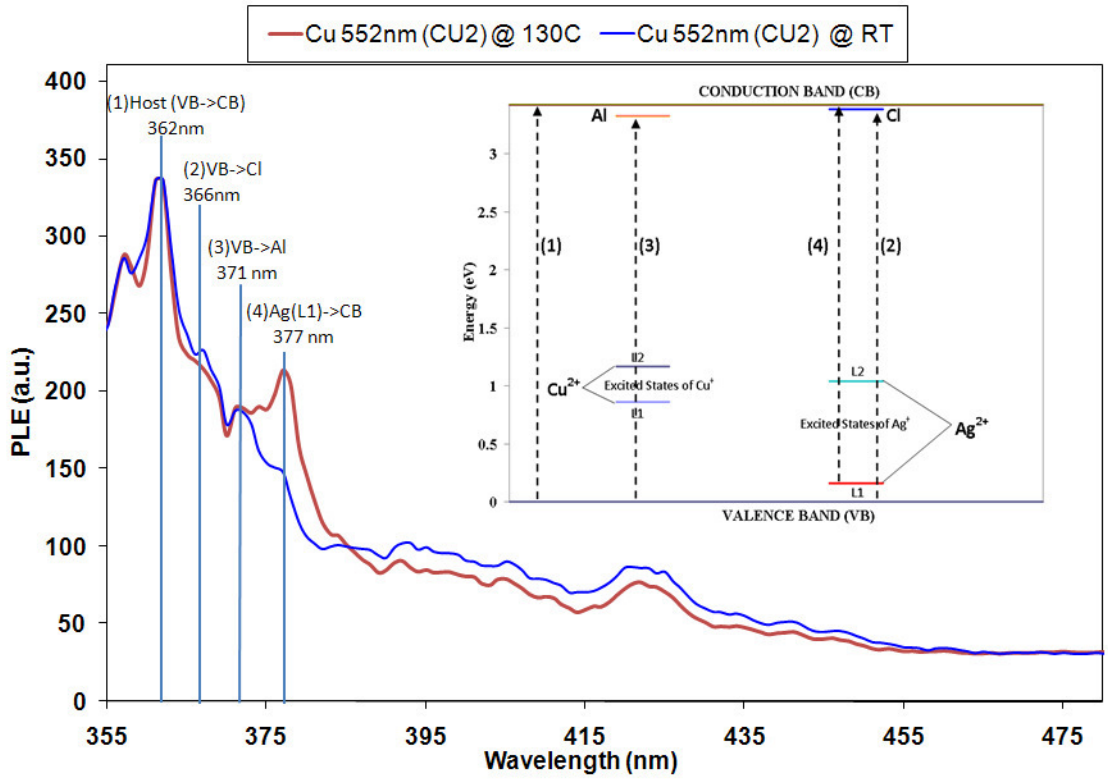

Figure 10. High resolution PLE data for Cu/Ag-doped $ZnSe_{0.2}5S_{0.75}$ phosphor system. Data was used to identify the donor levels and host excitation bands, as shown in the bandgap energy diagram in the inset.

Optimization of Efficiency and Spectral Range

Following the success of the synthesis and annealing protocols developed during the first phase of this program, and the improved understanding of phosphor properties, we next concentrated on: 1) further improving the synthesis and annealing protocols and exploring different dopants for improved efficiencies, 2) Investigating the mechanisms that contribute to enhancing phosphor efficiencies and responsible for saturation, 3) Evaluating alternate fabrication and composite structures for higher extraction efficiencies, and 4) performed LED studies – as reported in Task 5

Thus, during this second phase we synthesized a new series of "SeS" based phosphor materials to further improve their performance; primarily their color performance. In the first study, co-doping of the ZnSeS phosphor was investigated and then these studies were extended to the Sr- and Ca-thiogallate materials. One of the disadvantages of the ZnSeS:Cu system compared to the conventional YAG:Ce phosphor is their narrower emission peak, requiring a mixture of at least two phosphors in order to achieve similar or better spectral coverage and color rendering to YAG-based devices. Whereas YAG:Ce has a full-width-at-half-max (FWHM) of ~121 nm the FWHM of yellow-orange ZnSeS:Cu,Ag is only ~90nm. We have therefore investigated ways to broaden the ZnSeS spectrum towards the longer-wavelength range by the addition of red-emitting co-dopants such as erbium (Er) to the Cu/Ag-doped system. Samples of Er-codoped ZnSeS phosphors were prepared using water-soluble $ErNO_3$ as a precursor. Figure 11 illustrates the effect of Er-doping on the emission characteristics of ZnSeS:Cu,Ag under blue LED (455nm) excitation. The Er peak at 660 nm not only results in a slightly broader (~5nm) emission but is also found to have a positive effect on the conversion efficiency. In fact, the blue down-conversion efficiency increased as a result of the addition of Er.

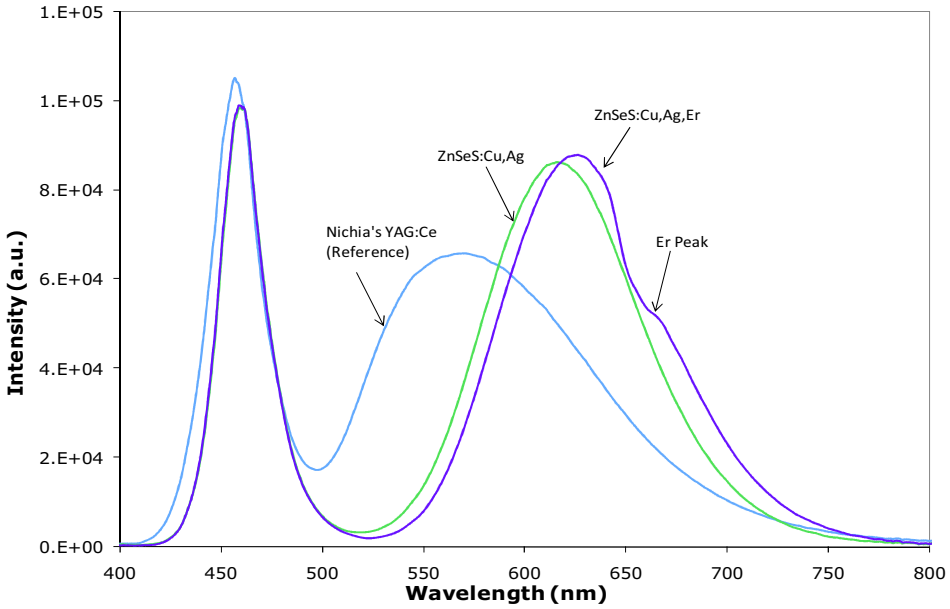

Figure 11. Effect of Er-codoping on ZnSeS:Cu,Ag emission spectrum.

Detailed characterizations on a series of samples with different Er concentrations and Er/Cu ratios showed that the quantum yield (QY) of orange-emitting sulfoselenide (ZnSeS:Cu) phosphors was increased from 88% to 91% using erbium (Er) as a sensitizer. The improvement in QY is believed to be a result of efficient energy transfer between Cu and Er centers within the ZnSeS bandgap. The resulting ZnSeS:Cu,Er phosphor was then mixed with a green Eu-doped strontium (Sr) thiogallate phosphor (QY~80%) to produce a 2-component phosphor system for blue LEDs. The mixture was optimized for high color rendering applications using a thiogallate/sulfoselenide weight ratio of 1.4/3.0. With a blue LED at 460nm and remote excitation of the phosphors, the irradiance spectra shown in Figure 12 were obtained. The 2-component system, using Sr thiogallate with an emission peak around 540nm and a ZnSeS:Cu,Er emitting around 617nm, exhibited a color rendering index (CRI) of 92 compared to the YAG:Ce CRI of 80.5. The (x,y) CIE coordinates and correlated color temperature (CCT) of both systems are fairly close, as shown in the inset. The FWHM of the 2-component system (147nm) was 22nm wider than that of YAG:Ce (125nm), which contributed to the improved CRI performance.

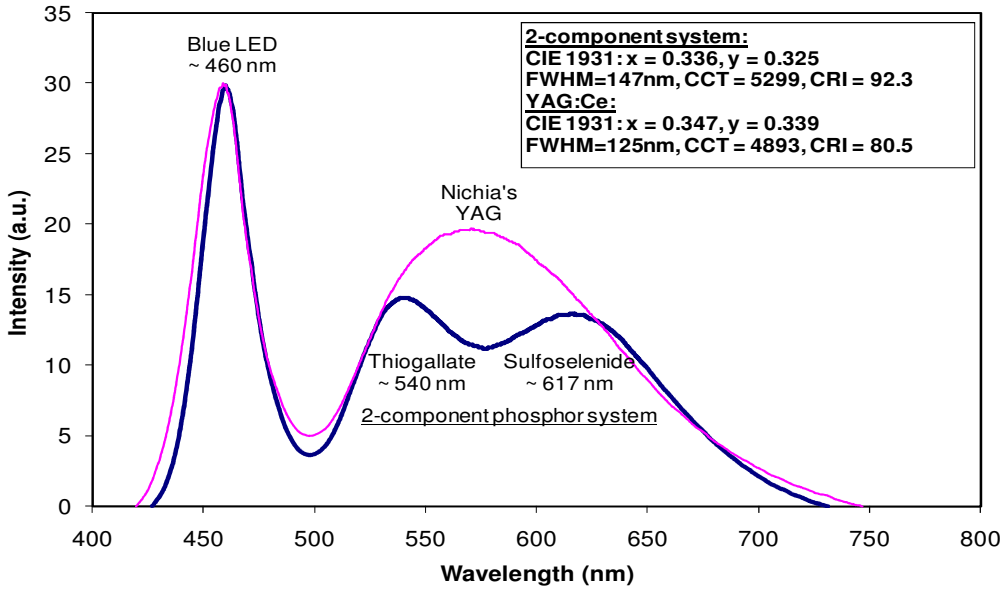

Figure 12. Comparison of 2-component phosphor system with YAG:Ce pumped with a 460nm blue LED.

During this optimization phase, we continued synthesis and testing of a series of samples based on the high **quantum yield (QY~91%) composition**. Both the Se/S ratio and the relative concentrations of various dopants were modified, as shown in Table 2. A blue LED at 460nm was used to test and compare the different phosphors, as shown in Figure 13. As expected, the composition with high Se concentration (60% ZnSe) exhibits better blue light absorption. The most efficient Er-doped samples (Yellow-emitting: CZ160, Orange-emitting: CZ161), were made with only Cu-doping. In each case, the addition of Ag co-doping resulted in a reduction of output intensity. This suggests that the Ag concentration may need to be re-adjusted when Er is used as a co-dopant in these systems.

Table 2. List of different ZnSeS:Cu,Ag,Er samples along with host and doping compositions

CZ#	ZnS	ZnSe	%ZnSe	$AlCl_3$	$ZnCl_2$	$CuCl_2$	$AgClO_4$	$Er(NO_3)_3$
160	5.84	2.94	**25%**	4.50	1.30	1.00		1.30
161	3.10	7.00	**60%**	4.50	1.30	1.00		1.30
166	5.84	2.94	**25%**	4.50	1.30	1.00	0.80	0.65
167	3.10	7.00	**60%**	4.50	1.30	1.00	0.80	0.65
168	5.84	2.94	**25%**	4.50	1.30	1.00	0.80	1.30
169	3.10	7.00	**60%**	4.50	1.30	1.00	0.80	1.30

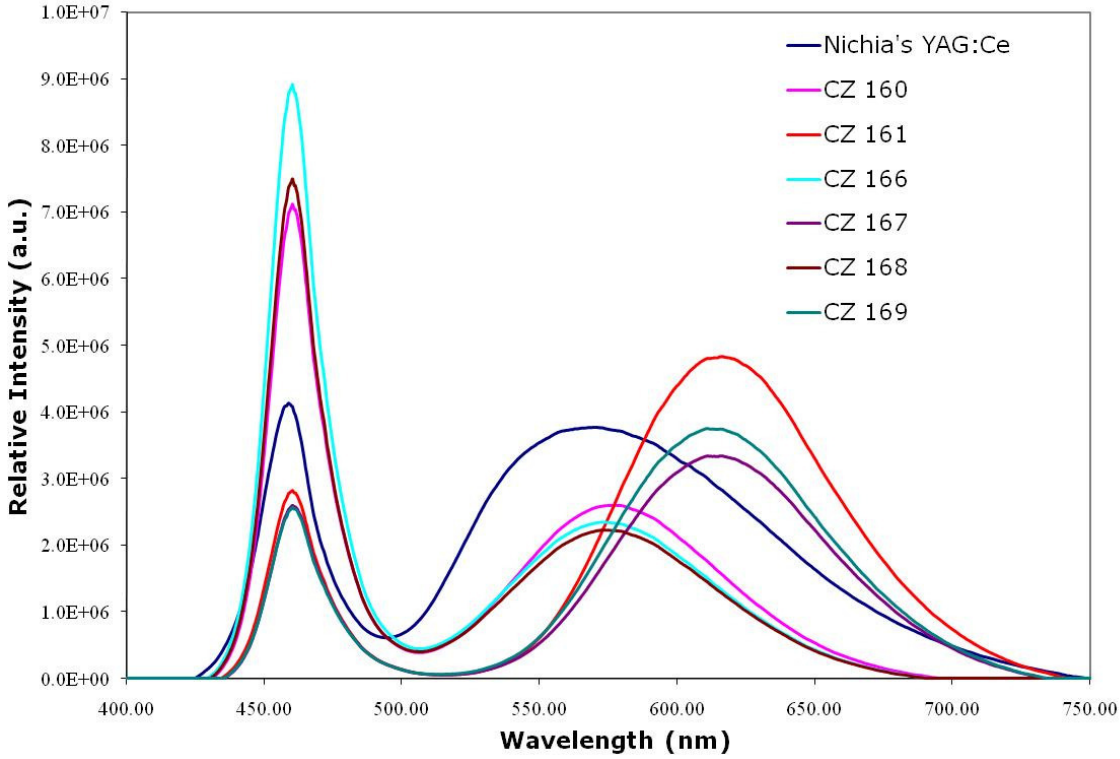

Figure 13 Spectral properties of the various Er-codoped ZnSeS phosphors.

Also the Er-doping scheme has been successful in the 60% Se samples of ZnSeS (ZSS) to samples containing only 25% Se. Several samples were made that scaled all dopants from our "best" Er sample in a range from 0.5 to 2. The goal was to optimize Er-doping in a 25% Se host to achieve a more desirable yellowish color for lighting applications. The results were surprising in that little differences were observed under blue LED excitation between samples with significantly different dopant concentrations. The peak position was on target around 574nm, comparable to YAG. Figure 14 shows the spectra of two of these phosphors compared with YAG, where CZ183 has twice the dopant concentrations as CZ160. Both samples show lower blue absorption compared to YAG, which is expected due to the larger bandgap resulting from the lower Se/S ratio.

Phosphor Blends

We also experimented with new ways to form a stable composite wafer of phosphor and glass, for use on the surface of an LED. The insets in Figure 14 demonstrate the results using the CZ160 ZSS sample encapsulated in glass and placed over a blue LED. The technique used to fabricate the device shown here utilizes a microwave and a crucible, lined with a graphite composite. The microwave heats the crucible up to 900^{o}C within a few minutes. The ZSS phosphor was sandwiched between two pieces of borosilicate glass, which are then fused together by the heat. This method preserves the optical properties of the phosphor, but quantitative testing is underway to confirm this observation.

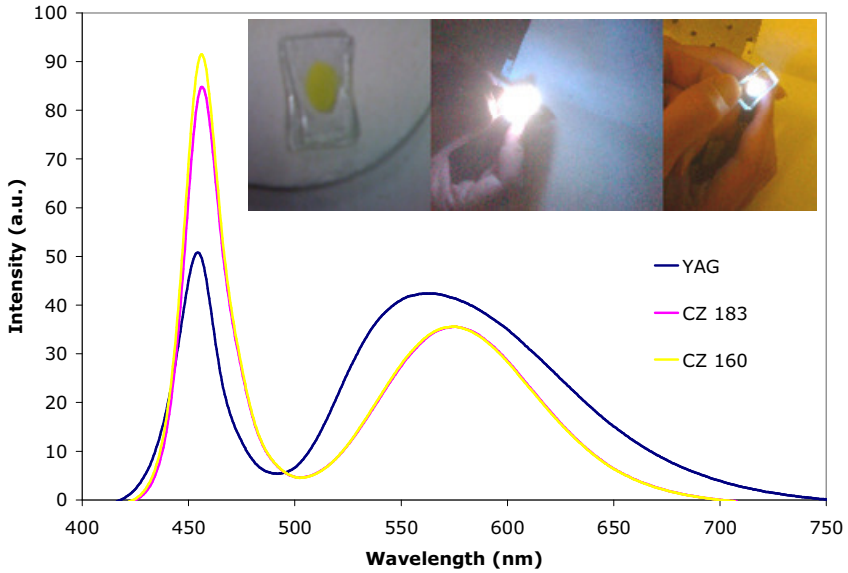

Figure 14. Comparison of YAG and ZSS doped with Er in a 25% Se host. CZ183 has twice the dopant concentration as CZ160, yet it shows little difference under blue LED excitation. Insets depict CZ160 encapsulated in glass and backlit using a blue LED.

The optimization study was also extended to investigation of various ratios of a two-component sulfoselenide phosphor system comprised of $CaSrGa_2(Se,S)_4$ (CTG) and ZnSeS:Cu (ZSS) for high luminous efficiency using a blue LED at 455nm. The phosphor blends were compared to YAG:Ce, which produces a "cool white" color when combined with the same blue LED. The concentration of the orange-emitting ZSS used in this study varied from 0% to 25%, by weight. The resulting spectra from these phosphor blends are shown in Figure 15, while the quantitative color and intensity data is presented in Table 3. The optical system was configured to yield a YAG:Ce normalized lumen value of 1.0. It is evident from the spectral data that increasing the ZSS phosphor ratio to 25% results in a 10% drop in the lumen value of the phosphor blend and a shift of the dominant wavelength from 563nm to 566nm. Interestingly enough, the full-width half max (FWHM) increases from around 44nm (100% CTG) by 5-6 nm for the various ZSS ratios, but still is highest at 51nm for the 75% CTG sample. This FWHM value is still less than half that of YAG:Ce, which is about 106nm. Such "narrow-band" emission from the CTG phosphor is the main reason why it provides 21% higher lumen content compared to YAG:Ce, since more of the CTG emission intensity is centered near the peak of the photopic eye sensitivity curve.

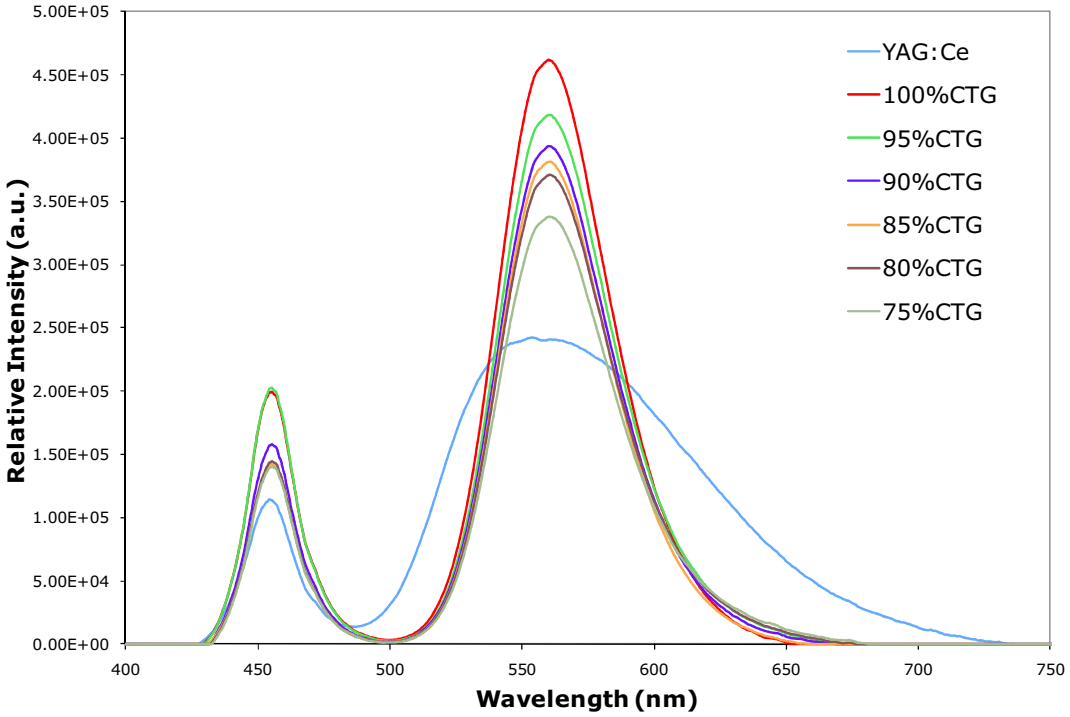

Figure 15. Spectra of various CTG/ZSS phosphor blends compared to YAG:Ce under 455nm excitation.

Table 3. Color and intensity data of various phosphor blends compared to YAG:Ce

Sample	Lumen	CIE x	CIE y	CCT	Dom Wave (nm)	Peak	Intensity	FWHM
YAG:Ce	1.0	0.404	0.469	4030	570	555	2.41E+05	106.39
CTG 100	1.21	0.365	0.467	4790	563	560	4.60E+05	44.41
CTG 95	1.10	0.367	0.456	4729	564	560	9.15E+05	50.16
CTG 90	1.04	0.374	0.473	4611	565	560	3.90E+05	49.78
CTG 85	0.98	0.375	0.479	4629	565	561	3.70E+05	49.46
CTG 80	0.99	0.381	0.476	4489	566	560	3.72E+05	50.41
CTG 75	0.91	0.380	0.468	4494	566	561	3.39E+05	51.3

Saturation Behavior of ZnSeS

The increasing output power of LEDs makes it essential to understand the effect of high pumping power on phosphor performance. Thus, we have investigated the optical power saturation properties of various ZnSeS:Cu,Ag phosphor systems as compared to the more traditional LED phosphor materials such as YAG:Ce and orthosilicates ($SrBaSiO_4$:Eu). In order to achieve high power densities on the phosphor surface, a blue (457nm) laser diode source was used in the experiments. The laser unit (model# BL457-500), manufactured by Laser Lab Components, Inc., has a maximum output of 500 mW, a 0.1nm spectral linewidth, and was

focused down to a 1 mm beam diameter. This resulted in a maximum power density ~135 W/cm^2, which was calculated using the following formula for a Gaussian beam profile:[1]

$$\text{Power Density (W/cm}^2\text{)} = 255*\text{Power}/d^2$$

Where d is the laser beam diameter in mm. A diode laser was used instead of a high power LED in order to spectrally de-couple the phosphor emission from the excitation source and achieve a variable power density (by laser current control) on the phosphor surface while maintaining a relatively constant beam diameter. With such an approach, the heating of the phosphor was kept to a minimum (due entirely to Stokes shift) in order to separate thermal quenching effects from the test results. Also the effect of heat generated from the Stokes shift was minimized by placing all phosphor particles in oil to quickly dissipate the heat.

The resulting optical saturation data is shown in Figure 16. While both the YAG:Ce and orthosilicate phosphors exhibited fairly linear behavior as a function of power density, the various ZnSeS phosphors chosen for this test showed significant differences. The sample doped only with Cu (ZnSeS:Cu(100%)) displayed the worst saturation behavior, reaching a plateau at around 120 W/cm^2. However, the sample co-doped with 200 ppm of Ag (ZnSeS:Cu,Ag(52%) exhibited a fairly linear saturation behavior similar to that of YAG:Ce and the orthosilicate phosphor. Interestingly, this same sample (ZnSeS:Cu,Ag(52%) also displayed "anti-quenching" behavior, as shown in Figure 10 from data obtained earlier. On the other hand, the Cu-doped sample (ZnSeS:Cu(100%)) displayed poor thermal quenching characteristics, also shown in Figure 17. When both the Ag and Cu doping levels are raised by 2X to the ~400 ppm levels, the phosphor begins to display saturation behavior, as shown in Figure 17. This is an unusual behavior since, in most phosphor systems, saturation properties can be improved by higher doping concentrations. These results seem, once again, to confirm the earlier work of Popovici[2] on ZnS-based systems, and our more recent data on ZnSeS-systems, suggesting that an optimal Ag concentration can enhance both the temperature quenching as well as the saturation behavior of these phosphor materials. This is believed to be a result of efficient energy transfer mechanism between Cu and Ag, consistent with the bandgap energy model we previously developed.

[1] Calculating Power Density – A Shortcut, Photonics Technical Note #2, Power Meters & Detectors, Newport Corporation

[2] E. Popovici et al., "Luminescence properties of some double activated zinc sulphide-type phosphors", SPIE Vol. 3405, pg 632-635, 1998

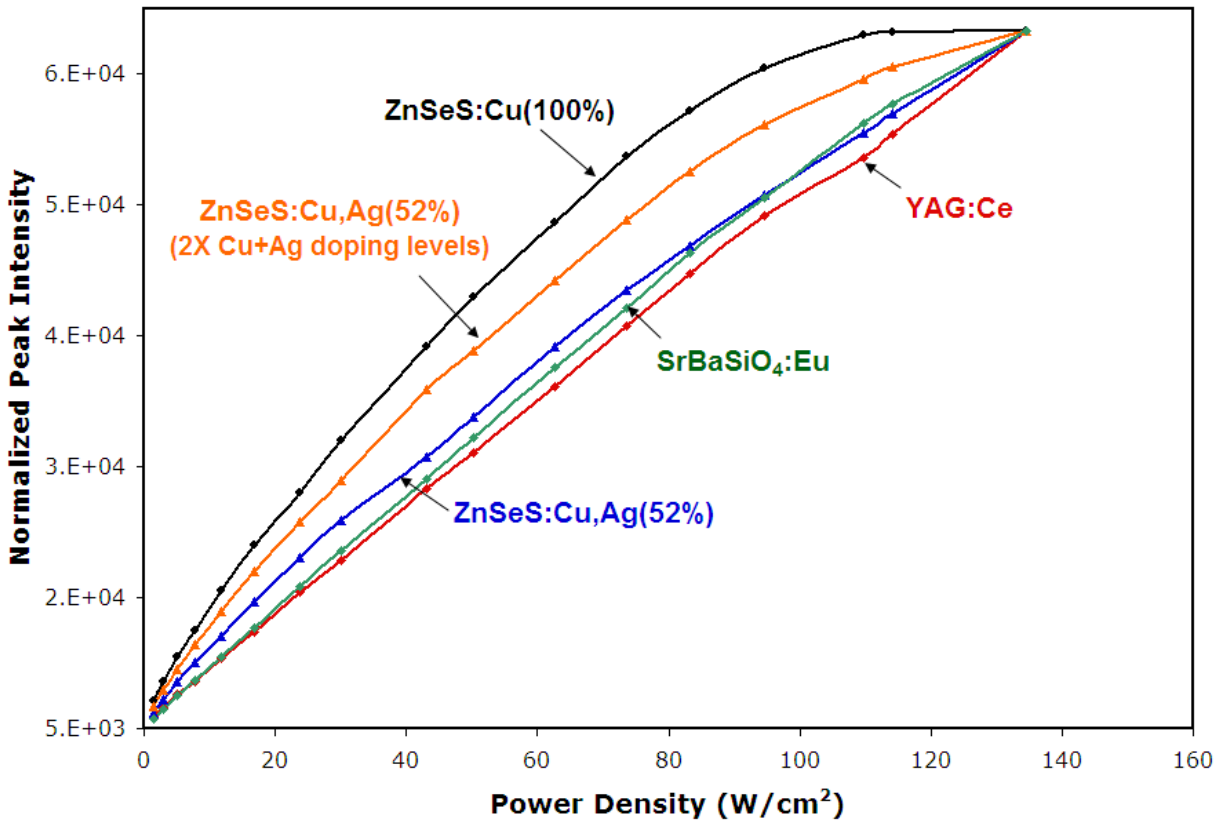

Figure 16. Optical saturation behavior of ZnSeS:Cu and/or Ag activated phosphors compared to conventional LED materials.

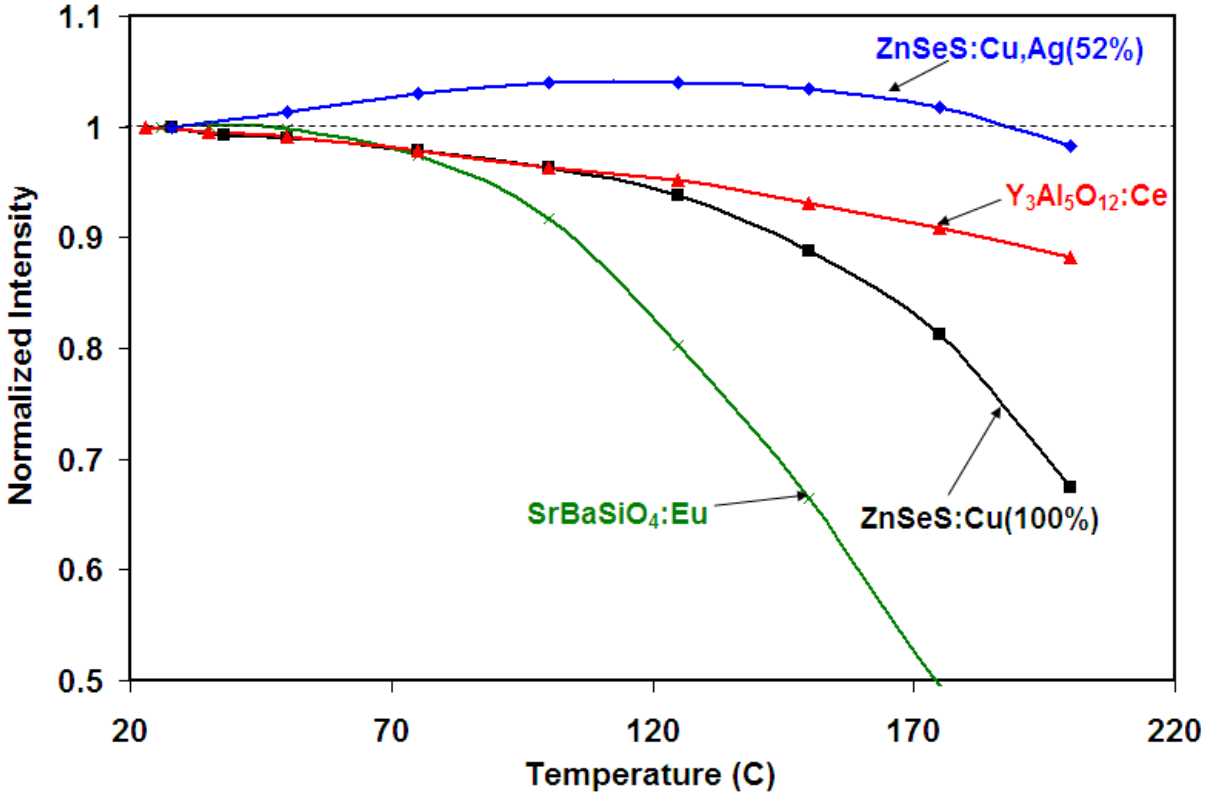

Figure 17. Thermal behavior of ZnSeS:Cu and/or Ag activated phosphors compared to conventional LED materials.

Annealing of Thiogallate Phosphors

Although good performance had been realized from the previous developments, a final study was initiated to see if annealing procedures could be developed to further increase performance, particularly for the thiogallate phosphors. Annealing is a common treatment used in materials engineering to improve crystallinity and consequently luminescent properties. Typically with annealing, the material is brought close to and maintained at a phase transition temperature to allow diffusion of internal atoms to relieve stress and form a more homogenous structure. Additionally for phosphors, by increasing the diffusion and reactivation of dopants, and reducing interstitial vacancies, a higher luminescent efficiency can be achieved. In the design scope of the annealing investigation, consideration of temperature and time were taken into account. Low temperatures cause less dopant leeching and phosphor degradation, but a slower diffusion rate and lower pressure is expected, which will limit or slow improvements in efficiency. Conversely, higher temperatures promote higher diffusion rates and a higher degree of homogeneity. Higher temperature annealing also provide sufficient energy for the phosphor to undergo phase transformations or reactivation of dopant sites.

Large batches (150g each) of both the thiogallates and zinc sulfoselenide phosphors were prepared for the annealing investigations. These batches were prepared in order to ensure a methodical approach to investigating and understanding the annealed sample space and to use the same starting material across several times and temperatures. Table 4 tabulates the spectral analysis of the starting materials and Figure 18 shows that the PL spectra and peak intensities are similar for the STG and CTG thiogallate samples. Consequently, the predicted lumen output for CTG is higher due to its closer proximity to the photopic peak.

Table 4 Spectral analysis of phosphors that will be used in annealing experiments

	Peak	Intensity	FWHM	Lumen	Photons	x	Y	Z
YAG	568.14	2.46E+00	119.06	1.07	1.13E+20	0.357	0.350	0.293
CTG	558.08	4.61E+05	49.73	1.21	8.59E+19	0.349	0.441	0.211
STG	537.18	4.71E+05	46.97	1.15	8.53E+19	0.238	0.456	0.306
ZSS 60%Se	616.27	2.43E+05	92.11	0.56	8.81E+19	0.454	0.284	0.262

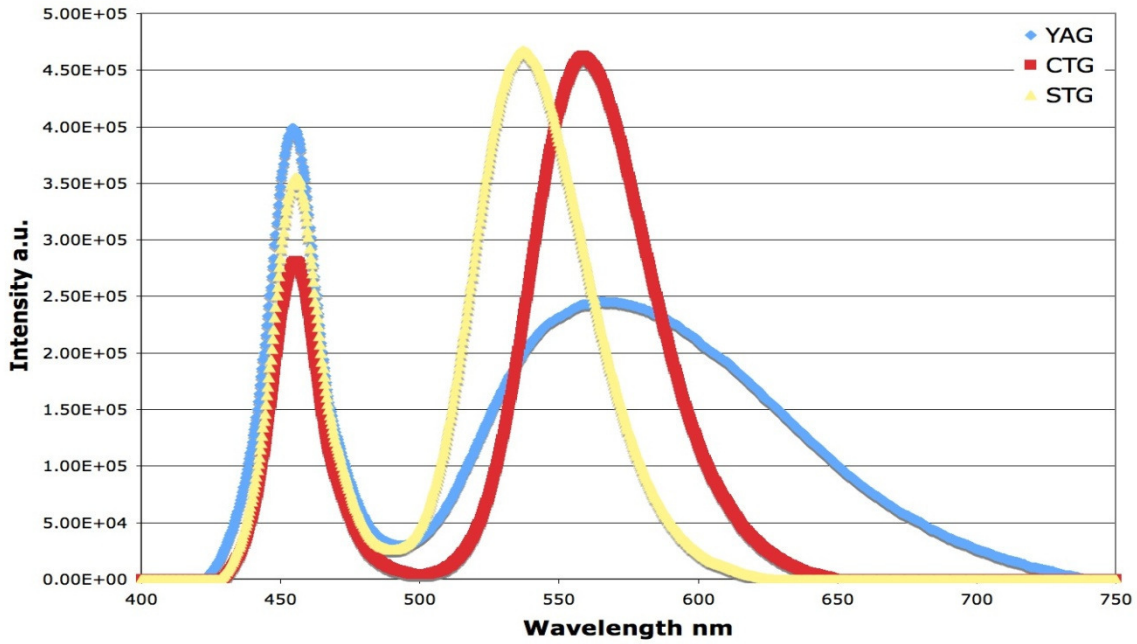

Figure 18. PL comparison between Strontium Thiolgallate (STG), Calcium Thiolgallate (CTG), and YAG:Ce.

A large sample space of annealing times and temperatures was explored for each phosphor. However, because the thiogallates are fired at lower temperatures; the sample space for these phosphors was shifted to a temperature range 200°C lower than for the ZSS samples. The design of experiment for the thiogallates is presented in Table 5, with the optimal time and temperature ranges highlighted. Figure 19 shows the PL spectra of the 60% Se ZSS starting sample compared to YAG phosphor.

Table 5 Design of experiments for anneal times & temperatures for thiolgallates phosphors

	°C	200	300	400	500	600	700	800	900	1000	1100
Hours		0.5	0.5	0.5	0.5	0.5	0.5	**0.5**	**0.5**	**0.5**	**0.5**
		1	1	1	1	1	**1**	**1**	**1**	**1**	**1**
		3	3	3	3	**3**	**3**	**3**	**3**	**3**	**3**
		6	6	**6**	**6**	**6**	**6**	**6**	**6**	6	6
		12	**12**	**12**	**12**	**12**	**12**	12	12	12	12
		24	**24**	**24**	**24**	**24**	24	24	24	24	24
		48	**48**	**48**	**48**	48	48	48	48	48	48

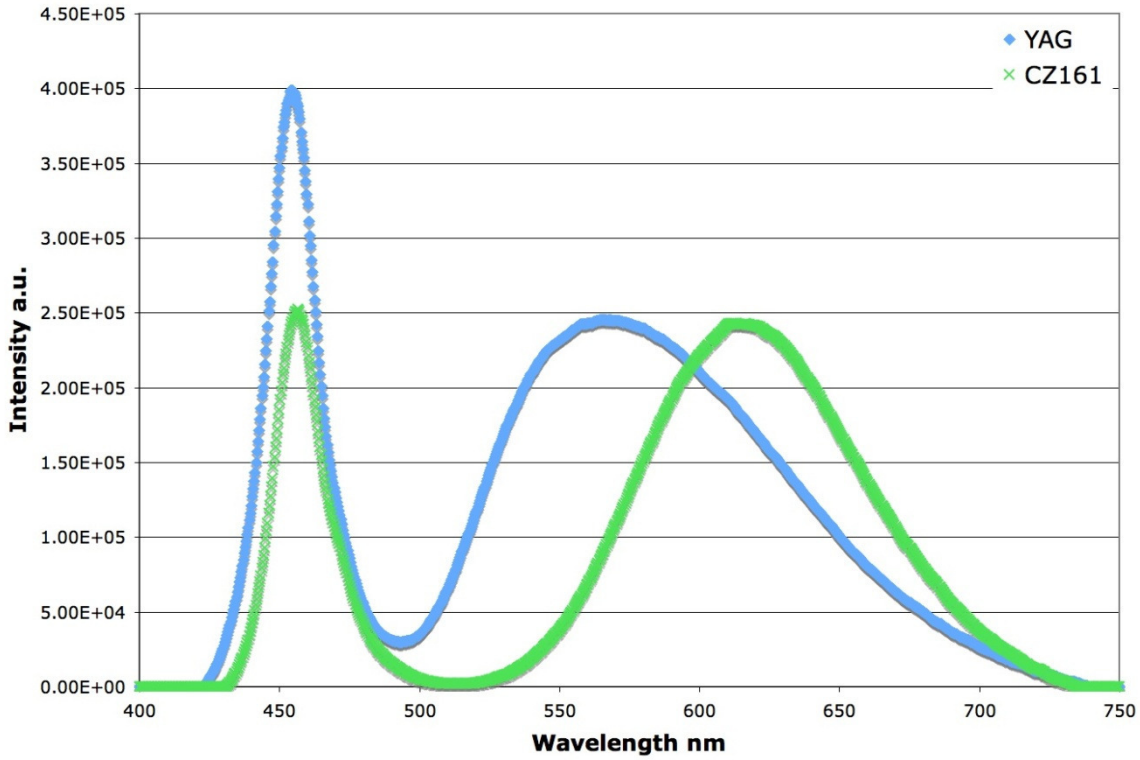

Figure 19. Photoluminescence of the 60%Se ZSSe starting material.

Initially, the annealing investigations on the thiolgallate phosphors (CTG and STG) were focused on using both hot- and cold-zone annealing techniques. (Note: In the hot zone technique the capsule is placed at the center of the furnace, whereas in the cold-zone technique a significant part of the capsule lies outside the furnace at room temperature). Figure 20 and Figure 21show the PL spectra for CTG and STG, respectively, after annealing for 3 hours at 800C and 900C, both with and without a cold zone. For CTG, significant improvements over the base material are observed after a 800C cold zone or a 900C non-cold zone anneal, with each giving gains of 14% in lumen output. For STG, unfortunately the tube fired at 800C without a cold zone exhibited deposits inside the ampoule which are believed to be the cause of the significant decrease observed in the emission. However, at 900C both cold-zone and non-cold zone anneals gave similar gains of 15% in lumen output. Cold zone annealing provided more consistent and improved results over the hot-zone anneals and thus were the focus of subsequent investigations.

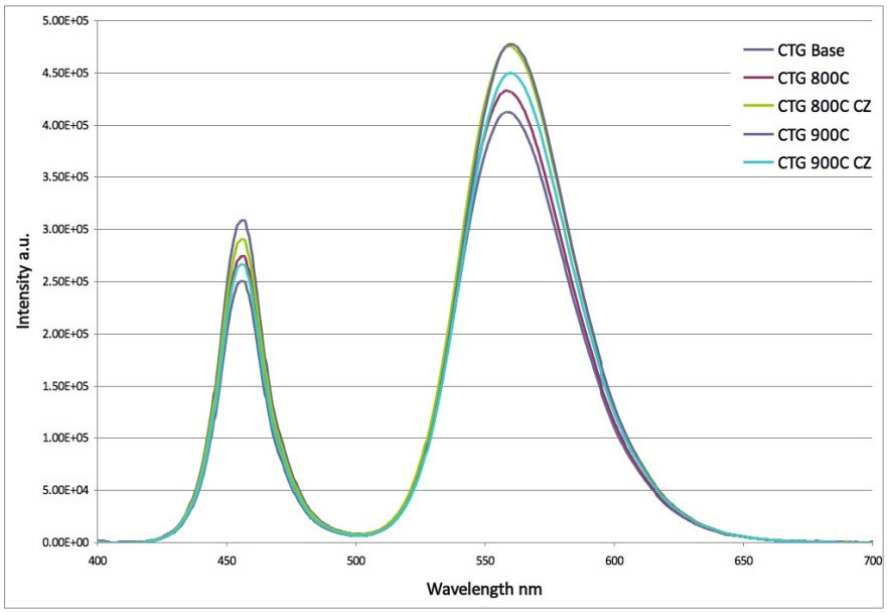

Figure 20. PL of CTG samples annealed with and without a cold zone for 3 hours.

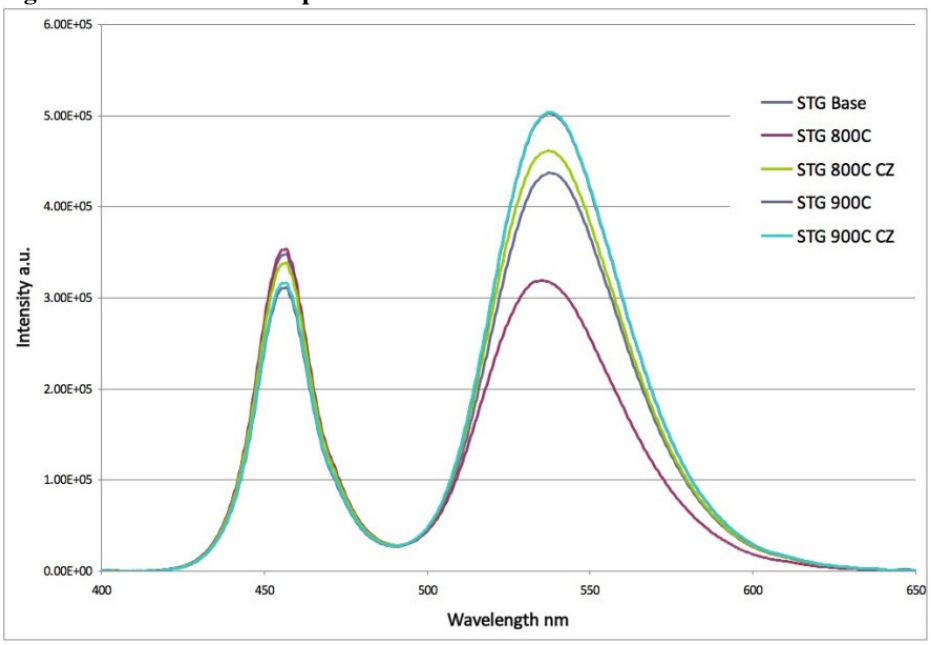

Figure 21. PL of STG samples annealed with and without a cold zone for 3 hours.

The full investigation for the CTG and STG phosphors were carried out in a large furnace that held 5 sample tubes. At the specified times, one of the five vacuum sealed sample tube was removed and allowed to cool to room temperature. This procedure was repeated for each of the sample tubes. The full isothermal lines from the annealing studies are shown in Figure 22 and Figure 24 for CTG and STG phosphors, respectively.

CTG Annealing Study

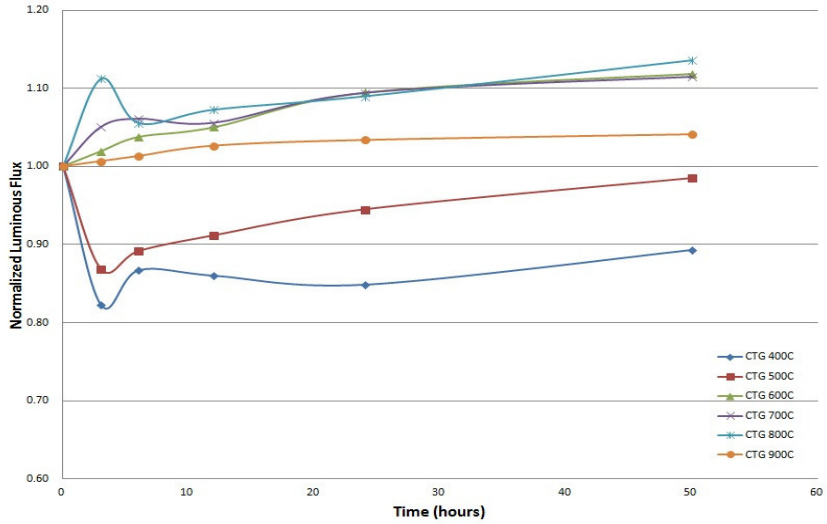

Figure 22. CTG isothermal plots for luminescent intensities annealed at different times. Of these annealing times and temperatures we see the best results at 800°C for 50 hours.

As depicted in Figure 22 the 400°C and 500°C anneals showed an initial and surprising decrease in photoluminescence after only 5 hrs. With continued annealing, the photoluminescence showed steady improvements, but never improved beyond that of the base material. However, at temperatures greater than 600°C the efficiency increased with time. For temperatures between 600°C to 800°C, the luminescence showed similar gains, suggesting that above 600°C, there is enough energy for the diffusion of dopants and the reduction of non-radiative recombination centers, such as vacancies and interstitial sites within the lattice. The intensity increases significantly, but experienced diminishing returns at longer times. At 50 hours, an increase of 12% was obtained. However, at 900°C, the mechanism seems to change, as the increase in luminescence is significantly lower than those observed at the lower temperature range of 600-800°C. Annealing at 1000°C, we observed an increasing phase separation with longer exposure time. Thus, no measurements were taken from samples annealed at 1000°C or above. Accordingly, the annealing space was expanded to account for 100+ hours, shown in Figure 23. The 100+hours annealing were performed at 500°C and 600°C to observe the effects of prolonged heating on samples which showed differing diffusion kinetics. The extended annealing at 500°C was able to offset the initial decrease in luminescence. At 600°C, the phosphor shows a slight increase in the luminescence over the 50 hours mark, to achieve an increase of 13%.

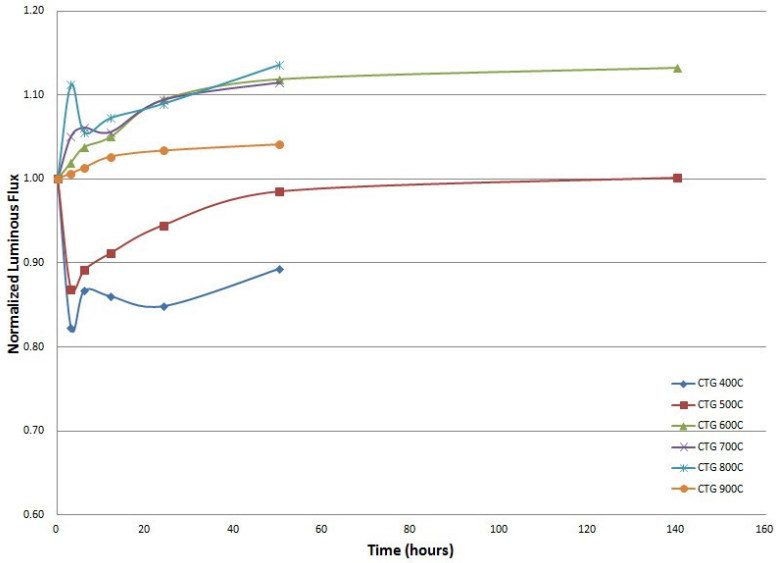

Figure 23. CTG isothermal plots for luminescent intensities annealed with extended annealing times of 140 hours. Of these annealing times and temperatures the best results from 600°C to 800°C for 50 hours.

STG Annealing Study

In Figure 24, the isothermal curves obtained for the STG annealing study show a greater variance in the effect of annealing than those seen for CTG. The STG annealing has a greater dependence on temperature than time. The sample's photoluminescence reached a steady state after only 12 hr, and for most samples, extended annealing showed diminishing returns.

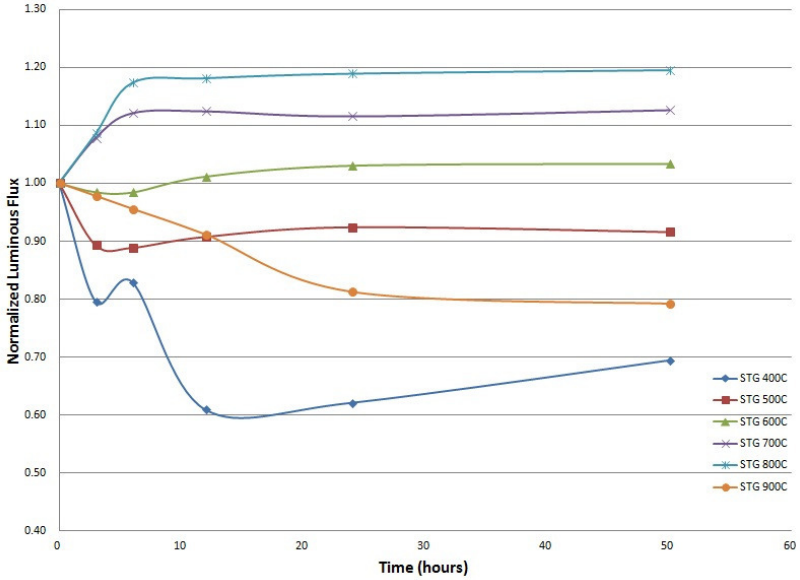

Figure 24. STG isothermal plots for luminescent intensities annealed at different times. Like CTG these annealing times and temperatures for STG show the best results at 800°C for 50 hours.

For annealings at 400 °C and 500 °C, there is, again, a sharp initial decrease in intensity, followed by a rise shortly after. There is a transition at 600°C, where, after 12 hours, the decrease in luminescence is offset and a net increase of 3% is observed after 50 hours. After 12 hours, the luminescence reaches a plateau where a small increase in annealing time showed little change in luminescence. Similarly, the temperatures of 700°C and 800°C show the same pattern of a

plateau around 12 hours. However, the gain in luminescence increases with rising temperature and the best result of a 19% increase was seen with the 800°C annealing after 12 hours. At 900°C there is a shift in the mechanism, causing dopants to precipitate out of the phosphor. This is related to a decrease in intensity with prolonged annealing time, reaching a limit of -20% around 24 hours. Temperatures over 1000°C caused considerable phase separation to occur and no measurements could be performed.

Extended annealing was also performed for the STG samples at 500°C, 600°C, and 800°C, shown in Figure 25, to understand more fully the effects of annealing time. Despite previously seen trends, the extended firing for STG showed further improvements, however, this was relatively inconsequential compared to the first 12 hours of annealing. After a 140+ hr anneal at 800°C the luminescent intensity from the STG phosphor increased by 22% over the base material, compared to ~18% for a 12 hr anneal.

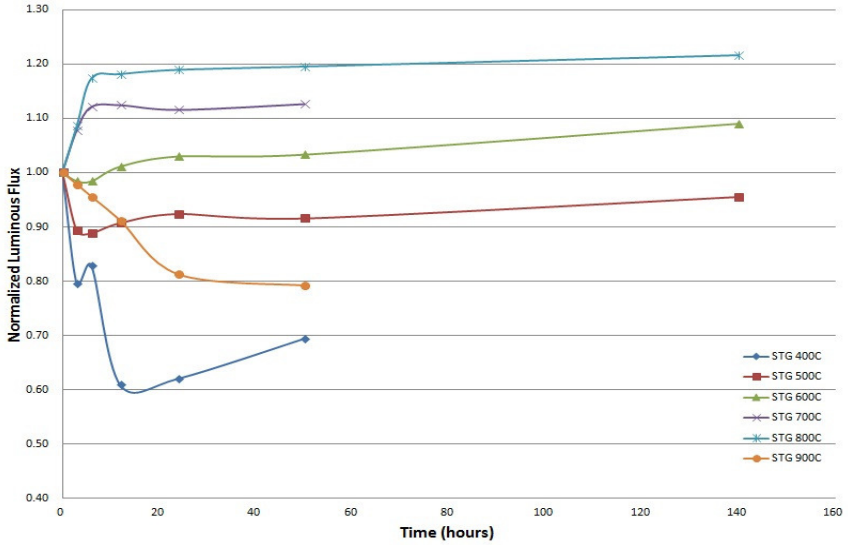

Figure 25. STG isothermal plots for luminescent intensities annealed at different times. These annealing times and temperatures for STG show the best results at 800°C for greater than 12 hours.

The annealing investigation was also carried out for the CZ161 (ZSS 60%Se) and the results can be seen in Figure 26.

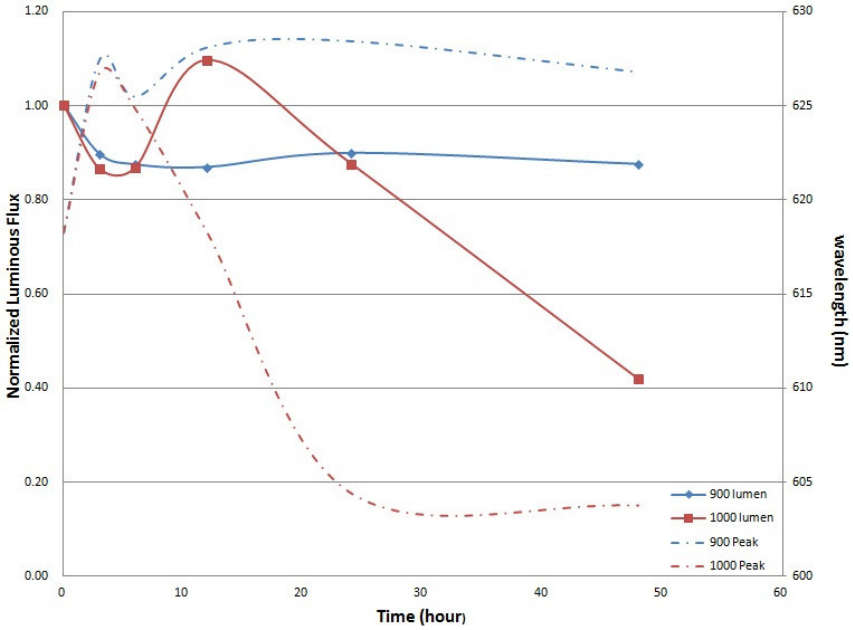

Figure 26. Isothermal curves for 900°C and 1000°C for CZ161 and their change in peak wavelength.

The CZ161 show an overall decrease in luminescent intensity at 900°C and 1000°C. At 900°C, the intensity decreased by 25% after 3-6 hours of annealing. The shift can be explained by a shift in the peak wavelength from 617nm to 627nm and an overall degradation of the phosphor, as dopants leech out. At 1000°C, the change is much more drastic than those seen in 900°C. The initial decrease in intensity matches those of 900°C for the first 6 hours, but at longer times, the peak shifts from 627nm to 604nm. The subsequent surge in intensity comes from this shift towards the photopic peak. However, the ZnSe separated from the ZnS content of the phosphor, and a degradation of the ZnS follows, resulting in a significant decrease in intensity.

Solid Slab Phosphors

During these same high temperature powder phosphor treatment experiments in vacuum, we also achieved Cu/Ag doping and bright green to red luminescence from solid forms of ZnS/ZnSe materials, varying in size from 1 to several millimeters, depending on the shape and size of the original precursors. Unlike powder phosphor systems, macro-size crystalline phosphors provide the unique advantage of high density and lower scattering compared to micron-sized particles. In addition, if these crystals can be directly fused onto LED dies without using any low-index polymers, it will be possible to take full advantage of the high refractive index properties of ZnSeS to maximize light extraction from UV and blue LEDs.

To demonstrate the potential of this geometry, the performance of solid ZnSeS (SFZSS) yellow phosphor crystals were investigated by fabricating a white LED using a blue (~460 nm) device, as shown in Figure 27. The spectral performance was compared to YAG:Ce, and our standard ZnSeS:Cu,Ag (ZSS) powder phosphor when pumped by a blue 455 nm LED. The luminescence and colorimetric results, in Figure 28, show that the SFZSS phosphor has more favorable properties than YAG:Ce and the powder ZSS phosphor. For example, the emission peak of SFZSS is ~577 nm (FWHM~99 nm), closer to YAG at 565-570 nm peak (FWHM~121nm) and the ZSS phosphor, peak ~600 nm (FWHM~89 nm). When combined with a blue LED, the SFZSS phosphor achieved color chromaticity cordinates CIE (x=0.332, y=0.317) and color temperature CCT=5530 compared to CIE (x=0.318, y=0.226) and CCT=9475 for the ZSS phosphor and (x=0.316, y=0.302) and CCT=6595 for YAG:Ce.

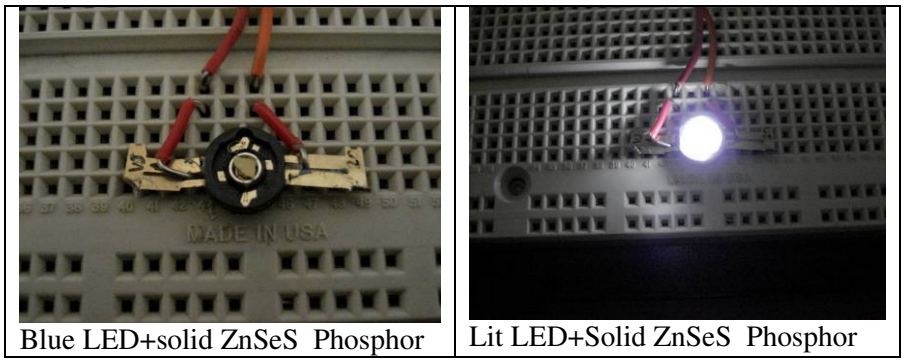

Figure 27. Top: Blue LED with no phosphor. Bottom: White LED made using blue LED and a solid ZnSeS:Cu,Ag yellow crystal.

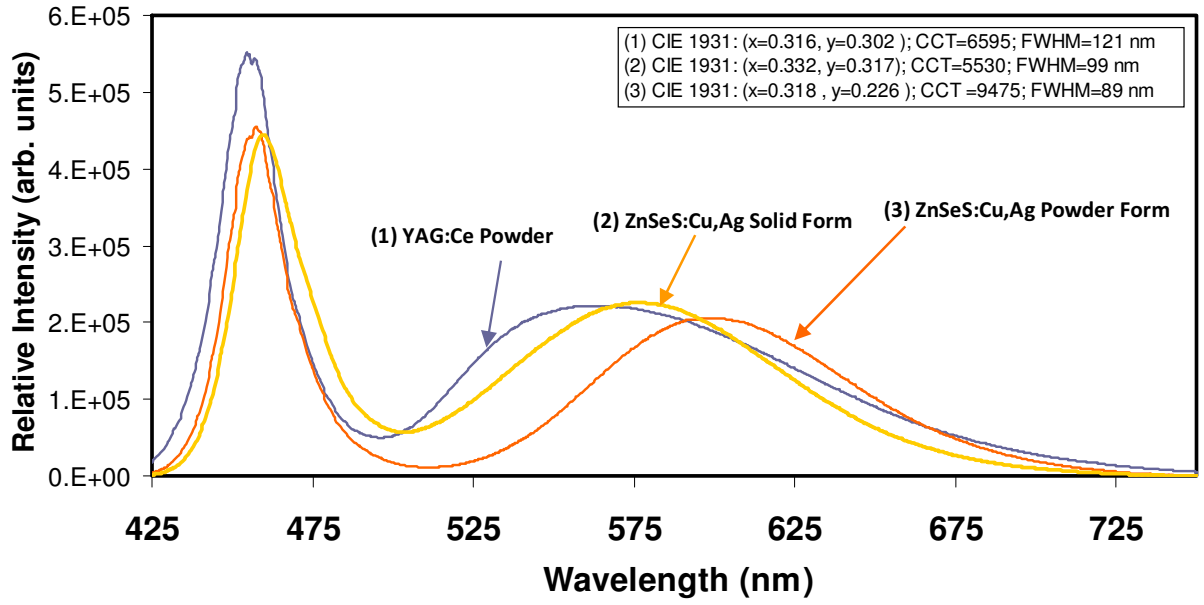

Figure 28. Spectral comparison between solid and powder ZnS/ZnSe and YAG:Ce for 455-460nm excitation.

Dynamic Cold Zone

Investigations into alternative processing methods to achieve higher ZnSeS phosphor crystallinity and large particle size were carried out using a mid-firing cold zone to create a dynamic environment that enhances crystal growth. The dynamic region enhances the growth of larger translucent luminescent particles in the region between the firing zone and the cold zone. The large crystal growth is due to the 1000^{o}C temperature gradient in this region, which

promotes crystalline dendritic growth through gas precipitation. These conditions enable the growth of large enough crystals that their translucence can be seen well with optical microscopy and even the naked eye. The experiments are similar to the cold zone firing previously used in the preparation of samples with two main differences: (1) the cold zone is introduced just before ramp down and; (2) the raw materials (precursors) are positioned along the temperature gradient instead of in the steady state region at the center of the furnace. Furthermore, the particles tend to grow preferentially on a substrate, which we believe will prove to be valuable in solid-state lighting for direct growth on either the LED or a remote substrate, depending on the application. Figure 29 and Figure 30 depict the larger particles that formed inside the ampoule when the raw material was distributed from the firing region and well into the cold zone thus passing through the greatest portion of the temperature gradient.

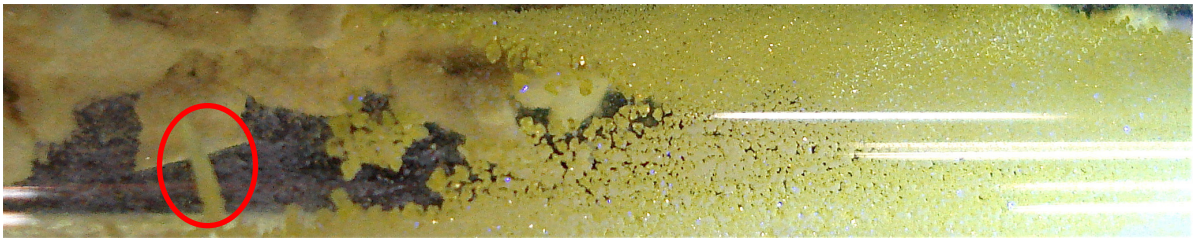

Figure 29. The circled crystalline structure measures approximately 3.8mm long. It gives perspective on the size of the particles in the foreground to the right, which have grown as large as 600µm.

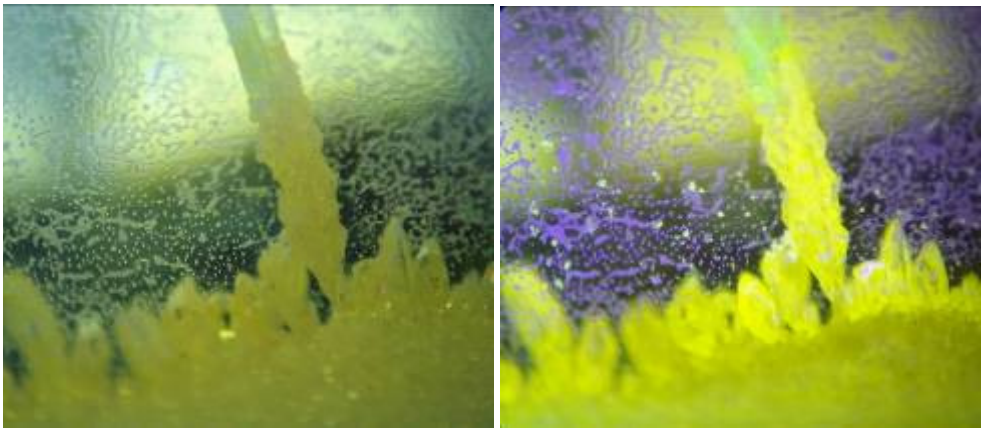

Figure 30. The images above are from optical microscopy of the circled portion of Figure 29. *The* left image is under room lighting and the right image shows the photoluminescence of the particles under UV.

Task 2: Development of Doped ZnSe Nanocrystalline Systems

The objective of this task is to develop a high efficiency ZnSe:Mn yellow nanophosphor emitting at 585 nm, the characteristic wavelength of Mn, when optically pumped with a 460 nm LED. This requires that the absorption edge of ZnSe extends to bulk like properties. Thus, we have applied QD synthesis techniques to fabricate particles with a diameter greater than 20 nm. The studies have been directed to a fuller understanding of the growth kinetics and the impact of particle architecture structure, the considerations of chemical synthesis protocols that are necessary to achieve high quality crystal growth and techniques for manufacturing. Also, investigations of other dopant elements were performed.

To perform on this program, a 72" wide fume hood was installed along with a glove box, which were dedicated for the synthesis of ZnSe:Mn,X nanophosphors (NP). Additionally, pressure-actuated dispensers and flask heating mantles were automated, to allow for a continuous unattended growth of NP materials and shells – a process that currently requires over 10hrs of manual precursor injections at regular intervals. This makes it possible to produce and optimize a large amount of NP samples at a fraction of the time it currently takes to do so, since the process can be designed to run unattended overnight.

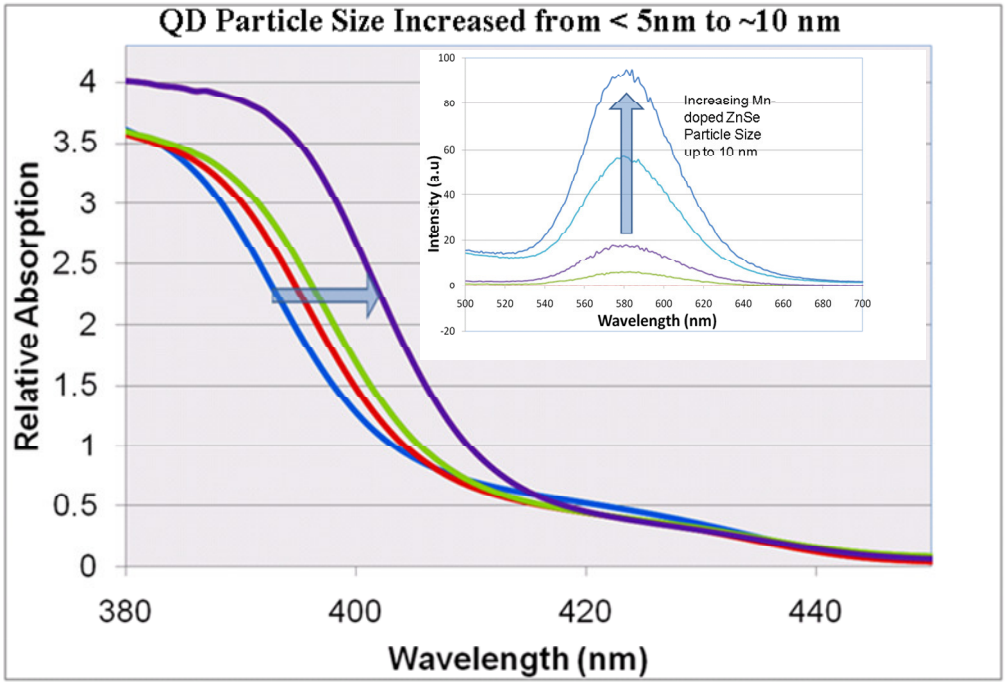

Figure 31. Absorption and emission (INSET) spectra of ZnSe:Mn nanocrystals prepared by the colloidal synthesis techniques described above.

Optimization of Synthesis Chemistry

The synthesis procedure used in these investigations is listed below and follows environmentally friendly "Green" synthesis techniques. These techniques have been shown to produce higher crystallinity and higher QE with narrower particle size distribution and at lower cost than aqueous or metalorganic syntheses. The key components are:

- Precursors
    - Manganese stearate, Zinc stearate, zinc acetate, Se powder

- Stabilizers:
  - Fatty acids: octadecylamine (ODA) or oleylamine (OA)
- Solvent:
  - Octadecene (ODE)

The general procedure is to first form MnSe nuclei and then to grow a shell of ZnSe around the core. In setting up the synthesis conditions, attention is paid to the fact that Mn is less reactive than Zn because Mn outer electrons are d-states. The specific details are given below:

Prepare Mn precursor: add $MnSt_2$ to ODE, heat to 280 C, under Argon, to dissociate $MnSt_2$ into cation and anion components

$Mn(C_{18}H_{35}O_2)_2 + C_{18}H_{36}$ (280 C) ➔ $Mn^{2+} + 2((C_{18}H_{35}O_2)_2)^{2-}$ -- in $C_{18}H_{36}$ solution

(Note stearic acid is $C_{18}H_{36}O_2$, or $CH_3(CH_2)_{16}COOH$)

Prepare Se precursor: Add Se to TBP and heat to 140 C to form TBPSe

$Se + (C_4H_9)_3P$ (140 C) ➔ $(C_4H_9)_3PSe + (C_4H_9)_3P$

Add $C_{12}H_{27}PSe$ with excess $C_{12}H_{27}P$ to stabilizer solution $CH_3(CH_2)_{17}NH_2$

Mix Precursors: Inject Se precursor solution into Mn precursor solution
Now have a "soup" of:

Mn^{2+} cations, $2((C_{18}H_{35}O_2)_2)^{2-}$ anions in $C_{18}H_{36}$ solution
$C_{12}H_{27}PSe$ with excess $C_{12}H_{27}P$ and stabilizer $CH_3(CH_2)_{17}NH_2$

Free Mn^{2+} cations & free Se^{2-} anions – combine to form nuclei of MnSe

Then inject a precursor solution of $ZnSt_2$ to grow a graded MnZnSe layer

Grow "shell" layer of ZnSe by injecting a similarly prepared $ZnSt_2$ solution and then further expand ZnSe shell thickness using Zn acetate and TBP

- During this process also add Mn

- Finally passivate Mn doped ZnSe shell by depositing an over-layer of ZnS

- In the surface nucleation kinetics that control the growth process, the attachment of steric acid to exposed Mn is very facile

- However, Se readily attaches to Mn core surface as do stabilizing ligands
  - This leads to a predominately Se-rich growth surface
  - Thus, Se attachment controls the growth rate
  - Se attachment moderated by relative concentrations of P/N stabilizers

Further refinements to the synthesis protocols have been to address the need for very pure precursors and to use a new stabilizer that remains liquid at all temperatures used in the process. The formation of efficient Mn-doped ZnSe nanophosphors relies initially on a very pure $MnSt_2$ starting precursor material. This precursor is formed by a combination of manganese chloride and stearic acid. As described previously, a protocol to separate unreacted stearic acid from pure manganese stearate has been developed and involves the use of repeated washings in hot methanol. We discovered that the subsequent removal of all methanol from this precursor is a key to the formation of very small MnSe core particles which are required for proper epitaxial growth of ZnSe. As a typical metal carboxylate, manganese stearate is composed of a Mn atom coordinated by two stearic acid chains. Both chains contain C=O bonds associated with the carbonyl section and are very sensitive to attack by nucleophiles. (Nucleophiles are compounds that readily donate electrons and the carbon atom in the C=O bond is susceptible to this because oxygen pulls the electron density away from O in the bond). Methanol is a very effective nucleophile and therefore, its presence in a heated solution of $MnSt_2$ and ODE will tend to cause the formation of manganese oxide (MnO) nanoparticles. Accordingly, we have developed a vacuum baking process to produce a high purity $MnSt_2$ precursor that contains a minimum of excess stearic acid and no residual methanol from the process. In this process, samples of $MnSt_2$ were heated inside quartz tubes held under vacuum for 48 hours at progressively higher temperatures from 60C to 80C.

A key stabilizer involved in the synthesis of impurity-doped ZnSe is the coordinating amine, octadecylamine (ODA). This material is a solid at room temperature and therefore, must be "hot injected" at 120^{o}C (well above its melting point). A significant amount of this amine precursor remains in solution following synthesis and, in the case of ODA, will begin to solidify as the reaction is reduced to room temperature for product collection. Its complete removal then requires the use of a large volume of chloroform and repeated centrifugation which often damages the doped-ZnSe product. Additionally, hot-injecting large amounts of this material as required for synthesis of multi-gram quantities of doped-ZnSe nanophosphors becomes very difficult. To improve product collection and to produce large amounts of doped-ZnSe, oleylamine (OA) was used rather than octadecylamine as the primary amine. While both compounds are C18 amines, oleylamine is preferred because it remains a liquid at room temperature and thus, multi-gram quantities of doped-ZnSe are possible. Additionally, the collection process requires only one centrifugation step with a minimum of chloroform stabilization.

To study and optimize ZnSe layer growth, a system for in-situ monitoring of particle formation has been developed (to be described later) in order to optimize ZnSe layer growth and to measure the luminescence performance of colloidal doped nanophosphors. For the case of Mn-doping, it is known that ZnSe must be epitaxially attached to MnSe core particles in a manner which produces a $Mn_{1-n}Zn_nSe$ alloy region and Mn_{Zn} substitutional doping. This relies on three primary parameters:

- very small MnSe core particle size
- temperature of ZnSe shell addition
- rate of ZnSe shell addition

A small MnSe core has a high attachment surface energy and optimization of this parameter was reported previously. The ZnSe shell addition temperature must be high enough to activate heterogeneous nucleation (attachment) kinetics yet not so high as to allow homogeneous nucleation of individual (undoped) ZnSe particles. The rate of ZnSe addition will strongly

influence particle quality and layer-by-layer epitaxial growth of ZnSe onto MnSe core particles must occur in a gradual fashion so that the occurrence of defects within the growth layers are kept to a minimum. Additionally, it is expected that a rate which is too high may lead again, to individual ZnSe particle formation.

Optimization of ZnSe:Mn nanocrystals using the in-situ monitoring system was first applied to investigating an alternative stabilizer, oleylamine, for improved product collection and performance. Figure 32 shows initial optimization results of ZnSe:Mn using OA as precursor. As expected, a large increase in emission is observed during the first Zn Acetate injection, followed by a more gradual increase. Interestingly enough, a plateau or a saturation point was reached only after the third injection, which indicates a fast growth rate. Therefore, a slower injection of Zn Acetate precursor may be needed in future runs. In addition, when the reaction temperature was increased from 180°C to 220°C, a drop in the emission intensity was observed. This trend was reversed once the heating mantle was turned off and the sample was allowed to cool down to room temperature (RT).

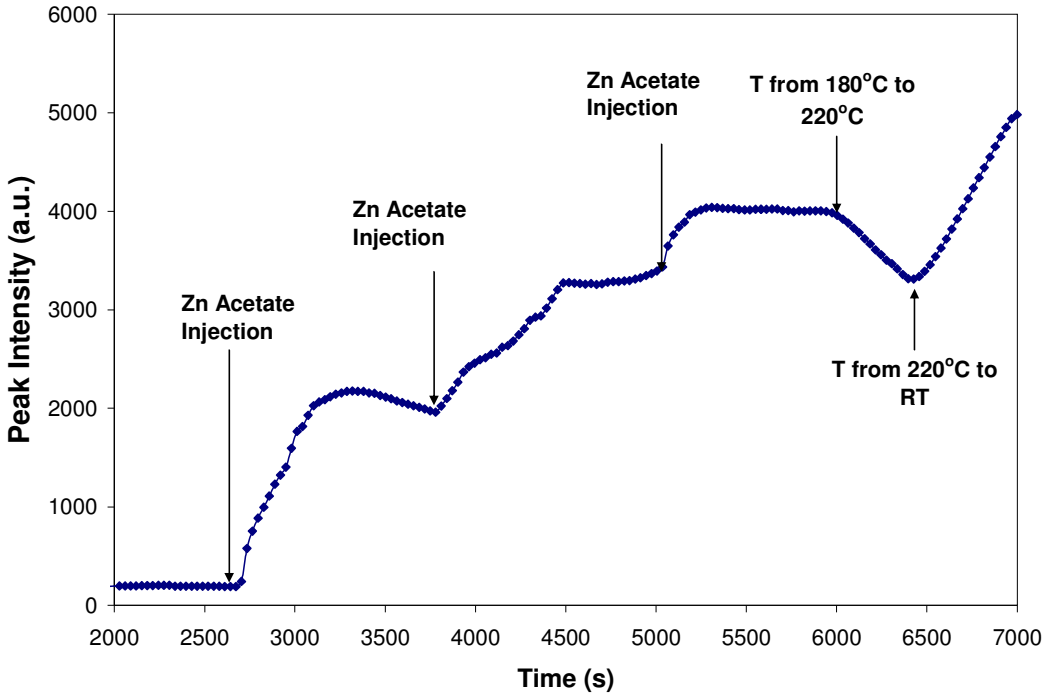

Figure 32. In-situ monitoring of ZnSe:Mn emission peak intensity using oleylamine as precursor.

Recent work on the doped ZnSe nanophosphor system has been focused on development of a new architecture in order to enhance impurity recombination. As shown in Figure 33(top left), the conventional Mn-doped system is composed of a 1-2nm MnSe core particle covered by a ~2nm thick shell of ZnSe. Electron-hole pairs formed in the lower band gap ZnSe shell recombine on Mn ions within the $Mn_xZn_{1-x}Se$ interface layer present between core and shell volumes. Much of our work has dealt with growing a thick ZnSe shell layer > 10nm. This was done in order to produce a bulk-like behavior and shift the overall absorption edge into the 440-460nm spectral region where standard blue diodes emit. We have also attempted intermittent Mn ion injections during ZnSe shell growth to produce the architecture displayed in Figure 33(bottom). By increasing the ZnSe shell, the absorption edge is shifted toward the blue region due to an inverse quantum confinement effect, yet band gap recombination from within this layer may not occur due to the consistent presence of substitutionally doped Mn ions. Figure 34

presents high temperature emission spectra taken during ZnSe shell growth with intermittent Mn ion addition. The slight rise in emission intensity as Mn is injected at each time point is proof of its incorporation within the lattice. Unfortunately, the intermittent Mn throughout the ZnSe shell resulted in reduced luminescent intensity (Figure 36), which could be a result of additional strain and defects introduced by the lattice mismatch between ZnSe and MnSe.

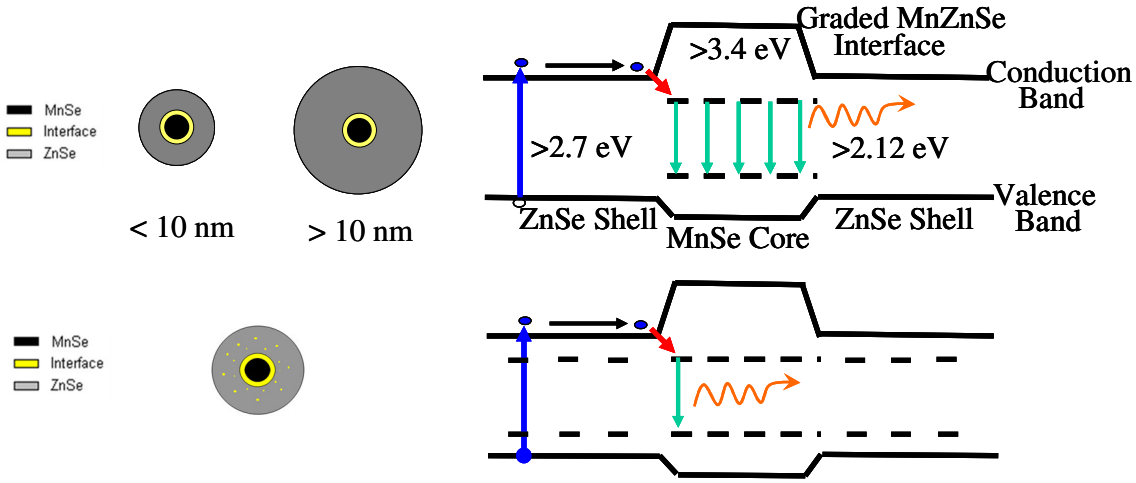

Figure 33. TOP: Basic architecture of the Mn-doped ZnSe nanophosphor system. BOTTOM: Modified nanophosphor architecture that includes intermittent Mn ion incorporation within the ZnSe shell layer.

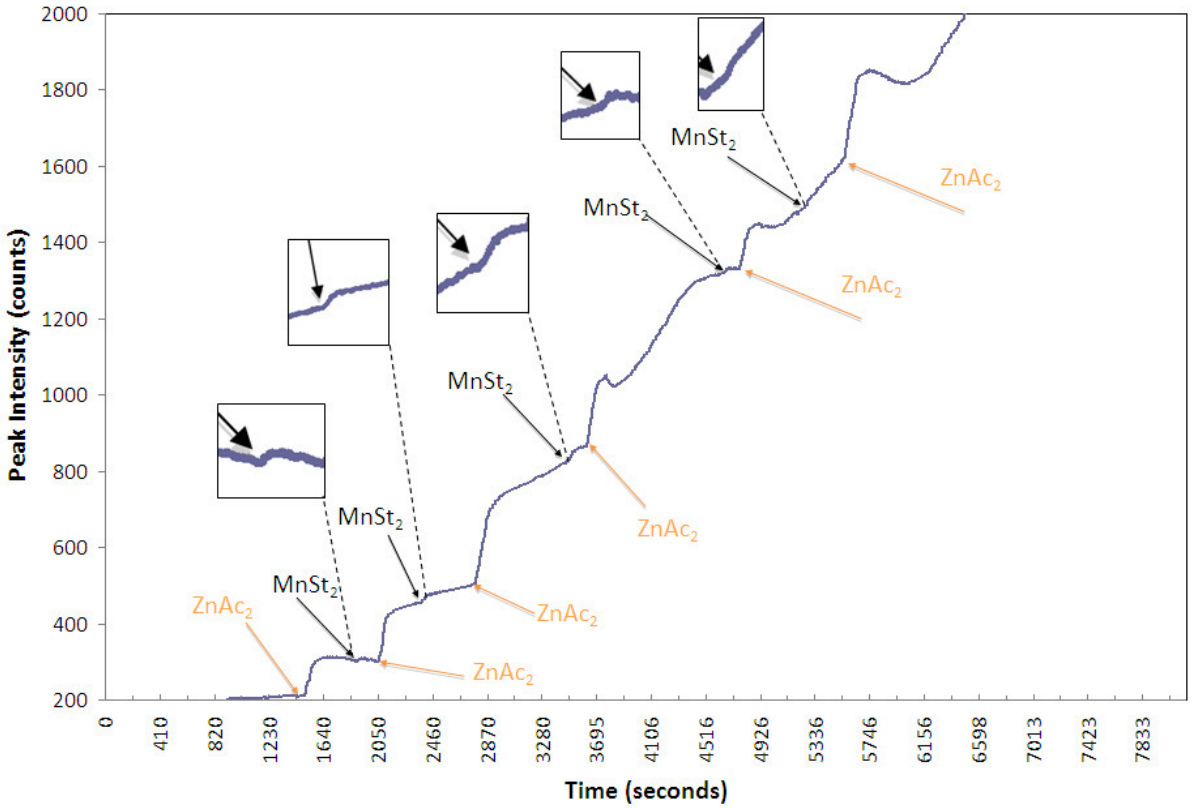

Figure 34. In-situ monitoring of ZnSe:Mn emission peak intensity with intermittent MnSt2/ZnAc2 injections.

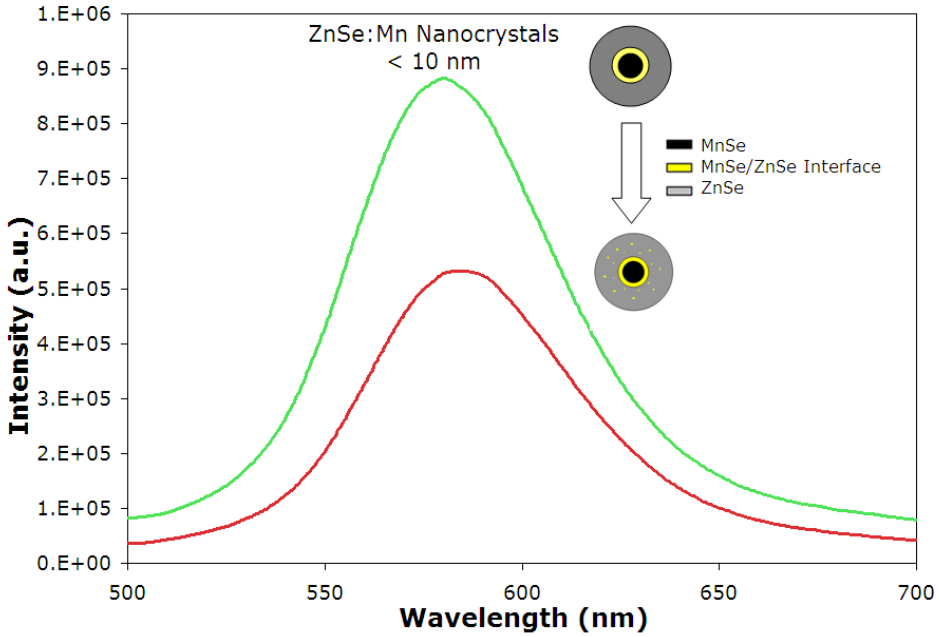

Figure 35. Relative comparison of two ZnSe:Mn samples with and without intermittent MnSt2/ZnAc2 injections.

In order to optimize the properties of ZnSe:Mn nanocrystals, the effect of various precursors and processing parameters on the optical and luminescent performance of the materials was performed. In one experiment, we synthesized and analyzed several samples with different precursor concentrations and ratios, and evaluated their relative spectral emission and absorption, as shown in Figure 36 and Figure 37. The emission spectra shown below exhibit two main emission bands: ZnSe host emission having peak wavelengths from 430nm to 450nm. As in typical undoped quantum dot systems, the shift of the host emission peak to longer wavelength indicates an increase in particle size. This is also evident in the absorption data of samples that exhibit absorption profiles that extend further into the blue part of the spectrum, indicating the presence of larger particles. Some of these samples also have broad host emission bands, implying a wider particle size distribution whereas others have relatively narrow host emission bands and steeper absorption edges, indicating a narrow particle size distribution. For blue-pumped applications, it is desirable to further shift the absorption edge to longer wavelengths and to minimize or eliminate emission from the ZnSe host material. The different precursor concentrations and ratios were also synthesized and analyzed, as shown in Table 6. The relative spectral emission (using a 405nm UV laser) of these samples is shown in Figure 36, while the absorption properties are graphed in Figure 38. Two samples (samples #012810 and 020210) have the best luminescence and also show the largest red-shift in the absorption edge. This indicates better crystallinity and larger particle size, which is also confirmed by the shift of the host emission peak to longer wavelengths. Sample# 020210 also exhibited very small host (ZnSe) emission peak, indicating the presence of a higher percentage of doped ZnSe:Mn particles in this sample.

Table 6. Recipes used for colloidal synthesis of recent ZnSe:Mn nanocrystals

Sample #	$MnSt_2$ / ODE		Se / TBP / OA			$ZnAc_2$ / TBP		$ZnSt_2$ / ODE	
121109	.31g	40mL	.4g	4mL	1mL	.75g	10mL	.075g	3mL
010510	.15g	40mL	.4g	5mL	1mL	.75g	10mL	.075g	4mL
011210	.15g	40mL	.4g	5mL	1mL	.75g	10mL	.075g	4mL
012110	.3g	80mL	.8g	10mL	2mL	1.25g	20mL	.15g	8mL
012610	.25g	40mL	.4g	5mL	1mL	.75g	10mL	.075g	4mL
012810	.25g	40mL	.67g	8.3mL	1.67mL	.75g	10mL	.075g	4mL
020210	.25g	40mL	.67g	8.3mL	1.67mL	1.5g	20mL	.075g	4mL

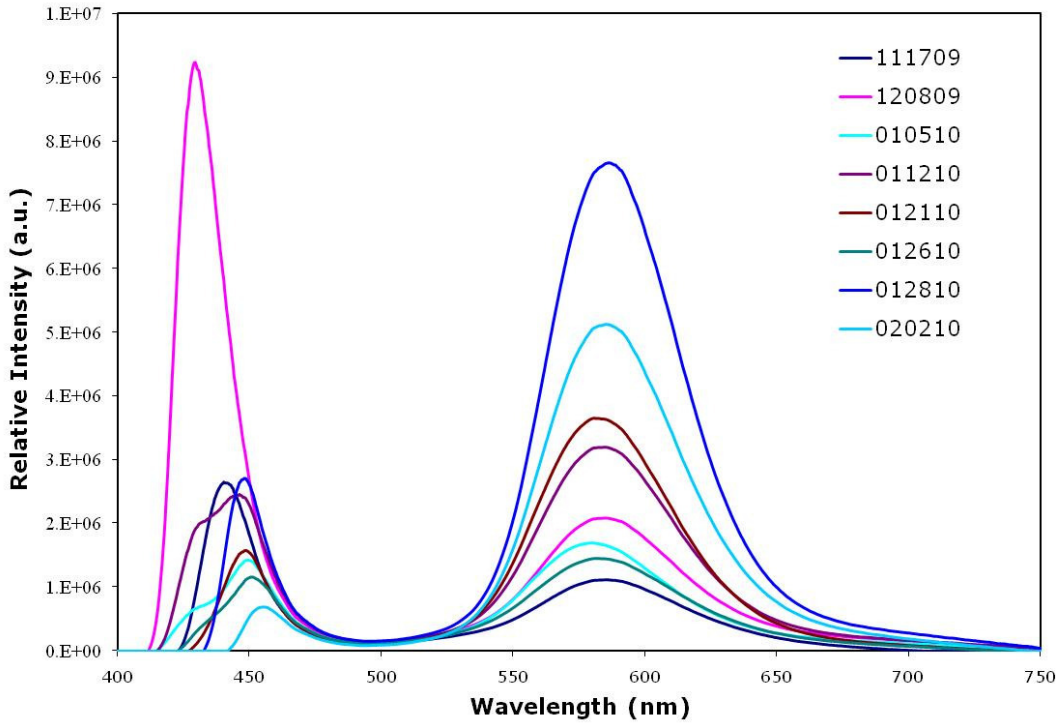

Figure 36. Luminescent spectra of various ZnSe:Mn nanophosphors showing both host and Mn emissions.

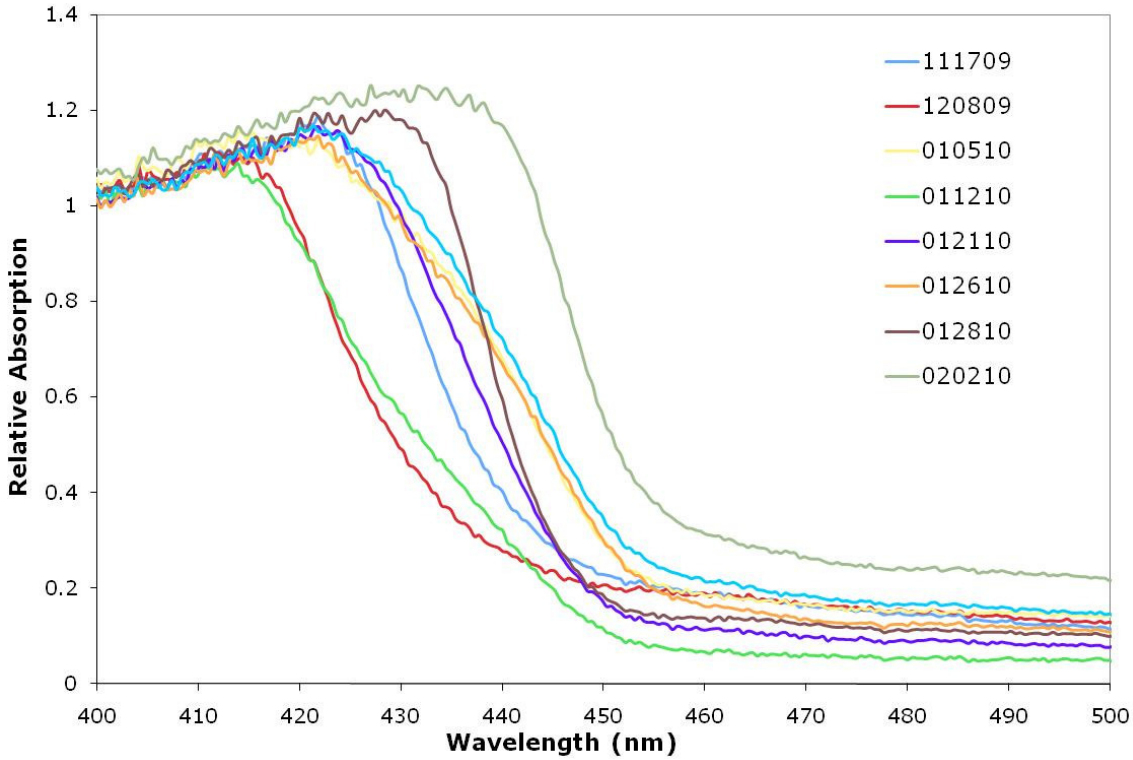

Figure 37. Absorption curves of ZnSe:Mn nanophosphors prepared under various conditions.

Summary of ZnSe:Mn Optimization Results

A significant shift (~20nm) in the absorption edge of ZnSe:Mn nanocrystals, as shown in Figure 38 (left), was obtained. The ~468nm edge corresponds to the bulk ZnSe bandgap of 2.65eV, indicating the formation of large particles and a departure from the quantum confinement mode into the bulk mode of ZnSe:Mn. The procedure for achieving these large particles was similar to our standard process until the $ZnAc_2$/TBP injection step. An additional tube containing $MnSt_2$/ODE was prepared to create additional shells. First we started by injecting 4mL of the $ZnAc_2$/TBP solution and we let that sit for approximately 12 minutes. The second injection consisted of 2mL $ZnAc_2$/TBP and directly after, 1mL of $MnSt_2$/ODE was also injected. There were a total of 8 injections that consisted of 2mL $ZnAc_2$/TBP & 1mL of $MnSt_2$/ODE. An annealing step was then applied after the injections were completed, which involved ramping up from 180^{o}Cto 260^{o}C. The solution was maintained at 260^{o}C for approximately 45 minutes and then cooled down to room temperature for subsequent collection. Although our goal of high blue light absorption has been achieved, a limit is reached due to the occurrence of non-radiative band gap recombination from within the ZnSe layer (i.e., the shell has become too thick). This could be due to higher concentration of defects associated with the longer time period required to grow thicker shells. The lower host emission in the 17nm sample could also be a result of increased self-absorption by the undoped ZnSe shell.

The large particle sizes of these samples was confirmed using a Coulter DelsaNano C particle size analyzer capable of measuring nanophosphors and quantum dots down to 0.6 nm. The new system was used successfully to confirm the range of ZnSe:Mn particle sizes that have been produced in recent months. As shown below in Figure 39, the results showed samples with average particle sizes as low as 6.9nm and as high as 17nm. The data seems to confirm that, while a larger particle size results in increased blue light absorption, the quantum yield (QY) of

the larger nanocrystals (17nm) is much lower (50%) compared to that of the smaller (6.9nm) ZnSe:Mn nanocrystals. Using an existing Rhodamine 6G reference dye, the 6.9nm sample exhibits a QY value as high as 82%, which is the largest QY value of any ZnSe:Mn sample produced to date. Since the existing Rhodamine 6G dye is several years old, we will be confirming this value using a newer Rhodamine 6G fluorescent reference standard that was recently purchased from AnaSpec, which has a confirmed QY value of 95%.

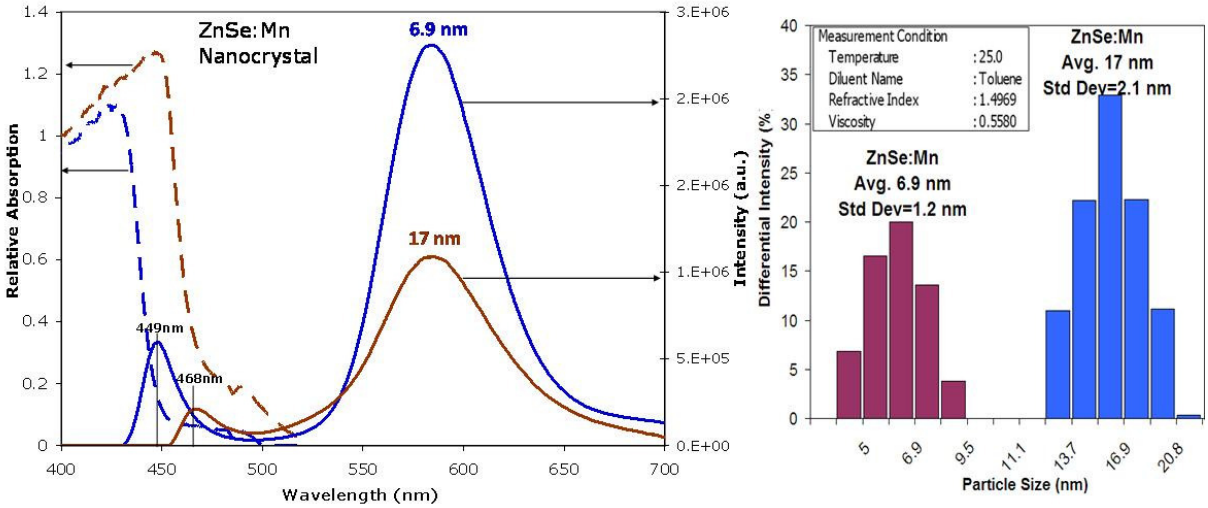

Figure 38. LEFT: Relative absorption and emission of ZnSe:Mn nanocrystals with different particle sizes. RIGHT: Coulter particle size distribution of the same samples showing average sizes of 6.9nm and 17nm.

Analysis of the data shown in Figure 39 reveal several interesting facts about the ZnSe:Mn nanocrystals: 1) Both the particle size (17nm) and energy bandgap (2.65 eV ➔ 468 nm) of the larger particle sample confirm that we have successfully transformed the ZnSe:Mn nanocrystals from the "quantum dot" regime to that of "nanophosphor"; and 2) the higher blue light absorption achieved by red-shifting the absorption edge of ZnSe into the bulk region comes at a relatively steep price in terms of QY performance. We believe this is primarily due to higher exciton recombination in the thicker ZnSe shell. In other words, when a thin ZnSe shell is produced, the energy from the electron-hole (e-h) pairs generated as a result of light absorption by the ZnSe can be effectively transferred to the Mn^{2+} ions in the core. However, in a thicker ZnSe shell, some of the e-h pairs have a higher probability of recombining in the shell before reaching the core. We have tried to address this issue by Mn^{2+} doping of the shells, but the efficiency did not improve, which is more likely a result of additional defects introduced due to the lattice mismatch between MnSe and ZnSe. Therefore, it appears the best option for producing large ZnSe:Mn particles with high QY is annular doping of alternating layers of ZnSe and MnSe, which would require a much higher degree of control and automation not possible with the existing colloidal synthesis system.

Investigation of Other Dopants

Our work on the ZnSe nanophosphor system has also involved analyzing and comparing various samples doped with Mn, Cu+Ag, and Mn+Cu+Ag. Similar to the NPs doped with the isoelectronic dopant Mn, the Cu/Ag ions are positioned within the ZnSe bandgap but now also act as acceptor levels which attract holes in the valence band and allow recombination from electrons in the conduction band. Figure 40 shows a comparison between the spectral emission characteristics of ZnSe:Mn, ZnSe:Cu,Ag, and ZnSe:Cu,Ag,Mn when excited by a UV source at

365 nm. The ZnSe:Mn NP exhibits the typical orange-yellow spectrum for this material system with a luminescent peak around 585 nm. In contrast, the ZnSe:Cu,Ag sample exhibits a broader spectrum peaking in the blue-green region (~500nm) with a tail extending well into the orange-red parts of the spectrum, up to 650nm. On the other hand, the hybrid ZnSe:Cu,Ag,Mn system showed a 2-peak emission; a strong peak at ~585nm and a weaker peak at about 500nm. Both the ZnSe:Cu,Ag and the ZnSe:Cu,Ag,Mn NPs appear "white" under UV excitation with the former sample having a "cool white" color while the latter sample exhibited a "warm white" emission similar to that of incandescent bulbs.

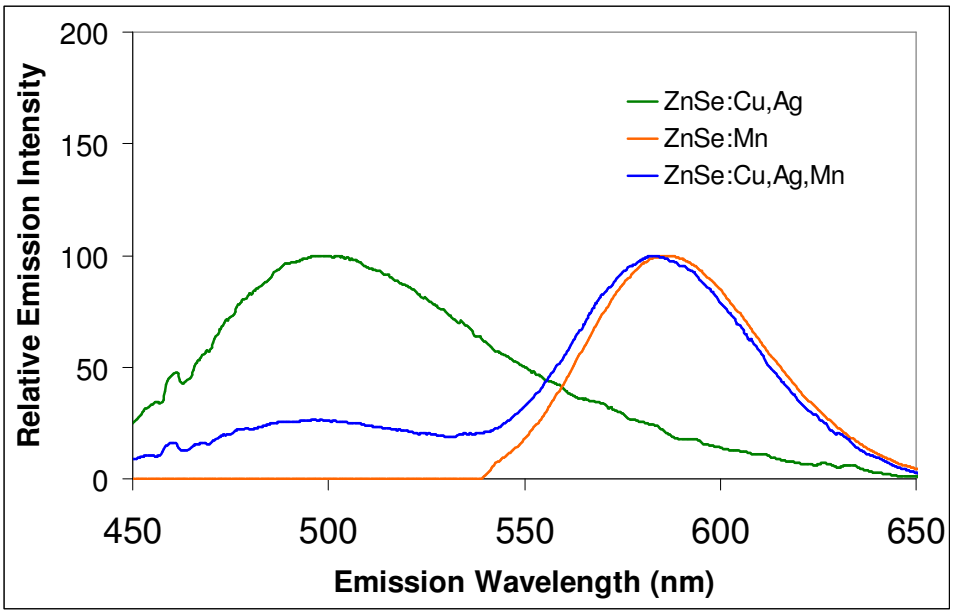

Figure 39. Comparison of various ZnSe nanophosphors doped with Cu, Ag, and/or Mn.

Development of In Situ Monitoring Tools and Automated Systems for Nanocrystalline Systems

In order to efficiently optimize these parameters of temperature and rate, we have constructed an in-situ emission monitoring apparatus, pictured in the inset of Figure 41. This system uses a fiber optic probe connected on one end to a 150mW 405nm UV laser and to a fiber optic spectrometer, on the other end. The probe is held outside the reaction flask in order to avoid disruption of the reaction solution. As shown in the figure below, this "initial monitoring data" provides instant feedback on the effect of each subsequent injection of Zn stearate and the reaction time on the optical properties of ZnSe:Mn nanocrystals.

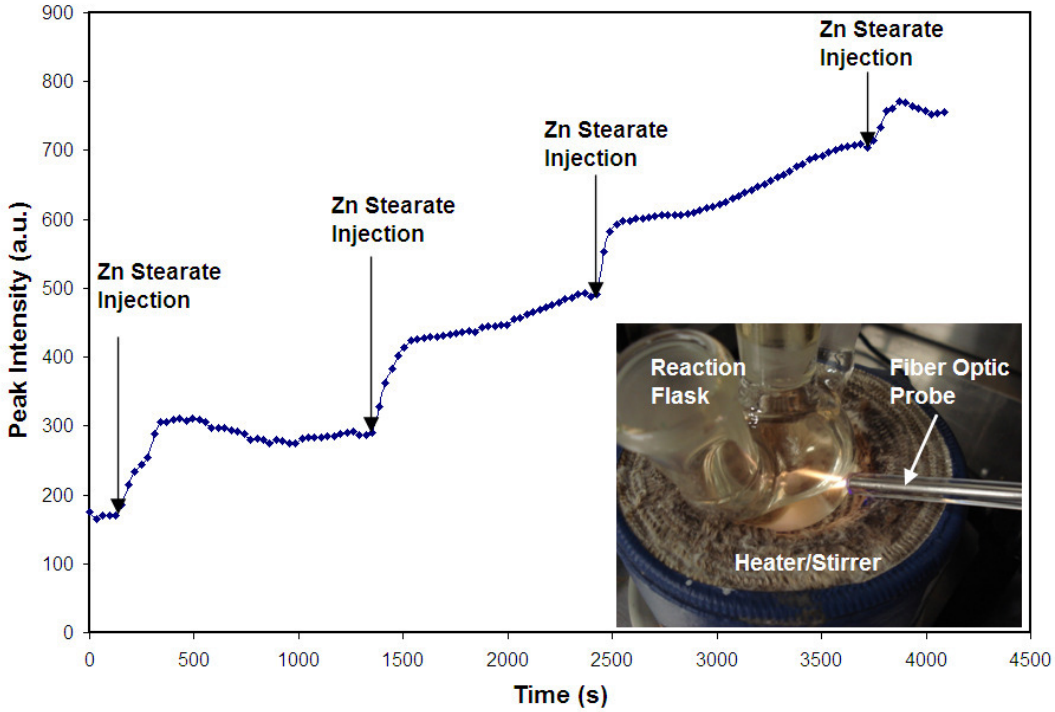

Figure 40. In-situ monitoring of ZnSe:Mn emission peak intensity during synthesis using a 405nm laser through a fiber optic probe and a spectrometer.

We've also added a second colloidal synthesis 3-line station (Figure 42) for parallel sample preparation in order to expedite the research and production of nanocrystals. This new system is not only capable of making three samples simultaneously, but it can also be easily expanded in the future. This flexibility is made possible by the custom-made temperature control system that can handle up to nine heating mantles at once. The system also includes a central cooling unit that constantly circulates cool water through the condenser columns, a manually adjusted stir plate for each heating mantle, and a hot oil bath that is also temperature controlled by the computer. Further automation has been developed that provides in-situ spectral data of up to six samples simultaneously. Both the temperature control and the optical feedback are processed through a central computer that is backed up on a battery pack. The current heating mantles fit 100 ml flasks but could be easily replaced with other sizes. The temperature control system is independent of the heating mantles, which simply plug into it. The optical system constantly monitors the full spectra from the various flasks allowing specific wavelength monitoring for growth plots versus time.

The 3-line nanocrystal colloidal synthesis station was successfully implemented and tested. There were few problems that occurred during the first run, all of which pointed to automation as the solution for both repeatable nanocrystal manufacturing and research with a combinatorial chemistry approach. At this point, the system is well automated in terms of heat control and optical feedback, but the preliminary results indicated that injection automation is the biggest variable and deserves the highest priority. Despite the difficulties with operating all three lines at once, our best results on ZnSe:Mn nanocrystals have been successfully repeated. Figure 41 shows the spectra of two of the samples that were made with the system. QD2 was the very first sample that was attempted on this system and QD1 is comparable to one of our best samples with a QE around 60%, which is similar to those prepared using the single-line system.

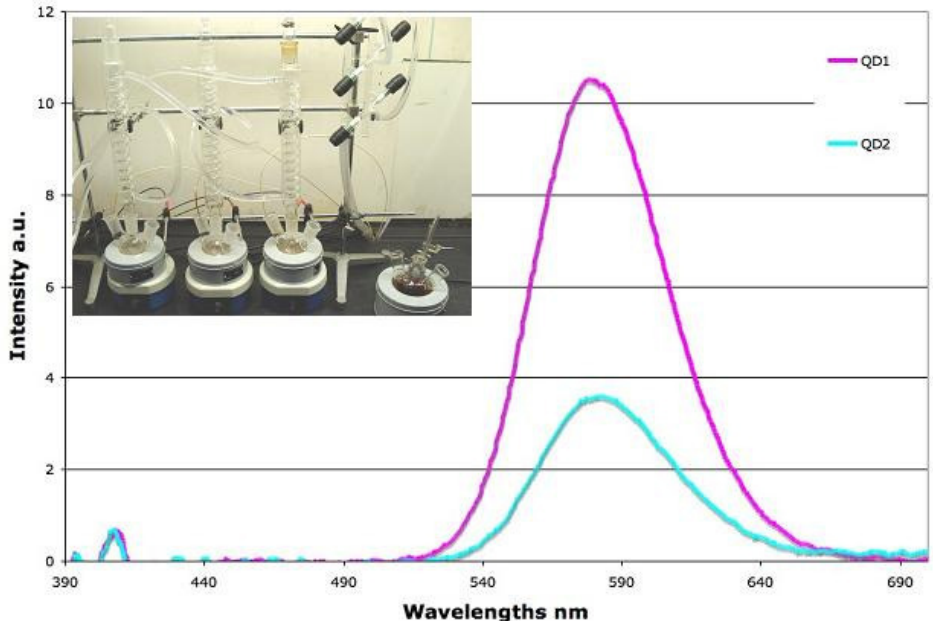

Figure 41. Emission spectra comparing performance of ZnSe:Mn recently made (QD1) using the 3-line system (inset) as compared to the first sample of ZnSe:Mn (QD2) that was attempted last month.

Manufacturing Study of Doped ZnSe Nanophosphors

Following the successful development of ZnSe:Mn nanophosphors, a manufacturable process for these doped ZnSe nanophosphors was developed to provide an alternative source of light emitting materials in solid state lighting. These materials have advantages in terms of solution processability over conventional materials. Moreover, compared to the commonly used quantum dots, these materials are less toxic, have zero re-absorption, high temperature stability and less susceptiblity to chemical degradation.[i]

Over the past few years, successful doping of various types of nanocrystals has been reported in literature. [ii,iii,iv] Among these dopings, zinc selenide with transition metals has received increased attention due to the possibilities of relatively greener synthetic processes that can be utilized to synthesize these materials. [i] At Phosphortech, we focused on synthesizing manganese doped zinc selenide nanocrystalline system due to our interest in developing emitters in the yellow-orange region. The presumed structure of manganese doped zinc selenide nanocrystals that are highly efficient orange emitters is shown in Figure 43.

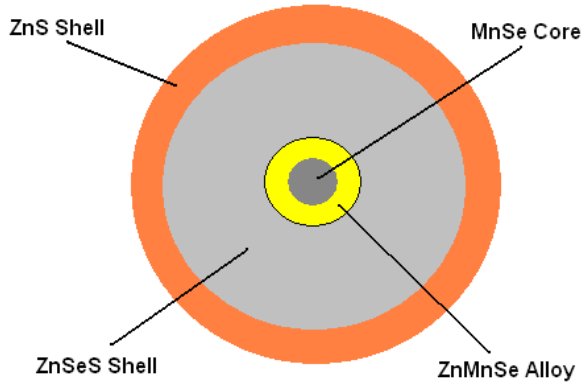

Figure 42. Manganese doped zinc selenide nanocrystal.

We focused on developing manganese doped zinc selenide nanocrystalline system as shown in Figure 43 with a focus on

1. Improving the synthetic methodology towards consistency and scalability,
2. Analyzing the stability of the material system
3. Augmenting the solution processability by improving the compatibility of the doped nanocrystals in aqueous media
4. Transfer of the emissive material into polymeric matrix.

Improving methodology for consistency and scalability

The synthetic methodology adapted at Phosphortech for synthesizing manganese doped Zinc Selenide nanocrystals involved the following stages:

(i) Nucleation and growth of MnSe core
(ii) ZnSe nucleation on the surface of MnSe surface to form a thin layer of MnZnSe and growth of ZnSe
(iii) Surface passivation by forming an outer ZnS laver over the manganese doped zinc selenide

Nucleation and growth of MnSe Core

We attempted two possible strategies in synthesizing the MnSe core - one involving injection of manganese precursor in a hot solution containing selenium and the other involving injection of selenium precursor in a hot manganese precursor solution. The synthesis of MnSe core was achieved by using manganese stearate as the precursor. It has been observed that the purity of manganese stearate plays a vital role at this stage. Also, it is important to maintain a steady growth temperature. A customized temperature monitoring and control system for the entire synthetic process has been set up in such a way that the temperature of the flask was raised to 290°C and maintained at 290°C for 15 minutes before the injection of TBP-Se. After injection, the temperature was maintained at 260°C for an hour.

ZnSe nucleation on MnSe to form a thin layer of MnZnSe and growth of ZnSe

After the growth of MnSe nanocrystals at 260°C for one hour, the temperature of the reaction system was dropped to 240°C. At 240°C zinc stearate was injected and the temperature was maintained at 240°C for half an hour. The relatively high temperature at this stage facilitates the nucleation of ZnSe on MnSe and subsequent alloying at the surface. The temperature was then dropped to 180°C and maintained at 180°C for injections of zinc acetate for the growth of zinc selenide and the alloyed ZnMnSe layer of the zinc selenide core. In optimizing the injection procedure of zinc acetate, syringe pumping systems were introduced to inject zinc acetate at a constant flow rate to achieve consistent and reproducible results

ZnS Surface Passivation

Initially, we attempted a two step method to overcoat, manganese doped zinc selenide sulfide nanocrystals with zinc sulfide. The synthesized core nanocrystals were precipitated with acetone and methanol, separated by centrifugation and then re-dispersed in chloroform or

toluene. To the re-dispersed nanocrystals, zinc sulfide precursors such as zinc acetate and sulfur or hydrogen sulfide for over-coating at temperatures ranging between 150° and 250°C. We found that we were able to over-coat the luminescent material with a zinc sulfide layer through drop-wise addition of zinc oleate and sulfur in 1-octadecene at 240°C. Though the core-shell material thus synthesized had better luminescence than the core (Figure 44), we also worked on less time consuming approaches that can potentially yield similar materials with consistent optical properties and stability.

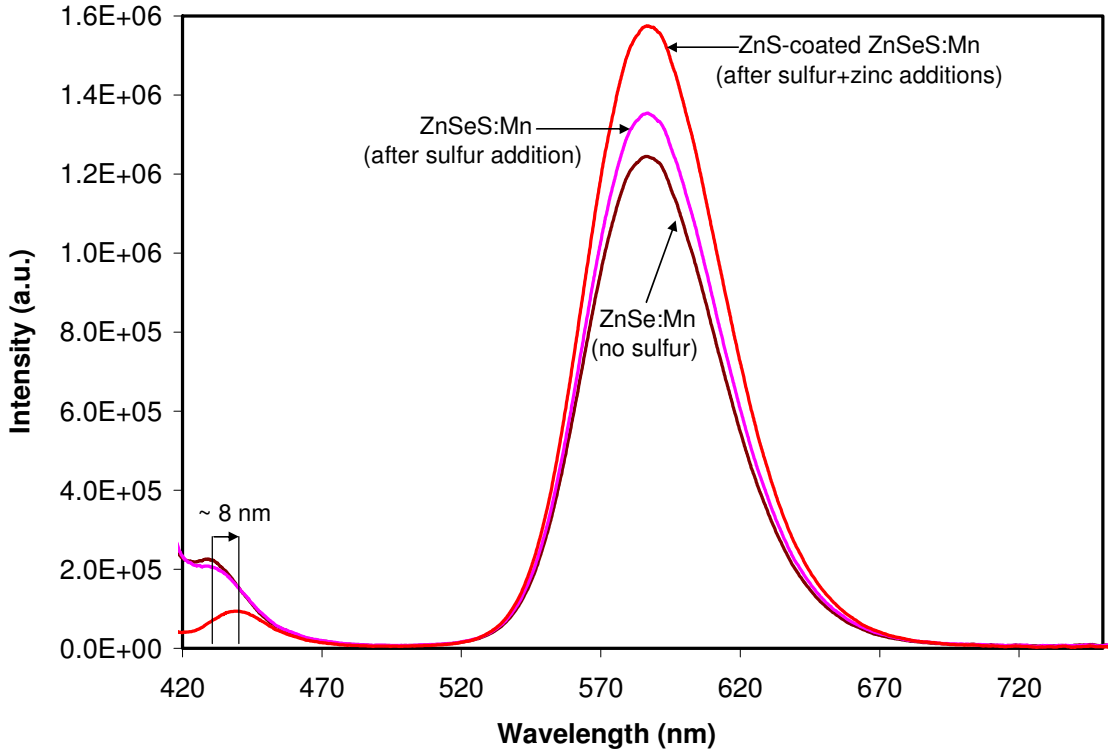

Figure 43. Emission spectrum of ZnSe:Mn and ZnS coated ZnSeS:Mn.

To address this issue a single pot method was designed to over-coat manganese doped zinc selenide nanocrystals with zinc sulfide. In this method, we used a syringe pump to inject a solution of sulfur in trioctylphosphine or tributylphosphine at 240°C half an hour after the injection of TOP-Se, and just before dropping the temperature to 180°C as required for zinc acetate addition. A bright luminescent material was produced by this process. Furthermore, in-situ UV laser excitation shows a strong peak around 577nm that shifts to 584nm with annealing (Figure 45). This may be an indication of the particles rearranging themselves by dissolving into solution and then re-growing throughout the annealing period. If this is so, then it is likely that the sulfur is moving to the surface of the particles given that it is slightly less reactive than the selenium. The significant advantage of this process over other methods is that it is a single pot reproducible procedure yielding bright luminescent material on a larger scale (2.25g) and has the potential to be scaled up further.

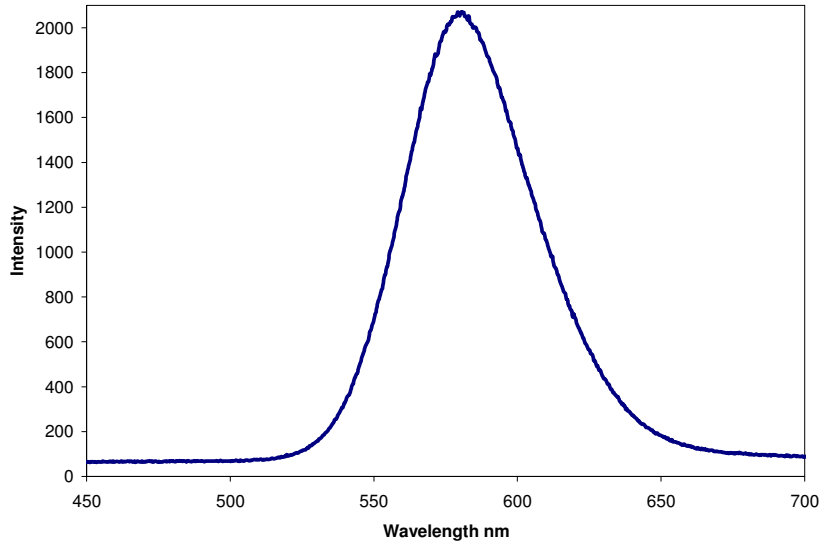

Figure 44. Emission spectrum of ZnS coated Mn:ZnSe.

Currently, we have developed procedures to synthesize manganese doped zinc selenide nanoparticles with zinc sulfide shells either through a single or two step processes. These synthetic procedures can be fine tuned to give materials with specific optical properties as per varying needs in their applications.

Long Term Stability

While developing synthetic methods that can yield materials with consistent optical properties, we also focused on analyzing the stability of the synthesized luminescent nanocrystalline systems over time.

In an attempt to gain insight into the optical stability of the synthesized doped nanocrystals, we performed an accelerated luminescence decay test using a high powered UV laser source. We observed the luminescence stability of ZnSeS:Mn nano-particles (without the zinc sulfide shell) as a function of particle concentration in solution using an above-bandgap ultraviolet (405nm) laser to rapidly degrade the particles inside a fixed glass cuvette. These measurements were done in transmission mode with a constant laser power while monitoring the emission from the ZnSeS:Mn at around 585nm. Several runs were conducted by introducing different concentration of particles while measuring the peak intensities of the emission peaks with time. We found that though there was a significant drop in luminescence over few hours, the drop in luminescence of the nano-particle suspensions was relatively lower for samples with larger particle concentrations (Figure 46).

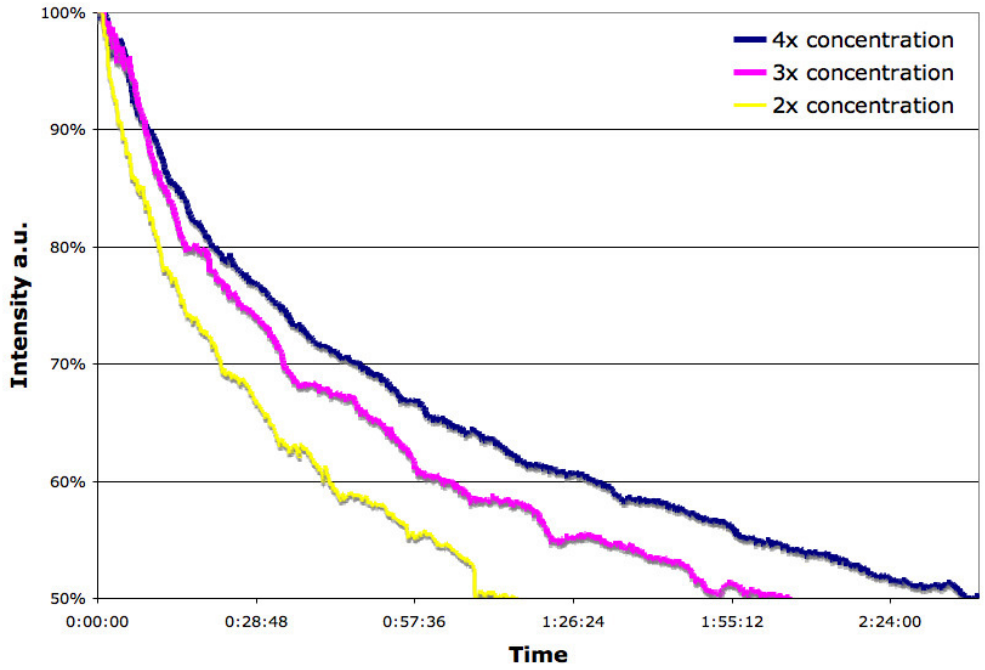

Figure 45. A plot of accelerated degradation of ZnSeS:Mn nanophosphors with different concentrations.

We then used a similar accelerated luminescence decay experiment to compare the drop in luminescence of the bare manganese doped zinc selenide nanocrystals and that of the sulfide encapsulated nanocrystals. Dispersions of zinc sulfide encapsulated manganese doped nanocrystals and bare manganese doped nanocrystals were prepared in separate vials. The samples were then kept under UV-visible radiation from a high powered source with laser beam emitting at 405nm. The samples were not kept free from air. The drop in intensity of the luminescent material over time was recorded using an Ocean Optics spectrophotometer system. As can be seen from Figure 47, the luminescence of bare manganese doped zinc selenide material dropped (red line) significantly and showed little sign of stabilizing under high irradiated power density. On the other hand, the emission from ZnS-encapsulated Mn-dope ZnSe nanocrystals (green line) stabilizes quickly and reaches a steady state output. These results suggest that the encapsulation of the doped nanocrystals indeed improves their stability and longevity.

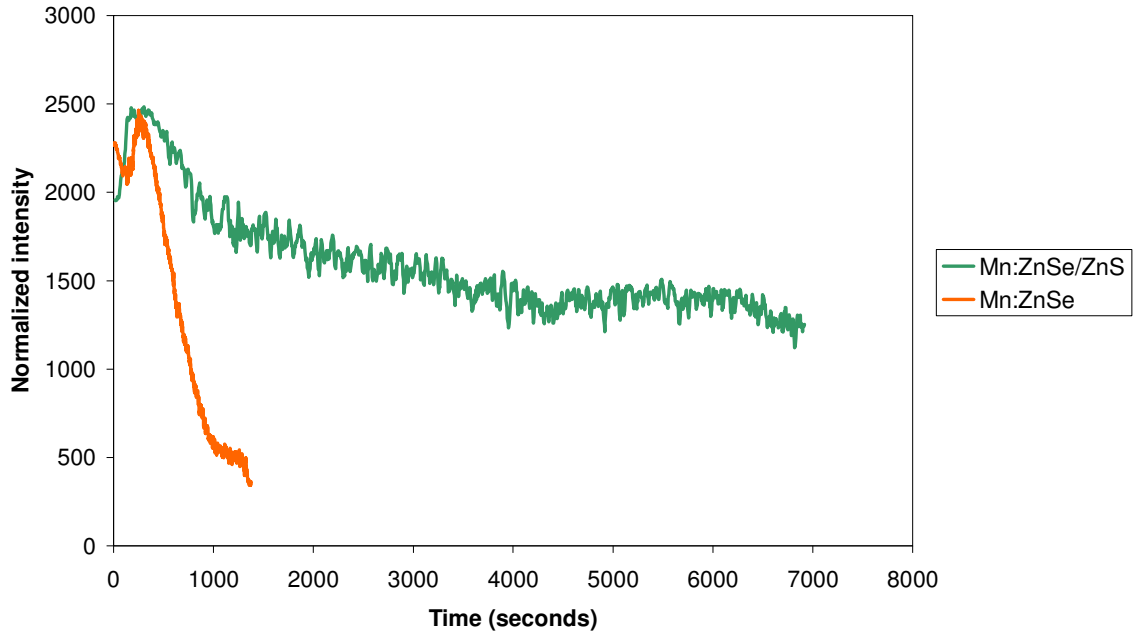

Figure 46. Accelerated luminescence decay of Mn:ZnSe and zinc sulfide coated Mn:ZnSe.

Improving processability and compatibility in aqueous media

The synthesized nanocrystalline systems were found to be stable dispersions in non-aqueous media over many months. But due to the hydrophobic nature of the capping ligands, they cannot be dispersed as such in aqueous media. Making them compatible with water, with options to disperse them in aqueous media, can potentially broaden the scope of their use through a wide set of processing methods. To make them compatible with water, the hydrophobic capping ligands had to be replaced with hydrophilic ligands. In general, the ligand exchange process from the surface can lead to a loss of luminescence due to various processing factors.

Initial attempts to transfer the synthesized nanocrystals without a sulfide layer into the aqueous media resulted in quenching of luminescence. The sulfide layer probably helps to protect the surface of the nanocrystals augmenting their stability in water. A hydrophilic ligand exchange process was adapted to transfer the dots capped with hydrophobic ligands so as to make them dispersible in water.

To a vial containing 0.5mL of the manganese doped zinc selenide nanocrystals dispersed in toluene, mercaptopropionic acid was added drop by drop until the solution became turbid. The mixture was agitated vigorously for 30 minutes. The reaction mixture was then transferred into a centrifuge tube and the contents were centrifuged for 5 minutes. The clear supernatant was collected separately. The residue was dried. De-ionized water was then added to the centrifuge tube and sodium bicarbonate solution was added drop by drop to the contents of the centrifuge tube, with agitation, to re-disperse the nanocrystals in water. The contents were centrifuged again and the clear supernatant water dispersion of nanocrystals was collected separately. The remaining residue was re-dispersed in toluene and the above transfer procedure was repeated to transfer the remaining hydrophobic nanocrystals into water.

Though the mercaptopropionic acid capped nanocrystals dispersed in water showed a mild drop in luminescence compared to the nanocrystals dispersed in toluene (of similar concentrations), they are found to be comparable in brightness (Figure 48).

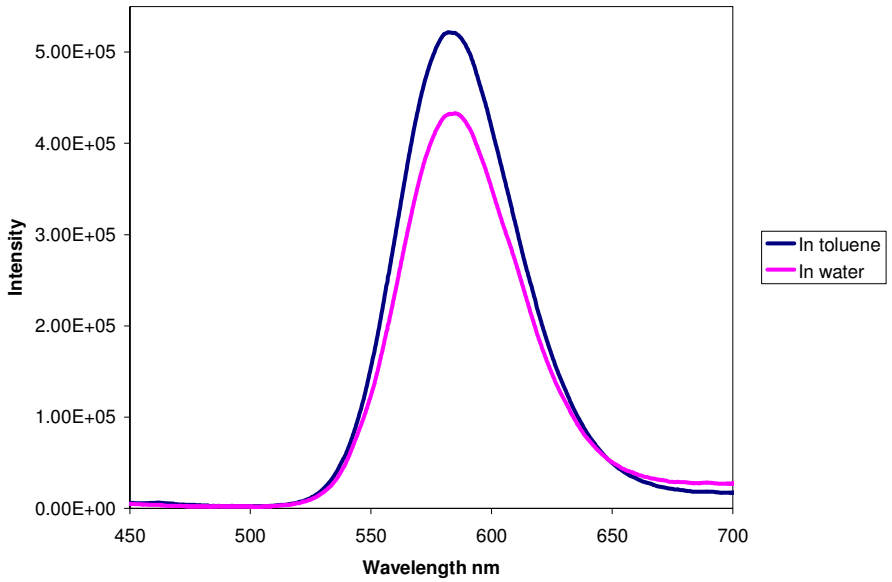

Figure 47. Photoluminescence of zinc sulfide coated manganese doped zinc selenide nanocrystals in toluene and in water.

Tuning optical properties of lighting device by using the doped nanocrystalline material

With adequate knowledge on synthesizing manganese doped zinc selenide nanocrystals, we started working towards tunability of the optical properties of these materials that can be very convenient for use in LEDs. We analyzed and categorized the various processing parameters that would allow us to produce and commercialize nanophosphors for a wide variety of applications, for both blue and UV-pumped LEDs. For example, various broadband-emitting ZnSe-based nanophosphors were demonstrated, which are particularly applicable for UV LED applications. By controlled Mn co-doping during particle shell growth, some of the ZnSe:Mn nanocrystals exhibited multiple peak emissions in both the blue and yellow-orange parts of the spectrum. Particle size of the nanocrystals having these optical characteristics varied from around 6 nm (quantum confinement mode) to over 20 nm (bulk mode), as analyzed from photon correlation spectroscopy (PCS) and evident from the size-dependent (< 10 nm) blue ZnSe emission. When pumped using a UV LED or laser (~405nm), the single-component ZnSe:Mn nanophosphor system produced a broad emission spectrum similar to that of conventional white LEDs that are based on a blue LED and a yellow-orange micron-sized phosphor. This unique property is the result of strong radiative transitions from both the Mn^{2+} activator sites as well as the ZnSe host, which typically exhibit weak or non-radiative bandgap emission. By controlling the amount, ratios, and timing of the precursor injections, it was possible to control both the blue peak emission wavelength (from 440 to 468 nm) as well as the blue-to-yellow emission ratio thus producing a wide range of spectral color gamut, as illustrated in Figure 49. For example, color chromaticity (CIE 1931) values ranged from (x=0.289, y=0.191) to (x=0.491, y=0.411) while the correlated color temperature (CCT) varied from around 2318K to 6450K. The red-shifted (~580nm) spectrum of the Mn^{2+} emission is particularly suited for warm white LED-based lighting applications, as shown by the LED prototype pictured in Figure 48.

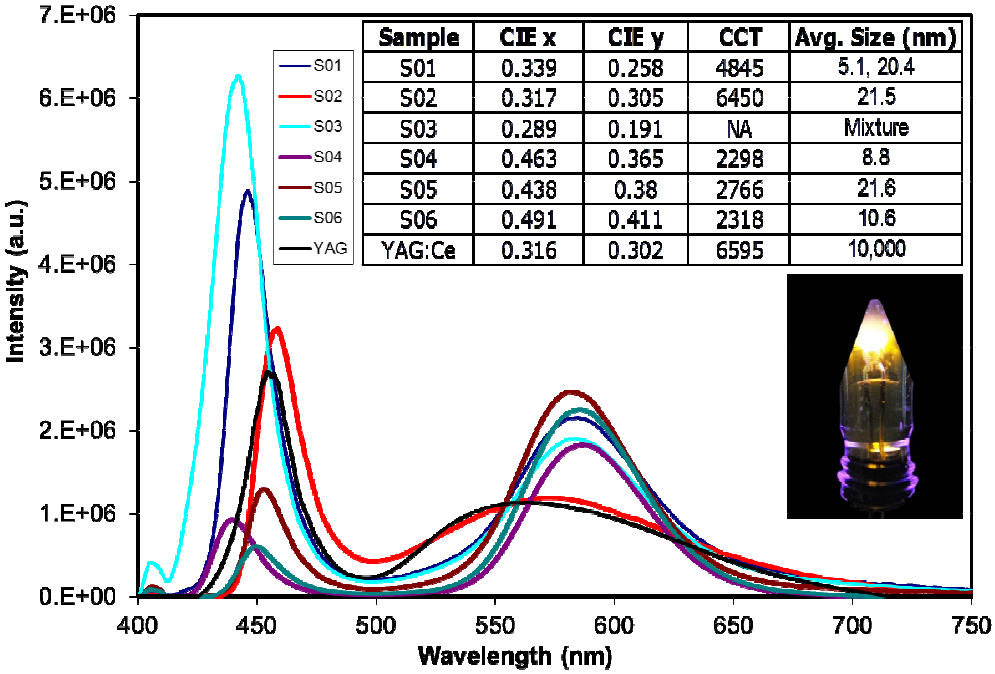

Sample	CIE x	CIE y	CCT	Avg. Size (nm)
S01	0.339	0.258	4845	5.1, 20.4
S02	0.317	0.305	6450	21.5
S03	0.289	0.191	NA	Mixture
S04	0.463	0.365	2298	8.8
S05	0.438	0.38	2766	21.6
S06	0.491	0.411	2318	10.6
YAG:Ce	0.316	0.302	6595	10,000

Figure 48. Broadband emission and spectral control achieved using various single component ZnSe:Mn nanophosphors under 405nm excitation. Inset photo shows a warm white LED constructed using a UV LED and a ZnSe:Mn nanophosphor.

Further continuing on efforts towards incorporating ZnSe:Mn into lighting device applications, we have recently developed methods of incorporating nanocrystals with conventional bulk phosphor materials in order to create a hybrid system with an value-added advantage that can be easily incorporated in conventional LEDs. To demonstrate the feasibility of such approach, we used a simple process of adsorption of the nanocrystals onto the surface of a bulk phosphor, specifically a green Eu-doped strontium thiogallate (STG) material. The emission spectra of STG, ZnSe:Mn nanocrystals and that of the new hybrid material are shown in Figure 50, below. The hybrid material clearly shows a bimodal color distribution having two emission peaks one at 535nm and another at 580nm. Further studies are currently in progress to produce various spectral characteristics using hybrid bulk-nano systems.

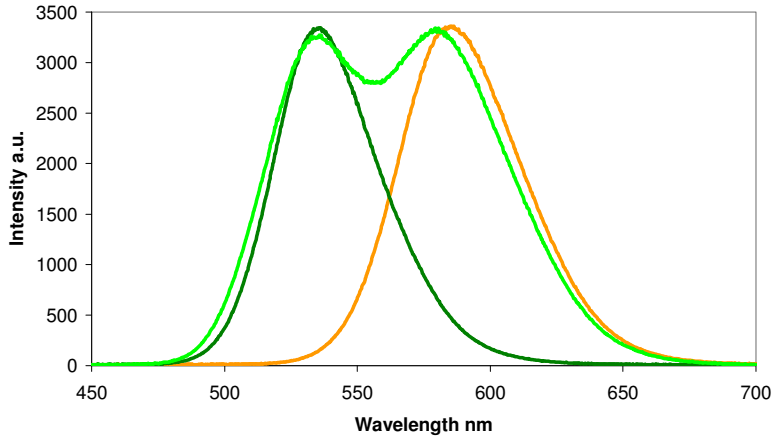

Figure 49. Spectra showing individual emission from bulk STG (dark green line), ZnSe:Mn nanocrystals (orange line) and hybrid bulk-nano system (light green line).

The experimental technique used to obtain the bulk/nanocrystal mixture involved mixing 0.5 g of STG with 0.3mL of a toluene dispersion of ZnSe:Mn nanocrystals in a vial and adding 1.5mL of acetone and 0.5mL of methanol. The contents were mixed well for 5 minutes and centrifuged for 5 minutes. After centrifuging, the clear solution was discarded and the residue was dried, allowing the nanocrystals to be adsorbed onto the surface of the bulk phosphor material. The various spectra were taken using a UV LED emitting at 405nm to prevent overlap with the LED spectrum.

Incorporation of emissive quantum dot materials into polymeric matrix

To extend the range of applications of nanocrystalline materials we have studied the incorporation of nanophosphors into polymers for use in various LED packages. We have been able to disperse nanocrystals in polymethyl methacrylate (PMMA) to produce a transparent orange light emitting material. A simple polymerization of methyl methacrylate monomer in the presence of the nanophosphors yielded a transparent matrix upon curing. 15mg of the dispersion of nanocrystals in toluene, 0.3g of methyl methacrylate and 1.5mg of 2,2'-azobis(2-methylpropionitrile) were taken in a vial, mixed well and then heated at 80°C for 1 hour in a nitrogen atmosphere to give a clear polymethyl methacrylate nanocomposite material.

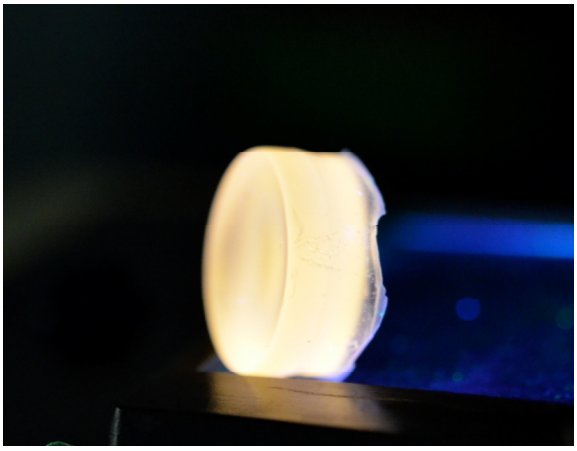

Figure 50. Photluminescence of ZnSe:Mn/ZnS - PMMA Composite on UV light exposure.

ZnSe:Mn Nanocrystals in Polymethyl-methacrylate (PMMA)

In order to prepare ZnSe:Mn/polymer nanocomposite, polymerization of mixture of MMA monomer with ZnSe:Mn QD solution in toluene or chloroform was investigated. For example, 5ml of QD solution in toluene was added into 15ml of MMA monomer in a glass vial. The mixture was clear and 20 mg of 2,2'-Azobisisobutyronitrile (AIBN) was added as the initiator. The glass vial was immersed into an oil bath at 50°C for 20h for polymerization. Then, a ZnSe:Mn/polymer nanocomposite was obtained. However, the sample turned cloudy after polymerization probably due to the agglomeration of nanocrystals in the process. It has been confirmed that toluene would not affect the clarity of PMMA if no nanocrystals were incorporated. Nanocrystals dispersed in chloroform were also tried for polymerization but the composite was not very transparent. Figure 52 shows the image of a composite sample under 365nm UV lamp.

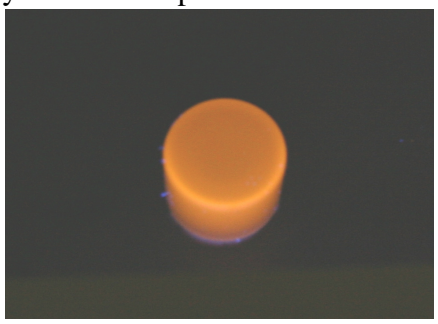

Figure 51. Image of a ZnSe:Mn QD/PMMA nanocomposite under excitation with a 365 nm UV lamp.

ZnSe:Mn Nanocrystals in Polystyrene

The agglomeration of ZnSe nanocrystals in PMMA is probably due to the non-compatibility of the nanocrystals with the MMA monomer. Dry ZnSe nanocrystals powders could not be dispersed into MMA to obtain a clear solution. In order to find an appropriate polymer matrix, other monomers were investigated including acrylic acid and styrene. It was found that styrene could serve as a solvent for ZnSe nanocrystals and a clear styrene monomer/ZnSe QD solution was obtained. In this case, bulk polymerization of a styrene monomer/ZnSe QD solution can be conducted without using any additional solvents such as toluene and chloroform. Because no solvent was involved during the polymerization process, bulk samples with any shape could be easily formed. The QD-styrene solution was polymerized in a glass vial in an oil bath at ~73°C for 20h using 0.1% of 2,2'-Azobisisobutyronitrile (AIBN) as initiator. However, the composite turned opaque again after polymerization.

In addition, Ag-doped ZnSe nanocrystals were also synthesized in the reaction systems using an isolation and purification process to separate the nanocrystals from the by-products and excess precursors. The procedure used for the synthesis of ZnSe:Ag NPs involves ZnSt2 (Zinc Stearate), ODE (Octadecene), AgAc (Silver Acetate), ODA (Octadecylamine), and TBP (Tributylphosphine). The solution was degassed under vacuum at 110^{o}C for 1 hour, the temperature was increased to 285 ^{o}C, where it was kept for 15 minutes during the reaction, and then reduced to 180 ^{o}C for 45 minutes in order to allow for the silver to attach to the surface. Afterwards, the solution is allowed to cool down and chloroform is injected at 80^{o}C. Following synthesis, the ZnSe solution appeared clear yellow/green under room lighting, while the silver source solution appeared light-brown. After overcoating with ZnSe, a purple/blue emission was seen at 180 ^{o}C (by UV excitation). After cooling to room temperature, a blue/green emission was seen, as shown in Figure 52.

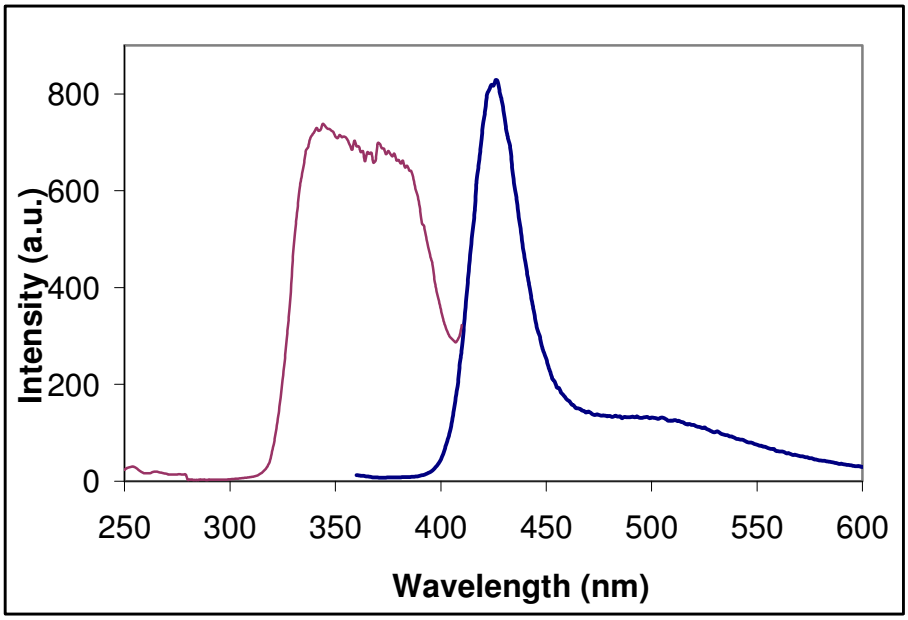

Figure 52. Photoluminescence excitation spectra and photoluminescence for the ZnSe:Ag NP.

We have also achieved the formation of ~10 nm diameter yellow-emitting Mn-doped ZnSe NCs with a narrow size distribution that displays blue-shifted absorption edge and high quantum efficiency around 65%. The emission intensity was observed to increase with temperature up to 100°C and then decrease by only ~8% at 200°C. This strong resistance to thermal quenching is a particularly attractive feature for applications of this material system to high-brightness white LED devices. Successful synthesis of nano-crystalline materials was conducted using the automated system described above with a pressure-actuated EFD 1500XL dispenser and flask heating mantles. Mn-doped ZnSe NP synthesis was achieved by first dissolving manganese stearate in octadecylene (ODE) and then purging/filling with nitrogen and degassed at 110°C for 1 hour under Argon. Selenium powders are then dissolved in tributylphosphine (TBP) at 140°C under nitrogen and then injected into the manganese stearate flask. Finally, zinc acetate is dissolved in 9mL TBP at 140°C under Nitrogen and then slowly injected into the heated flask over an extended period of time.

Task 3: Encapsulation of Sulfoselenide Systems for Chemical Stability

The major objective of this task was to acquire a commercial particle coating system for coating individual sulfur-selelenide based phosphor particles by the fluidized bed, or a similar technique, and to demonstrate a manufacturing process for the coating of large particle charges. However, as described below, this was not possible and so this task was refocused with the objective to: 1) design a fluidized bed atomic layer deposition (FB-ALD) reactor capable of coating reasonably large charges 200-500 gm and; 2) to apply the current capabilities at our disposal (principally at Georgia Tech) to investigate other coating techniques (such as screened phosphors) and by coating smaller phosphor charges to provide a proof-of-concept study. As a result of these investigations we have demonstrated the effectiveness of hermetically sealing phosphor particles with a conformal thin film of a metal oxide and showed that this procedure dramatically improved aging and performance. The details of these investigations are described below.

At the initiation of this program an NDA was signed and discussions held with an ALD vendor on the requirements for a fluidized bed atomic layer deposition system for encapsulating

ZnSSe phosphor particles with diameters ranging from ~20 μm to ~50 nm; in >500 gm quantities. These discussions led to a comprehensive series of tests in the vendor's tool to assess the potential of their fluidized bed system and to define a viable system for our needs. Consequently, 4 sulfoselenide samples were prepared and shipped for encapsulation in their Atomic Layer Deposition (ALD) system. The samples consisted of (1) 10g of ZnSeS:Cu,Ag (Yellow-orange), (2) 10g $CaSrGa_2(Se,S)_4$:Eu (Yellow), (3) 10g SrSeS:Eu (Red), and (4) 10g ZnSe:Cu,Ag (Deep Red)

Unfortunately, due to other commitments and the complexity of the materials, the vendor was unable, in the available time, to modify a system to our specifications. (However, they did make a considerable effort to coat small quantities of a number of samples using a slight modification of their system). As a consequence we reviewed other chemical vapor deposition (ALD/CVD/MOCVD) systems and manufacturers for powder coating and the option to build an in-house facility. After determining that it would be very difficult to obtain a large batch (>1Kg) fluidized bed system in a reasonable time frame and following consultation with the DOE Program Manager, permission was granted to develop and extend the capabilities of an in-house system with Georgia Tech and to seek other approaches. This involved a 3-month no-cost program extension in order to use the research prototype ALD system at Georgia Tech to encapsulate ZnSeS crystals using Al_2O_3 or other oxides and to seek partners skilled in powder coating. Currently, we have the capability to coat 200 gm charges and have demonstrated the deposition of alumina and titania on ZnSSe materials. The results on samples that were encapsulated both by the vendor and at Georgia Tech are reported below.

Our request to the prime vendor was for all samples be encapsulated with a 40-50 nm thick Al_2O_3 layer and then returned to PhosphorTech for comparison with the un-encapsulated materials. Accelerated aging experiments test were then made by immersing the powders in a 1:50 $AgNO_3$: H_2O solution while their emission intensity under blue light excitation was monitored by a fiber optic probe connected to a spectrometer. This is a practical and quick method for comparing the effectiveness of encapsulation on sulfide-based phosphors since silver reacts quickly with sulfur to produce silver sulfide (Ag_2S), which has a grey-black color that blocks the light emission from the phosphor particles. (Note: This reaction is similar to the one that takes place on the surface of the LED dies when the sulfide-based phosphors come in contact with the Ag metal used in the electrical contacts). In these aging experiments, the coloration of an uncoated phosphor turns black very quickly after contact with the $AgNO_3$ solution while the coated phosphor takes longer to degrade since the coating provides a protective layer that prevents the sulfur compounds from diffusing and reacting with silver. Since the rates of diffusion and reaction also depend on the stability of the specific compounds, different un-encapsulated phosphors will degrade at different rates. Therefore, we caution that even though the $AgNO_3$ aging experiment is very effective, it is only useful for comparing similar sulfoselenide phosphor compounds subjected to different encapsulations or surface treatments.

Due to the small size of our powders, the prime vendor used a modified holder – open glass vials capped with a 0.2μm Ag mesh, affixed with high temperature kapton tape and agitated the sample holder during the deposition. The run was made in the expo mode, whereas ideally, a flow through type of setup, where the precursors have access to both above and below the powder is desirable. The samples were coated with approximately 40nm of ALD Al_2O_3 for depositions at 250C using alternating pulses of trimethylaluminum and water where each reactant was exposed to the substrate under static vacuum (~0.1 torr) for 25 seconds and then purged for 30 seconds before the next precursor was introduced. The film thickness was measured via ellipsometry on a bare Si wafer, placed in the reactor during the depositions and

then later observed directly by SEM. Although a 40-50 nm Al_2O_3 coating was targeted, based on previous ALD encapsulations performed at Georgia Tech, some of these samples appear to have a coating as thick as 300 nm, as evident from the SEM data. Accelerated aging tests on coated and uncoated samples showed significant stability improvement for Al_2O_3-coated ZnSeS phosphor, as a result of the ALD process, as shown in Figure 53.

The PL from uncoated ZnSeS drops by ~40% during the first 200 seconds of exposure to $AgNO_3$, while the change in the Al_2O_3-coated ZnSeS phosphor is less than 5%. Also, this decrease is most likely caused by non-conformal coating and/or cracking in the Al_2O_3 layer, leading to exposed areas on the phosphor particles, as shown in Figure 54. The Eu-doped $(Sr,Ca)Ga_2(Se,S)_4$ phosphor showed less of an improvement when comparing the coated versus uncoated phosphors, which is probably due to the severe agglomeration of the particles, as illustrated in Figure 55. This highlights the importance of a fluidized bed ALD coating process, which prevents agglomeration and provides ~100% conformal coating on individual particles.

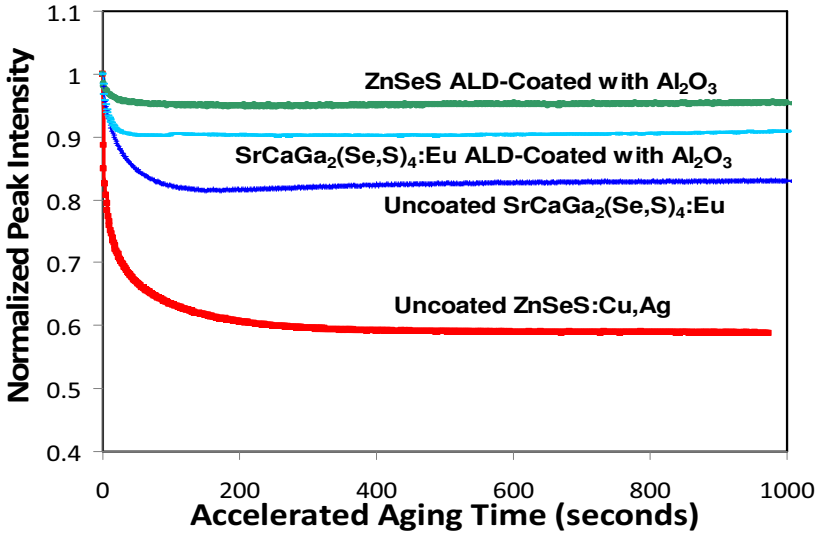

Figure 53. Effect of Al_2O_3 coating by ALD on the intensity degradation of various sulfoselenides. Note, after 1000 s the aging behavior became independent of time for periods of several days.

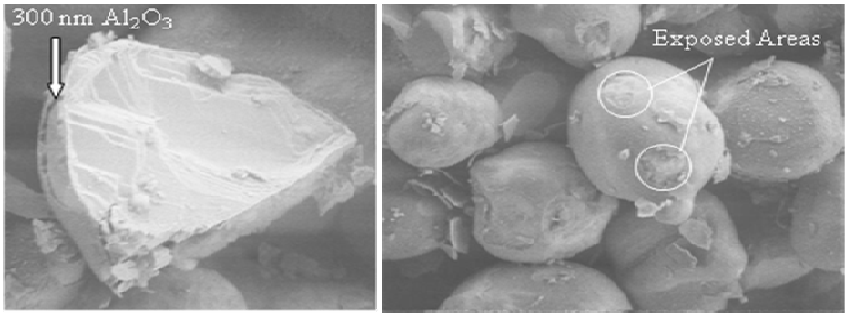

Figure 54. SEM showing Al_2O_3-coated (~300 nm) ZnSeS phosphor using a commercial ALD system. Exposed areas and cracks in coating are highlighted.

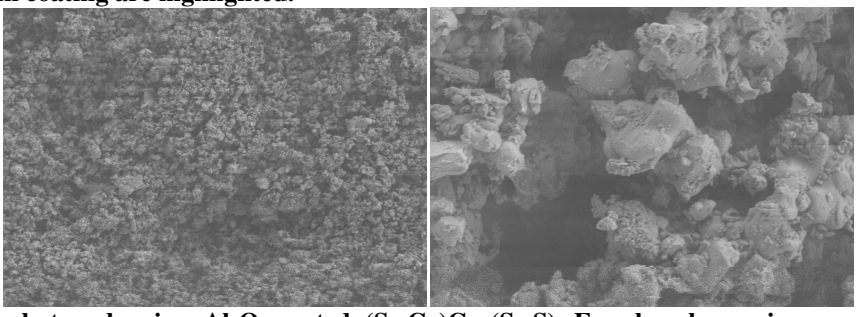

Figure 55. SEM photos showing Al_2O_3-coated $(Sr,Ca)Ga_2(Se,S)_4$:Eu phosphor using a commercial ALD system. Severe particle agglomeration is evident in this system.

Following the vendor study, several ZnSeS samples were encapsulated at Georgia Tech by ALD using a 40nm Al_2O_3 layer. A few grams of each sample were placed inside open glass containers and into the ALD chamber operating at 70 mtorr. The samples were heated to 100°C, then the process was initiated using 20 second pulses (at 50 sccm) of TMA (Trimethyle Aluminium), followed by 20 seconds of H_2O (at 50 sccm) with 100 seconds purging with nitrogen at 25 sccm. Total process time needed to achieve a 40 nm thickness was 20.1 hours. The two samples chosen for the initial ALD experiments were: a Cu-doped $ZnSe_{0.25}S_{0.75}$ phosphor and a Cu/Ag-doped $ZnSe_{0.40}S_{0.60}$. Figure 56 shows the spectral comparison for the two samples before and after encapsulation. The peak intensity for the $ZnSe_{0.25}S_{0.75}$:Cu phosphor increases by ~6%, while the $ZnSe_{0.40}S_{0.60}$:Cu,Ag sample exhibited over a 20% increase following ALD encapsulation under the same conditions. At this time, the cause of this better performance following ALD is not known, but the improvement is most likely due to surface passivation and defect reduction as a result of the Al_2O_3 layer. Also the degree of improvement is most probably dependent on the initial surface defect density prior to ALD encapsulation.

Following these initial surveys, the effort was re-directed. The principal thrusts and achievements have been to demonstrate the effectiveness of particle coating for the ZnSSe and other sulfide based phosphor systems and to develop a FB-ALD manufacturing technology for coating large batches or charges of phosphor or nanophosphor materials. Also we studied the conformal coating of screened phosphor particles and surveyed some novel coating systems. Throughout, a continuing emphasis was to investigate the issues concerning the design and development of a Fluidized Bed–Atomic Layer Deposition (FB-ALD) system and thus, this work will be described first.

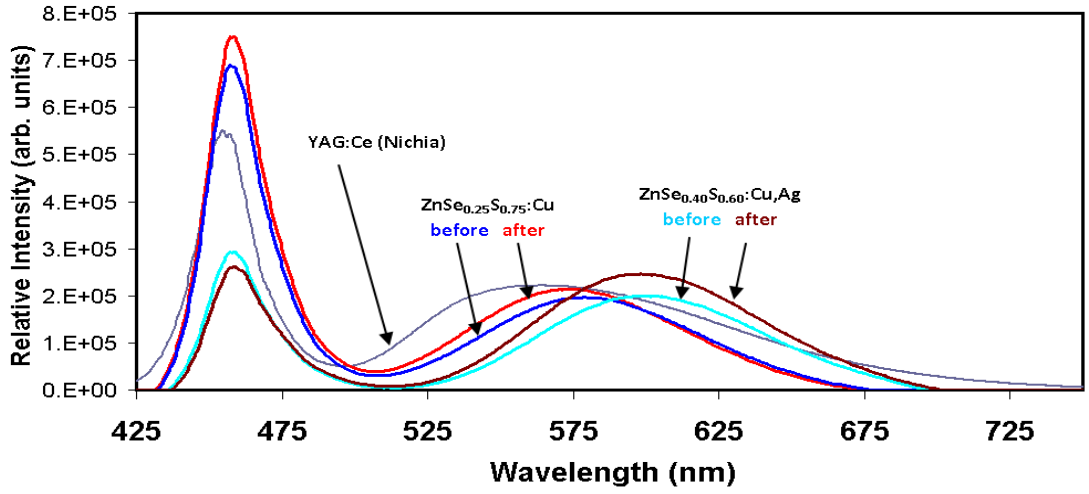

Figure 56. Comparison of Cu- and/or Ag-doped ZnSeS before and after ALD encapsulation by Al_2O_3.

Fluidized Bed Development

As a first step in this process, we re-evaluated and developed a comprehensive program to aid in the design and prediction of the conditions for ALD coating of a variety of structures: from planar substrates to particles. This is necessary because when working with phosphor particles of different diameter, there is a need to account for the very large change in surface area and to understand their interaction with the gas stream. The system was designed for a nominal charge of 400 gm and because the surface area increases as r^2, the amount of precursor needed to coat phosphor charges with particle diameter of 10 µm to 50 µm will increase by a factor of 25.

This change in "loading" will significantly impact precursor pulse times and pressures as well as the purge requirements. The program can model up to three precursors (for example, TMA, $TiCl_4$ and H_2O – for multilayer coatings), and for each precursor the pulse time, the nitrogen purge time following each precursor pulse, and the pressures for each. Up to now, these setting were obtained from many experiments, and in fact were used to calibrate the model to obtain a reliable baseline.

To operate the program, the user enters the different characteristics for each sample (precursor 1, precursor 2, identity of the sample, density of the sample, particle diameter, mass per sample, thickness of coating expected) and the program automatically calculates the necessary pulse and purge times, length of cycle, and the expected total time. This was achieved by first computing the precursor conditions needed to coat one particle and then extending it to the entire sample charge. The whole procedure can then be repeated for a range of precursor flow conditions. By this means the required precursor volume is calculated and then, from the pressure and velocity of the gases, the exposure time for the precursors. Many parameters strongly affect the pulse and purge time results, for instance, the flow rate of the precursor and nitrogen gas, the film growth rate, the thickness of the film and the length of the tube in contact with the gases. Also, other parameters, such as; density of sample, particle diameter, mass per sample; affect the total process time and therefore, both thermodynamic and fluid mechanic reactions, although very difficult to anticipate, must be considered. Consequently, we programmed in a large security factor and assumed that only 10% of the precursor gases were adsorbed onto the particles. Indeed, it is necessary to ensure that there are enough precursors during each cycle in order to completely encapsulate each particle. Also, this program allows us to adapt the computation to samples having different geometries; from planar surfaces to free particles, and particles screened onto a flat surface. To accomplish this, we considered both the total surface area of the sample and the volume of the precursor(s) needed for the coating to tune the ALD system for optimum coating results with the most efficient use of the precursors.

The main practical issues in the development of a FB-ALD system is to fully incorporate the principle of the fluidizing process such that the motion imparted to the particles ensures that they are continually exposed to the precursor gasses and therefore become completely encapsulated by the coating layer. An additional consideration is to establish coating conditions that prevent particle agglomeration, either through direct physical contact and/or agglomeration mediated by the presence of the coating.

Approaches to implementing the fluidized bed ALD process have been to hold the charge in a vertical column so that the precursors and purge gasses flow through the charge, in which case, ideally the buoyancy effect can be used to separate the particles due to the vertical gas flow – while they are also being coated. (Note: that in the ALD technique the precursors are swept through the system by a background flow of nitrogen which is increased during the purge cycle so that the total gas flow remains constant). However, for large phosphor charges this approach needs to be augmented by a highly controlled vibration system to enhance fluidization, and/or by a lifting rotating helix system enclosed within the reactor column. This is necessary to counteract the fact that the lower particles can become highly compacted for large phosphor charges. Possible horizontal geometries are to hold the phosphor charge in a porous rotating tube and/or horizontal mixer (like the motion of a concrete mixer). However, for both geometries, one needs to model not only the effect of gas flow on deposition but simultaneously its interaction with the particles. Consequently, both thermodynamic and fluid dynamic properties must be considered. In both the vertical and horizontal geometry, the mechanical force available to elevate the particles must be accurately computed, so that the gas flow is not so strong that particles are blown out of the container.

Conformal Particle Coating

For these investigations, we modeled the parameters of a fluidized bed ALD system for particle coating with the purpose of designing and constructing a more flexible system. These studies have looked in depth into the gas flow-particle interaction for an ALD system, configured with its sample chamber mounted so that the carrier gas, growth precursors and flush (purge gases), flow vertically through the system. This set up is shown in Figure 57 which depicts the

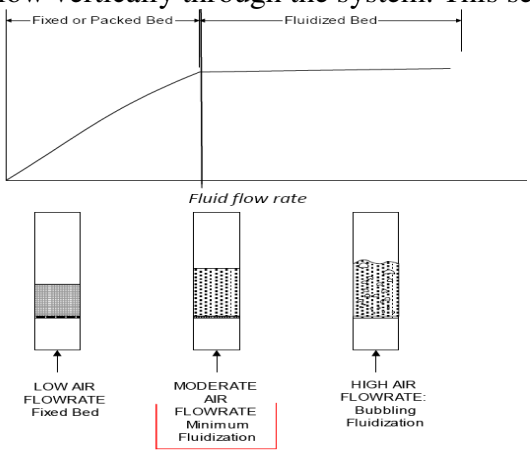

Figure 57. Schematic of the different states of "fluidization" for a fluidized bed system.

different situations that can occur when a fluid (liquid or gas) is passed through a packed bed of particles. As shown, depending of the fluid flow rate, there are three main states. If the flow rate is smaller than the "minimum fluidization flow rate" the bed remains static or fixed: this state is called *fixed bed.* As the flow rate is increased, there occurs a "minimum fluidization velocity", where the bed expands and the particle-fluid mixture now behaves as though it is a fluid. In this state, when the frictional force acting on the particles or the pressure drop off, the gases flowing through the bed equals or exceeds the weight of the bed and the powder particles become suspended. In this regime, for a fluidized bed without bubbles: *smooth fluidization* occurs. For further increases in flow rate, the bed expands slightly, but if the flow rate becomes larger than a maximum fluidization flow rate, bubbles start to form inside the bed and particles may be carried out with the fluid when it exits the system, this state is called *bubbling fluidization.* Obviously it is necessary to design for the ***smooth fluidization regime*** corresponding to an expanded bed without bubbles such as the middle drawing in Figure 57.

There are many parameters controlling the impacts on the fluidization coating, which have been extensively modeled and are summarized in Table 7. These calculations are explained at length in the Appendix accompanying this report. Of most importance for designing the system are the parameters: minimum fluidization velocity and settling velocity and the void fraction. As mentioned previously, the ideal regime of fluidization of the particles is "the smooth fluidization" regime and this in principle allows perfect mixing and coating. Unfortunately, to obtain this regime, very exact conditions (such as tight control over, ε and V_f, complete vacuum, homogenous temperature and pressure) are required, which are very difficult to realize particularly for very small particles. Additionally, for particles ranging between micrometers and nanometers in size, fluidization is complicated due to the cohesive forces between the particles and an additional mechanical system is needed to minimize agglomeration. Therefore, in addition to the agitation produced by the gas flow, two additional mechanical agitation schemes are used: vertical agitation and rotation, to ensure full agitation of the particles during coating so as to reach the conditions of smooth fluidization.

Table 7. Parameters Controlling Operational Characteristics of a FB-ALD System.

Re: Reynolds number*
f_p: Friction factor between particles (coefficient of friction between particles)
Δp: Pressure drop (*Pa*)
L: Length of the bed (*m*)
D_p: Equivalent spherical diameter of the particles (*m*)
ρ_f: Density of the fluid (kg/m^3)
ρ_p: Density of particles (kg/m^3)
ε: Void fraction of the bed
μ: Dynamic viscosity of the fluid (*Pa.s*)
A: Cross-sectional area of the bed (m^2)
Q: Flow rate of the fluid (m^3/s)
V_s: Superficial velocity (*m/s*) $V_s = Q/A$
G: Acceleration due to gravity (m/s^2) $g = 9.81\ m/s^2$
M: Mass of the charge (kg)
V_{mf}: Minimal fluidization velocity (*m/s*)
$V_{settling}$: Maximum fluidization velocity (*m/s*)
V_f: Fluidization velocity (*m/s*)

$$D_p = 6.\frac{Volume\ of\ the\ particle}{Surface\ area\ of\ the\ particle}$$

$$\varepsilon = \frac{space\ unfilled\ by\ packing}{Total\ volume\ in\ column}$$

* Reynolds number can be defined for a number of different situations where a fluid is in relative motion to a surface (the definition of the Reynolds number is not to be confused with the Reynolds Equation or lubrication equation). These definitions generally include the fluid properties of density and viscosity, plus a velocity and a characteristic length or characteristic dimension.

For flow in a pipe or tube, the Reynolds number is generally defined as:

$$\mathrm{Re} = \frac{\rho V D_H}{\mu}$$

ρ: Density of the fluid through the pipe (kg/m^3)ε
V: Mean fluid velocity (*m/s*)
D_H: Hydraulic diameter of the pipe (*m*)
μ: Dynamic viscosity of the fluid (*Pa.s*)

According to many studies, the experimental conditions necessary to obtain the best coating conditions depend on the flow rate, particle diameter and density, and the phosphor charge that defines the diameter and column length of the experiment. Using current theory, we have calculated the flow conditions needed for coating a phosphor charge of 300 g as a function of particle diameter. This data is shown in Figure 58 and indicates that the smooth fluidization regime should be obtainable with slight modifications to our system. We therefore designed for these conditions and developed a vibrational platform and rotational (stirring) system to enhance particle separation during coating and to increase the charge flexibility of the system.

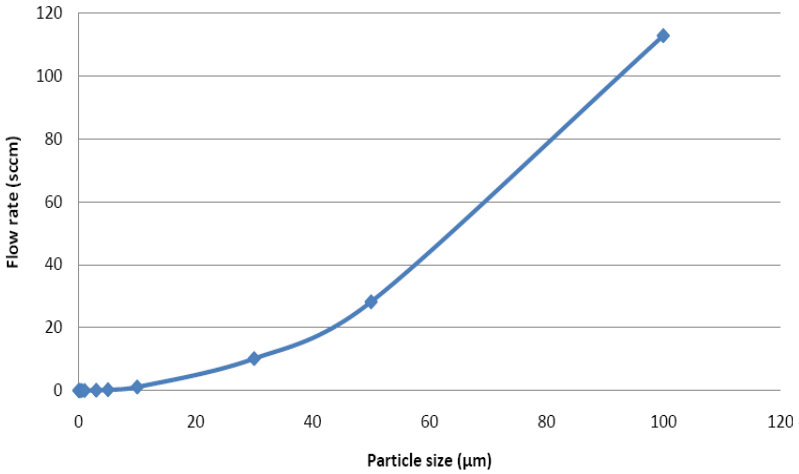

Figure 58. Calculation of minimum fluidization velocity as function of particle size: phosphor charge 300 g.

These preliminary studies were necessary to clearly indentify the key issues that must be addressed when designing an atomic layer deposition fluidized bed (ALD-FB) system for coating phosphor charges between 50-200 gm with particle sizes between 5-20 microns. To cover this range of particle sizes and phosphor charges, a fluidized bed reactor combining the three fluidization technologies was built. Thus, fluidization was achieved by:

- controlling and adjusting the gas pressure flowing through the system
- using an external vibration table to agitate the charge
- rotating a vane inside the bed/or magnetic agitation

To monitor system conditions, manometer gauges were placed at each end of the fluidization bed to detect the onset of fluidization of the charge, that is, when the particles are moving independently of each other (floating) and so can be coated without agglomerating. By this means a wide range of conditions can be addressed. The precursor gases were controlled by our conventional system and then introduced into the FB chamber. This was attached to a customized table supported by 4 heavy springs with the vibration mechanism mounted on the other side. By this means, the entire bed is vibrated but mechanical stress on any parts of the FB reactor is avoided

The objective of such a system is to freely coat particles so that throughout the coating process they are completely free, undamaged, and homogeneously encapsulated. In an ALD-FBR and for large charges (quantities) of particles (between 10g to 300g), a combination of various inter-particle forces such as London-Van der Waals and electrostatic interactions may occur. These forces promote the formation of particle aggregation, affecting the fluidization process and become very important for the smaller nano-sized particles, thus we incorporated all three ways to elevate particles: by gas flow, vibration and stirring. Our aim was to design a comprehensive system and to build a system for an average charge size of 50-100 g – but to have a more comprehensive system designed and priced, which can be quickly brought on-line if needed. The important parameters are therefore:

Gas flow: In the fluidization process a gas flows through a packed bed (charge of solid particles). When a fluid (liquid or gas) passes through a packed bed at a minimum necessary velocity (minimum fluidization velocity), the packed bed begins to expand and the particle-fluid mixture behaves as though it is a fluid. Therefore, the theoretical analysis was conducted to determinate the **minimum fluidization velocity (V_{mf})**, **the maximum fluidization velocity** called **settling velocity ($V_{settling}$),** and the necessary conditions to obtain a homogenous and smooth fluidized mixture were graphed as shown in Figure 59.

External vibration: In this approach, an electric imbalanced vibrator is attached to the structure of the FB and the entire structure of the machine is mounted on a soft and flexible plate in order to maintain the motion. This mechanism is made of four springs specially designed in accordance with the forces applied on the system. Theoretical design calculations have been made to select the right spring strength and the best matched vibrator as shown in the vibration amplitude vs. frequency plot in Figure 60.

Stirring: As a second inner mechanical solution, a high-vacuum manipulator (stirrer or vane) helps the particles to be in motion during the entire ALD process. This manipulator is connected to a shaft that extends down to the bottom of the particles bed. A well-designed propeller is welded at the end of the shaft and an electrical motor (with the necessary torque) is attached to the top of the shaft to provide homogenous and smooth stirring to the bed of particles.

ALD Implementation: The final consideration is to ensure that the agitation of the particles is such that they are moved several times within the precursors pulse times used to complete the chemical reaction, typically the precursor pulse times are within the range of 4 to 8 seconds. The proper design of these three techniques in consideration of the reaction parameters of the ALD-FBR will allow us to first, avoid any aggregation of particles, and second to achieve smooth fluidization and particle coating. The system design details are quite complicated and are described in detail in the appendix. However, an example of these considerations is given below.

The void fraction (Figure 59) is a parameter that is calculated and which depends on the size of the bed and the size of the column. Theoretical analyses show that this parameter has to be within the range from 0.4 to 0.45 to obtain a smooth fluidization. By controlling this parameter, we can determine the quantity of particles that can be coated under given conditions and the minimum flow rate needed for the fluidization. Alternately, depending on the size of the phosphor we can design the FB column with a new void fraction.

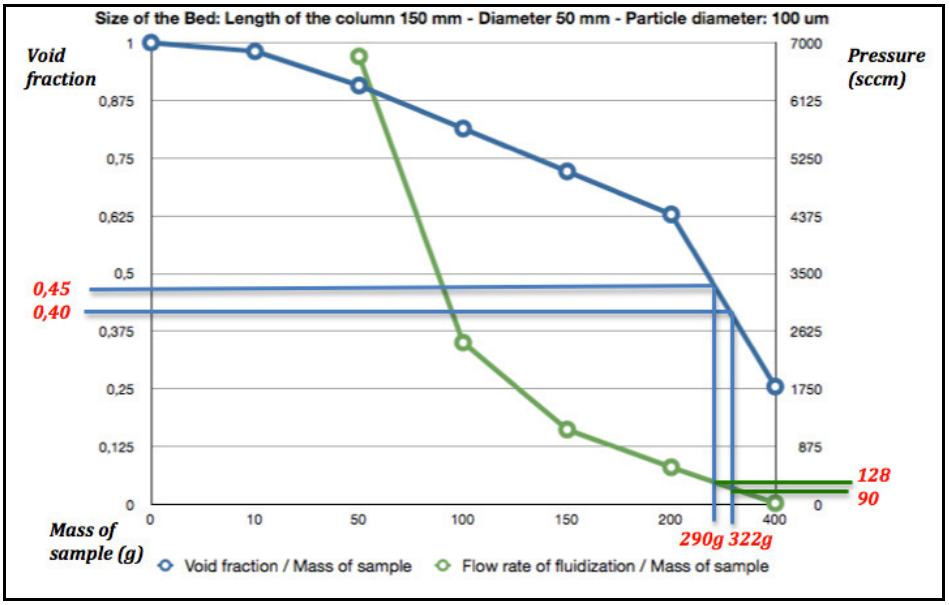

Figure 59. Study case of a parameter design of the bed (void fraction) versus the mass of the sample to obtain the flow rate of fluidization.

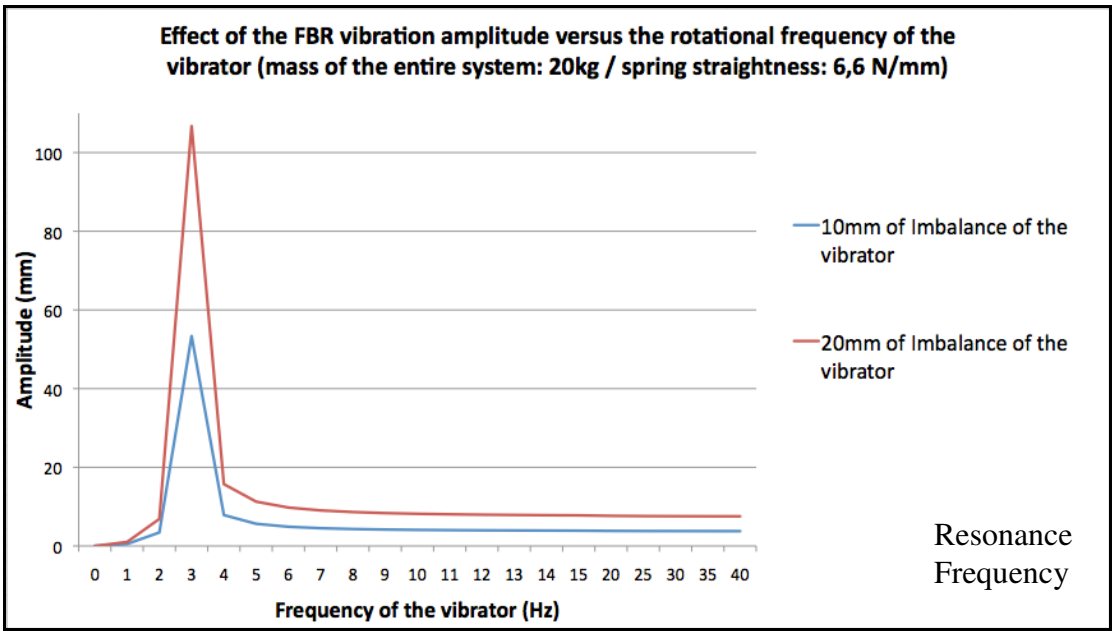

Figure 60. Influence of the vibrator imbalance and rotational frequency on the vertical amplitude motion of the Fluidized Bed Reactor.

Figure 60 shows the vertical amplitudes that can be obtained for a given system (weight of system, unbalance of motor) as a function of the vibrator frequency. The theoretical study leads to the understanding of the vibration behavior of the FB. Essentially Figure 60 gives the amplitude that the free particles in the column will experience for given conditions. This result takes into consideration the spring strength, the initial forces on the system, and the characteristics of the vibrator. One important part of this chart is the fact that for a certain frequency of the vibrator (f =3 Hz ⇔ 180 RPM) we achieve the resonance frequency of the system. This specific frequency determines the maximum vertical displacement of the FBR and directly the bed movement. If the frequency of the vibrator is increased above the resonance frequency (for instance f = 15 Hz ⇔ 900 RPM) the system is driven at a stable state in a lower amplitude motion. The second result demonstrates that the higher the vibration imbalance, the higher the FB vertical motion amplitude. According to the vertical amplitude vibration we would like to setup, we can clearly define and choose the right vibrator to use for our process. The details of this system are reported in an "ALD-FB Design and Fabrication Manual" that is attached as an Appendix to this Final Report. In addition, based on the above study, a high vacuum Atomic Layer Deposition -Fluidized Bed was implemented to coat smaller phosphor charges.

Small Charge Fluidized Bed ALD System

To continue to perform experiments in the GT system, a small charge fluidized bed atomic layer deposition system was designed and constructed. This system was designed with all the capabilities as the larger system, gas mixing, agitation and stirring. The latter included a special vacuum rotary motion feed-through for the stirrer. After the prototype version of the small charge ALD-FB was assembled, it was attached to the existing Al_2O_3/TiO_2 atomic layer deposition system and tested to ensure smooth operation. These included a leak test to ensure that the inner pressure in the entire ALD-FB system was unaffected by the addition of the fluidized bed (equal or less than 65 mtorr). The fluidized bed system was calibrated by coating thin Si slabs under various conditions and measuring the thickness by optical interference

measurements. These tests included different coating materials and thickness. Once the tests were concluded, the ALD system was used to coat sulfide-based particle phosphors to confirm that the ALD can be used to coat both flat and particles samples with high precision.

Figure 61 shows the modified small charge fluidized bed setup that was incorporated into the existing ALD system. The new revision of the design includes a NW25 rotary feedthrough that is mounted on top of a four-way cross (instead of the NW25 Tee) and on the right side a pressure transducer is mounted to measure the flow conditions. The precursors are introduced through the base of the four-way cross and the vacuum is pulled through the left hand port. The rotary motor drives a vane that is positioned just below the sample chamber. Inside the chamber, a fine mesh was placed just below the vane to hold the phosphor charge and above the vane two additional filters were placed to prevent particles from being pulled through the system. This was found to be necessary following several test runs preformed without the use of any precursors. To ensure a uniform temperature during depositions at 100°C, heat tapes were wound around the Fluidized Bed and then wrapped with Al foil. A 90VDC generator powers the NW25 Rotary motion feedthrough (black device on the top of the FB). Figure 62 shows the speed of rotation as a function of the voltage rotary motion control of this system. The rotated arm is able to reach a 14 revs/min speed under 90V. Thus by changing the voltage of the generator, we can easily tune the rotational speed.

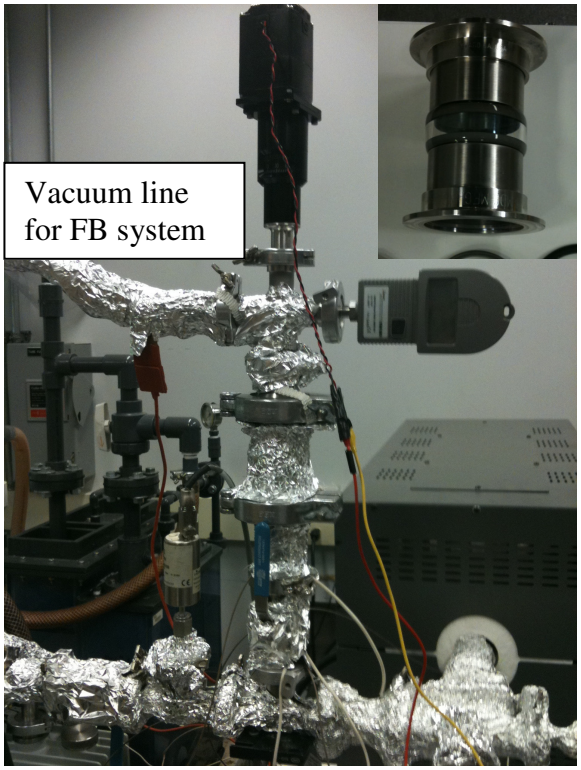

Figure 61. (a) Overview of the FB set up on the existing ALD system, (Insert) Close up of the FB chamber.

Thickness coating tests were made on silica samples inserted inside the Fluidized Bed. For these runs the operational conditions of the ALD system were a 0.14nm/cycle growth rate for Al_2O_3 coating with a purge and pulse time equal to 4 seconds each and a 0.075nm/cycle growth rate for TiO_2 with the same pulse and purge times. A series of 30 and 60nm thick films of TiO_2 and Al_2O_3 were deposited on 4g of ZnTe-O, where larger particles were sieved by a micron filter. Post coating optical measurements confirmed that the right coating thickness was obtained.

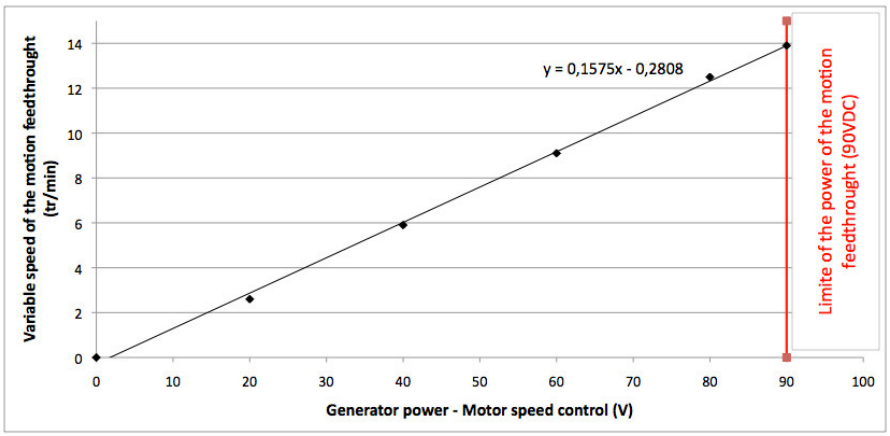

Figure 62. Rotation speed as a function of generator voltage for the NW25 rotary feed through.

The FB system was used to coat several sulfur based phosphor systems and the properties and performance of the coatings evaluated by SEM and measurements of the degradation that occurs in the photoluminescence, when the particle are immersed in a $AgNO_3$ solution.

Following the successful test of the FB-ALD system, measurements were made to extend the range of the system to smaller particles. For these applications to maintain the phosphor charge inside the Fluidized Bed reactor, it was necessary to place meshes within the system in order to confine the position of the phosphor charge. Two meshes were used in the system, one on the bottom of the double-ended glass and one on the outlet of the exhaust tee, as shown in Figure 63, to prevent particles from being flushed out of the system. Manual Ball Valve 1 (MBV1) is normally opened while MBV2 is normally closed while the system is under vacuum. The system was tested with two sizes of mesh:

- 100-microns stainless steel mesh
- 35-microns stainless steel mesh

Coating studies were first made using the 100-micro mesh and then with the smaller 35 micron mesh. The results of this study showed that it was difficult to obtain a coating on the particles when the smaller mesh size was used. This result was traced to the pressure conditions in the reactor. Results of the pressure study showed the following:

- Absolute system vacuum: 48.3 mtorr
- Vacuum with 100-microns mesh: 53.9 mtorr
- Vacuum with 35-microns mesh: 573.9 mtorr.

It appeared that for the smaller mesh size the inner pressure was too high to promote chemical reactions on the particle surface. Additionally the presence of nucleated crystals along the inside of the mechanical system suggested that the high pressure promotes a re-reaction of the precursors before the sample chamber. Thus, the fact that the mesh size had a critical effect on particle coating required further investigations to develop a more viable system.

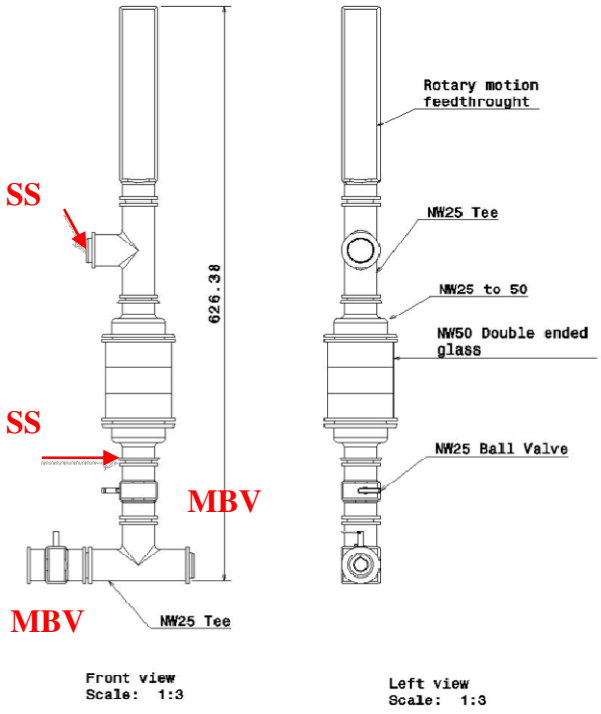

Figure 63. ALD-Fluidized Bed system showing position of the meshes inserted to confine the phosphor charge.

During the course of this study, we also investigated coating phosphor particles using a horizontal Fluidized Bed ALD system, where the phosphor charge was loaded into a stainless steel tube, the ends of which are "sealed," using stainless steel meshes with various porosities, depending on the average diameter of the particles of the charge. Thus, the phosphor can be enclosed within the evacuated chamber while the precursor gases are sequentially flowed through the system to deposit a thin film. In the horizontal chamber, the particles were agitated by the gas flow, mechanical vibration, or by rotation using a vacuum pull through. Conventional ALD protocols were followed and the precursor gases alternatively pulsed through the chamber. Each precursor pulse was followed by a nitrogen purge pulse to clean the chamber from unreacted precursors or small particles.

The pulse and purge times were chosen in accordance with the type of charge, the porosity of the mesh, the inner operating pressure and the volume of the phosphor charge. It is important to highlight that the pulse and purge times are strongly affected by the reaction tube operating pressure. For this experiment, the ZnSSe charge was trapped between two 35 μm meshes. The ALD working pressure (vacuum) was 45 mtorr and the particles were encapsulated with a 100 nm thick alumina film (Al_2O_3) using the following ALD precursor parameters:

- 1s pulse of H_2O / 4s purge of Nitrogen
- 1s pulse of TMA / 6s purge of Nitrogen

Following the deposition of the ALD thin film the spectral properties of the photoluminescence from the phosphor charge was measured using a UV/blue LED excitation source, and measurements were then conducted to analyze the integrity of the conformal thin film by monitoring the PL spectra as the phosphor charge was exposed to water and immersed in a solution of silver nitrate. As described previously, a silver nitrate solution rapidly attacks sulfur based materials. Thus, if the films do not form a complete hermetic seal around each phosphor particle they will be dissolved and no longer contribute to the photoluminescence signal. This is a very effective way of performing accelerated aging tests to assess the effectiveness of the coating procedure. For the spectral measurements a UV LED was used as an excitation source and the total spectral output was analyzed by a spectrometer as shown in Figure 64. Thus the relative magnitudes of the UV LED absorption (403nm) and photoluminescence from ZnSSe (580nm) could be obtained for each sample.

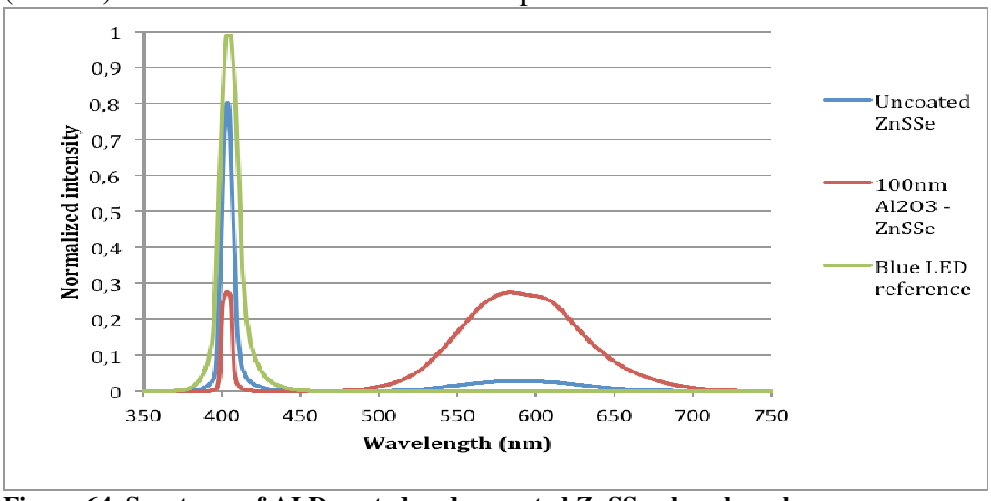

Figure 64. Spectrum of ALD coated and uncoated ZnSSe phosphor charges.

Figure 64 demonstrates that the coated charge absorbs 72% of the UV LED reference while the uncoated phosphor charge only absorbs 19% of this excitation. At the same time, the

ZnSSe emission was 25% higher than the uncoated charge. These two observations are consistent; as it appears that the coating enhances the excitation efficiency. The reason for this is not understood; a possible cause could be a lower reflectance from coated materials due to a blooming effect.

The ALD coating studies were therefore continued with the main goal being to deposit a very thick coating of Al_2O_3. The deposition parameters were TMA and water precursor pulse times of 6 s, each followed by a 20 s nitrogen purge for a total deposition time of ~ 20 h. As shown in Figure 65a, b and c very thick films were obtained. In Figure 65a, a ~270 nm thick film was measured on a flat Si substrate, which is used as a control in the deposition, and a ~ 260 nm thick highly conformal film measured on a ZnSSe phosphor particle approximately 15 μm in diameter.

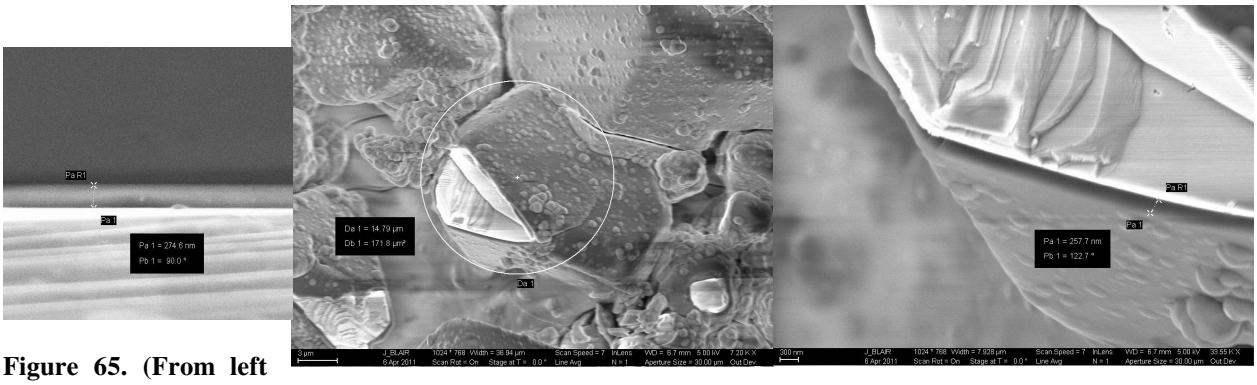

Figure 65. (From left to right): a) SEM of Al_2O_3 layer on Si control sample, 4b) SEM of cracked phosphor particle showing the deposition of a highly conformal coating of Al_2O_3, ~ 260 nm thick, 4c) magnified view of a section of the phosphor showing a very conformal film in intimate contact with the phosphor material.

To acquire the SEM data, some samples were purposely cracked using a spatula. The measured thicknesses were significantly thicker than the target thickness of slightly greater than 200 nm. The reason for this is not understood, but using these deposition parameters resulted in some agglomeration of the phosphor particle charge. A possible explanation could be that there was some conventional chemical vapor growth due to a build up of precursor gases during the length of the deposition run. (In the ALD system designed for manufacturing this problem should not occur). The photoluminescence spectra for the uncoated and coated particles are shown in Figure 66. As has been observed before, the coated samples show stronger absorption of the pump radiation, in this case at 404 nm, and also higher photoluminescence output intensity. Also significant, the particles that became agglomerated during the coating exhibited larger enhanced absorption effects and photoluminescence intensity. The correlation between the stronger absorption and more intense photoluminescence is consistent. However, we are not sure about the origin of the large effect observed in the agglomerate samples. This effect could be attributed to the fact that scattering of both the pump light and the emitted light was reduced, because of the greater homogeneity of the agglomerated particles.

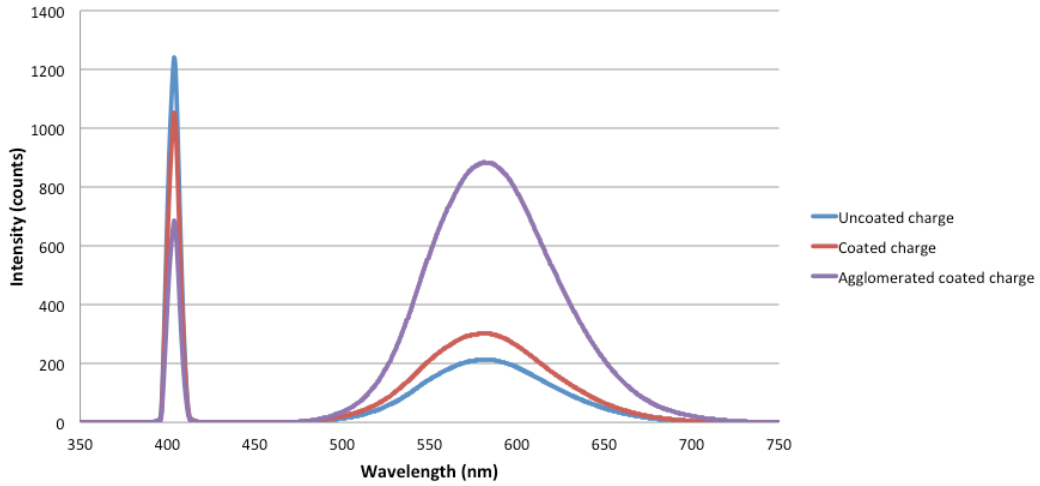

Figure 66. Photoluminescence spectra of uncoated phosphor particles, ALD Al2O3 coated phosphor particles, and agglomerated coated particles.

A wide range of aging studies of the ALD coated ZnSeS samples were conducted for the 260 nm Al_2O_3 coatings and augmented by SEM, photoluminescence measurements and aging studies when immersed in a silver nitrate solution. Figure 70 shows the dependence of the photoluminescence emitted respectively from uncoated and coated phosphors as a function of aging time in a silver nitrate solution. The measurements were made for a 0.07g charge in 2mL of DI water. Ten drops of diluted silver nitride ($AgNO_3$) were injected into each cuvette while recording the data. The red line is the light emitted at ~600 nm from the coated ZnSSe while the blue line represents the uncoated sample. After 2.2 hours the PL intensity from both samples was reduced to 38% of their initial photoluminescence intensity and only the coated samples showed signs of stabilization. Improvements to the optical set were also made to collect the emitted light at 584nm when excited by pulsed UV light (404nm). The photoluminescence measurements indicate an improvement in the quantum yield of approximately 1.3 for the monolayer (15µm thick) and 2.38 times better for the thicker films. These results again show that ALD coating was effective against acid attack and that the photoluminescence was stable after 22 hours of silver nitride attack.

In a further test of the effectiveness of encapsulating a phosphor a very thick layer of Al_2O_3 was deposited that would provide an impenetrable barrier. For this study the set atomic layer deposition parameters were: Targeted film thickness 250 nm Al_2O_3, Growth rate: 0.14nm/cycle, TMA flow rate 25 sccm, H_2O flow rate 25 sccm: TMA and H_2O precursor pulse times: 6s, Nitrogen purge time: 20s, deposition time 20 - 25 hours. Before making these runs, the system was rigorously cleaned and the pump oil, precursors and nitrogen flush refilled. Under these conditions, the inner system pressure was 49 mtorr. Accelerated aging tests were again performed to evaluate the effectiveness of the deposited film using the parameters:

- UV excitation wavelength: 404 nm
- ZnSSe peak emission wavelength: 584 nm
- Etching agent: Silver Nitride
- Duration of Aging Test: 22 hours

The aging tests were performed on phosphor particles deposited to form a monolayer of particles on a substrate and as free standing particles. For each configuration both uncoated and coated ZnSeS charges were investigated.

As reported before in all of the aging tests, a quick decrease in PL intensity was observed from the coated samples after which the PL intensity leveled off and remained constant. However, as expected, the PL intensity for the uncoated showed the same initial behavior, but continued to decrease with time. We believe that the reason for the initial decrease in PL intensity for the coated samples is due to the fact that not all of the phosphor particles were completely hermetically sealed by the ALD deposition and therefore, are etched away and destroyed, with a corresponding loss in PL intensity. Thus, a second test was made on the same sample used for the first aging test in order to check the stabilization of the remaining coated particles. The result for this experiment is shown in Figure 67 and shows no degradation throughout the entire aging time of 22 hours in a $AgNO_3$ solution. To complete this investigation, the PL spectra, before and after etching, was recorded and these results are shown in Figure 68. The two spectra are in complete registration, confirming the effectiveness of ALD conformal coating techniques to protect sulfur and selenium based phosphors in an extreme aging experiment.

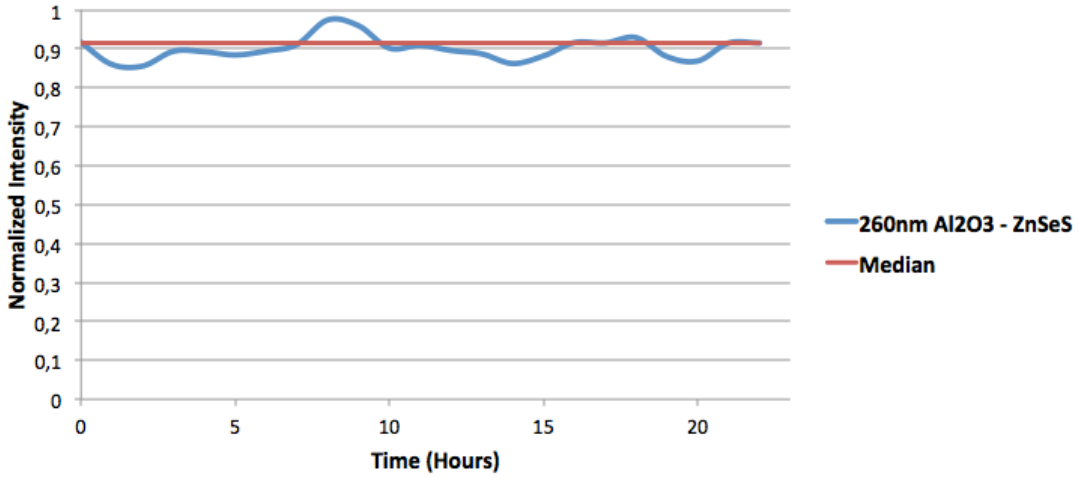

Figure 67. Dependence of PL intensity on etching time for the second etching test on ZnSSe phosphors conformally coated with a 260 nm thick film of Al2O3. This test was conducted on the coated ZnSSe charge that remained after the first aging test.

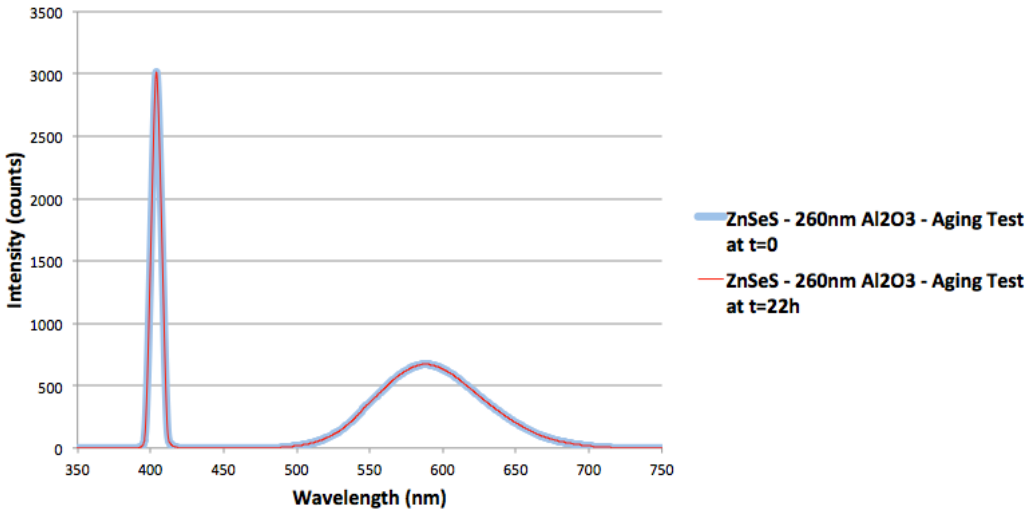

Figure 68. Spectral dependence of PL from a blue LED pumped ZnSSe phosphor measured before and following a 22 hour aging test immersed in AgNO3.

In conclusion, analysis of all the ALD/Fluidized Bed data, showed that despite the set-back in not being able to purchase a suitable system for this work, as had been originally planned, this concept has been well proven and shown to lead to enhancements in both maintenance and phosphor performance. Scale up routes have been demonstrated and can be implemented when appropriate.

Encapsulation of Screened Phosphor Samples

In addition to fully understanding the issues involved in conformally coating a large number of individual particle phosphors, we have also investigated another approach: that is to first screen a layer of particles onto a substrate and then to conformally coat the entire layer by atomic layer deposition. In this study, different weights of a ZnSSe:Cu powder phosphor which emits in the yellow at 567nm, when excited with blue light at 400nm, were settled onto a glass substrate and then, an Al_2O_3 coating was conformally deposited by ALD at 100°C. The deposited weights ranged from 0.6mg/cm^2 to 3.2mg/cm^2 and the thicknesses of the alumina coatings ranged from 20 to 200 nm.

Briefly, as described before, the growth of the thin films was carried out in a horizontal flow-type custom made ALD reactor and both Al_2O_3 and TiO_2 depositions investigated. TMA, $TiCl_4$ and H_2O precursors were used as the aluminum, titanium and oxygen sources, respectively, and N_2 was used as the purge gas. The pulse period was 8-10 seconds and the purge period varied between 10 and 40 seconds. The default deposition temperature was 100 °C. In order to determine the effectiveness of this approach in a reasonable time, accelerated aging tests were performed. To accelerate the aging process, the phosphor sample was placed into a $AgNO_3$ solution and the photoluminescence of the screen monitored as a function of time. Ag+ strongly reacts with sulfur and thus, if it comes into contact with ZnSSe, it will very quickly destroy the matrix of the phosphor and the luminance intensity will decrease quickly. In these aging tests the concentration of the $AgNO_3$ solution was 6mg/mL and the screen was excited by a 400nm light and the wavelength of the emitted light was monitored at 567nm. The intensity of the luminescence was then recorded as a function of time to a maximum duration of 5000 s (~1.4 hr). To assess the effectiveness of the accelerated aging test and to estimate its equivalent to normal usage, an aging time factor was determined. For this study, the aging of an uncoated sample was measured in air at a relative humidity of 20% at a temperature of 24°C, and then compared to the results obtained from a similar sample immersed in $AgNO_3$. From this comparison, an acceleration factor of ~ 1000 was obtained. Thus, for the time periods measured (5000 s) the effective aging time was estimated to be ~ 1400 hours.

As a calibration for these studies, the ZnSSe phosphor was screened at different weights and aging studies performed on uncoated sample screens. Figure 69 shows the aging results obtained for uncoated phosphor screens with weights ranging from 0.6 mg/cm^2 to 3.2mg/cm^2; this is equivalent to phosphor thicknesses ranging from partial coverage, ~ 1 particle layer to ~ 4 particle layers. The results show a decrease in intensity by more than 50% for the measured time and that the thicker screens aged slightly faster than the thinner screens. This is because Ag^+ reacts with both the top and lower particle layers in the thicker screens. With aging the surface color of the particles changes and becomes dark gray (due to the presence of silver sulfide) which blocks both the excitation and luminescence through adjacent layers. As a result, both the luminance efficiency and also the excitation efficiency of the thicker samples are reduced.

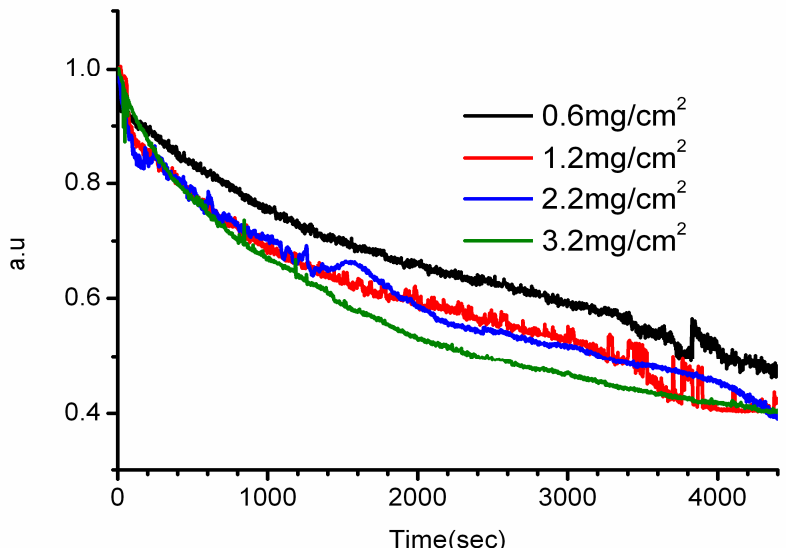

Figure 69. Aging of uncoated phosphor screened with different weights (thickness). Plot of luminescent intensity observed from screen as a function of time during accelerated aging test with AgNO3.

Al_2O_3 Film Depositions

The Al_2O_3 films were deposited using TMA and H_2O precursors. The aging results for coated and uncoated phosphor samples for a 2.2mg/cm^2 ZnSSe screen and Al_2O_3 coating thickness of 80 nm are showed in Figure 70. As observed from the figure, the luminance of the uncoated sample decreases very quickly with time and after one hour was ~ 30% of the original signal, while the luminance of the coated sample was very stable and only dropped by a few percent by the end of the test run. Thus, the stability of the Al_2O_3 coated phosphor sample was dramatically increased by using the alumina passivation layer and has an estimated half-life in excess of 5000 hrs. These encouraging results led us to pursue a more detailed study.

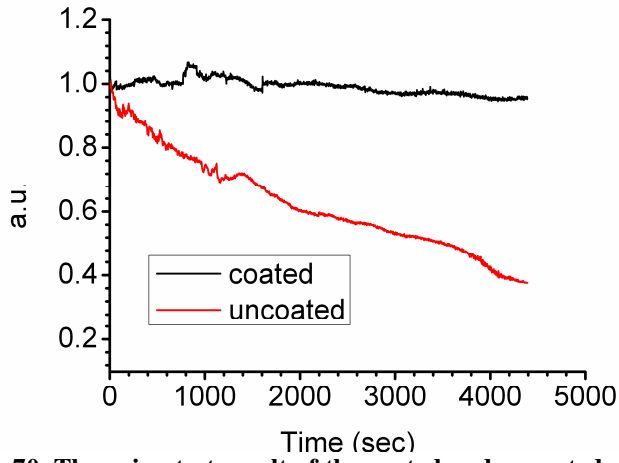

Figure 70. The aging test result of the coated and uncoated phosphor. The weight of the phosphor screen was 2.2mg/cm2 and the thickness of the Al2O3 film 80nm.

The aging results for different screened weights (thicknesses) of the ZnsSe phosphor for an 80 nm conformal coating of Al_2O_3 is illustrated in Figure 71. As shown, the luminance of thin screen samples decreased quickly; it is assumed that this is because the sample is only about 1-particle layer thick and so the surface to bulk ratio is high. Thus, the quenching effect due to the corroding $AgNO_3$ solution is very pronounced. At first, one would expect that by increasing the thickness of the sample, the aging process will become slower. However, because the lower layer

of the thicker screens will also be corroded and change color, just as for the uncoated samples, the excitation efficiency will be reduced, and consequently the entire luminance will decrease at a faster rate. This indicates that there is an optimized value for the thickness of the phosphor screen.

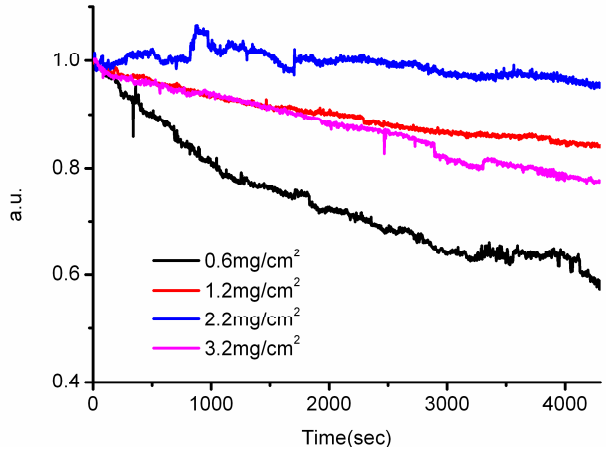

Figure 71. Aging results for different weights (thicknesses) of a ZnSeS phosphor screen after conformally coated with a 80nm thick Al2O3 film.

We also investigated increasing the thickness of the Al_2O_3 coating layer and found that the stability was enhanced dramatically. Figure 72 shows the effect of increasing the Al_2O_3 film thickness from 20nm to 200nm. The luminance for the uncoated and 20 nm coated screens are somewhat similar, decreasing to 50% and 60%, respectively, of the original intensity after a 5000s etch in $AgNO_3$ with, as expected, the coated screen showing slightly better performance. For the 200 nm coated sample, the average change in luminescence was ~12% and at the end of the etching period the luminescence was close to 90% of the original luminescence intensity and was very stable.

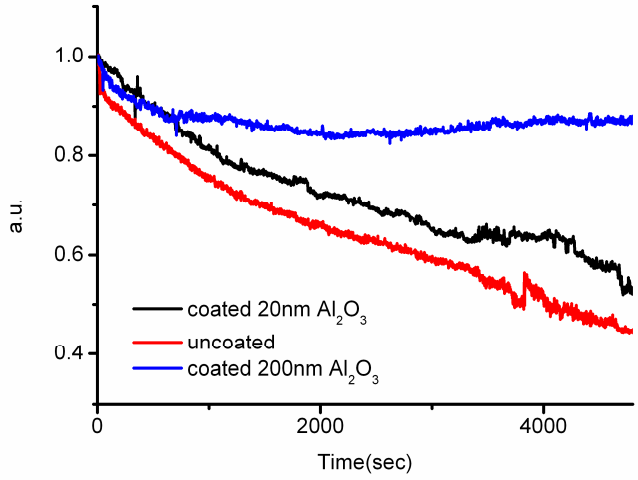

Figure 72. Aging results for different Al2O3 film thicknesses coated on screened phosphor sample. The phosphor screen thickness was 0.6mg/cm2, or ~ 1 monolayer.

In the final study, we increased the growth temperature for the ALD of alumina to 300 °C, to investigate if a denser and therefore more protective Al_2O_3 layer could be formed, with a subsequent increase in the stability of the phosphor screen. As shown in Figure 73, the properties of the film produced at high temperature was slightly better than the lower (100° C) temperature deposition and both were far better than an uncoated phosphor screen, included for comparison.

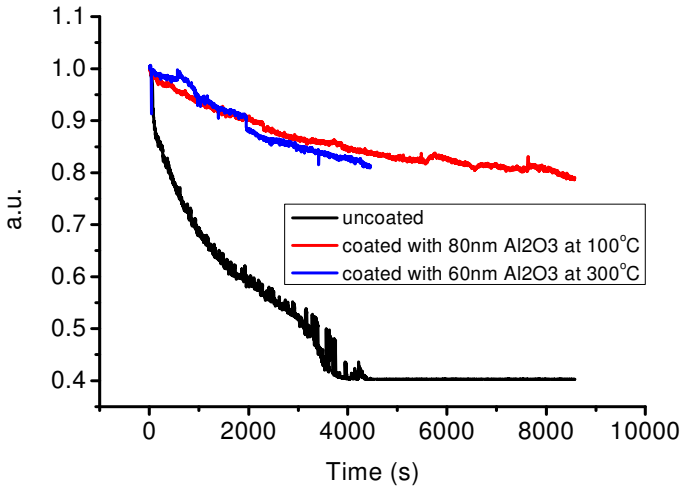

Figure 73. Aging results for different deposition temperatures of Al2O3.

TiO_2 Film Depositions

The deposition temperature for TiO_2 film growth is doubly important in the ALD process because it determines the structure and thickness of the thin film. Titania has three states: amorphous, anatase, and rutile, with refractive indices of approximately 2.3, 2.6, and ~3.1. For low growth temperatures, the film structure is amorphous, and for high growth rates, the film quality can be compromised and not provide a good passivation layer. Figure 74 shows the growth rate as a function of temperature for the conditions: pulse time 8 s and a purge time of 20s. This test result shows that the growth rate drops quickly with increasing temperature. However, the film also becomes denser with increasing temperature.

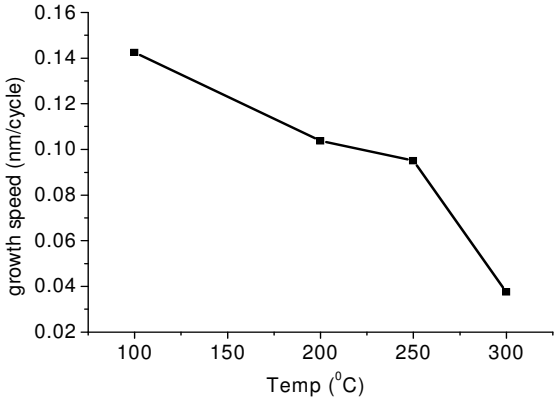

Figure 74. Dependence of growth rate on growth temperature for TiO2.

The aging results, shown in Figure 75, indicate that the film deposited at a high temperature is of higher quality than the film produced at a low temperature. However, it was found that the low temperature deposited TiO_2 coated screens aged faster than the Al_2O_3 coated screens even though the Al_2O_3 films were grown at a comparable temperature. However, from Figure 76, which shows a comparison between the aging results for a higher (300°C) temperature grown TiO_2 film, Al_2O_3 and an uncoated screen, it appears that comparable performance to Al_2O_3 coating can be obtained using TiO_2.

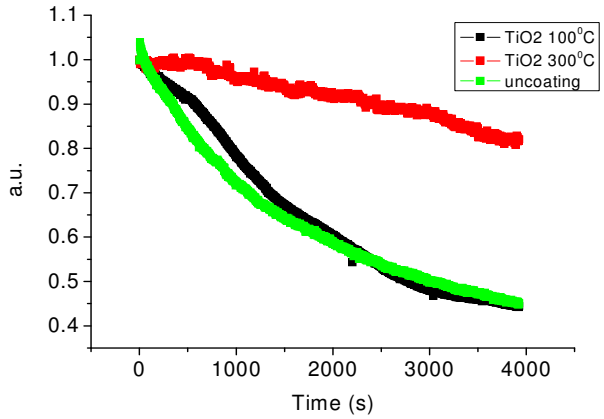

Figure 75. Aging results for uncoated and TiO2 coated phosphor screens for films grown at 100 and 300°C.

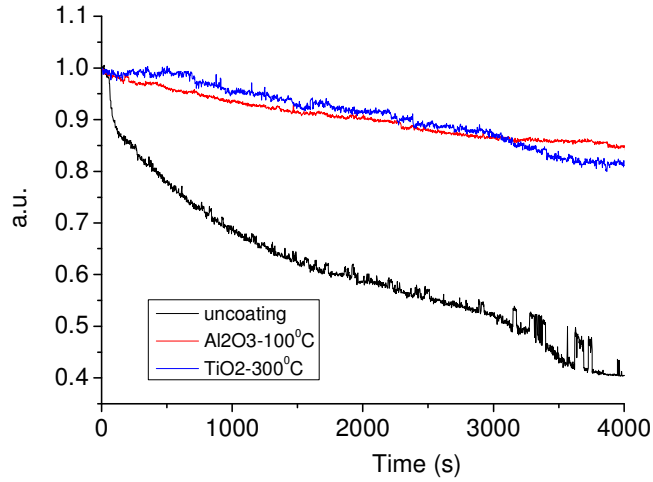

Figure 76. Comparison of the aging between Al2O3 and TiO2 coated phosphor screens.

These preliminary results confirm that Al_2O_3 films deposited by ALD provide a very good passivation and protective coating for the ZnSSe phosphor, and that increasing the thickness of the Al_2O_3 film continues to improve the aging characteristics. However, this "slab" coating technique seems to be less effective for higher weight screens, when the thickness phosphor is increased to ~3-4 particle layers. High temperature TiO_2 growth can also provide a good passivation layer for the phosphor layer, but generally does not appear to be as effective as Al_2O_3 films. The growth temperature determines both the thickness and the phase of TiO_2 and thereby, can affect the passivation of the thin film. However, the use of TiO_2 can be used to adjust the effective index of the composite to maximize light output. Therefore, in principle, the combination of these two oxides can be used to maximize the aging properties and the luminescence output.

Although there is some variation in properties, all coating experiments showed a marked improvement and indicate that more robust routines could be developed. For example, because the interface region between the phosphor and the substrate was the most common cause of failure, using alumina substrates and/or recoating them with alumina could give a more viable structure. However, by using a fluidized-bed ALD system each individual particle can be coated to provide good aging properties, so this approach received most of the effort in the passivation

study. Potentially, the combination of both techniques could be useful in achieving ultra high quality passivations.

Task 4: Optical Simulation of Material and Device Structures

During the course of this project, optical simulations tools were utilized to evaluate and optimize various phosphor mixtures and configurations. These processes were particularly important to take advantage of PhosphorTech's diverse phosphor materials, and the forms of those materials, such as glass encapsulated, nanoparticles, index matching, etc. The simulation efforts thus concentrated on evaluating PhosphorTech's phosphor mixtures, particle size effects, high refractive index materials, as well as placing phosphors directly on an LED die, remotely located phosphors (both as reflective and transmissive configurations) and as phosphor layers remotely located in a dome of sufficiently large radius to overcome the deleterious effect of the LED die absorption of the phosphor converted light. Also, during the course of these efforts, discussions with Optical Research Associates (LightTools) and Zemax technical personnel led to the development of procedures and in some cases, new software modifications, to handle more complex LED/phosphor configurations. Highlights of the results are presented below.

Figure 77 shows examples of the ray tracing models developed in LightTools and Zemax models and one physical configuration of LED/phosphors developed at PhosphorTech. During the development of these models, initial limitations became evident with LightTools. The first of these was a lack of capability to handle phosphor mixtures. This is especially important for our range of phosphors, which provide a flexible means of mixing phosphor to optimize for desired CRI and spectra. Inputs were provided and an alpha and eventually beta software was provided for evaluation that included these capabilities, which were then added to the release versions. In addition, their phosphor model utilizes a matrix and phosphor particle mix and calculates scattering based upon the index difference, particle size and particle density. In the case of phosphors directly on the LED surface, and for the case of ceramic phosphors, this model fails as any phosphor interaction in the software is based upon scattering. So when the matrix has the same index as the phosphor, for example, no light conversion occurs in the software even though physically it should happen. Through discussions, work-around procedures were developed to handle this issue.

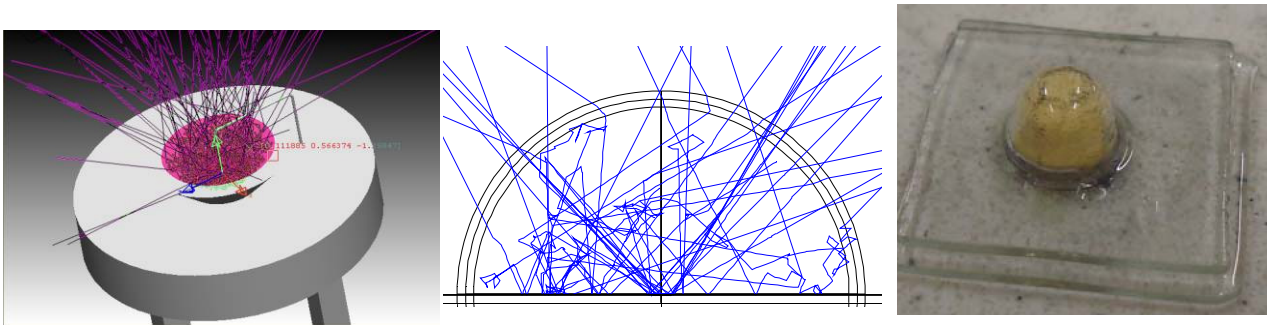

Figure 77. Examples of ray tracing models and one physical LED/phosphor configuration.

One of the major optimization constraints of phosphor converted LEDs is the amount/concentration of phosphor placed on the die. This becomes even more critical when using multiple phosphors to control color while maintaining maximized output. The output will be a function of absorption coefficient, both of the LED light and the other phosphor output, as well as scattering parameters. Thus, simulations were carried out; investigating the use of

PhosphorTech's high index ZnSSe based yellow and orange phosphors. Phosphor data including emission spectra, excitation spectra, and absorption spectra were used in the calculation of results. Figure 78 and Figure 79 show the simulated LED + yellow and orange phosphors. The two-endpoint curves correspond to 100% yellow phosphor to 100% orange phosphor with various mixtures in between. For Figure 78, the total particle amount was conserved for the various ratios, while in Figure 79, the particle concentration was not kept constant but rather added to. The two endpoint curves (i.e., 100% yellow phosphor and 100% orange phosphor) are the same in both graphs. Note that in Figure 78 as opposed to Figure 79, the LED spectral intensity remains the same. This is due to reduced scattering because of the reduced particle concentration. In fact for the data in Figure 79, a reduction in total output power is observed in the middle curves. Also as shown in Figure 79, it is found that the two-endpoint curves output more power compared to the intermediate curves. This is due to increased scattering of the mixture, primarily because of increased particle density.

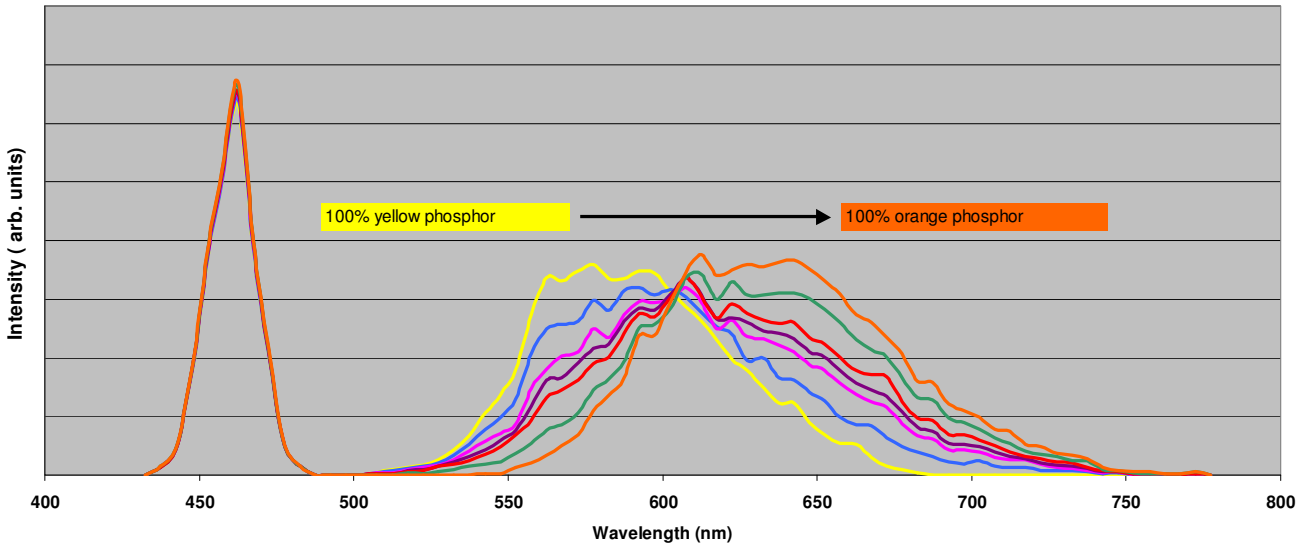

Figure 78. Simulated LED/phosphor emission spectra for various mixtures of yellow and orange phosphors. In this case the total phosphor content is held constant. See text for details

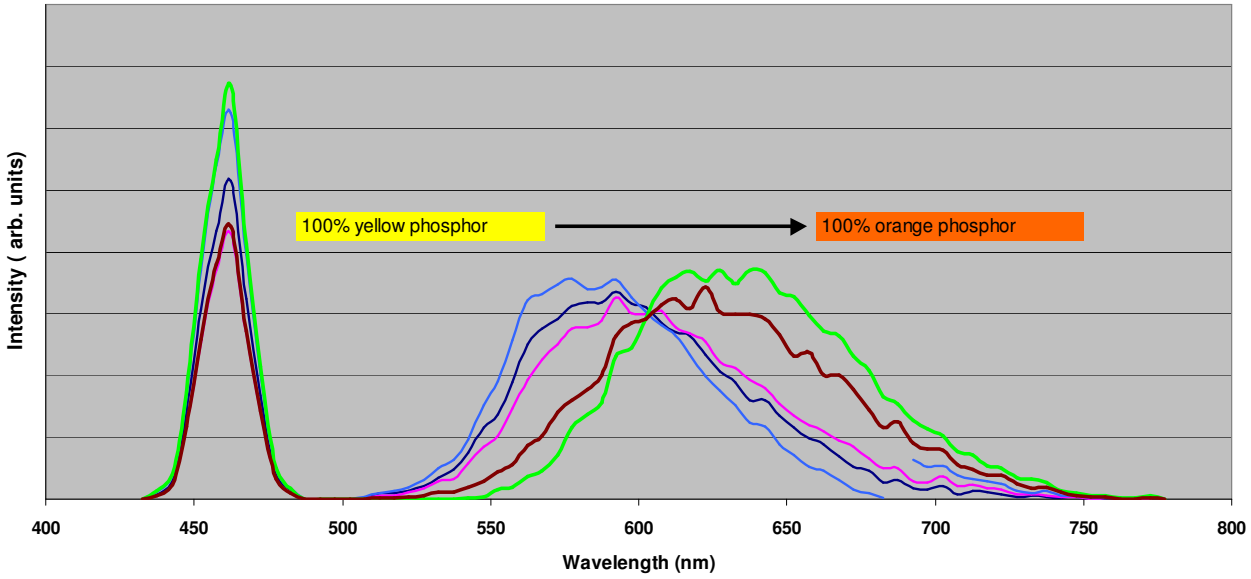

Figure 79. Simulated LED/phosphor emission spectra for various mixtures of yellow and orange phosphors. In this case the total phosphor content varies with the greatest total amount in the middle curves. See text for details.

Studies were also carried out to evaluate the use of PhosphorTech's phosphors in a remote reflection mode. This differs from the standard remote phosphor configurations in that the phosphor loading must be optimized for backscattered light rather than transmitted light. Also, the phosphor can be attached to a highly reflective metal substrate thus maximizing reflectance, as well as thermal transfer. Thus, this configuration will take advantage of controllable scattering properties, reduced thermal loading, and high reflectance backings. It should be pointed out that cathodoluminescent screens exhibit about twice the efficiency in reflection mode compared to transmission mode, due to light scattering in the phosphor layer. Example variations for this study include blue LED/reflector/lens combinations, source/phosphor separation distance, phosphor layer thickness, loading and particles size (i.e., scattering properties), as well as reflector optical design.

For this analysis, a standard blue LED model was used, except that the phosphor layer was removed from the die. The phosphor was placed remotely located but in front of the emitting blue LED. Additionally, a backside reflective coating was placed on the phosphor. In this way, the emission was only directed in the reflected direction. Using the PhosphorTech ZnSeS:Cu orange emitting phosphor, model runs were made with variable particle density (placed in an epoxy plate) and particle size. Figure 80 shows the results obtained for particle sizes ranging from 1 to 20um, a particle loading density of 20000 per mm^3 of epoxy and a phosphor layer thickness ranging from 50um to 525um. The phosphor index is 2.3 and the matrix index is 1.5. The figure plots the integrated reflected light power as a function of the above aforementioned variables. It is obvious that the smaller scattering materials yielded improved light output.

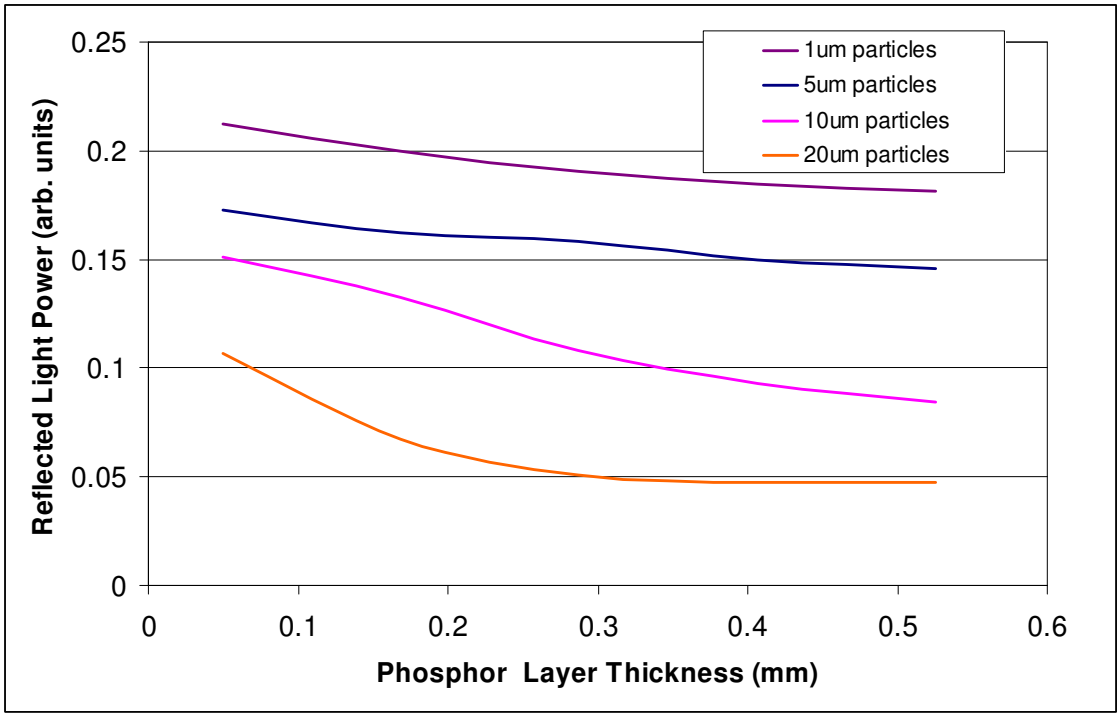

Figure 80. Reflected light output power vs. phosphor layer thickness and phosphor particle size.

Considering the transmitted light output for such a configuration by removing the reflective back plate, it was found that the results are quite similar in character to the reflected results, indicating that the scattering properties of the phosphor were actually less than expected. Indeed, a calculation of the mean free path at these parameters yielded values that are a significant proportion of the thicknesses investigated. Thus, higher particle loadings were next investigated.

In this case, the particle sizes investigated were 1 and 20µm, the loading density varied from 10000 to 200000 particles per mm^3, and the phosphor layer thickness ranged from 50µm to 525µm. Figure 81 plots the integrated transmitted light power as a function of the above aforementioned variables. It is apparent that the mean free path through the phosphor layer is quite significantly affected by the particle size and density. If one calculates the volume of phosphor for the 1 and 20µm particles, a mass ratio of 8000 is obtained. Thus, the 20µm particle is more ideally suited for absorbing the light. However, the MFP is much greater for the 1µm particles, due to their small size relative to the 20µm phosphors, thus yielding greater light output.

The next step involved the evaluation of light output vs. relative phosphor loading in terms of mass density. Figure 82 shows the results obtained for particle sizes ranging from 0.5 to 20µm, a fixed loading density of 200000 particles per mm^3 and a phosphor layer thickness ranging from 0.05 to 0.525mm. The figure plots the integrated transmitted light power as a function of the relative mass of phosphor for the range of phosphor layer thicknesses. The relative mass in this case is the particle volume times the particle number density per mm^3. It is interesting that for these conditions, an apparent break point exists around the 10^7 value of relative mass, where the light output begins to fall more dramatically. This type of analysis may provide directions for optimizing loading. However, careful attention must be paid to the attending chromaticity results.

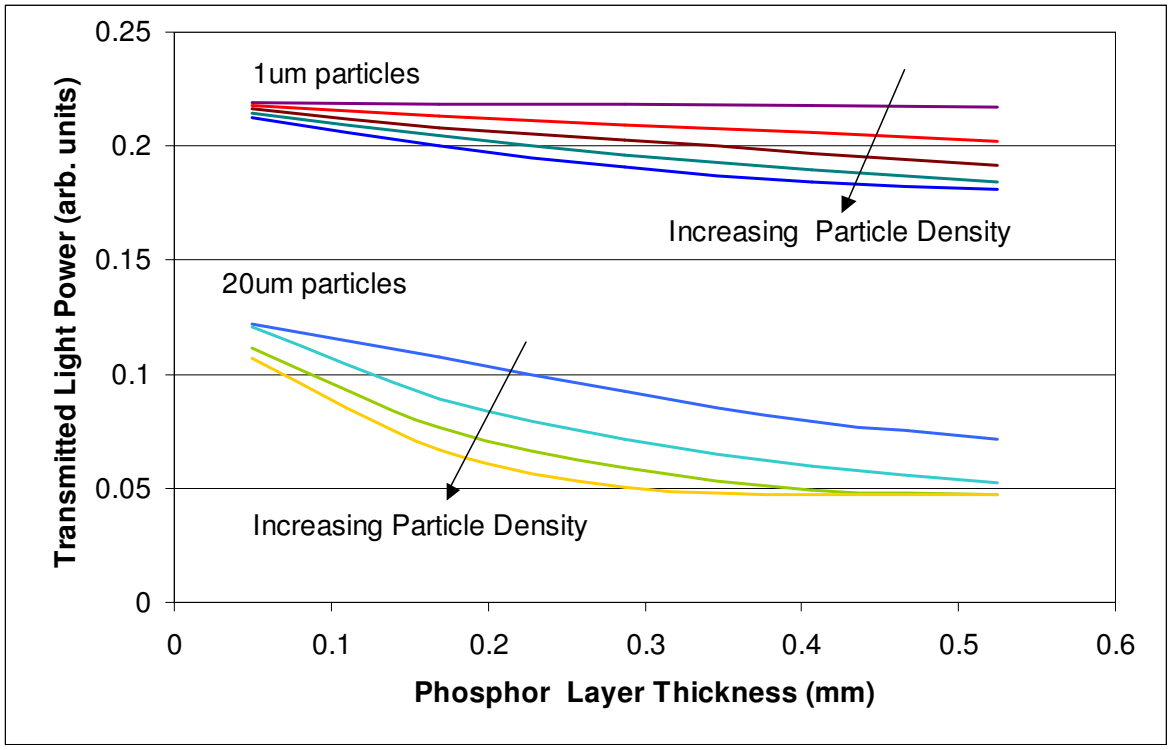

Figure 81. Transmitted light output power vs. phosphor layer thickness and phosphor particle size, density (see text for details).

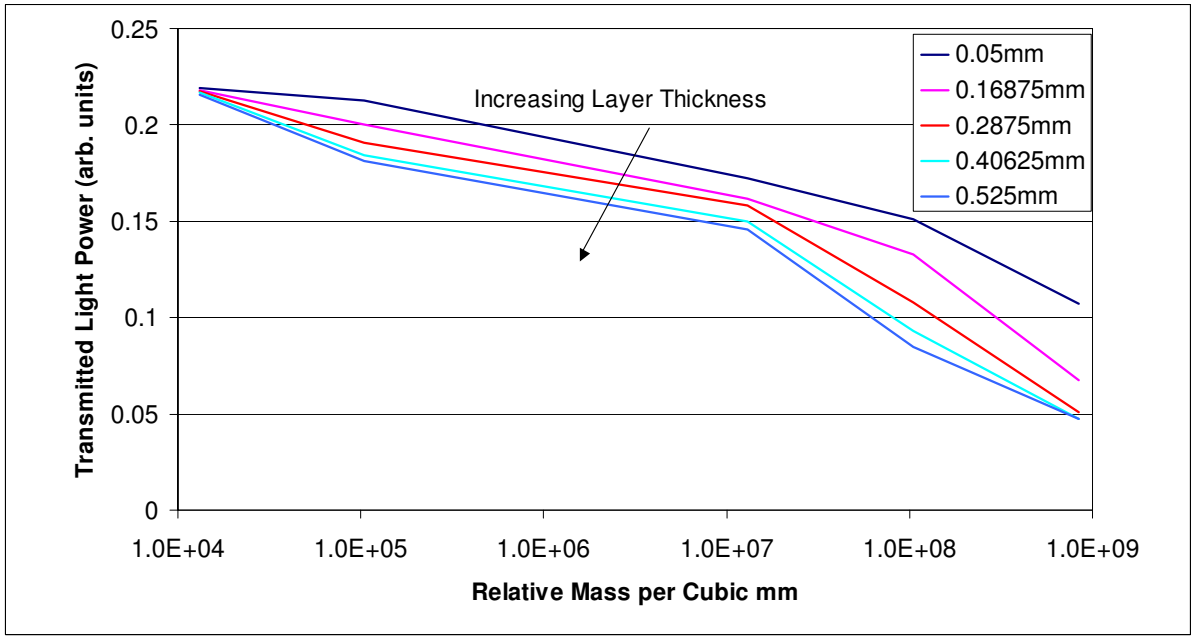

Figure 82. Transmitted light output power vs. relative mass of phosphor (see text for details).

Further optical models were developed, pursuant to recent results reported for enhanced light output through the use of index matched phosphor layers placed on the inside of a large (relative to LED die dimensions) spherical dome with a large air gap between the phosphor layer and the LED die. This type of structure lends itself well to PhosphorTech's nano and quantum dot phosphors as well as glass-encapsulated phosphors. The concept basically requires that the intercept cross-section of the optically lossy LED die for any ray reflected/scattered from the

dome is small. This is accomplished by using a relatively large dome such that the die subtends a small solid angle of the base of the dome. The region on the base around the die is then made reflective or scattering. Additionally, for PhosphorTech, the index of the phosphor layer can be varied through the use of its various phosphors or through phosphor loaded composites. Figure 83 below shows preliminary results based upon this structure, comparing the effect of phosphor layer index and radius of the domes for an outer dome index of 1.5. For the purposes of this initial study, the region below the LED die was considered to be totally absorbing and scattering was neglected. The phosphor layer in all cases was chosen to be 1mm thick. From the figure, it is apparent that while there is some scatter in the data, the trends indicate that phosphor layer index matching is still important and that the smaller radius dome does indeed reduce light output at the lower index values.

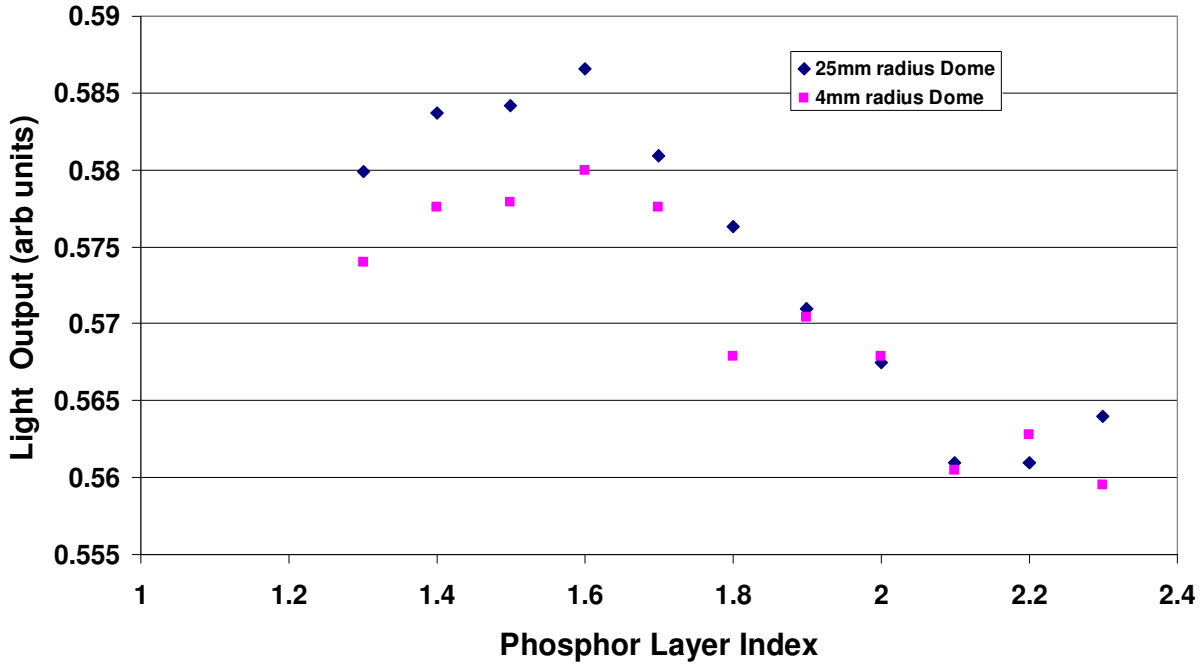

Figure 83. Comparison of the effect of phosphor layer index and radius of domes on light output. See text for details.

A refinement of this model using a Lambertian scattering surface surrounding the die (rather than a reflective surface) led to results that reduced the advantage of the large dome. Next, the effect of phosphor scattering upon performance was investigated. Initial results were obtained using a reflective region around the LED die and assuming a mean free scattering length of 1mm, the thickness of the phosphor layer. Again, the region below the LED die is considered to be totally absorbing. Figure 84 shows results based upon this structure comparing the effect of phosphor layer index and radius of the domes for an outer dome index of 1.5. From the data shown below it appears that the bulk scattering has tended to equalize the effect of the two dome radii. It is obvious that phosphor scattering will play a large role in determining the efficacy of this design and indeed points to the need for controlled scattering properties.

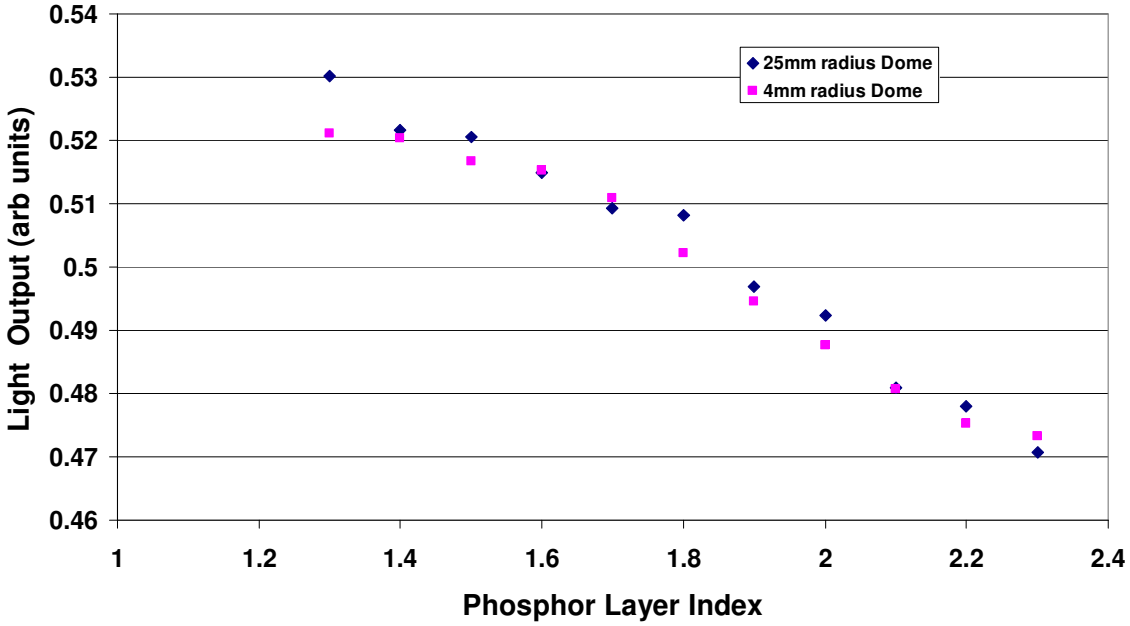

Figure 84. Comparison of the effect of phosphor layer index and radius of domes on light output for a phosphor layer including bulk scattering. See text for details.

The above discussion and results point to the need to investigate and control the relative scattering properties of the phosphor system. Several approaches are available to address this issue. These include index matching at any of the several phosphor/environment interfaces, particle size control, particle coatings for scattering/reflection modification, and the use of ceramic or glass-ceramic phosphors.

To evaluate the utility of a ceramic phosphor, simulations were carried out comparing particulate phosphors with non-scattering ceramic phosphors. In this case, a ~50µm layer of particular phosphor/polymer matrix composite was compared to a 50µm thick ceramic phosphor placed directly on the LED die. For the purposes of this study, a 455nm emitting LED was used along with the yellow emitting ZnSSe phosphor (and its associated optical excitation/emission parameters) described elsewhere. Parameters varied include the absorption length (1/e point) for the ceramic phosphor and the index of the phosphors while the index of the polymer matrix was held at 1.5. The data was normalized to the emission of the particulate phosphor at the refractive index of YAG (1.8), presented in both terms of integrated photon flux and total power output. This was necessary because the maximized power out would simply be that of unconverted blue LED spectrum due to losses associated with Stokes shift. Figure 85 shows the combined LED/phosphor spectra obtained during these simulations for a fixed absorption length of 40µm for the ceramic phosphor while the scattering parameters were calculated for Mie scattering for particles of 15µm in diameter. Figure 86 shows the results as a function of phosphor refractive index for the integrated photon yield and power output normalized to that obtained for the powder phosphor with the YAG index. It is seen that the ceramic phosphor shows greater outcoupling efficiency than the scattering phosphor and peaks over a range of refractive indices of 2-2.2. The fact that the optimum index does not exactly match that of the LED die (n=2.4) is most likely due to the matching required as the photons enter the LED epoxy dome with its refractive index of 1.5.

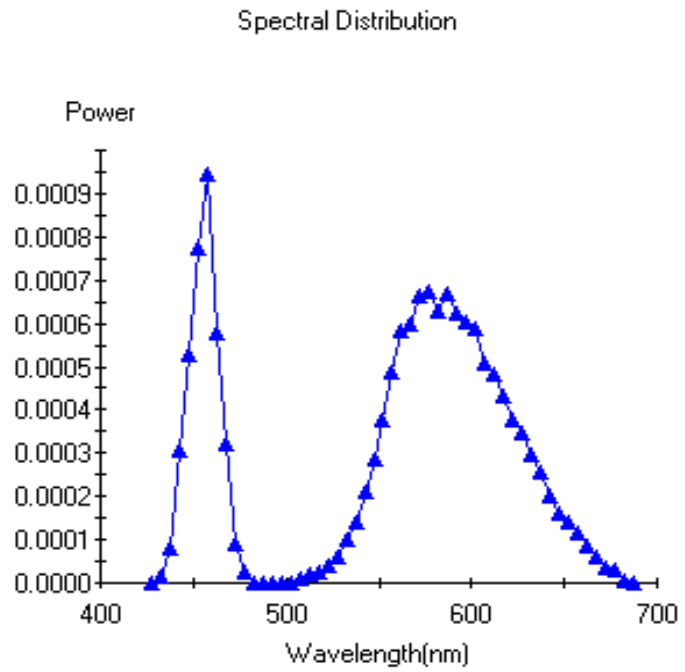

Figure 85. Simulated spectrum of blue LED/ZnSSe phosphor combination

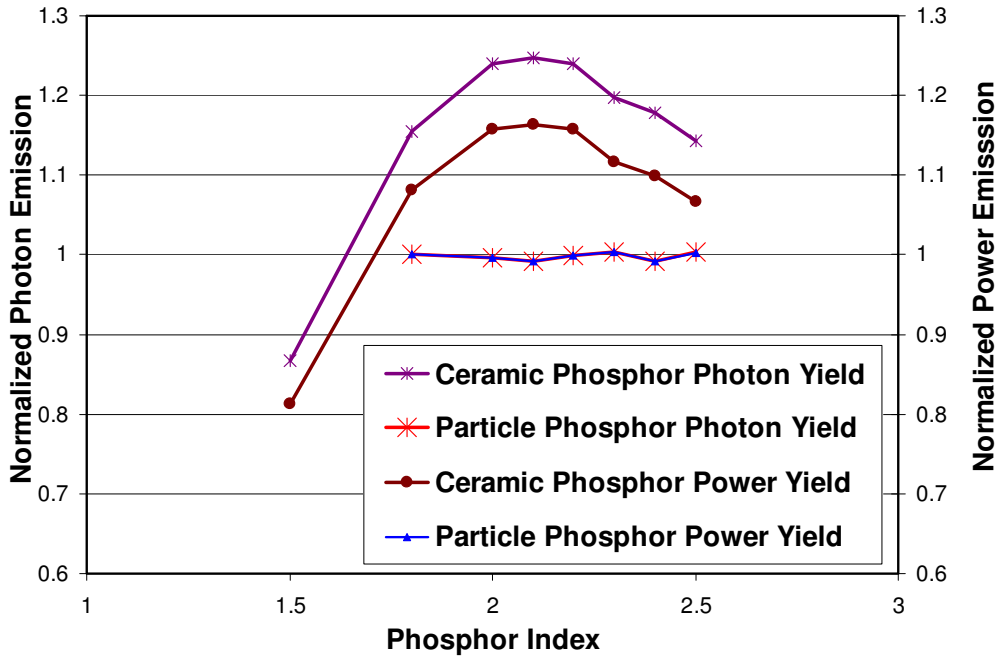

Figure 86. Simulated normalized output comparison of particulate and ceramic phosphor combination obtained using LightTools. See text for details.

Another means of reducing scattering is to reduce phosphor particle size to a small fraction of a micrometer in diameter. Mie scattering calculations were carried out and converted to mean free path length (MFP) (i.e., related to scattering efficiency and particle density) to provide an idea of the contributions of the number of particles, refractive index difference with respect to the epoxy matrix and the size of particles. From these calculations, it was found that for ~50% mass loading of high index phosphor (n=2.4) in epoxy (n=1.5), scattering drops very quickly as the phosphor particle diameter drops below 20nm. On the other hand, better MFPs

were obtained by increasing the particle number density when increasing the phosphor loading density from the nominal 50% level.

To evaluate the effect of the use of these nanoparticles on LED output, optical simulations were carried out. For the purposes of this study, a simple 300µm square trapezoidal LED die was placed on an absorbing substrate, covered with a 30µm thick phosphor layer and encapsulated in an epoxy dome. The refractive index of the LED die, epoxy and phosphor were set at 2.4, 1.5 and 2.4 respectively. An aggregate phosphor/phosphor matrix refractive index was assumed using the rule of mixtures. Relative LED output efficiencies were calculated compared to the LED/dome structure without a phosphor layer, as it is expected that scattering induced in the structure will reduce output efficiency.

Calculations were carried out for single wavelengths of 405, 460 and 585nm photons with the 405nm and 460nm light being generated in the LED die and calculated separately from the 585nm emission being generated in the phosphor volume. The aggregate output efficiency was then calculated based upon the product of the excitation wavelength efficiency and the phosphor emission efficiency.

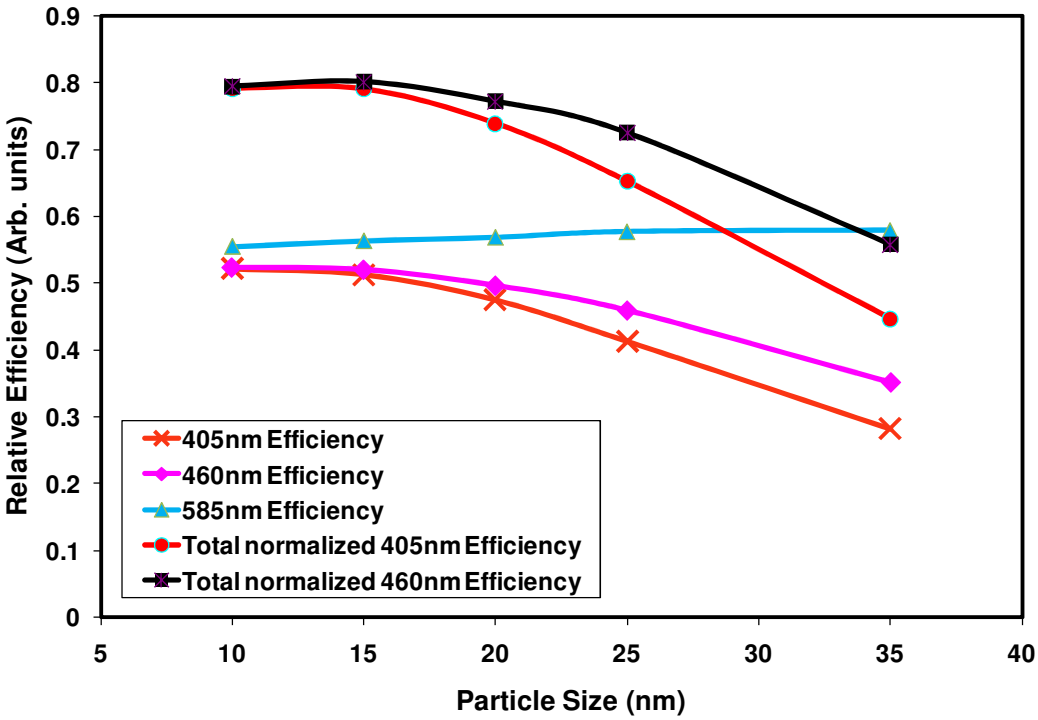

Figure 87 shows relative efficiencies simulated as a function of nanoparticle diameter for the two excitation wavelengths, the emission wavelength, and the combined excitation and emission efficiency for the two excitation conditions. The results indicate that for the LED structure simulated, either excitation wavelength produces similar results at particle dimensions below ~20nm. The output efficiency of the phosphor emission on the other hand appears relatively insensitive to particle size for the range of values studied. The combined excitation and emission efficiency results (normalized to non scattering simulations) indicate that maximum performance is obtained for particle diameters ~15nm and below. These results indicate that the use of relative large nanophosphor particles with high bulk like absorption coefficients, large band emission Stokes shifts and the commensurate reduction in phosphor loading may provide improved performance.

As a further study of the relative insensitivity of the emission efficiency, simulations were performed to examine a larger range of 585nm photon MFPs. Figure 88 shows the

efficiency of the phosphor emission normalized to the non-scattering value as a function of MFP plotted as a fraction of the phosphor layer thickness. From these results it appears that some scattering can be beneficial. This may be due to enhanced out-coupling from the higher index phosphor layer into the lower index epoxy dome.

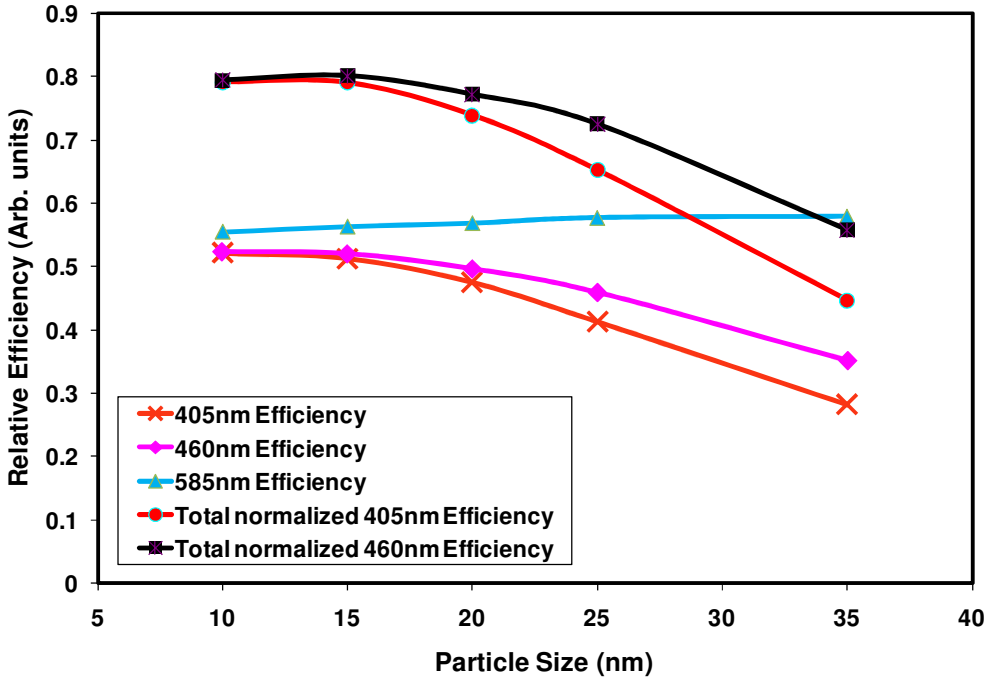

Figure 87. LED output efficiency as function of nanoparticle diameter for 405 and 460nm excitation wavelengths, 585nm emission wavelength, and combined excitation and emission.

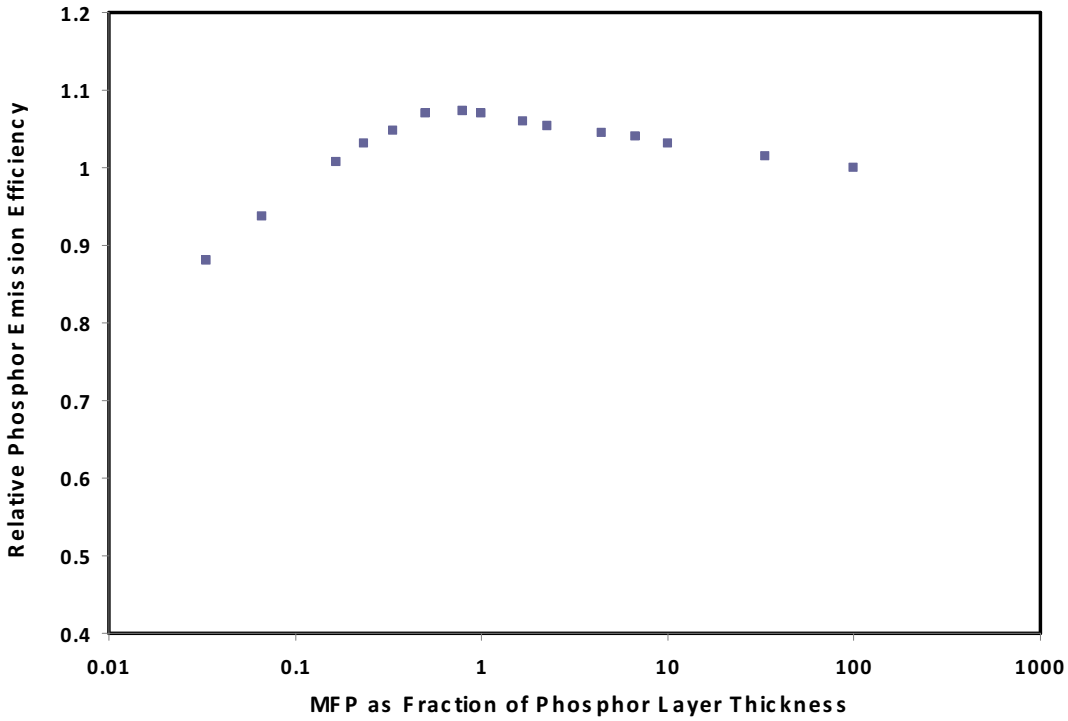

Figure 88. Relative LED phosphor emission efficiency as a function of MFP normalized to the phosphor layer thickness.

Phosphor scattering is further influenced by coatings. Coatings on phosphor particles can provide multi-functional attributes. These include, for example, environmental barrier, surfactant, flow modifier, efficiency enhancer and refractive index/scattering modifier. As a test of this, ALD coatings of alumina were applied to our ZnSSe phosphors as an environmental protection layer. Figure 89 shows the optical results obtained for a phosphor coated with 100nm of alumina. As is seen, the coated ZnSSe phosphor exhibits increased 405nm absorption (~3.7x) and increased 590nm emission (1.25x) vs. the uncoated phosphor.

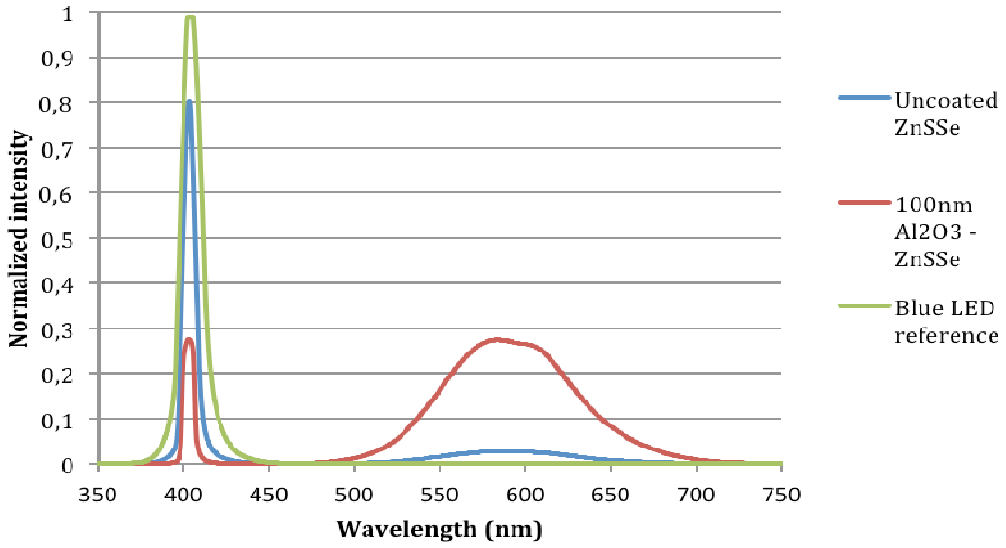

Figure 89. Comparison of blue+phosphor spectra for 405nm LED and alumina coated and uncoated ZnSSe.

A simple reflectance model was used to evaluate the effect of the 100nm coating on the phosphor. As shown in Figure 90, this model predicts a decrease in average (over angle and polarization) reflection of 405nm excitation by 2x and scattering calculations indicate a 3-5% drop in scattering efficiency at the output wavelength of 590nm.

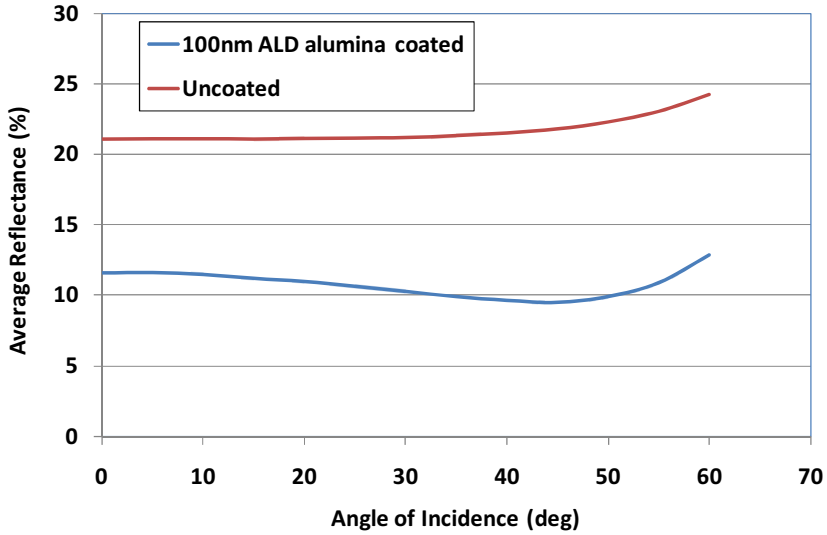

Figure 90. Average reflectance vs. angle of incidence for 405nm light impinging on coated and uncoated ZnSSe phosphors.

As a further study of the coated phosphor optical properties, scattering calculations were carried out and combined with ray tracing models to determine the effect upon LED performance. For the parameters generally of interest in phosphor coated LEDs, scattering in optical simulations is typically handled through Mie scattering. Based upon the phosphor loading density, the difference in matrix and phosphor refractive indices and the phosphor particle size distribution, scattering efficiencies are calculated along with angular dispersion of the scattering. These parameters affect how the particle interacts with both LED and phosphor optical emissions, thereby, directly affecting both the chromaticity and efficiency of the LED. However, few optical ray-tracing packages contain the ability to calculate the scattering properties of coated or core-shell particles. New variables that must be considered are the thickness of the shell and the refractive index of the shell. As our simulation software does not include such capabilities, a search was made for code that could handle the multilayer particle calculations. Two such tools were found. The first was evaluated in the limit of a homogeneous particle to compare its output with standard Mie solutions. It was found that this software did not reliably produce results that compared to standard Mie scattering models and in fact appeared to be off by a constant based upon the particle size. The second tool was able to recreate previously validated results and as such was chosen for this study. It should be pointed out that these codes are not integrated with ray tracing software and thus any output must be manually included in the LED simulations.

For this study, the scattering efficiency of coated particles was studied as a function of wavelength, shell refractive index and matrix refractive index. The parameters held constant for this study were a 1:1 ratio of core to shell thickness (i.e., the core radius is half the particle radius), a total particle radius fixed at 100nm, and a core particle refractive index of 2.3. The matrix refractive index was set at 1.5 and 1.8, the wavelength varied from 405 to 635nm and the shell refractive index from 1.3 to 2.2. (The matrix refractive index of 1.8 corresponds to doping the matrix with high index nanoparticles to control the index of the epoxy for increased performance through better index matching.) Once the scattering efficiency was calculated, it was converted to MFP using the total particle cross-section and a phosphor loading density of $100\mu m^{-3}$, equivalent to about 40% by volume. Figure 91 and Figure 92 show the MFP in mm, calculated as a function of the above parameters, for matrix refractive indices of 1.5 and 1.8, respectively. As expected, the MFP increases with wavelength. However, the slopes of the curves are not all equal, with a shell refractive index value of 1.3, just under the matrix index of 1.5, yielding both the largest slope and the largest MFP. A similar situation is seen for the matrix index of 1.8 curves with the shell index of 1.7 yielding the highest slope and MFP. Other interesting details are also seen with, in some cases, the curves crossing over each other. This may provide some flexibility in tuning parameters for different wavelengths. The data is compared more directly at 465nm in Figure 93. As is seen, the higher index medium provides a slight better performance at an index of 1.7 while the peak performance at a shell index of 1.3 is somewhat less, but marks the lowest practical shell solid material index (e.g., MgF_2). One could argue that having a shell index of less than the matrix index (at 50% of the radius of the particle) reduces the overall average index of the particle leading to better index matching with the matrix. However, the effect can only go so far, as there is still an increasing index mismatch between the shell and the matrix as the shell index is decreased, leading to two competing effects. It may also be this type of competition that leads to the varying slopes vs. wavelengths for the MFP curves.

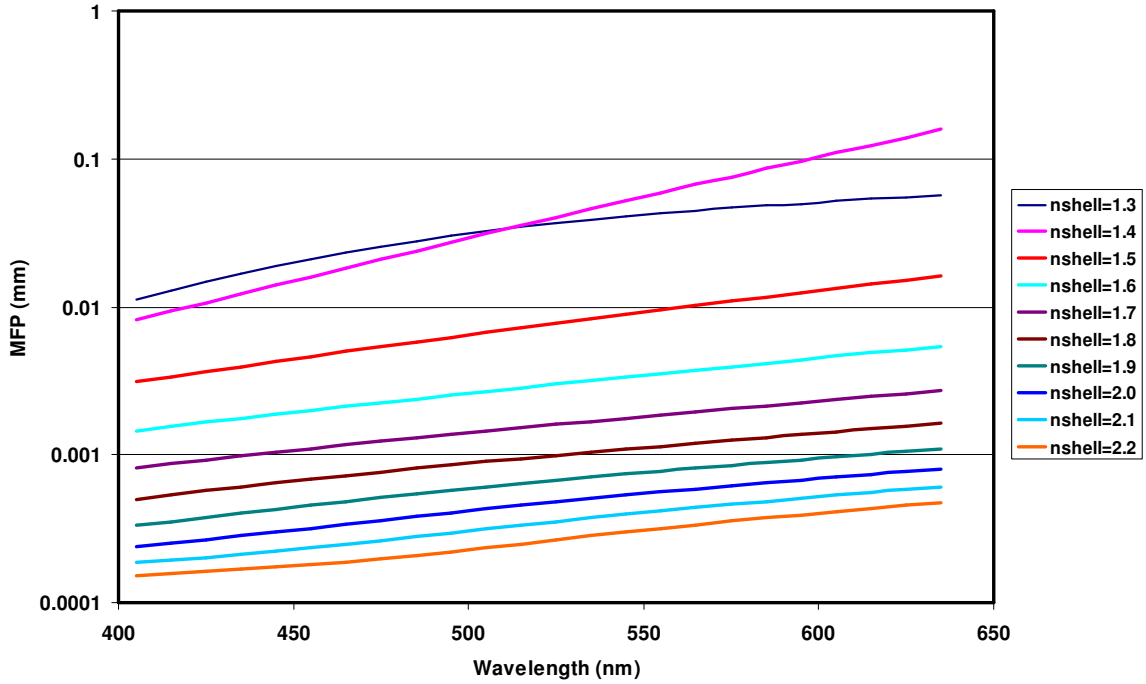

Figure 91. Comparison of the effect of shell refractive index on MFP for a matrix refractive index of 1.5. See text for details.

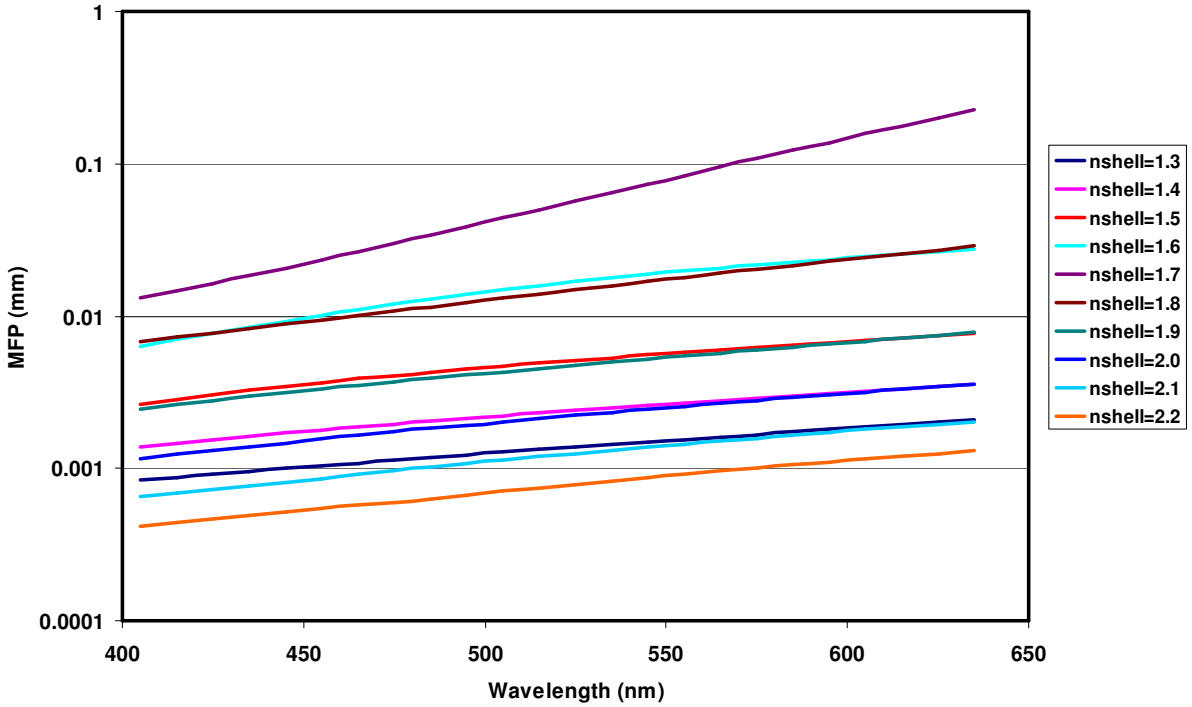

Figure 92. Comparison of the effect of shell refractive index on MFP for a matrix refractive index of 1.8. See text for details.

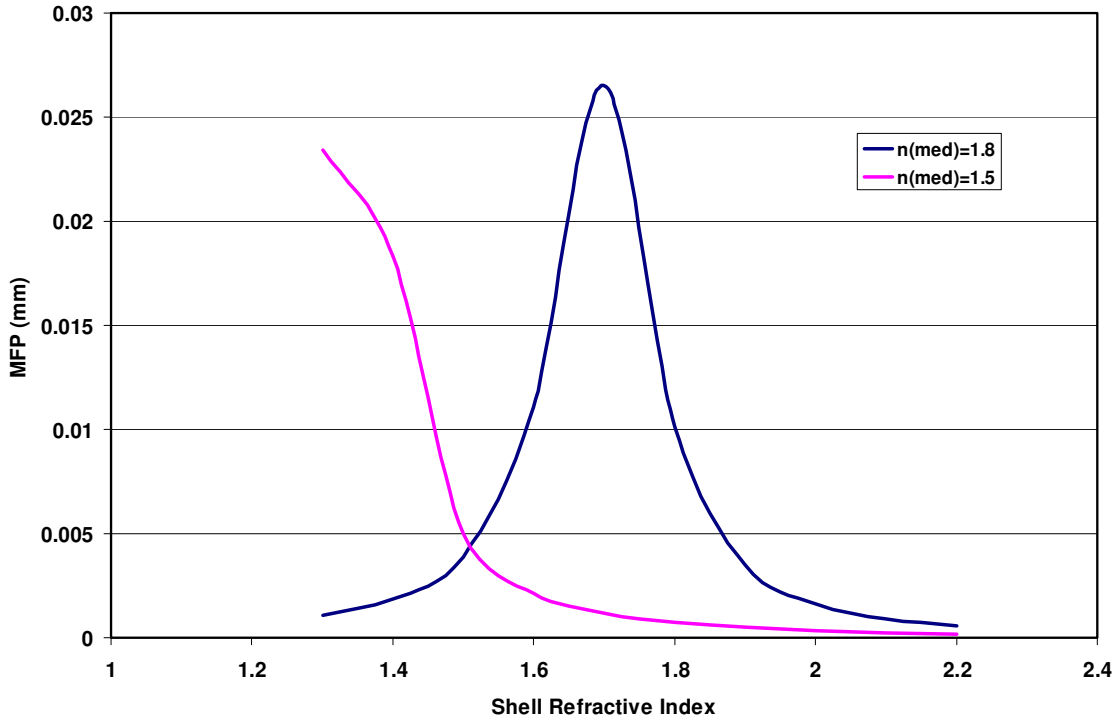

Figure 93. Comparison of the effect of shell refractive index on MFP at 465nm for matrix refractive indices of 1.5 and 1.8. See text for details.

As a comparison, the particle radius was next decreased to 50nm while maintaining a 1:1 ratio of core to shell thickness (i.e., the core radius is half the particle radius), and a core particle refractive index of 2.3. Note that this reduction in particle size should decrease the scattering cross-section. Once the scattering efficiency was calculated, it was converted to mean free path (MFP) using the total particle cross-section and a phosphor loading density of 750μm^{-3}, equivalent to about 40% by volume. This is to compare with previous results for 100nm particles loaded at ~40% by volume in the matrix. It is also important to note that by volume, the ratio of coating to phosphor particle has remained the same in these calculations. Thus, there is no change in active phosphor material volume between the two cases. The data is compared directly at 465nm in Figure 94 (note the log scale). Note that there is a large increase of MFP compared to 100nm particles. This implies from a scattering perspective that smaller particles are better. Also, the lower index medium provides a slightly better performance at an index of 1.4 while the peak performance at a shell index of 1.7 is somewhat less. Compared to the 100nm results, the best performance has changed from higher to lower matrix indices.

These results were next applied to the LED ray tracing models to determine the effect upon LED performance. Figure 95 compares the 405 and 465nm MFP and relative LED die output as a function of shell refractive index for a 40%vol phosphor loaded n=1.5 matrix, n=2.3 cores for 100/100nm radius core/shell particles. Substantial improvement is seen using the 465 vs. 405nm. Figure 96 on the other hand compares 585 and 535nm phosphor emission MFPs and relative phosphor outputs as a function of the same variables. In this case, the 585nm gives slightly improved results.

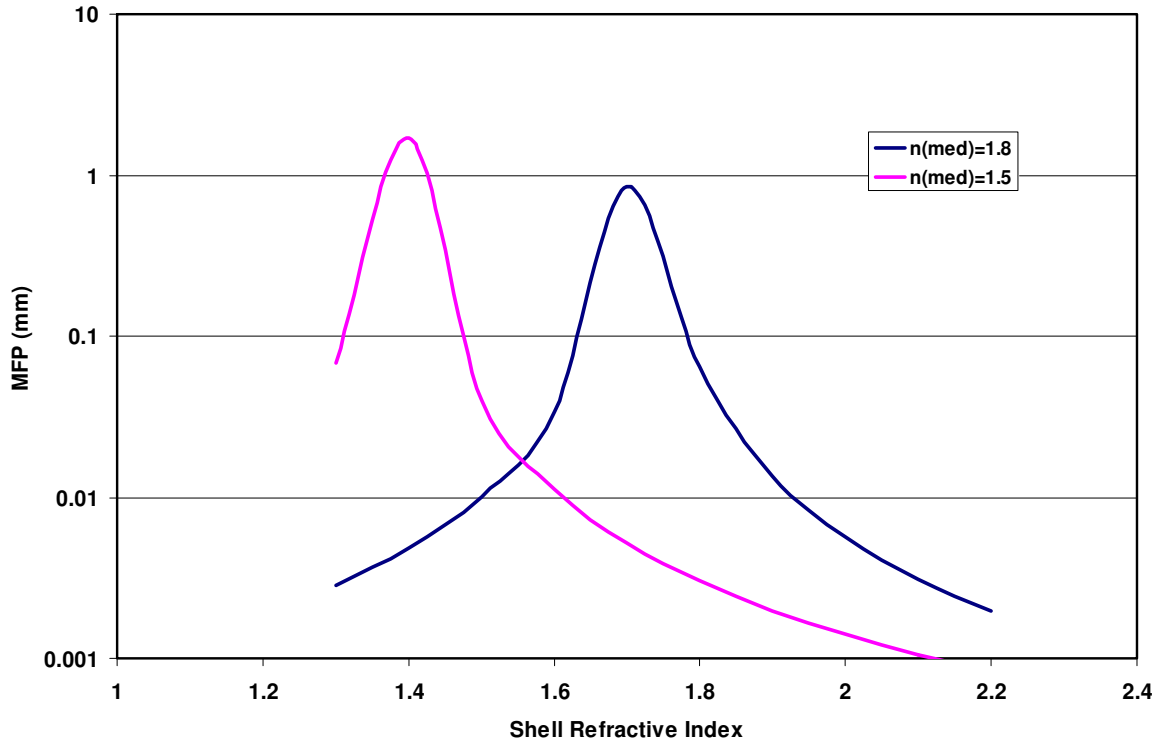

Figure 94. Comparison of the effect of shell refractive index on MFP at 465nm for matrix refractive indices of 1.5 and 1.8. See text for details.

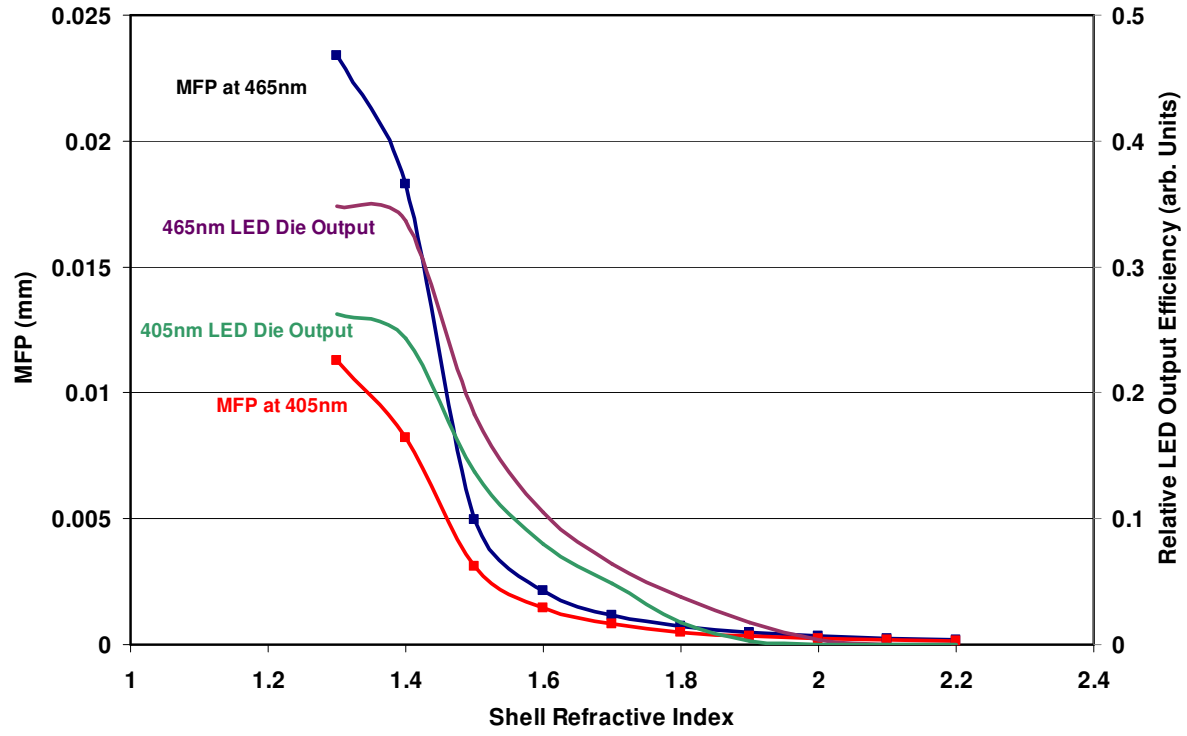

Figure 95. MFP and relative LED die output as function of shell refractive index. See text for details.

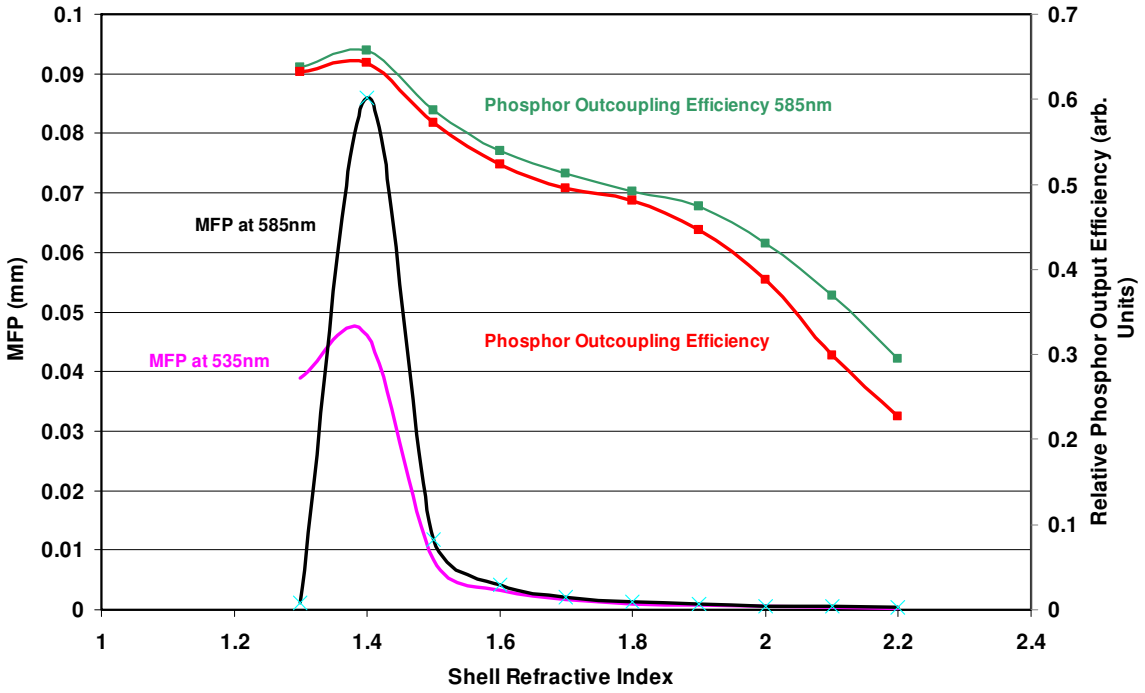

Figure 96. MFP and relative phosphor output as function of shell refractive index. See text for details.

From these studies, it is apparent that much work remains, in particular with respect to scattering, in both materials and device structures for fully optimized solid-state lighting devices. Scattering properties play a key role and can be addressed through particle size, particle loading density, refractive index matching and the use of longer wavelengths. Future studies will continue to evaluate device and material performance with respect to obvious physical constraints and performance trade studies.

Task 5. Material and Device Analysis and Characterization: LED Studies

Under this Task, we have evaluated several high power LEDs as potential excitation sources to complement the phosphor development reported in Tasks 1 and 2. The first study assessed the performance of 10 Watt devices made in S. Korea with white output flux specified at 600 lumens. As shown in Figure 97, three different types of high power LEDs were acquired and tested: (1) a 10W blue LED emitting at around 465nm, (2) a 10W "cool white" LED with a YAG-based emission around 555nm, and (3) a 10W "warm white" LED with an orthosilicate-based emission at around 589nm. The devices consisted of a 3x3 array of dies inside a ceramic package, encapsulated with silicone gel. For the "white" devices, a layer of phosphor (Ce-doped YAG for the "cool white" and Eu-doped orthosilicate for the "warm white") was deposited on top of the array and covered the entire bottom surface of the package.

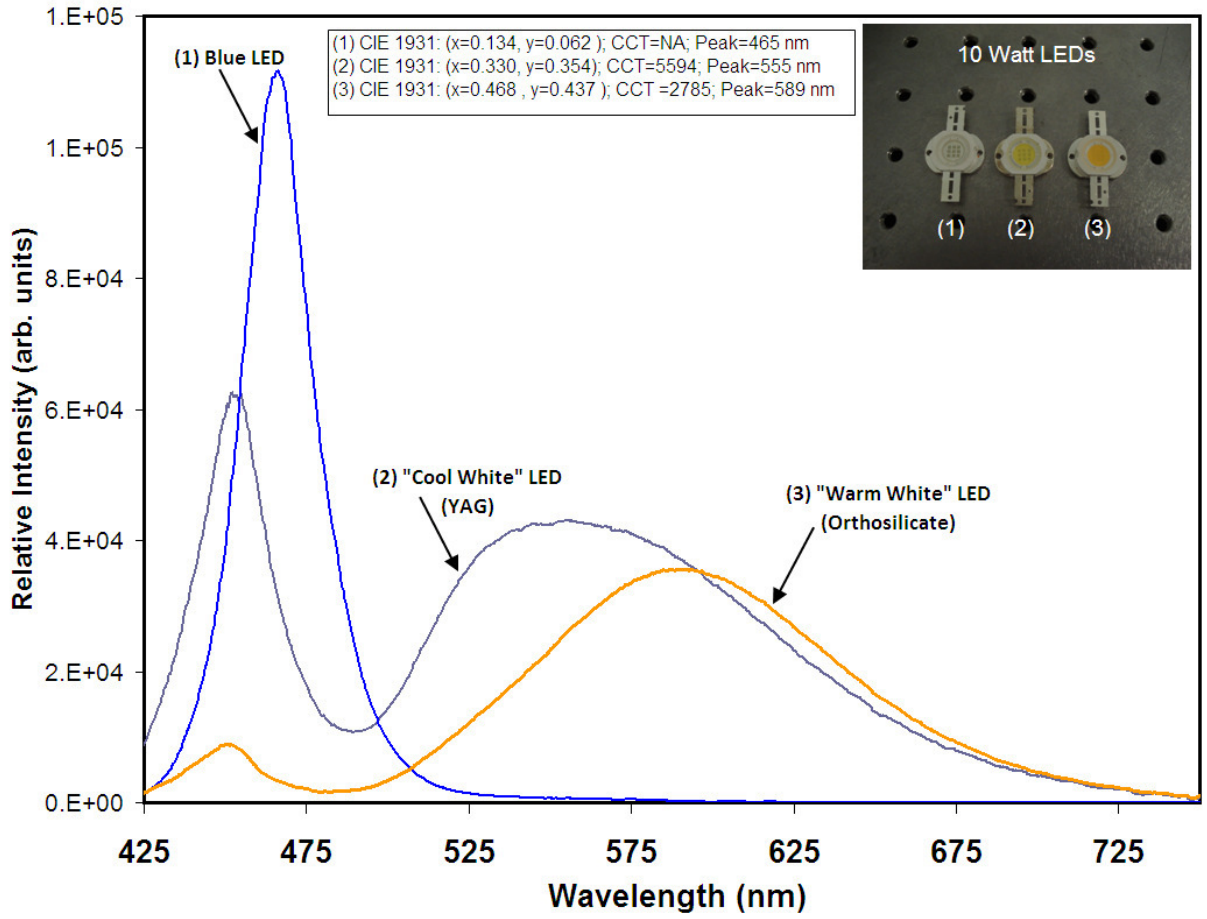

Figure 97. Spectral and color properties of high power (10W) blue (1), cool white (2), and warm white (3) LEDs operated at 1 A current and around 10 Volts. Inset: photo of LEDs in ceramic packages.

For these characterizations, the LED was heat sunk by pressure-mounting the die on an optical table so that the stainless steel surface was used as a large heat sink. An integrating sphere coupled to a fiber optic spectrometer (see inset of Figure 98) was used to collect light from each LED. The stability tests were conducted on each LED in order to determine variations during operation at high power (10W). The data shown in Figure 98 illustrates the variations in the peak intensity of each LED during the first 700 seconds of operation. During this period, the surface temperature of the LEDs was determined to vary from 22^{o}C (RT) to a stable 110^{o}C after 700 s. As shown below, the output from the blue LED dropped by ~7%. The intensity of the "cool white" device dropped by 13%, while that of the "warm white" LED decreased by as much as 17%, which is expected as a result of thermal quenching of the phosphors.

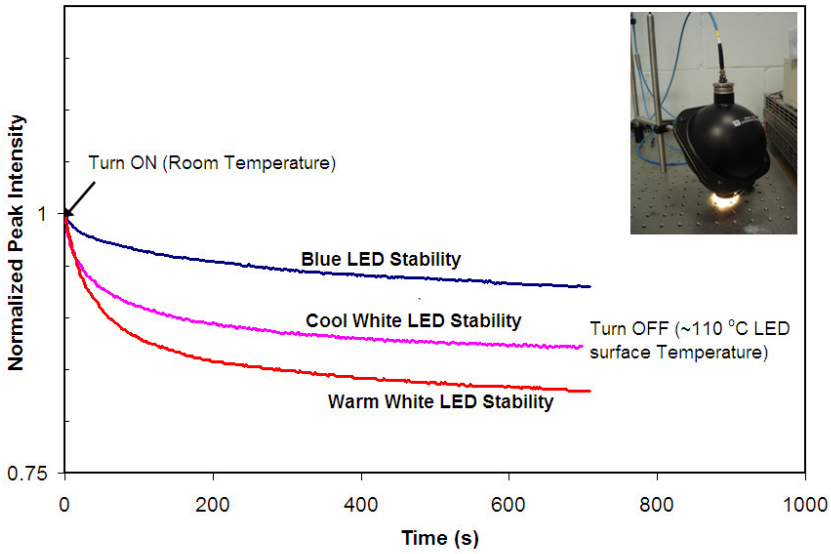

Figure 98. LED stability as a function of operating time at ~10W for the blue, cool white, and warm white LED devices. Inset: integrating sphere and fiber optic setup used to acquire above data.

Also several Philips Lumileds high power LEDs were evaluated for use in assessing our phosphors in a real world application. These consisted of (1) Royal Blue Luxeon Rebel SMT Emitter with 350 mA operating current and a blue peak around 447nm, and (2) White Luxeon Rebel SMT Emitter with 5000K Correlated Color Temperature (CCT) and 90lm/65CRI when operated at 350mA. The Luxeon white LED spectrum is shown in Figure 99, where the yellow emission appears to be from a single component YAG:Ce phosphor.

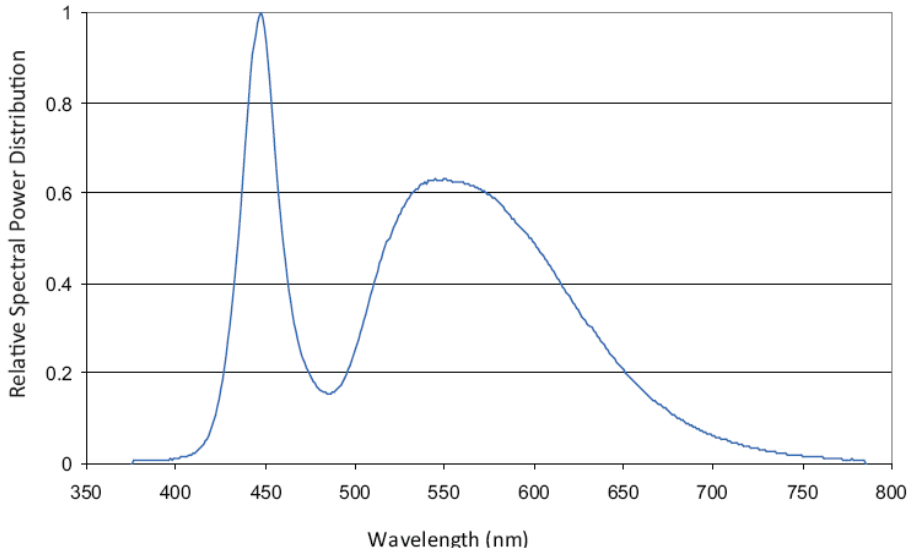

Figure 99. Emission spectrum of a YAG-based White Luxeon Rebel SMT Emitter with 5000K CCT

For stability comparison testing, each LED was mounted on a 1cmx1cm sapphire substrate (acting as a heat sink) using a thermal compound. Three types of LEDs were tested as shown in the inset of Figure 100: (1) Blue Luxeon Rebel with silicone encapsulant; (2) Blue Luxeon Rebel with the silicone encapsulant removed; and (3) White Luxeon Rebel with silicone encapsulant. As previously, an integrating sphere coupled to a fiber optic spectrometer was used to collect light from each LED. Each stability test was conducted during LED operation at

350mA. The data shown in Figure 100 illustrates the variations in the peak intensity of each LED during the first 250 seconds of operation. As shown below, the output from all three LEDs dropped by about 11% in 200 seconds. The intensity of the silicone-encapsulated devices stabilizes after 100 seconds, while the output from the non-encapsulated device continues to drop, but at a slower rate. This is expected since silicone enhances thermal dissipation and acts to stabilize output degradation due to increased junction temperature.

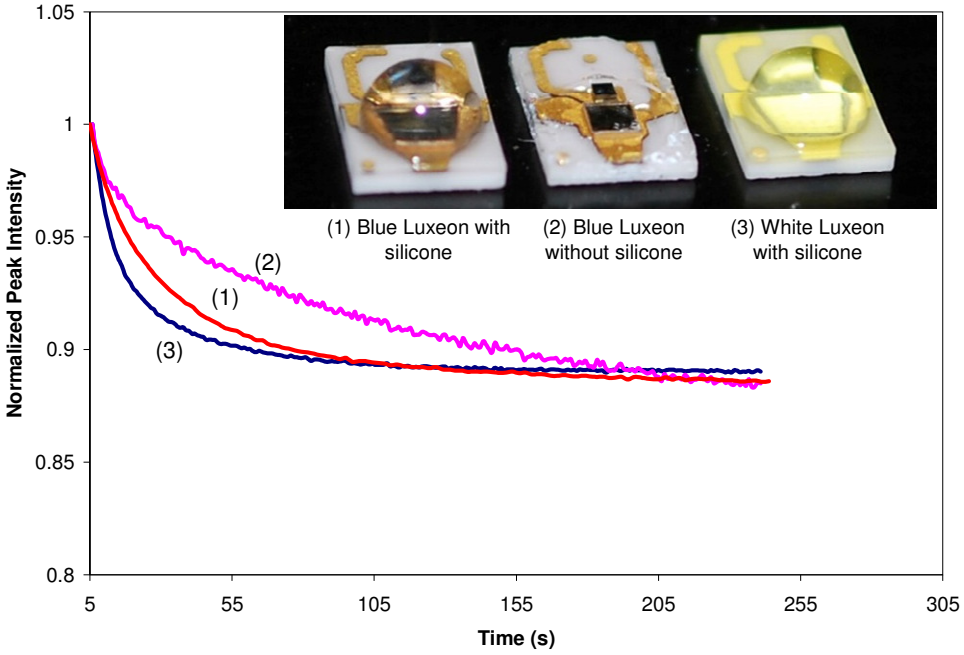

Figure 100. LED stability as a function of operating time at ~350mA for the blue and white Luxeon Rebel LED devices pictured in inset. Inset: photos of blue & white Luxeon LEDs

3. Program Budget & Cost-Sharing

Table 8 summarizes the 3-year program budget, expenditures, and cost-sharing by category. The originally planned ALD equipment purchase was reconsidered in BP1 and funds diverted to use GIT ALD system instead, following recommendation and approval by the program manager. Some of these costs were used for the ALD custom fluidized bed design and construction, the details of which are attached in the appendix. In addition, about $11k of equipment funds in BP1 were used to setup a dedicated fume hood & glove box for nanophosphor synthesis with automated temperature controllers and optical monitoring system. Finally, a Coulter DelsaNano demo system was purchased in BP2 for $39,212 to use for particle size measurements down to 0.6 nm

Table 8. Summary of 3-year program budget & cost-sharing

CATEGORY	BP1 (DOE)	BP1 (PTC)	BP2 (DOE)	BP2 (PTC)	BP3 (DOE)	BP3 (PTC)	Total Costs	Project Costs %
a. Personnel	$246,954	$45,500	$260,960		$296,990		**$850,404**	**45.6%**
b. Fringe Benefits	$12,794	$35,969	$35,008	$30,232		$59,398	**$173,401**	**9.1%**
c. Travel	$6,312		$5,588		$5,300		**$17,200**	**0.9%**
d. Equipment	$10,824		$2,547	$39,212			**$52,583**	**9.9%**
e. Supplies	$40,183	$27,105	$39,789	$7,500	$23,084	$10,714	**$148,375**	**7.9%**
f. Sub-recipient (GIT)	$40,000	$30,934	$33,400	$33,434		$34,684	**$172,452**	**5.6%**
g. Indirect Charges	$97,018		$112,468		$135,427		**$344,913**	**20.8%**
Total Project Costs	**$454,085**	**$139,508**	**$489,759**	**$110,378**	**$460,802**	**$104,796**	**$1,759,328**	**100.0%**

4. Summary and Conclusion

As described in previous sections (and the highlights) in this extensive study, we have developed high-index, high efficiency bulk luminescent materials and novel nano-sized phosphors for improved solid-state white LED lamps. These advances can potentially contribute to reducing the loss in luminous efficiencies due to scattering, re-absorption, and thermal quenching. The bulk and nanostructured luminescent materials investigated are index matched to GaN and have broad and size-tunable absorption bands, size and impurity tuned emission bands, size-driven elimination of scattering effects, and a separation between absorption and emission bands. These innovations were accomplished through the use of novel synthesis techniques suitable for high volume production for LED lamp applications. The program produced a full-color set of high quantum yield phosphors with high chemical stability.

In the bulk phosphor study, the ZnSeS:Cu,Ag phosphor was optimized to achieve >91% efficiency using erbium (Er) and other activators as sensitizers. Detailed analysis of temperature quenching effects on a large number of ZnSeS:Cu,Ag,X and strontium- and calcium-thiogallate phosphors lead to a breakthrough in the understanding of the "anti-quenching" behavior and a physical bandgap model was developed of this phenomena. In a follow up to this study, optimized phosphor blends for high efficiency and color performance were developed and demonstrated a 2-component phosphor system with good white chromaticity, color temperature, and high color rendering. By extending the protocols of quantum dot synthesis, "large" nanocrystals, greater than 20 nm in diameter were synthesized and exhibited bulk-like behavior and blue light absorption. The optimization of ZnSe:Mn nanophosphors achieved ~85% QE The limitations of core-shell nanocrystal systems were addressed by investigating alternative delta-doped structures. To address the manufacturability of these systems, a one-pot manufacturing protocol was developed for ZnSe:Mn nanophosphors.

To enhance the stability of these material systems, the encapsulation of ZnSeS particle phosphors and ZnSeS screens with Al_2O_3 and TiO_2 using ALD was shown to improve the stability by >8X and also increased the luminescence efficiency due to improved surface passivation and optical coupling. A large-volume fluidized bed ALD system was designed that can be adapted to a commercial ALD or vapor deposition system.

Throughout the program, optical simulations were developed to evaluate and optimize various phosphor mixtures and device configurations. For example, to define the scattering properties of nanophosphors in an LED device or in a stand-off screen geometry. Also this work significantly promoted and assisted in the implementation of realistic phosphor material models into commercial modeling programs.

PhosphorTech is very proud that in 2009, this work was recognized by the U.S. Department of Energy by an award for "significant achievements in solid-state lighting". Based on the above developments, PhosphorTech currently offers a broad range of conventional

particle phosphor and nanophosphors. The following external recognitions resulted from this work.

Presentations

1. **Invited**: B. K. Wagner, Z. Kang, H. Menkara and C. J. Summers, "Quantum Dots, their Properties, Synthesis and Applications," 14th International Diffuse Reflectance Conference, Wilson College, Chambersburg, PA., Aug. 4, 2008
2. R. A. Gilstrap Jr., H. M. Menkara, B. K. Wagner, and C. J. Summers, "Doped Quantum Dots for Solid-State Lighting," Proceedings of the 2008 Conference on Electroluminescence and the Science and Technology of Phosphors and Emissive Materials. Rome, Italy, 7-11th September, 2008
3. H. Menkara, T. R. Morris II, R. A. Gilstrap Jr, B. K. Wagner, and C. J. Summers, "Sulfoselenide Phosphors And Nanophosphors For Solid-State Lighting", Proceedings of the 33rd International Conference & Exposition on Advanced Ceramics & Composites, Daytona, January 2009.
4. Christopher J. Summers, Hisham M. Menkara, Richard A. Gilstrap Jr., Mazen Minkara, and Thomas Morris, "Nanocrystalline Phosphors for Lighting and Detection," Pacific Rim International Materials Conference: PRICM 7, Nanomaterials: Symposium D, Cairns, Australia, 2-6th August (2010)
5. C. J. Summers, T. R. Morris, M. Minkara, A. Thamban, R. Gilstrap, B. Wagner, and H. Menkara, "Broadband Nanocrystalline Phosphors for UV to White LED Applications", 2rd NanoToday Conference, 9-12 December 2011, Hawaii

Publications

1. Christopher J. Summers, Hisham M. Menkara, Richard A. Gilstrap Jr., Mazen Minkara, and Thomas Morris, "Nanocrystalline Phosphors for Lighting and Detection," Proceedings of Pacific Rim International Materials Conference: PRICM 7, Nanomaterials: Symposium D, Cairns, Australia, 2-6th August (2010)

2. **Invited**: H. Menkara, R. A. Gilstrap Jr., T. Morris, M. Minkara, B. K. Wagner, and C. J. Summers, "Development of nanophosphors for light emitting diodes," Special Edition on Solid State Lighting; Optics Express, 19, A972 (2011)

---

5. References

[i] Zeng, R.; Rutherford, M.; Xie, R.; Zou, B.; Peng, X. *Chem. Mater.* 2010, *22(6),* 2107-2113.

[ii] Radovanovic, P. V.; Gamelin, D. R. *J. Am. Chem. Soc.* **2001**, *123*, 12207-12214.

[iii] Pradhan, N.; Goorskey, D.; Thessing, J.; Peng, X. G. *J. Am. Chem. Soc.* **2005**, *127(50)*, 17586–17587.

[iv] Pradhan, N.; Battaglia, D. M.; Liu, Y. C.; Peng, X. G. *Nano Lett.* **2007**, *7*, 312–317.

APPENDIX: Fluidized Bed - Atomic Layer Deposition System for Coating Particles Phosphors

Fluidized Bed - Atomic Layer Deposition

System for coating Particles Phosphors

Jean-Sebastien Lemaire
Florian Zambito
Christopher J. Summers

Partial Fulfillment of Department of Energy Contract

Monday, August 27, 2012

Table of content

1. Introduction

The objective is to freely coat particles so that throughout the process they are completely free and undamaged and homogeneously encapsulated. In a Fluidized Bed – Atomic Layer Deposition (FB-ALD) system, and for large charges (quantities) of particles (between 10g to 400g), a combination of various interparticle forces such as London-Van der Waals, electrostatic interactions may occur. These forces promote the formation of particle aggregation affecting the fluidization process and become very important for small nano-sized particles.

2. Operation of the ALD process

Atomic layer deposition (ALD) is a thin film deposition technique that is based on the sequential use of a gas phase chemical process. The majority of ALD reactions use two chemicals, typically called precursors. These precursors react with a surface one-at-a-time in a sequential manner. By exposing the precursors to the growth surface repeatedly, a thin film is deposited.

As a first step in the development of the Fluidized Bed –Atomic Layer Deposition (FB-ALD) system, we have developed a comprehensive program to aid in the design and prediction of the conditions for ALD coating a variety of structures: from planar substrates to particles. This is necessary because of the need to account for the very large change in surface area when working with phosphor particles of different diameter and to understand their interaction with the gas stream. The system is designed for a nominal charge of 400g and, for example, because the surface area increases as r^2 the amount of precursor needed to coat phosphor charges with particle diameters of 10 μm to 50 μm will increase by a factor of 25. This change in "loading" will significantly impact precursor pulse times and also the purge requirements. The program can model up to three precursors (for example, TMA, $TiCl_4$ and H_2O – for multilayer coatings), and for each precursor the pulse time, the nitrogen purge time following each precursor pulse, and the pressures for each. Up to now these setting were obtained from many experiments, and in fact have been used to calibrate the model to obtain a reliable baseline.

To operate the ALD machine parameters for coating program the user enters the different characteristics for each sample (precursor 1, precursor 2, identification of the sample, density of the sample, particle diameter, mass per sample, thickness of coating expected) and the program automatically calculates the necessary pulse and purge times, length of cycle, and the expected total time. This is achieved by first, computing the precursor conditions needed to coat one particle and then, extending it to the entire sample. The whole procedure can then be repeated for a range of precursor flow conditions. By this means the required precursor volume is calculated and then from the pressure and velocity of the gases the exposure time for the precursors. Many parameters strongly affect the pulse and purge time results. For instance, the flow rate of the precursor and the nitrogen gases, the film growth, the thickness of the film and the length of the tube covered by gases. Also other parameters such as; density of sample, particle diameter, mass per sample; affect the total process time and therefore both thermodynamic and fluid mechanic reactions, although very difficult to anticipate, must be considered. For example, we considered a security factor and assumed that only ten percent of the precursor gases are absorbed onto the particles. Indeed, it is necessary to ensure that there are enough precursors during each cycle in order to completely encapsulate each particle. Also, this program allows us to adapt the computation to samples having different geometries from planar to free particles, to particles screened onto a flat surface. To obtain the final result, we consider both the total surface area of the sample and also the volume of the precursors' needed for the coating so as to tune the ALD system for optimum coating results with most efficient use of the precursors.

3. Design

The main issue in the development of a FB-ALD system is to fully incorporate the principle of the fluidizing process such that the motion imparted to the particles agitates them such that they are continually exposed to the precursor gasses and therefore become completely encapsulated by the coating layer. An additional consideration is to establish coating conditions that prevent particle agglomeration, either through direct physical contact and/or agglomeration mediated by the presence of the coating.

Approaches to implementing the Fluidized Bed ALD process have been to hold the charge in a vertical column so that the precursors and purge gasses flow through the charge, in which case, ideally the buoyancy effect can be used to separate the particles due to the vertical gas flow – while they are also being coated. (Note: that in the ALD technique the precursors are swept through the system by a background flow of nitrogen which is increased during the purge cycle so that the total gas flow remains constant).

However, for large phosphor charges this approach needs to be augmented by a highly controlled vibration system to enhance fluidization, or by a lifting rotating helix system enclosed within the reactor column. This is necessary to counteract the fact that the lower particles can become highly compacted for large phosphor charges. As show in *Figure 1a and Figure 1b*, possible horizontal geometries are to hold the phosphor charge in a porous rotating tube and/or horizontal mixer (like the motion of a concrete mixer). The concrete mixer design is to insert the charge in the rotating tank to agitate the particles all the chemical coating process long. While the motion, the gas would go through the tank from one side to another and encapsulate the particles. The second suggested design is based on the sieve process. Charge would be placed on the sample plate (orange part) and be agitated thanks to two imbalanced motors on each side of the plate. Gases would come from the top and leave the chamber by the side. For both geometries one needs to model not only the effect of gas flow on deposition – but also simultaneously its interaction with the particles. Consequently, both thermodynamic and fluid dynamical properties must be considered. In the vertical geometry the mechanical force available to elevate the particles must be accurately computed, and likewise for the horizontal geometry so that the gas flow is not so strong that particles are blown out of the container. All of these solutions were evaluated and implemented within the next two months for a chosen system design.

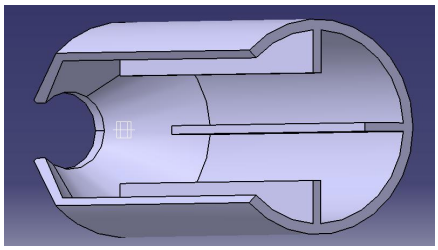

Figure 1a: *Concrete mixer design*

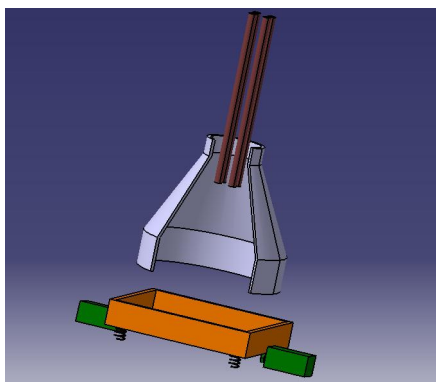

Figure 1b: *Sectional view of a vibratory design*

An illustration of the proposed setup to carry a large amount of particles (for 500g sample) is shown in the *Figure 2.* The ALD-Fluidized Bed distributor is made of a quartz to stainless steel *Kwik-Flange* double-ended glass adapter, 50mm diameter and 250mm height. The samples are contained in the bed by two stainless steel 20 µm porous filters placed on each edge of the tube.

Vacuum is controlled by variating the pump inlet diameter ball valve. The precursors gases are carried using a fluidizing gas obtained from high purity liquid nitrogen source. Gas flow rate is controlled and measured with an MKS 247-C mass flow controller.

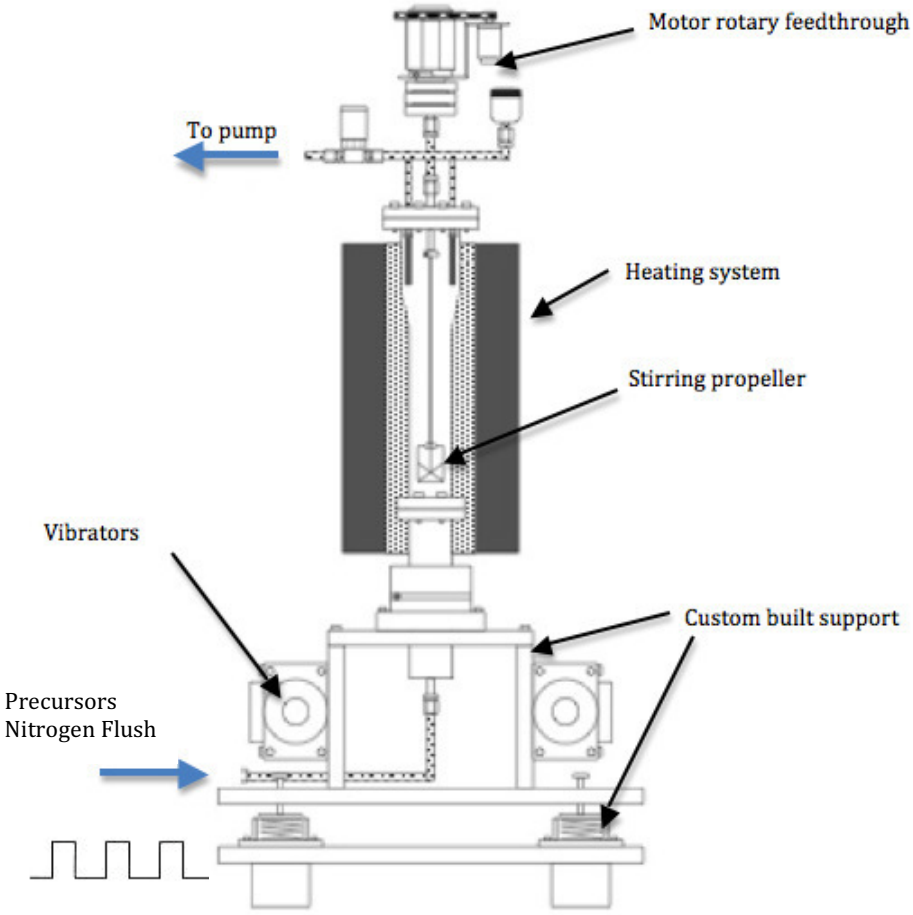

Figure 2: *Design of proposed FB-ALD*

The system will also be equipped with manometer gauges placed at each end of the fluidization bed so as to detect the onset of fluidization of the charge. By this means it is possible to detect when the particles are moving relatively independently of each other (floating) and so can be conformed coated without significant agglomerization of particles. By this means a wide range of conditions can be addressed.

Vibration is realized by the use of two vibrators from *Martin Engineering* and the vibration frequency is controlled with an ACS 140 adjustable speed electrical driver from *ABB Drive*. A custom flexible apparatus support made of four springs evenly distributed along two parallel plates is attached at the bottom of the Fluidized Bed in order to attached the vibrators. By this means, the entire bed is vibrated but mechanical stresses on any parts of the FB reactor are avoided.

A stirring system will also be incorporated. The stirring is mounted on a *Kwik-Flange* heights vacuum motor rotary stainless steel feedthrough from MDC. Teflon propellers are attached to this rod at various high to ensure the homogeneity of the particles mixture.

The entire system is surrounded by heat tapes and aluminum foil paper to maintain a constant temperature of 100°C ensuring the chemical reaction.

In this system the precursor gasses will be handled as in our conventional system and then flow into the FB chamber. The ALD chemical process is managed by a Lab View

program that allow setting the necessary precursor pulse time and nitrogen purge time. Moreover, the film thickness could be adjusting allowing a large range of experiments and results. At the end, the system is composed of three precursors; Water, Titanium tetrachloride and Trimethylaluminum; to generate aluminum oxide (Al_2O_3) or titanium dioxide (TiO_2) layers.

4. System assessment of issues

The objectives of designing an atomic layer deposition fluidized bed (ALD-FB) system that will allow the coating of phosphor charges between 50-400g with particle sizes between 10-50 microns. A combination of various interparticle forces such as London-Van der Waals, electrostatic interactions may occur. These forces promote the formation of particles agglomeration and aggregations affecting the fluidization process. To cover, these physical issues, this range of particle sizes, phosphor charges a fluidized bed reactor combining the three fluidizations technologies will be built. In this system it will then be possible to achieve fluidization by:

- A gas flow controlling and adjusting the gas pressure flowing through the system
- Using an external vibration table to agitate the charge
- Rotating a vane inside the bed/or magnetic agitation

a. Gas flow

i. Overview

In the fluidization, a gas flows through a packed bed (bed of solid particles) to behave it like a liquid. When a fluid (liquid or gas) passes through a packed bed at a minimum necessary velocity (minimum fluidization velocity), the packed bed begins to expand and the particle-fluid mixture behaves as though it is a fluid. It exists three behavior states for a bed: fixed bed, smooth fluidization and bubbling fluidization. Theoretical synthesis was conducted to determinate the minimum fluidization velocity (V_{mf}), the maximum fluidization velocity called settling velocity ($V_{settling}$) and the necessary conditions to have a homogenous and smooth fluidized mixture.

ii. Theory

To achieve the fluidization, there are many conditions to ensure this phenomenon. This is a difficult process, and it is necessary to be precise. If one of the conditions is not respected, the phenomenon will not happen and the mixture will not be homogenous and by the way completely coated.
When a fluid (liquid or gas) is passed through a packed bed at a minimum necessary velocity (minimum fluidization

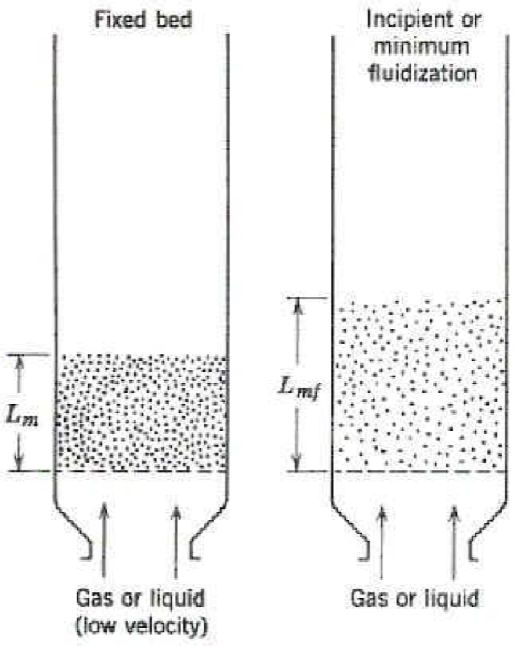

velocity), the packed bed begins to expand and the particle-fluid mixture behaves as though it is a fluid. Indeed, when the frictional force acting on the particles or pressure drop, of the flowing, gases through the bed equals or exceeds the weight of the bed, the powder particles become suspended (*Figure 3*). However, depending of the fluid flow rate, there are three main states. If the flow rate is smaller than the minimum fluidization flow rate the bed is fixed: state called fixed bed. It the flow rate is included between the minimum fluidization flow rate and the maximum fluidization flow rate the bed is expanded, and it might have presence of bubbles inside the bed: state called fluidized bed, and for a fluidized bed without bubbles: smooth fluidization. If the flow rate is bigger than the maximum fluidization flow rate, there are many bubbles inside the bed and the particles carry out with the fluid at the exit, stated called bubbling fluidization (*Figure 4*).

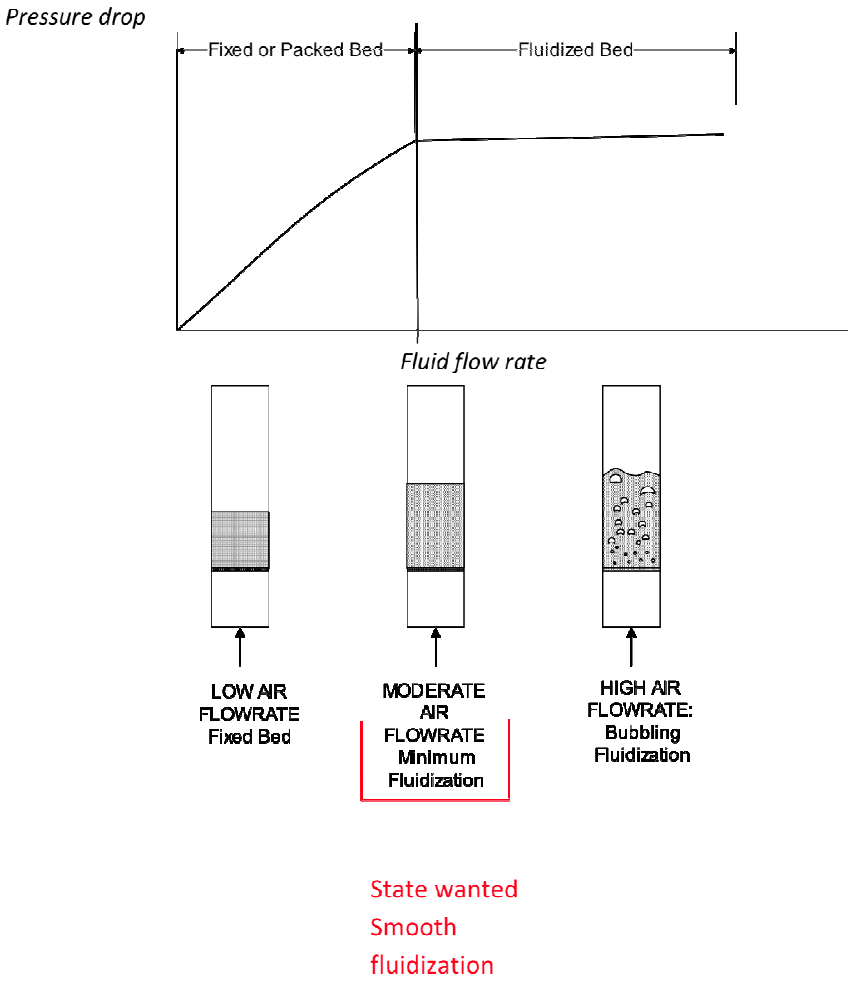

Figure 4: *Different states of fluidization bind to the level of gas flow rate*

In our case, the best state we would like to obtain is the smooth fluidization corresponding to an expanded bed without bubbles such as the middle drawing on Figure 4.

iii. Calculation

There are many parameters controlling the impacts on the fluidization coating, which have been extensively modeled by Florian Zambito and Jean-Sebastien LEMAIRE, and there are summarized below:

Re: Reynolds number*
f_p: Friction factor between particles (coefficient of friction between particles)
Δp: Pressure drop (*Pa*)
L: Length of the bed (*m*)
D_p: Equivalent spherical diameter of the particles (*m*)

$$D_p = 6.\frac{Volume\ of\ the\ particle}{Surface\ area\ of\ the\ particle}$$

ρ_f: Density of the fluid (kg/m^3)
ρ_p: Density of particles (kg/m^3)
ε: Void fraction of the bed

$$\varepsilon = \frac{space\ unfilled\ by\ packing}{Total\ volume\ in\ column}$$

μ: Dynamic viscosity of the fluid (*Pa.s*)
A: Cross-sectional area of the bed (m^2)
Q: Flow rate of the fluid (m^3/s)
V_s: Superficial velocity (*m/s*) $V_s = Q/A$
G: Acceleration due to gravity (m/s^2) $g = 9.81\ m/s^2$
M: Mass of the charge (kg)
V_{mf}: Minimal fluidization velocity (*m/s*)
$V_{settling}$: Maximum fluidization velocity (*m/s*)
V_f: Fluidization velocity (*m/s*)

* Reynolds number can be defined for a number of different situations where a fluid is in relative motion to a surface (the definition of the Reynolds number is not to be confused with the Reynolds Equation or lubrication equation). These definitions generally include the fluid properties of density and viscosity, plus a velocity and a characteristic length or characteristic dimension.

For flow in a pipe or tube, the Reynolds number is generally defined as:

$$\mathrm{Re} = \frac{\rho V D_H}{\mu}$$

ρ: Density of the fluid through the pipe (kg/m^3)ε
V: Mean fluid velocity (*m/s*)
D_H: Hydraulic diameter of the pipe (*m*)
μ: Dynamic viscosity of the fluid (*Pa.s*)

For flow of fluid through a bed of approximately spherical particles of diameter D in contact, if the voidage (fraction of the bed not filled with particles) is ε and the superficial velocity V (i.e. the velocity through the bed as if the particles were not there - the actual velocity will be higher) then a Reynolds number can be defined as:

$$\mathrm{Re} = \frac{\rho V D}{\mu(1-\varepsilon)}$$

Laminar conditions apply up to Re = 10, fully turbulent from 2000.

Hypothesis: Particle Diameter smaller than 0.1 mm

The flow condition: The Reynolds Number is smaller than 10 (Re ≤ 10), because on one hand the fluid flow rate available is between 0 and 1000 sccm and on the other hand, the particles diameter size is below 0.1mm.

We use the Ergun Equation $f_p = \frac{150}{Re_p} + 1.75$ (1)

The friction factor (f_p) of the packed bed and the Reynolds number (Re) are defined as follows

$$f_p = \frac{\Delta p}{L} \cdot \frac{D_p}{\rho_f . V_s^2} \cdot \left(\frac{\varepsilon^3}{1-\varepsilon}\right) \text{ (2)} \qquad Re_p = \frac{D_p . V_s . \rho}{(1-\varepsilon)\mu} \text{ (3)}$$

Because the Reynolds number of our system is smaller than 10, we can use the Ergun equation (1) to the Kozeny-Carman equation (4) as following:

$$f_p = \frac{150}{Re_p} \quad , Re \leq 10 \text{ (4)}$$

In order to have Vs, we need to have a notion of Δp in the equation (2).

Upward Force on the bed: $F_{gases/bed} = \Delta p . A$ (5)

Volume of particles: V = (1-ε).A.L *(6)*

The net weight on the particles:

$$P_{particles} = m . g = \rho . V . g$$
$$P_{particles} = (\rho_p - \rho_f)(1-\varepsilon) . A . L . g \text{ (7)}$$

At the balance

$$\sum \overrightarrow{Forces} = \vec{0}$$

$$\overrightarrow{F_{gases}/_{bed}} - \overrightarrow{P_{particles}} = \vec{0}$$

$$\overrightarrow{F_{gases}/_{bed}} = \overrightarrow{P_{particles}} \quad (8)$$

We deduce:

$$\Delta p = (1-\varepsilon)(\rho_p - \rho_f).L.g \quad (9)$$

Combining (2) and *(3)* to the Kozeny-Carman Equation *(4)*, we obtain **the minimal fluidization velocity:**

$$V_{mf} = \frac{(\rho_p - \rho_f).g.D_p^2}{150.\mu} . \frac{\varepsilon^3}{1-\varepsilon} \quad (10)$$

To prevent particles from carrying out with the fluid at the exit we impose one boundary condition: $V_f < V_{settling}$

According to Stokes law

$$V_{settling} = \frac{(\rho_p - \rho_f).g.D_p^2}{18.\mu}$$

$$V_f < \frac{(\rho_p - \rho_f).g.D_p^2}{18.\mu} \quad (11)$$

For small particles

$$\frac{V_{settling}}{V_f} = \frac{25}{3} . \frac{1-\varepsilon}{\varepsilon^3} \quad (12)$$

According to McCabe Smith and Harriott (2001), they suggested ε lies in the range of 0.40-0.45 for nearly spherical particles and this yield (12) lies in the range 78-50.
They suggest equally that it is common to operate fluidized beds at velocities as high as 30 V_f.

Using theories developed it is possible to determine the minimum fluidization velocity (V_{mf}) and the maximum fluidization velocity called settling velocity ($V_{settling}$). It is also possible to determine the conditions that product a homogenous mixture. In our fluid mechanism case, the Ergun equation is the starting point because it contains the value that we will determine the minimum fluidization velocity (V_{mf}).

iv. Case Study

This study is based on the current equipment (ALD + existing fluidized bed): length of the column 150 mm; diameter 50 mm.
The optimum condition to have a homogenous mixture is: $0.40 < \varepsilon_m < 0.45$ ε_m is the void fraction when the fluidization begins. Usually we fill the bed in atmosphere and so we have some air between each particle and by the way we obtained a specific ε. However,

to simplify our case, we consider that we filled the column in vacuum and so we suppose that ε_m is the same that the ε of the packed bed.

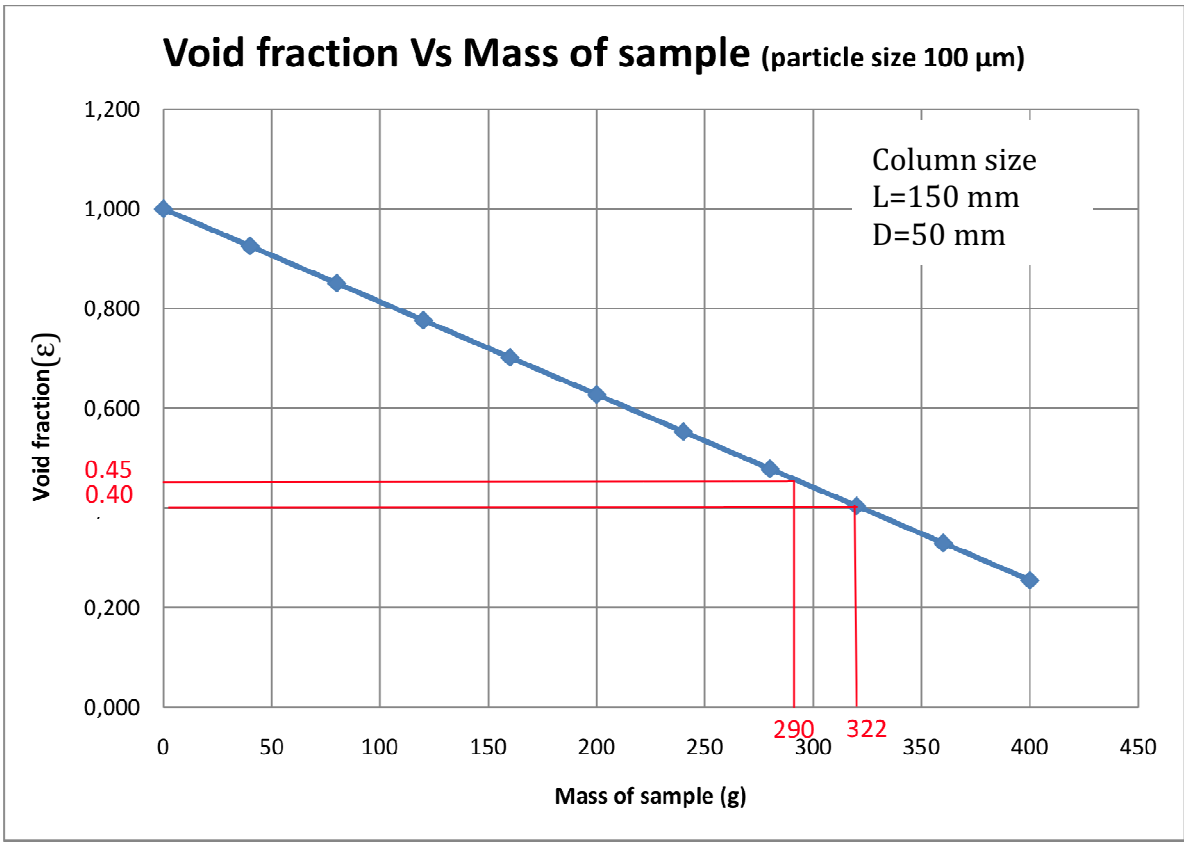

Figure 5: *Evolution of the void fraction (ε) in function of the mass of the sample (particle size 100 µm)*

According to many theoreticians and studies, the experimental condition to obtain the best mixture of the particles is to have $0.40 < \varepsilon < 0.45$. In our case, that condition means, with the below equations, that with the current equipment, we can fill the column (150 mm of length and 50 mm of diameter) from 290 g to 322 g (*figure 5*). L is the length of the column; h_{bed} is the length of the charge load in the column; S is the surface area of the column; D the diameter of the column; m the mass of the chare and ρ the density of the particles.

$$\varepsilon = \frac{(L - h_{bed})S}{L \times S} \qquad S = \frac{\Pi \times D^2}{4} \qquad h_{bed} = \frac{m}{\rho_{particles} \times S}$$

If we want to coat a different quantity of particles we have to change the dimension of the column. Generally, for each range of the quantity of particles, there is a specific dimension of the column. This is not practical because we want to coat on a bigger range of quantity (from 10 g till 300g).

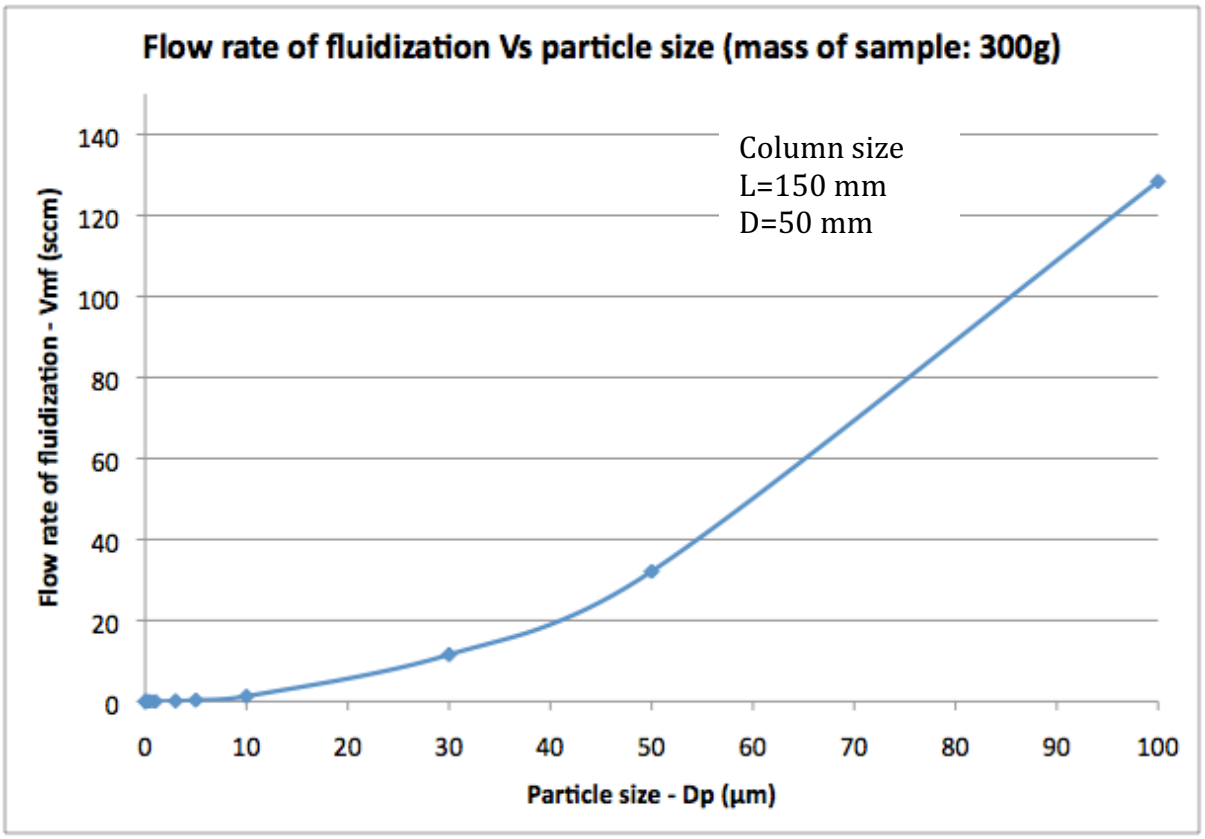

Figure 6: *Minimum fluidization velocity (V_{mf}) in function of particle diameter (D_p)*

For very small particles (from nanoscale), we obtain very low flow rates that we are not able to tune on the current device.
Flow rate of fluidization V_{mf} is calculated thanks to the equation:

$$V_{mf} = \frac{(\rho_p - \rho_f) g \times D_p^2}{150\mu} \times \frac{\varepsilon^3}{1-\varepsilon}$$

If we take the example presented on *figure 6*, to coat 300 g (equal to the average value between 290 g and 322 g) of particles, which have a size about 30 nm, the minimum fluidization flow rate is 1.156×10^{-5} sccm.

In the document entitled *"Powder coating in a high pressure fluidized bed process"* (by U.Teipel and H.Kröber), they use for very small particle (<100 µm) a fluidized bed with high pressure (20 bars – 40 bars) more commonly called RESS (Rapid Expansion of Supercritical Solution). Indeed, in case of very small size of particles, the main issue is their agglomeration. The consequence of this phenomenon will lead to a non-homogeneous mixture and coating of the particles. With the current equipment we are not able to have high pressure inside the system.

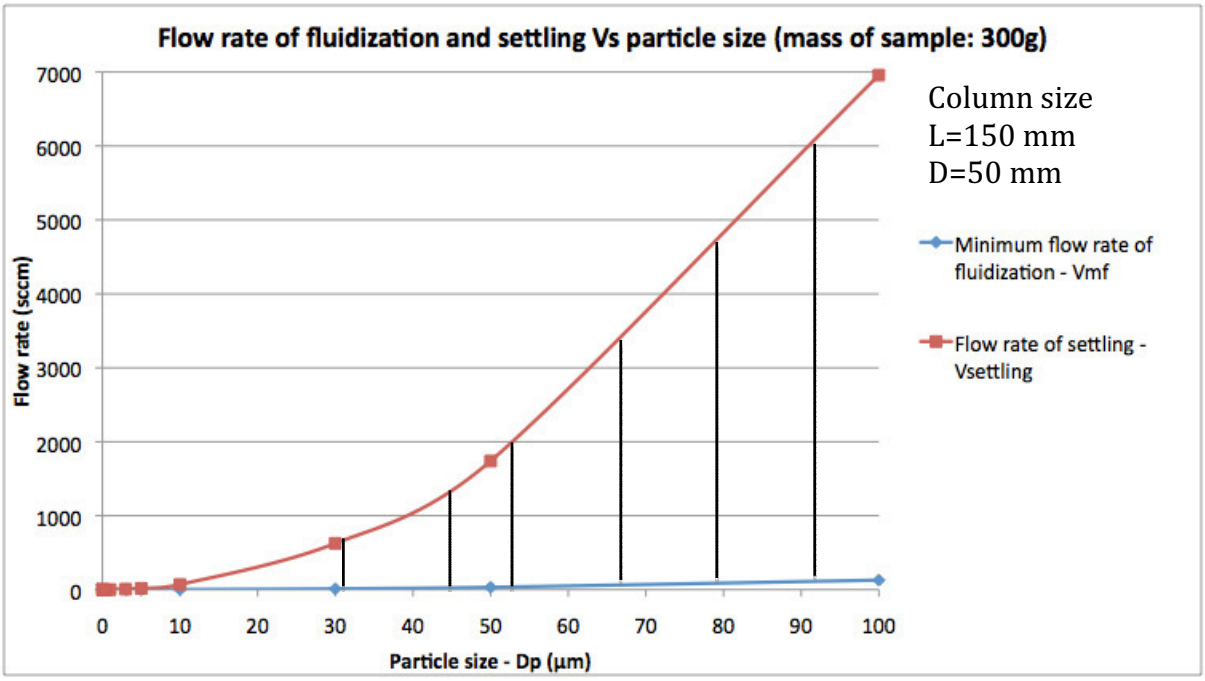

Figure 7: *Minimum fluidization velocity (V_{mf}) and settling velocity in function of the particles diameter (D_p)*

Figure 7 represents the minimum fluidization flow rate and the maximum fluidization flow rate (settling flow rate) in function of the particle size. The hatched part on this graph is the range of the velocity for each particle size that we can use to coat our sample with de fluidization phenomenon.

Flow rate of fluidization V_{mf} is calculated thanks to the equation:

$$V_{mf} = \frac{(\rho_p - \rho_f)g \times D_p^2}{150\mu} \times \frac{\varepsilon^3}{1-\varepsilon}$$

Flow rate of settling $V_{settling}$ is calculated thanks to the equation:

$$V_{mf} = \frac{(\rho_p - \rho_f)g \times D_p^2}{18\mu}$$

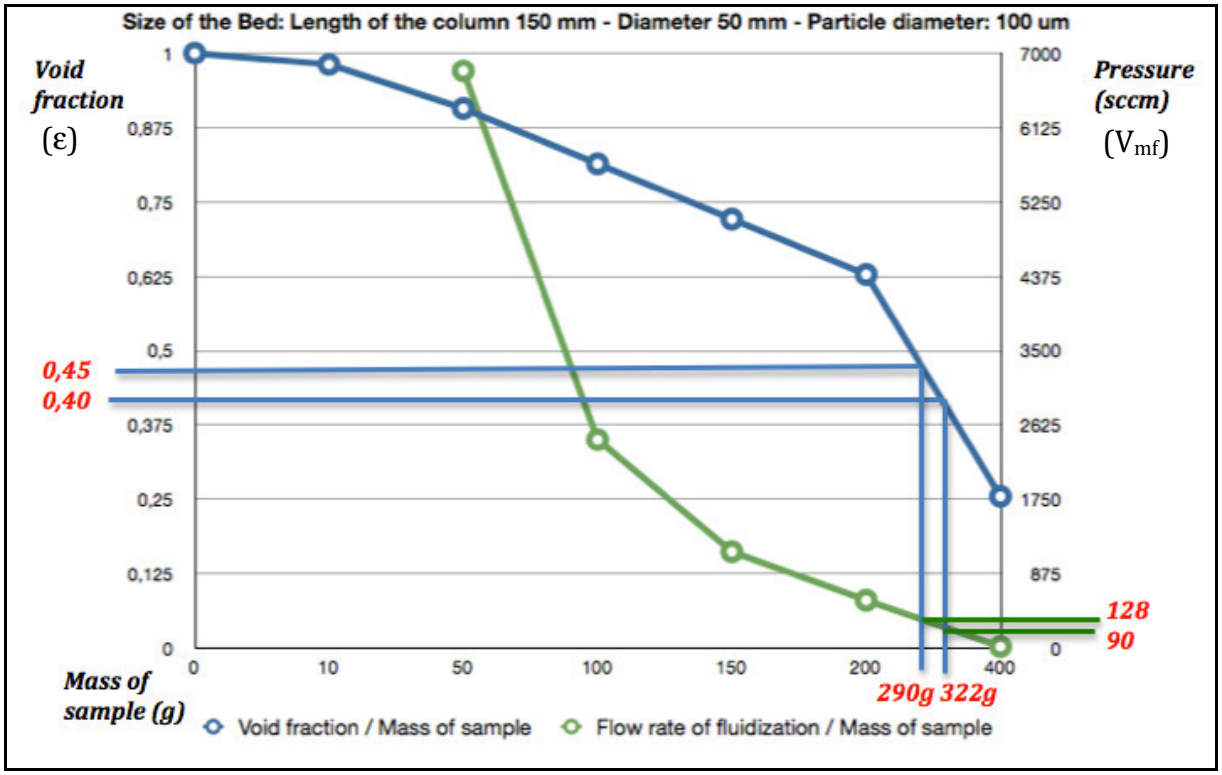

Figure 8: *Study case of a parameter design of the bed (void fraction ε) versus the mass of the sample to obtain the flow rate of fluidization (V_{mf})*

Figure 8 is a computation summary to coat a certain charge of particles in a specific designed FB column. Indeed, the choice of a void fraction value in a range of 0.40 to 0.45 leads to a charge in a range of 290 to 322g. The flow of gases will have to be between 90-128 sccm to achieve the smooth fluidization.

It is important to understand that this technique tends to its own limitations for several reasons:

- First, if we always want to respect the void fraction parameter we have to have several column sizes in accordance with the quantity of sample we want to coat. *Figure 8* is a theoretical analysis with a specific size of the column (150mmx50mm) that would allow a smooth fluidization for a charge in a range from 290g to 322g. If we want to coat a charge of 500g, a void fraction close to 0.45 is needed with a column having the dimensions: 250mmx50mm instead of 150mmx50mm for the previous example.

- Second, if we use the following dimension (150mmx50mm) for the column, we are limited by the quantity of sample. The maximum mass of sample allowed is 483g that lead to the fact we could not reach the 500g objectives.

- Third, if we do not use the calculated charge for a specific column size, this will have an impact on the flow rate of fluidization. Indeed, the more you decrease the quantity of the sample, the more the void fraction value increase also and has the flow is proportional to the void fraction, the higher the flow rate of fluidization will be. However, we have to be careful because the actual system can only provide a 1000 sccm flow rate.

Which is why it is necessary to employ the use of additional mechanical motion systems such as vibrators and stirring as explained below.

v. Conclusion

The ideal regime of fluidization is "the smooth fluidization" and in principle allows perfect mixing and coating. Unfortunately, to obtain this regime, exact conditions (such as tight control over ε and V_f, complete vacuum, homogenous temperature and pressure) are required, which are difficult to realize particularly for very small particles. For micron and nano particles, fluidization is delicate due to the added cohesive forces between them and additional mechanical system is needed to minimize agglomeration.

b. External vibration

i. Overview

To achieve external vibration an electric imbalanced vibrator is attached to the structure of the Fluidized Bed Reactor. Moreover, the entire structure of the system has to be on a soft and flexible ground in order to maintain the motion (mechanism made of four springs specially design in accordance with the forces applied on the system). Theoretical designs were made to choose the right springs and the best matched vibrator.

ii. Theory

Before starting the calculations on the vibration behavior of the system and the type of vibrator to use, it is important to design the springs needed to support it.

The value we are looking for is the spring straightness (R) define by the equation:

$$R = \frac{Gd^4}{8nD^3}$$

R = spring straightness (N/mm)
G = characteristics of the material
d = wire diameter (mm)
n = number of useful turn
D = average diameter of the wire

However, in order to reach this point it is important to set initial parameters:

- Choose the material of the spring (G)
  - Steel: 81500 N/mm^2
  - Stainless Steel: 70000 N/mm^2
- Choose the spring spacing (w)
  - 6 ➔ lower limit (close wire that leads to thick spring)
  - 10 ➔ regular value for balanced and easy built spring
  - 16 ➔ higher limit (very thin spring wire)

In our case of study, we decide to work with the standard value (w=10)

- Choose the number of spring turn (n_i)
  - 1.5 for loose close edges
  - 3 for close edges

In our case of study, we decide to work with the loose close edges design (n_i=1.5)

- Choose the free length (L_0)

In our case of study, we choose a length of 50mm

First, we have to determine the initial force on the system. The only force that exists is the mass.

$$P = \sum M \times g$$

$$P = (M_{FB} + M_{Support} + M_{Vibrator}) \times g$$

Then, we can obtain the wire diameter (d), the external diameter (De), the average diameter (D) and the number of useful turn (n):

$$d = \sqrt{\frac{8Pw^3}{G(0,3w-1)}}$$

$$De = (w+1)d$$

$$D = w \times d$$

$$n = \frac{L_0 - (n_i \times d)}{0,3D - O,15d}$$

Finally, with all of these data we can obtain the spring straightness (R) and the total amount of turn (n_t) with the equations:

$$R = \frac{Gd^4}{8nD^3} \qquad \text{and} \qquad n_t = n+2$$

With the design of the springs that will be used to maintain the vibration of the system we will be able to design the vibrator needed to generate these vibrations. The amplitude (A) is calculated thanks to the equation:

$$A = \frac{R \times ar^2}{\sqrt{(1-r^2)^2}}$$

A = amplitude of the vibration (*mm*)
R = ratio of the mass of the system
a = imbalance of the vibrator (*mm*)
r = ratio of the rotational speed over the uncharged rotational speed
w = rotational speed (*rad/s*)
w_0 = uncharged rotational speed (*rad/s*)

The ratio of the mass of the system is calculated by the equation:

$$R = \frac{M_{Vibrator}}{M_{Vibrator} + M_{FB} + M_{Support}}$$

"r" is given by the equation:

$$r = \frac{w}{w_0}$$

$w = 2 \times \Pi \times f$ (f = frequency of the vibrator) and $w_0 = \sqrt{\frac{R}{P}}$

iii. Case Study

The theoretical study leads to the understanding of the vibration behavior of the FBR. *Figure 9* describes the amplitude required to free the particles in the column. The study of parameters such as the spring straightness, the initial forces on the system and the characteristics of the vibrator led to the motion behavior.

The amplitude of the system via the vibrator frequency is given by the equation:

$$A = \frac{R \times ar^2}{\sqrt{(1-r^2)^2}} \qquad r = \frac{w}{w_0} \qquad w = 2 \times \Pi \times f$$

One important part of this chart is the fact that for a certain frequency of the vibrator (f =3 Hz ⇔ 180 RPM) we achieve the resonance frequency of the system. At this specific frequency is bound the maximum vertical displacement of the FBR and directly the bed. If we keep on increasing the frequency of the vibrator above the resonance one (for instance f = 15 Hz ⇔ 900 RPM) it leads the system to a stable state in a lower amplitude motion.

The second result demonstrates that the more is the imbalance of the vibrator, the higher is the vibration amplitude.

According to the vertical amplitude vibration we would like to setup, we can clearly define and choose the vibrator to use for our process.

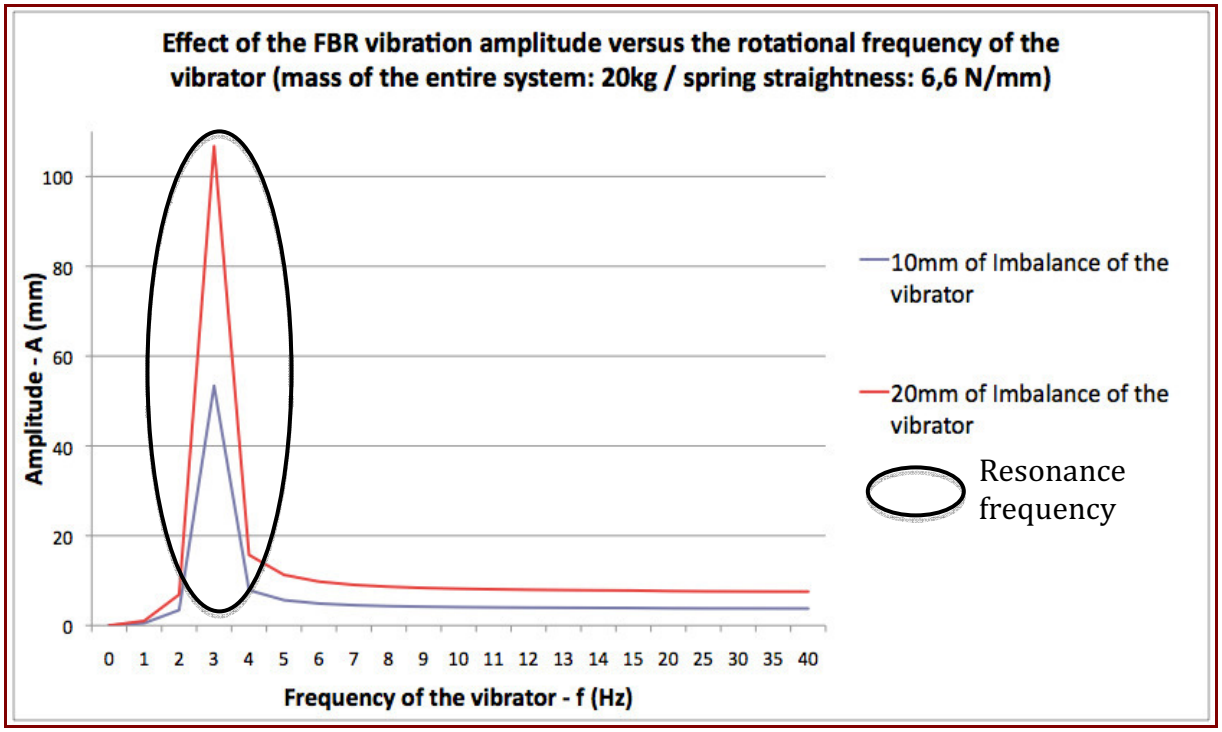

Figure 9: *Influence of the vibrator imbalance (a) and rotational frequency (f) on the vertical amplitude (A) motion of the Fluidized Bed Reactor for a specific design*

iv. Conclusion

Thanks to the theoretical study, we can pre-determine the behavior of the vibration motion of the system. Moreover, we know the type of vibrator to choose in accordance to the mass of the system, the spring design and straightness. Furthermore, to coat a maximum charge of particle (500g), it is suggested to get spring straightness within the range of 6 to 7 Nm, combined with two 10 mm imbalanced stainless steel vibrator (about 26 lbs heavy).

c. Stirring

i. Overview

As a second inner mechanical solution, a high-vacuum manipulator helps the particles to be in motion during the entire ALD process. This manipulator is connected to a shaft that extend down to the bottom of the particles bed. A well-designed propeller is welded at the end of the shaft and an electrical motor (with the necessary torque) is attached to the top of the shaft also to provide homogenous and smooth stirring to the bed of particles.

ii. Theory

The main purpose of this study part is to determine the design of the propeller and the minimum torque needed on the top of the system for the electric motor. Obviously, these results are bind to various initial parameters such as the diameter of the column bed (D), the density of the particles, the mass of the sample, the number of blade on the propeller, the height of the blade (H) and the rotational speed of the blade (rotational speed of the stirring in industry for particles motion: 0<N<0,75 Rd/s).

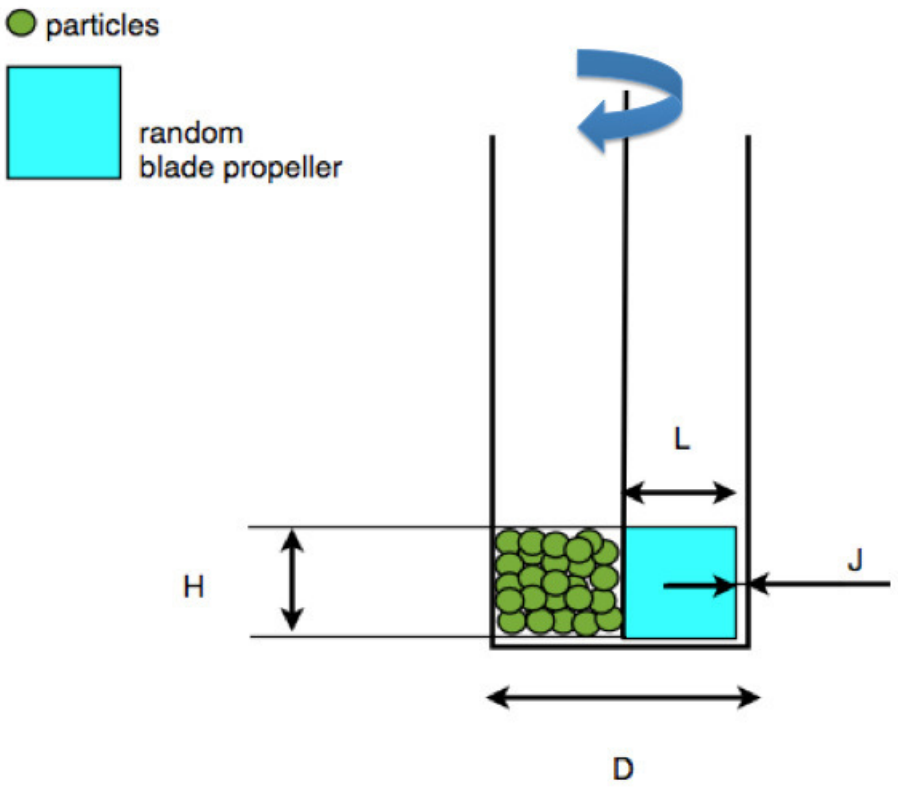

Figure 10: *Principle of the propeller mechanical mechanism*

Some parameters such as, the torque and the electrical power are needed to choose the electrical motor to provide the rotation of the manipulator. The electrical power is given by the equation:

$$P_{elec} = C \times 2\Pi \times N$$

P_{elec} = electrical power of the motor (*W*)
C = torque of the motor (*Nm*)
N = rotational speed of the motor manipulator (*rd/s*)

The torque of the motor is define by the equation:

$$C = F_{Friction} \times (\frac{L}{2})$$

with

$$F_{Friction} = \frac{\rho \times g \times n_b \times L \times h}{2} \quad \text{and} \quad L = \frac{D - (D \times \frac{J}{100})}{2} \quad \text{and} \quad h = \frac{M_{particles}}{S \times \rho}$$

and $$S = \frac{\Pi \times D^2}{4}$$

$F_{Friction}$ = Particle friction force (*N*)
L = length of the blade (*mm*)
ρ = density of the particles (kg/m^3)
g = earth gravity constant (*N/kg or* m/s^2)
n_b = number of blade per stage
h = length of the bed (*mm*) (=space occupied by the particles in the column)
D = inner diameter of the column (*mm*)
J = blade fit, margin of error
$M_{particles}$ = quantity of particles (*g*)
S = Cross-sectional surface of the column (m^2)

iii. Conclusion

Thanks to these preliminary data, we are able to determine the number of blade stage needed to cover the entire length of the sample bed, the length of the blade (L) in accordance to the blade fit (J – margin of error) to avoid unwished friction with the glass, the particles friction, the torque and finally the electrical power of the motor.

It is important to underline that the design of the blades, which determines the surface contact area with the particles, has a direct impact on the output electrical power of the motor information. *Figure 10* is just an example of a random squared design blade but a custom blade computation line is present in a program to tune the theoretical approach.

5. 3 Implementation of the design

Two mechanical solutions have been designed to create an automatic and controlled system to coat a large quantity of micro particles with the existing Atomic Layer Deposition machine.

a. Small charge coating design

Figure 11 is an isometric view of the first version of this high vacuum Fluidized Bed to coat a charge of sample in the range of 1 to 10 g.

The entire system is clamped with Kwik-Flange equipments from MDC Vacuum that are made of stainless steal material. It is composed of the following items:

- 2 NW25 Tee
- 12 NW25 O-rings
- 2 NW25 Manual Ball valves
- 2 NW25 to 50 adaptors
- 2 NW50 O-rings
- 1 NW50 Double ended glass tube
- 1 NW50 Stainless Steel mesh
- 1 NW25 Stainless Steel mesh
- 1 NW25 Rotary motion feedthrough
- 1 Sleeve coupling
- 1 rod (ground stock)
- 1 helix
- 3 Screws CHC M1.4

It is attached to the end of the existing ALD and the gas flow is directed with the use of the two ball valves and flexible stainless steel couplings.

In order to get the sample is motion during the coating process, two helixes are used to stir the charge at 0.5 Round/minutes speed with an output 90V DC power supply connected with the rotary motion feedthrough. This low velocity provides a smooth motion of the charge without disturbing the chemical attachment process. Moreover, to ensure the rotation of the helix, a minimum torque from the motor feedthrough has to be well determined. (Computation provided by the ALD-FB Excel program)

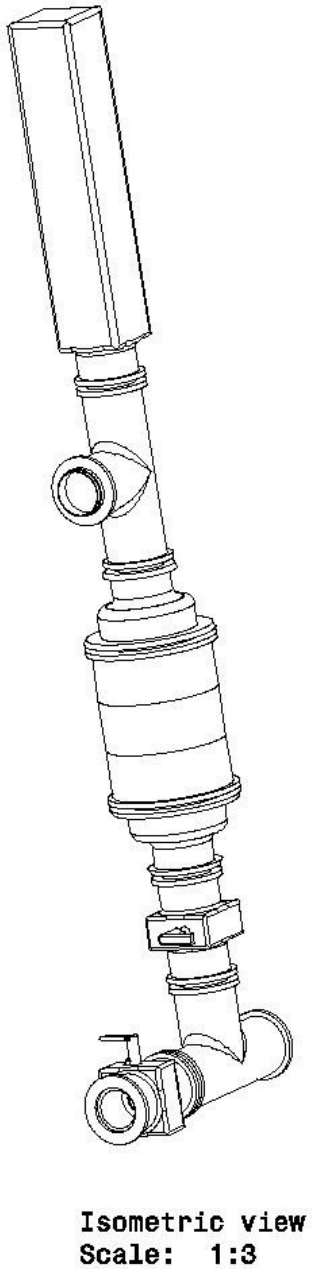

Figure 11: *Isometric view of the small charge FB design*

The complete system is 5 kg heavy and 24.6 inches (626.38 mm). The figures beside and below are showing dimensions of the stirring system.

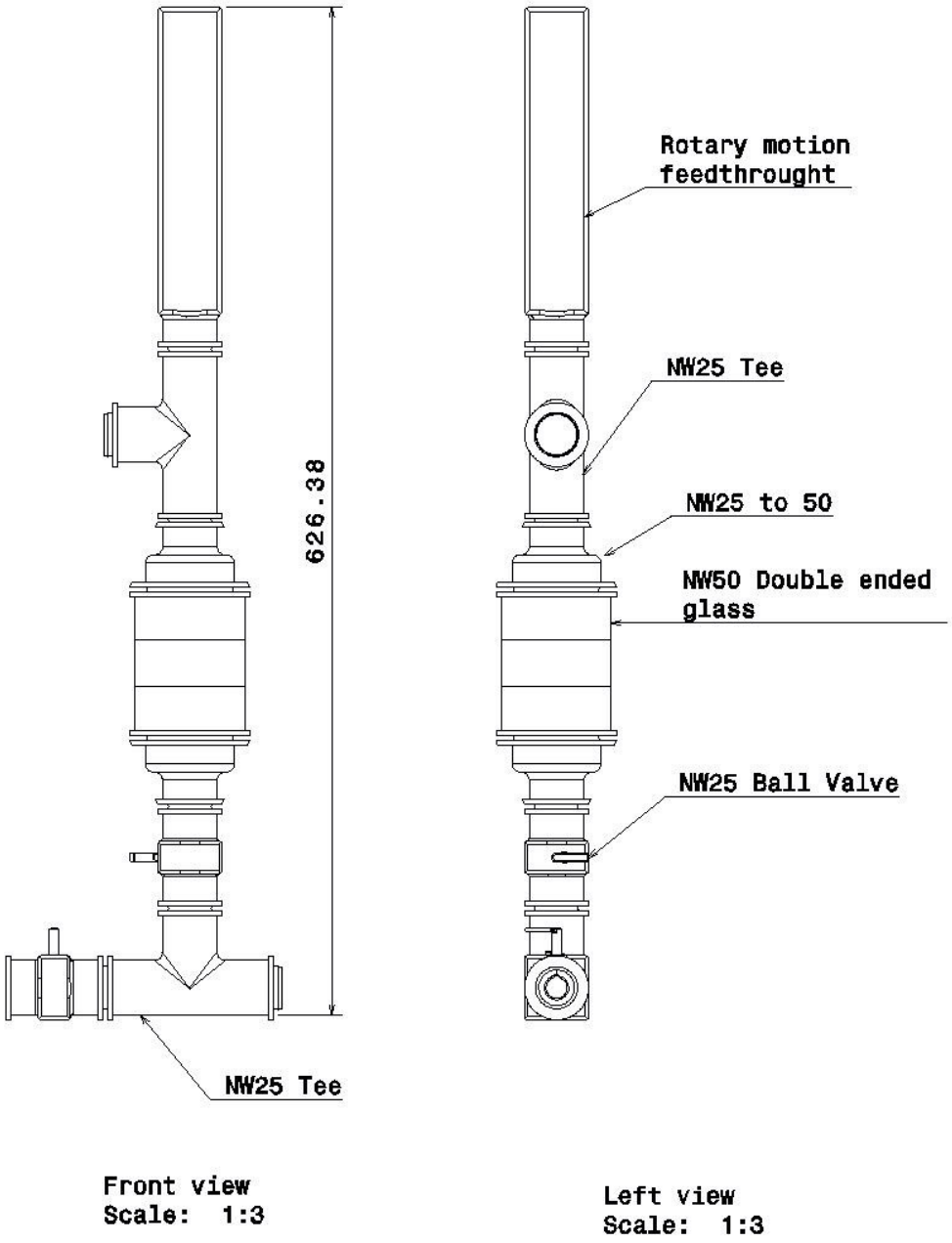

Figure 12: *Front and left view of the small charge Fluidized Bed design*

A new revision of the designed system will incorporate a NW25 four way cross instead of the top NW25 tee to clamp a pressure transducer (MKS) and get more control of the actual pressure during the coating process.

b. Large charge coating design

Figure 13 is an isometric view of the second version of this high vacuum Fluidized Bed designed to coat a charge of sample in the range of 10 to 400 g.

This upgrade was made from the same technology base as used for the previous system but with the addition of MDC vacuum equipment and the stirring system.

It is composed of the following items:

- 1 Steel plate to support the two vibrators
- 2 Del-Seal copper gasket (8")
- 2 NW25 to Del-Seal connectors
- 6 Del-Seal plate nuts
- 1 NW25 blank flange
- 2 NW25 Tee
- 12 NW25 O-rings
- 2 NW25 Manual Ball valves
- 2 NW25 to 50 adaptors
- 2 NW50 O-rings
- 1 NW50 Double-ended glass tube
- 1 NW50 Stainless Steel mesh
- 1 NW25 Stainless Steel mesh
- 1 NW25 Rotary Motion feedthrough
- 1 Sleeve coupling
- 1 rod (ground stock)
- 2 helixes
- 4 Screws CHC M1.4
- 6 12-Pt. Bolts/Washers (for NW25 Del-Seal)
- 3 plate nuts
- 4 Springs (4.4 N/mm)
- 1 Bottom steel plate
- 2 XHA-0.5T vibrators
- 8 Screws CHC M10 (to attach the vibrator to the top steel plate)

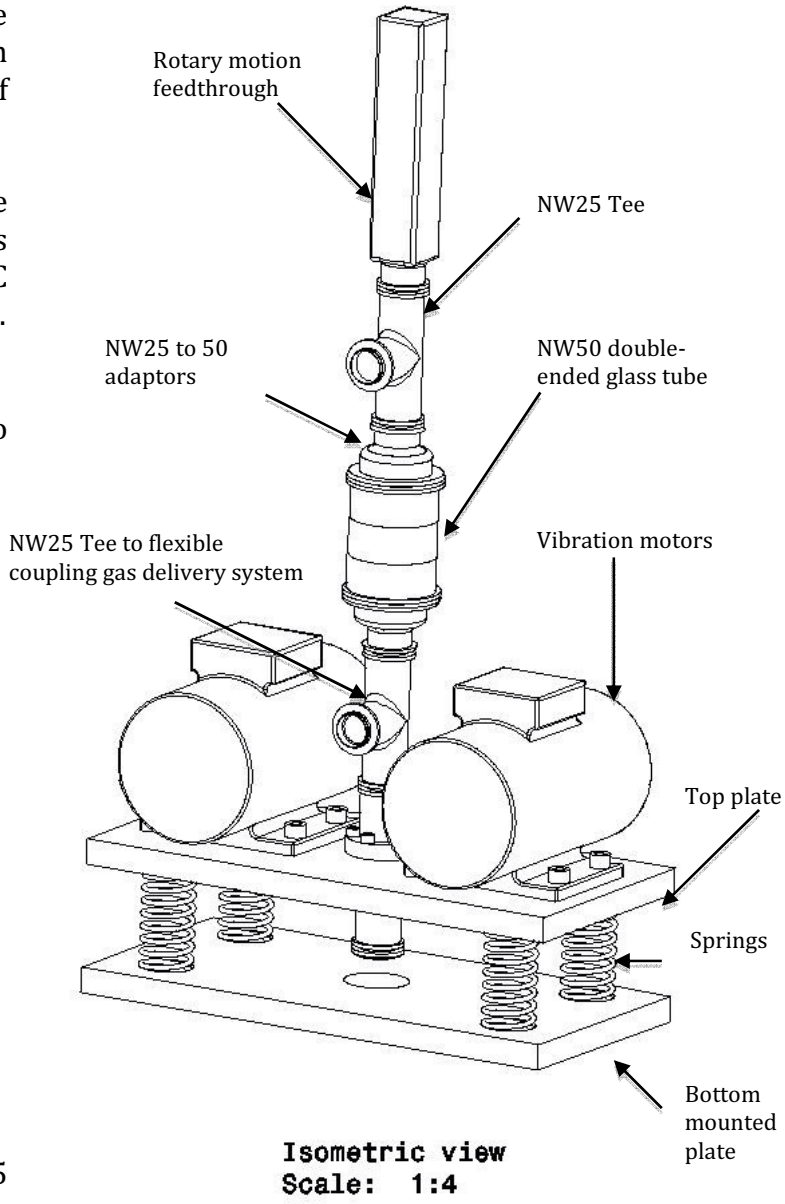

Figure 13: *Isometric view of the large charges FB design*

The difference from the old version of the FB is that we have added a mechanical vibrating system to improve the efficiency of the motion of a larger charge of particles. The Fluidized Bed is attached to the top plate (400mm x 200mm x 20mm / 15.7in x 7.87in x 0.78in) via the NW25 to Del-Seal flange with the two vibrators. *Martin Engineering Company* provides vibrators (see references below). These parts stand on four springs (4.4 N/mm spring straightness – 100mm free length – 3.8mm wire diameter and 38mm average diameter) with control and ensure the motion of the entire Fluidized Bed.

The complete system weighs 29.4kg/63.9lbs (5.4kg/11.9 lbs for the FB, 12kg/26.4 lbs for the two vibrators and 12kg/26.4 lbs for the steel support) and 30.53 inches long (775.68mm).

With this equipment, we calculate the maximum bed amplitude equal to 0.53 inches (13.52mm) with a vibrator frequency equal to 2Hz (120 RPM) with an unbalance of 0.0667 inches (1.7mm).

All of the physical and mechanical components (sizing of the springs, vibrators) are listed in an Excel computation program created especially for the development of this machine.

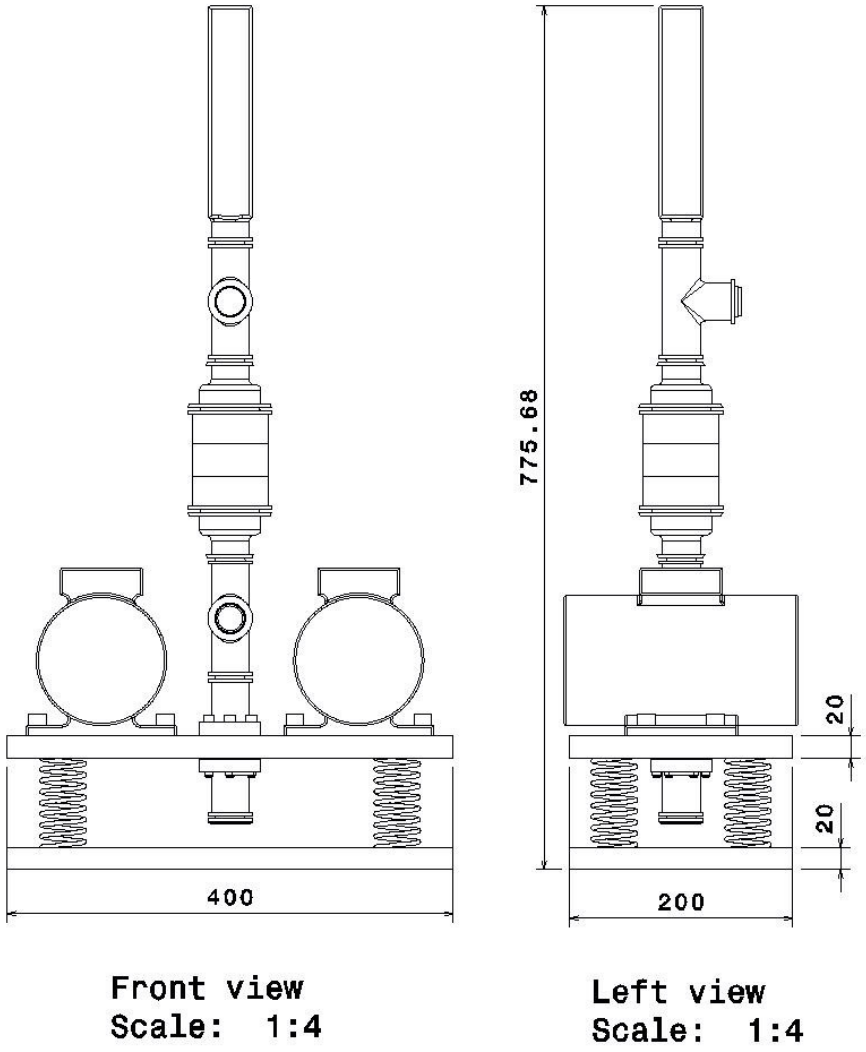

Figure 14: *Front and left view of the large charges FB design*

6. Computer Program

A computation program has been written under EXCEL software in order to control and get more understanding of the ALD chemical process and the mechanical behavior of the new designed Fluidized Bed Reactor.

Indeed, the software is made of three distinct parts:

1. Introduction of the ALD process
    - ALD machine parameters for coatings
2. Mechanical motion techniques for the FB-ALD system
    - Fluidized Bed ➔ Gas motion
    - Fluidized Bed ➔ Vibrator motion
    - Fluidized Bed ➔ Stirring motion
3. Misc
    - Budget

The first part of this program allows us to determine the minimum and necessary precursor's pulse time and nitrogen purge time to ensure the complete coating for any kind of sample. Indeed, with the actual ALD machine, we can coat a large scale of flat samples such as ceramic fiber, carbon/diamond plate, silica slabs…

The second part deals with the motion technologies designed for the good functioning of the Fluidized Bed Reactor.

To operate the "Fluidized Bed ➔ Gas motion" program, the user enter the different characteristics (dimensions of the quartz column, particle diameter, density of the particles, the weight of sample ready to boated and the ALD thickness) and the program automatically calculates the void fraction ε to determine the gas flow rate limits (lower: flow rate of fluidization and higher: flow rate of settling) to obtain a smooth fluidization state. This is achieved by first computing the friction factor thanks to the Ergun equation and the Reynolds number. By this way, we can determine the variation of pressure in the bed and complete the Kozeny-Carman and Stokes law equations to respectively finally obtain the minimal fluidization velocity and the flow rate of settling to prevent particles from carrying out of the system with the gas. The entire procedure can then be repeated for a variety of size column, charges and type of particles. Several parameters such as particles priority strongly affect the flow rates. To obtain the final results, we also consider the maximum weight of particles allowed in the bed for optimum coating results.

To operate the "Fluidized Bed ➔ Vibrator motion" program, the user enter the different parameters such as, the mass of the system (mainly composed by the weight of the Fluidized Bed, the vibrators and the custom-built support), the spring characteristics (the material, the spring pacing, the number of spring turn and the free length) and the details of the vibrator (frequency and imbalance). Then, the program will automatically calculate the parameters to design the spring and the vibrator. The amplitude of the bed is achieved by the determination of the spring straightness computing with the material, the mass applied on it, the rolling ratio (choice of three values – 6, 10, 16 – where the

value 6 means a thick and close wire and 16 is the opposite) and the number of spring turn (this determine the design of the end of the spring with two different states: loose close edges of only close edge) and physical/mechanical equations. Also, parameters listed before affect the mechanical behavior of the system. For instance, the imbalance of the vibrator and the spring straightness will change the resonance amplitude and the level of the stable state of vibrations. This procedure can be repeated for a variety of frequency of the vibrator to optimize the charge motion for better coating results.

To operate the "Fluidized Bed ➔ Stirring motion" program, the user set various characteristics (diameter of the quartz column, density of the particles, charge of particles, number of blade per stage, the height of the blade and the rotational speed of the blade) and the program automatically calculate the electrical power of the motor. This is achieve by first, computing the length of the bed determine by the charge of sample and then, extending to the particles friction force to result to the minimum necessary mechanical torque to mix the entire bed. Parameters such as the charge and the rotational speed affect the electrical power of the motor. However, it is important to highlight that the design of the blade strongly affects the particles friction force and so the result of the calculus. Indeed, to the design is attached the surface of the blade that is proportional to the friction force. Moreover, the rotational speed of the blade is determined by mixture industrial references. As far as concerned our system, it is recommended to get a velocity lower than 0.75 rd/s (equal to 7.5 rpm). To obtain the final result, we consider both the particles friction force caused by the charge and also the torque needed for the stirring so as to control the motion process.

At the end, this application establishes an estimation of the cost of such installation.

7. Estimates Costs/ Schedule

According to the previous study, we have listed in *Tables 1 and 2* (see appendix) the equipment that will be used to mount this small charge Atomic Layer Fluidized Bed Reactor. The cost is estimated to $3.680,31. Moreover, the revision A of the previous system composed by an additional pressure transducer is estimated to $4.024,31.

We also have listed in *Tables 3 and 4* (see appendix) the equipment that will be used to mount this large charge Atomic Layer Fluidized Bed Reactor. The cost is estimated to $7.054,27. Moreover, the revision A of the previous system composed by an additional pressure transducer is estimated to 8.188,27 dollars.

Moreover, it is estimated that it will take approximately 2-3 months to bring the system on line and to be in a position to encapsulate particles on a regular bases. During this period we expect to need two months to order all of the equipment and one additional month to mount the system, incorporate it to the existing gas machine and to make mechanical tests before the coating step.

8. Summary/Conclusion

We are now able to mount a device specially designed for the coating of large charge of micro particles. This device is called: Fluidized Bed Reactor. It has been really important to consider the forces existing between each particle, the agglomeration behavior of any charge in order to get a homogeneous distribution of the particle in the entire bed. Indeed, fluidization theoretical studies lead to the use of three different mechanical processes to stir the charges: gas, vibrator and stirring motion.

Moreover, these studies allowed us to clearly design and quote any part of the Fluidized Bed Reactor. The material to use (such as stainless steel), the vibrator characteristics (such as the imbalance, the frequency), the design of the springs to maintain the entire system in motion, and the motor to use for the stirring of the charge inside the bed of the reactor.

In addition to this work, a budget has been established and the cost was reduced as low as possible.

This entire work gives the opportunity to completely control the encapsulation of any kind of charge of particles.

References

- *"Flow through packed beds and fluidized beds"* by R. Shankar Subramanian
- *"Powder coating in a high pressure fluidized bed process"* by U.Teipel and H.Kröber
- *"Fluidized bed coating using RESS and ALD"* by Daniel Lepek
- *"Correlation of pressure drop and flow rate using packed beds"* by B.Hui, G.Kim, A.Edison, J.Kim, A.Chang
- *"Unit operations of chemical engineering"* by McCabe, Smith and Harriott
- *"Surface modification of nanoparticles using Atomic Layer Deposition in a fluidized bed reactor"* by Luis Felipe Hakim
- *"Coating particles with alumina nanolayers utilizing Atomic Layer Deposition in a fluidized bed reactor"* by Jeffrey R. Wank
- *"Fluidization of fine particles and its application"* by Chunbao Xu
- *"Introduction to Atomic Layer Deposition and Molecular Layer Deposition"* http://www.colorado.edu/chemistry/GeorgeResearchGroup/intro/IntroALD.pdf
- *"Correlation of Pressure Drop and Flow Rate Using Packed Bed"* http://rothfus.cheme.cmu.edu/tlab/pbeds/projects/t8s06/t8_s06_r1s2.pdf
- *"Diffustion and Reaction in Porous Catalysts - Fluidized Bed"* http://www.engin.umich.edu/~cre/12chap/html/12prof2a.htm
- *"Nanocoating Individual Silica Nanoparticles by Atomic Layer Deposition in a Fluidized Bed Reactor"* http://www.colorado.edu/chemistry/GeorgeResearchGroup/pubs/238.pdf
- http://www.nanodynamics.com/files/ALD.pdf
- http://www.icknowledge.com/misc_technology/Atomic%20Layer%20Deposition%20Briefing.pdf
- http://www.meca.insa-toulouse.fr/~paredes/Ressorts/Methodes/Compression/compression.htm (Spring design lessons)
- http://web.univ-pau.fr/~maron/mecanique/sommai.htm#sch1 (Vibratory mechanical lessons)

Appendix

Detailed view of the large charges FB design

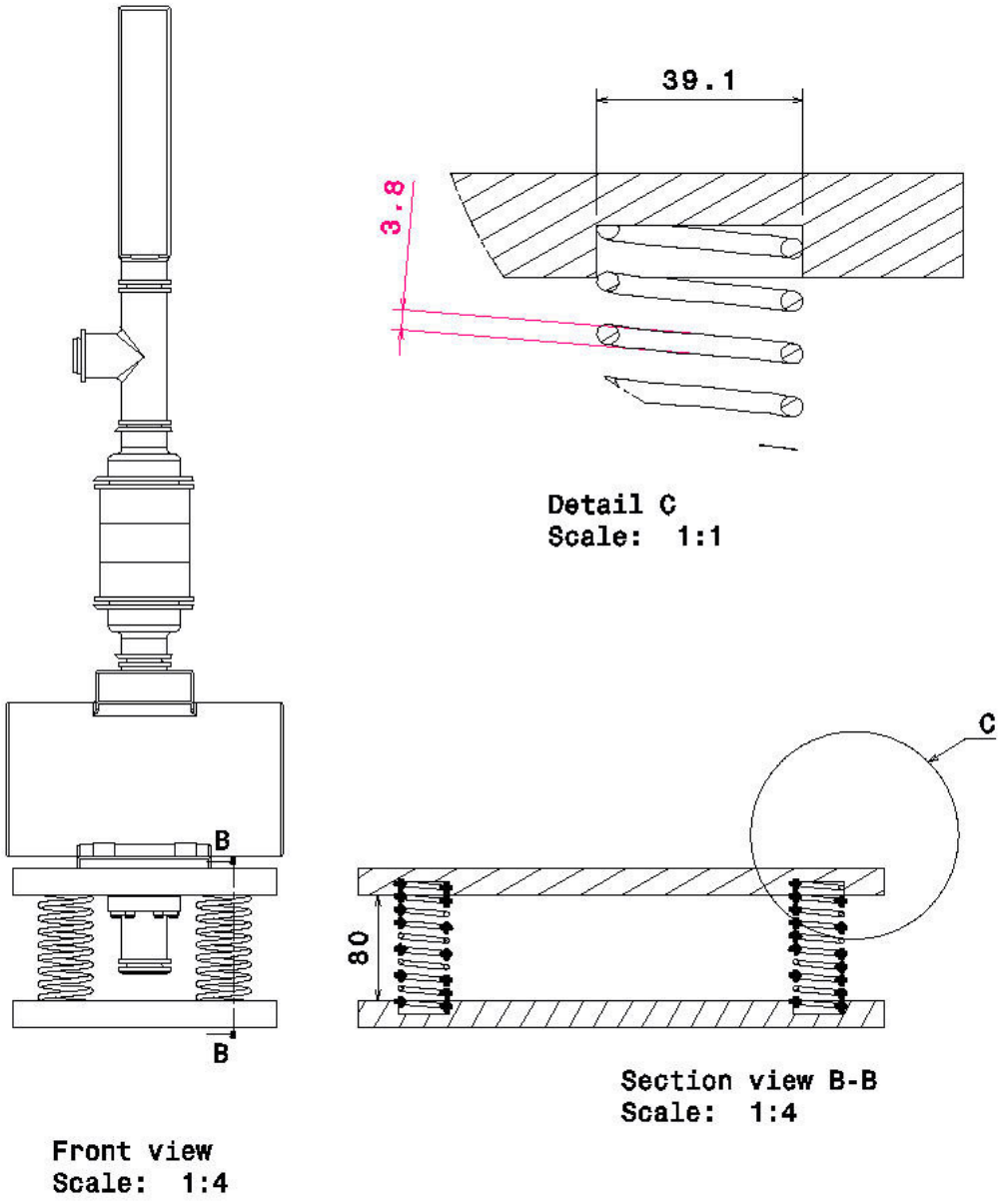

Figure 15: *Detailed view of the large charges FB design - Springs*

Budget of the small charge Fluidized Bed design (FB V1.0)

Type	Name of equipement	Supplier	Reference	Quantity needed	Unit Price
Vacuum parts	NW25 SS Tee	MDC	724001	2	$70,00
	NW25 to 50 SS Conical reducer	MDC	732008	2	$60,00
	NW25 SS Manual ball valve	LDS	KMBV-NW25-VE	2	$289,00
	NW50 SS double ended glass adapter	MDC	462023	1	$370,00
	NW25 SS Flexible couplings - thick wall	MDC	722021	1	$95,00
	NW25 Aluminium Hinged clamps	MDC	701001	12	$8,00
	NW50 Aluminium Hinged clamps	MDC	701003	2	$15,00
	NW25 SS O-ring	MDC	710001	12	$6,00
	NW50 SS O-ring	MDC	710003	2	$12,00
	NW25 Rotary motion FT	MDC	670000-02	1	$1 015
	Sleeve coupling	MDC	683000	1	$10,00
	Ground Stock - ASI-12	MDC	684001	1	$12,00
	NW25 SS Manual ball valve	MKS	1000158531	2	$395,00
Filter	SS Mesh - 140 micron - 6"x6"	Ted Pella	42-6110	2	$10,70
Mixing	Stirrer	VWR	59030-002	1	$40,96
Misc	90V DC Power supply	MPJA	9313-PS	1	$265,95
Total					**$3 680,31**

Table 1: *Budget of the small charge Fluidized Bed design (FB V1.0)*

Budget of the small charge Fluidized Bed design (FB V1.0 - Rev.A)
The system has been designed with the addition of a pressure transducer.

Type	Name of equipement	Supplier	Reference	Quantity needed	Unit Price
Vacuum parts	NW25 SS Tee	MDC	724001	2	$70,00
	NW25 to 50 SS Conical reducer	MDC	732008	2	$60,00
	NW25 to 16 SS Reducing nipples	MDC	732000	1	$39,00
	NW25 SS Manual ball valve	LDS	KMBV-NW25-VE	2	$289,00
	NW50 SS double ended glass adapter	MDC	462023	1	$370,00
	NW25 SS Four-way cross	MDC	725001	1	$110,00
	NW25 SS Flexible couplings - thick wall	MDC	722021	1	$95,00
	NW25 Aluminium Hinged clamps	MDC	701001	12	$8,00
	NW50 Aluminium Hinged clamps	MDC	701003	2	$15,00
	NW25 SS O-ring	MDC	710001	12	$6,00
	NW50 SS O-ring	MDC	710003	2	$12,00
	NW25 Rotary motion FT	MDC	670000-02	1	$1 015
	Sleeve coupling	MDC	683000	1	$10,00
	Ground Stock - ASI-12	MDC	684001	1	$12,00
	NW16 - 10 torr - Baratron Pressure Transducer	MKS	722B12TGA2FA	1	$985,00
Filter	SS Mesh - 140 micron - 6"x6"	Ted Pella	42-6110	2	$10,70
Mixing	Stirrer	VWR	59030-002	1	$40,96
Misc	90V DC Power supply	MPJA	9313-PS	1	$265,95
Total					**$4 024,31**

Table 2: *Budget of the small charge Fluidized Bed design (FB V1.0 – Rev.A)*

Budget of the large charge Fluidized Bed design (FB V2.0)

Type	Name of equipement	Supplier	Reference	Quantity needed	Unit Price
Vacuum parts	NW25 SS Tee	MDC	724001	2	$70,00
	NW25 to 50 SS Conical reducer	MDC	732008	2	$60,00
	NW25 SS Manual ball valve	LDS	KMBV-NW25-VE	2	$289,00
	NW50 SS double ended glass adapter	MDC	462023	1	$370,00
	NW25 SS Flexible couplings - thick wall	MDC	722021	1	$95,00
	NW25 Aluminium Hinged clamps	MDC	701001	12	$8,00
	NW50 Aluminium Hinged clamps	MDC	701003	2	$15,00
	NW25 SS O-ring	MDC	710001	12	$6,00
	NW50 SS O-ring	MDC	710003	2	$12,00
	NW25 SS Blank Flange	MDC	712001	1	$9,00
	Del-Seal Flange to NW25	MDC	730002	2	$66,00
	8" OD Del-Seal copper gasket - Pack of 10	MDC	191017	2	$53,00
	20 Plate nuts, 40 12-Pt. Bolts/Washer Pack	MDC	190052	1	$88,00
	NW25 Rotary motion FT	MDC	670000-02	1	$1 015
	Sleeve coupling	MDC	683000	1	$10,00
	Ground Stock - ASI-12	MDC	684001	1	$12,00
	NW25 SS Manual ball valve	MKS	1000158531	2	$395,00
Filter	SS Mesh - 140 micron - 6"x6"	Ted Pella	42-6110	2	$10,70
Mixing	Stirrer	VWR	59030-002	2	$40,96
	Vibrator	Martin Engineering	XHA-0.5T	2	$399,00
Misc	Screw CHC M1.4	-	-	4	$50,00
	Screw CHC M10	-	-	8	$75,00
	Springs (4.4N/mm)	-	-	4	$200,00
	Steel plate support (15.7in x 7.87 in x 0.78 in)	Home depot	-	2	$200,00
	Work to design the steel plates	-	-	1	$200,00
	90V DC Power supply	MPJA	9313-PS	1	$265,95
Total					**$7 054,27**

Table 3: *Budget of the large charge Fluidized Bed design (FB V2.0)*

Budget of the large charge Fluidized Bed design (FB V2.0 – Rev.A)
The system has been designed with the addition of a pressure transducer.

Type	Name of equipement	Supplier	Reference	Quantity needed	Unit Price
Vacuum parts	NW25 SS Tee	MDC	724001	2	$70,00
	NW25 to 50 SS Conical reducer	MDC	732008	2	$60,00
	NW25 SS Manual ball valve	LDS	KMBV-NW25-VE	2	$289,00
	NW50 SS double ended glass adapter	MDC	462023	1	$370,00
	NW25 SS Flexible couplings - thick wall	MDC	722021	1	$95,00
	NW25 Aluminium Hinged clamps	MDC	701001	12	$8,00
	NW50 Aluminium Hinged clamps	MDC	701003	2	$15,00
	NW25 SS O-ring	MDC	710001	12	$6,00
	NW50 SS O-ring	MDC	710003	2	$12,00
	NW25 SS Blank Flange	MDC	712001	1	$9,00
	Del-Seal Flange to NW25	MDC	730002	2	$66,00
	8" OD Del-Seal copper gasket - Pack of 10	MDC	191017	2	$53,00
	20 Plate nuts, 40 12-Pt. Bolts/Washer Pack	MDC	190052	1	$88,00
	NW25 Rotary motion FT	MDC	670000-02	1	$1 015
	Sleeve coupling	MDC	683000	1	$10,00
	Ground Stock - ASI-12	MDC	684001	1	$12,00
	NW25 SS Manual ball valve	MKS	1000158531	2	$395,00
	NW16 - 10 torr - Baratron Pressure Transducer	MKS	722B12TGA2FA	1	$985,00
	NW25 SS Four-way cross	MDC	725001	1	$110,00
	NW25 to 16 SS Reducing nipples	MDC	732000	1	$39,00
Filter	SS Mesh - 140 micron - 6"x6"	Ted Pella	42-6110	2	$10,70
Mixing	Stirrer	VWR	59030-002	2	$40,96
	Vibrator	Martin Engineering	XHA-0.5T	2	$399,00
Misc	Screw CHC M1.4	-	-	4	$50,00
	Screw CHC M10	-	-	8	$75,00
	Springs (4.4N/mm)	-	-	4	$200,00
	Steel plate support (15.7in x 7.87 in x 0.78 in)	Home depot	-	2	$200,00
	Work to design the steel plates	-	-	1	$200,00
	90V DC Power supply	MPJA	9313-PS	1	$265,95
Total					**$8 188,27**

Table 4: *Budget of the large charge Fluidized Bed design (FB V2.0 – Rev. A)*